UNIVERSITÀ DEGLI STUDI DELL'INSUBRIA
Facoltà di Scienze, Como - Dipartimento di Fisica e Matematica

DOTTORATO DI RICERCA IN FISICA E ASTROFISICA
XXII CICLO

OPTIMIZATION OF THE SINGLE MODULE OF DETECTION FOR THE CUORE-0 EXPERIMENT

THESIS SUBMITTED
BY

Chiara Salvioni

A doctoral dissertation in partial fullfillment
of the requirements to obtain the Degree of
Doctor Philosophiae in Physics

June 2010

Supervisor: **Prof. Andrea Giuliani**
Program Coordinator: **Prof. Philip G. Ratcliffe**

To things that happen and to what
we say about them, remembering that

“Capacity to terminate
is a specific grace”

-Emily Dickinson

Contents

Introduction

Neutrino physics is nowadays one of the most discussed research fields in the study of the fundamental constituents of matter and their interactions. Its popularity has been increasing in the last years, supported by the wealth of experimental facts that have given model-independent proof of neutrino oscillations: the observation of oscillating neutrinos, first discovered by SuperKamiokande, then confirmed by SNO, has contributed significantly in pushing the efforts of the physics community towards a revision of the Standard Model. The fact that neutrinos oscillate between flavours can be understood only if a mixing mechanism, similarly to what happens in the hadronic field, is introduced, which leads directly to the request that these particles are admitted to be massive; and, for the Standard Model to incorporate non-zero neutrino masses, a certain number of its foundations should be relaxed. Among them, the redefinition of neutrinos as equal to their own anti-particles, which is a condition defined as "Majorana nature", is particularly appealing to theorists.

Experiments on flavour oscillations by neutrinos will shortly follow the path of precision measurements. This perspective, however, although needed, does not lead to any radical clarification about the topics that are still open today: a measurement on oscillating neutrinos does not quantify their mass eigenvalues but only the difference between their squares, nor it is capable of determining which nature, Majorana or Dirac, is valid for them. The values of squared mass differences obtained by these experiments are compatible with three possible scenarios: one where all masses are of order $\sim$1 eV and very similar to each other, and two that require one mass to be much smaller (inverse hierarchy) or larger (normal hierarchy) than the other ones. It is true that the absolute values of neutrino mass eigenvalues could be determined by cosmological measurements or by end-point study in single β-decay, but the first is model-dependent and the second one cannot identify the correct nature.

The only instrument capable of answering these questions at once is the search for Neutrinoless Double Beta Decay (0ν-DBD). The observation of this very rare nuclear decay would put a lower limit on the mass of the electron neutrino, would clarify which mass scenario holds, and would imply that neutrinos are Majorana particles. In fact, 0ν-DBD is assumed to occur by exchange of a light Majorana neutrino and would be impossible in the Dirac case; however, it has been proved that witnessing a 0ν-DBD would always mean that neutrinos are Majorana fermions, even if the dominant mechanism differs from the one mentioned above. Moreover, the conservation of lepton number would be violated.

The decay, which is possible for nuclides where single-β is energetically forbidden, is very rare and has never been observed, apart from a discussed claim on ^{76}Ge. Experiments on 0ν-DBD can explore a range of values for a peculiar combination of neutrino mass eigenvalues called *effective Majorana mass* $m_{\beta\beta}$: current researches have explored the region of $m_{\beta\beta}$ that would hold in the case of similar masses, but must now

move down to effective Majorana mass values of order 0.1 meV. The goal is very challenging. Due to the rarity of the decay (foreseen half-lives are higher than 10^{20} years) large quantities of nuclides must be observed for long times, and in an environment free of radioactive contaminants whose counting rates could mask the ones searched for.

0ν-DBD, in principle, is marked very clearly in the spectrum obtained by summing over the energies of both the electrons emitted in the decay. One should look for a peak at the Q-value of the decay enlarged only by the finite energy resolution of the detector; many different techniques are suitable to approach the problem. One of the most promising detection strategies relies on the use of macro-bolometers, which are phonon-mediated detectors with mass of order 1 kg operating at extremely low temperatures ($\sim$10 mK). Bolometers are feasible and guarantee outstanding energy resolutions. The Cuoricino experiment, a tower of 62 bolometers, has searched for the 0ν-DBD of ^{130}Te from 2003 to 2008 at the Italian Gran Sasso National Laboratory, reaching one of the best sensitivities on $m_{\beta\beta}$ of the old generation. Its descendant for the investigation of the inverted hierarchy region will be the CUORE experiment.

CUORE will start taking data in 2013 and will be constituted by nineteen Cuoricino-like towers, increasing the total mass of a factor 20. The possibility for CUORE to enter the inverted hierarchy range depends on many factors. A mere increase in mass would not be sufficient, and time would also cease to be effective after a few years of data-taking. Therefore, a thorough review of all the detector's aspects is necessary, from the parameters related more directly to the sensitivity of the experiment, to detection performances, paying also attention to the modularity of the final array which becomes extremely relevant when such a large number of bolometric units is to be assembled and operated. The starting point is fixed, of course, by the achievements gained by Cuoricino in the technique's application. An intermediate step will precede the beginning of CUORE: its first tower will be cooled-down and measured as a stand-alone experiment, with the beginning of data-taking foreseen in the first part of 2011. CUORE-0 will provide an imminent verification of the R&D work performed, but will also constitute a powerful experiment on its own, capable of improving the limit on $m_{\beta\beta}$ fixed by Cuoricino. The precise focus of the Ph.D. work that I pursued in the last three years and will present in this thesis is, therefore, the optimization of the single module of detection in the view of the incoming CUORE-0, which will validate the innovations for their introduction in CUORE.

The Ph.D. activity has been performed both at the Insubria University's Cryogenics Laboratory in Como, with the development of small prototypes and preliminary tests, and at the Gran Sasso National Laboratory, where bolometers of the ultimate size have been operated in conditions similar to those of the final experiment. My work focused on optimizing some crucial aspects of the single module of detection in Cuoricino, by contributing in the following R&D activities: the fight against the background contribution in the range of interest due to surface contaminations of the materials surrounding the detector; the uniforming of protocols for the production and processing of energy absorbers (aiming at an increase of both bolometric performances and radio-purity); a striking innovation in the geometry of the semiconductor sensors that convert temperature pulses in voltage signals; a dedicated study aiming at optimizing and automating the coupling between the energy absorbers and the sensors, which is a delicate point in the determination of performance reproducibility. The tuning of all of these aspects, as will be seen in the course of this thesis, is necessary for CUORE to reach the goal of sensitivity to $m_{\beta\beta}$ in the range of inverted hierarchy.

Chapter 1

Neutrinoless Double Beta Decay in theory and practice

"Man has to know, man has to remember
that there is no empty space from sky to the ground
but all is filled with crowds and multitudes" [1]

The existence of neutrinos, neutral leptons, was first proposed in 1931 by W. Pauli, who tried to find a theoretical interpretation for the continuous energy spectrum of electrons in β-decay. E. Fermi [2] relied on Pauli's idea when he developed his theory of β-decay, published in 1934. The properties of neutrinos were investigated with more depth in the Fifties with parity violation, hypothesized by Lee and Yang [3] and experimentally proved by Wu in 1956: neutrinos were determined to possess left-handed helicity and anti-neutrinos right-handed helicity, a characteristic not shared by other particles in the Standard Model (SM). Reines and Cowan [4] observed for the first time in 1959 the existence of anti-neutrinos with electronic flavour in an experiment at a nuclear reactor; in 1962, experiments at the Brookhaven laboratory and at CERN discovered that neutrinos produced in association with muons behave distinctly from those associated to electrons, and therefore the first two flavours of these particles could be distinguished. The existence of the third flavour, which identifies neutrinos associated to τ leptons, was then proposed [5].

Many questions regarding the nature and property of neutrinos are still open. One of the hot topics in particle physics concerns the possibility for neutrinos to have non-zero mass, similarly to charged fermions. In the construction of the Standard Model, the absence of experimental observations in favour of massive neutrinos became a postulate. The assessment was coherent with the empirical fact that the single leptonic flavours seemed to be conserved, together with lepton number. Nonetheless, a general consensus exists today regarding the search for extensions of the SM. Various pictures beyond the SM foresee the existence of a non-zero neutrino mass, as well as other consequences on the nature of this particle.

Experimental hints concerning the existence of neutrino mass began to be collected in 1968, when Homestake, the first experiment aimed at detecting solar neutrinos, observed less than half of the particles expected [6]. While the initial explanation was based on the inadequacy of the Standard Solar Model, the assumption that electronic neutrinos had converted to something different started to gain strength. This approach has been investigated in the last years and is supported by the wealth of information about oscillating neutrinos. This was the starting point for the development of new theo-

ries, still under discussion, regarding the characteristics of these particles. In particular, we will see that the observation of oscillating neutrinos is strictly connected to the fact that they are massive.

1.1 Introducing the neutrino puzzle

The Standard Model of elementary particles and their fundamental interactions provides accurate descriptions of all known particle physics phenomena and has successfully passed many precise experimental tests. The SM is a renormalizable gauge theory that assumes the local gauge invariance of the Lagrangian under the transformations of $SU(3)_C \otimes SU(2)_L \otimes SU(1)_Y$. In this theory, the fundamental particles are all fermions. A free fermion with spin 1/2 may be represented by a four-component spinor field ψ which satisfies the Dirac equation, and may be decomposed in two chiral projections. The chiral projectors are operators defined as

$$P_{L,R} = \left[\frac{1 \mp \gamma^5}{2}\right] \tag{1.1}$$

The chiral operator γ^5 is the product $i\gamma_0\gamma_1\gamma_2\gamma_3$ of Dirac matrices. A four-components spinor ψ, eigenstate of the Hamiltonian, can therefore be decomposed as a sum of a *left* or *right* component $\psi = \psi_L + \psi_R$ according to $\psi_{L,R} = P_{L,R}\psi$. The two projections are characterized by having defined chirality, as $\gamma^5\psi_R = +\psi_R$ and $\gamma^5\psi_L = -\psi_L$.

Neutrinos are neutral particles: there is no way, hence, to define an intrinsic quantum number that operates a distinction between a neutrino and its anti-particle as, for example, in the case of an electron. However, one can consider helicity, which is defined as the projection of the particle's spin $\vec{\sigma}$ along its momentum $\vec{p}$:

$$H = \frac{\vec{\sigma} \cdot \vec{p}}{|\vec{p}|} \tag{1.2}$$

Helicity is not strictly a good quantum number: should the particle be massive, an observer travelling at higher speed would see its helicity flip sign. Neutrinos, as already mentioned, were introduced in the SM as massless, which means that helicity can be used to separate them from their antiparticles:

$$H(\nu) = -1 \qquad H(\overline{\nu}) = +1 \tag{1.3}$$

In the case of $m = 0$ helicity is the same as chirality, because a right-handed or left-handed helicity eigenfield is also a right-handed or left-handed chirality eigenfield [7]. Therefore, if the zero-mass condition holds, all neutrinos are left-handed and anti-neutrinos are right-handed. Besides helicity, another quantum number can be used for the distinction of ν and $\overline{\nu}$ starting from the phenomenology of this particle's interactions: lepton number. In fact, given the generic lepton l associated to the neutrino ν_l,

$$\nu_l + X \rightarrow l^- + Y \qquad \overline{\nu_l} + X \rightarrow l^+ + Z \tag{1.4}$$

This behaviour allows to use lepton number, which is conserved in all the interactions of the SM, as a good quantum number in the neutrino vs. anti-neutrino issue:

$$L(\nu_l, l^-) = -1 \qquad L(\overline{\nu_l}, l^+) = +1 \tag{1.5}$$

We will see later that the use of the previously defined quantum numbers fails under the new conditions on these particles unveiled by experimental observations.

In view of the considerations made above, the neutrino content of the SM includes the three left-handed particles ν_l ($l = e, \mu, \tau$), which, together with their corresponding left-handed charged leptons, are doublets under the SU(2)$_L$ gauge symmetry:

$$L_l \equiv \begin{pmatrix} \nu_{lL} \\ l_L \end{pmatrix} \tag{1.6}$$

At the same time, no right-handed neutrinos are included in the SM, and the right-handed charged leptons l_R are singlets under SU(2)$_L$. The postulate of the absence of a right-handed counterpart implies immediately that neutrinos are massless in the SM. This is explained by reminding the Higgs process of mass generation. Given the Higgs doublet

$$\Phi \equiv \begin{pmatrix} \phi^+ \\ \phi^0 \end{pmatrix} , \tag{1.7}$$

the Yukawa interaction term in the Lagrangian is gauge invariant. In the mechanism that generates the mass of a charged lepton l, with $l = e, \mu, \tau$, the Yukawa term is

$$\mathscr{L}_{\text{Yukawa}} = -\lambda \overline{L_l} \Phi l_R = -\lambda(\overline{\nu_{lL}}\phi^+ + l_L\phi^0) l_R + \text{h.c.} \tag{1.8}$$

λ is an adimensional Yukawa coupling coefficient. When, following the spontaneous symmetry breaking, the Higgs doublet takes the vacuum expectation value $\langle \Phi \rangle = (0, v/\sqrt{2})$, the Yukawa interaction generates a mass contribution of the form

$$\mathscr{L}_{\text{Yukawa}} = -\frac{\lambda v}{\sqrt{2}} (\overline{l_L} l_R + \overline{l_R} l_L) \tag{1.9}$$

The expression reported in Eq. (1.9) is called a *Dirac mass term* and involves both left-handed and right-handed fields: the previous mechanism generates all fermionic masses in the SM apart from neutrinos, for which the Yukawa interaction cannot give rise to a mass term because no right-handed neutrinos are included in the model. There are other two independent reasons for neutrino mass being zero in the SM, which will only be mentioned in this context: namely, there are only Higgs doublets of SU(2)$_L$ and non-renormalizable interactions are excluded [8]. All these conditions apply in the SM, so that neutrinos are included as massless fermions inside its framework.

1.1.1 A theory with neutrino masses

However, something is missing in the picture, as there are a number of experimental hints for neutrinos being massive particles: a brief review will be given in Sec. 1.1.2. To generate neutrino masses, one or more of the conditions mentioned at the end of the previous section must be relaxed.

The first approach to the problem consists in asking what mass terms other than Dirac's can be generated for the neutrino, without considering the introduction of a right-handed component in the model. Let's define ν_L and ν_R as the vectors of left-handed and right-handed neutrino fields

$$\nu_L = \begin{pmatrix} \nu_{eL} \\ \nu_{\mu L} \\ \nu_{\tau L} \end{pmatrix} \quad \nu_R = \begin{pmatrix} \nu_{eR} \\ \nu_{\mu R} \\ \nu_{\tau R} \end{pmatrix}$$

One can try to construct a term involving fields with equal chirality, using the charge conjugate spinor:

$$\bar{\psi}^C \psi + \overline{\psi} \psi^C , \tag{1.10}$$

where $\psi^C \equiv \mathscr{C}\overline{\psi}^T$ and $\mathscr{C}$ is the charge-conjugation matrix. This is called a *Majorana mass term* and it is possible just for neutrinos, because it is invariant under the electromagnetism gauge symmetry U(1) only if the particle is neutral. However, Majorana masses for ν_L are forbidden in the SM: in fact, the Higgs field forms a doublet Φ, neutrinos are part of a lepton doublet L and the gauge invariance $SU(2)_L \otimes U(1)_Y$ forbids a Yukawa interaction like ΦLL. Majorana mass terms of the type described before arise only if possibilities external to the SM are worked out. For example, neutrino Majorana masses can originate from operators $\Phi\Phi LL$ involving two Higgs doublets and two lepton doublets, which, being of higher order, must be suppressed by some large mass scale M. The result is not renormalizable. When the Higgs doublets take the vacuum expectation value, the Majorana mass term $v^2/(2M) \cdot (\overline{\nu}_L^C \nu_L + \text{h.c.})$ is generated for ν_L. Summing up, if ν_R is not introduced in the model no Dirac mass terms appear; nonetheless, opening the door to non-renormalizable terms, a Majorana term is generated which introduces a new mass scale M. The large Higgs vacuum expectation value, $\sim$175 GeV, can lead to small neutrino masses provided that the new scale is large enough: should M be comparable to the GUT scale, $\sim 10^{16}$ GeV, then neutrino masses would be of order $\sim \lambda_\nu \cdot 10^{-3}$ eV. We will see later some fundamental implications of the existence of a Majorana mass term.

Given the implications of the introduction of a Majorana mass term for ν_L, the most straightforward approach is to allow right-handed neutrinos ν_R into the model. This leads to the generation of a Dirac mass term by the same Higgs mechanism that holds for charged leptons and quarks:

$$\mathscr{L}_D = -m_D(\overline{\nu_L}\nu_R + \text{h.c.}) \tag{1.11}$$

It should be noticed that, if neutrino masses are generated with this mechanism, it is very difficult to understand why, as we will see later, they are estimated to be five orders of magnitude smaller than m_e. But the Dirac term is not the only mass contribution to be born when ν_R is incorporated in the model. In order to construct the most general gauge invariant and renormalizable Lagrangian, the Majorana mass term

$$\mathscr{L}_M = -\frac{1}{2} M_R(\bar{\nu}_R^C \nu_R + \text{h.c.}) \tag{1.12}$$

should also be included. As already mentioned, the term is allowed because ν_R is electrically neutral; as opposed to the ν_L case, it is also permitted by the symmetries of the SM, being ν_R a singlet of $SU(3)_C \otimes SU(2)_L \otimes SU(1)_Y$. The most general mass term to be allowed in the SM model is therefore $\mathscr{L}_{D+M} = \mathscr{L}_D + \mathscr{L}_M$. The consequence of having the two mass terms described by equations (1.11) and (1.12) can be understood by writing

$$\mathscr{L}_{D+M} = -\frac{1}{2} N_L^T \mathscr{C}^\dagger M N_L + \text{h.c.}\,, \tag{1.13}$$

where $N_L = (\nu_L, \nu_R^C)$ is the column matrix of left-handed chiral fields, $\mathscr{C}$ is the charge conjugation operator and

$$M = \begin{pmatrix} 0 & m_D \\ m_D & M_R \end{pmatrix} \tag{1.14}$$

is the symmetric mass matrix, which can be diagonalized in order to obtain

$$\mathscr{L}_{D+M} = \sum_i m_i \overline{\nu}_i \nu_i \tag{1.15}$$

If M_R is non-zero, the fields of definite mass satisfy the condition $\nu_i = \nu_i^C$: this is known as the *Majorana condition* [9], generally written as

$$\psi = \psi^C \tag{1.16}$$

The previous formula translates into $\psi_R = \psi_L^C$, which means that the left-handed and the right handed component are not independent. Hence, a *Majorana particle*, which is a particle for which the Majorana condition holds, can be described by a spinor with just two components; not only that: lepton number is violated, as the consequence of Eq. (1.16) is that $L(\psi) = -L(\psi^C)$. Lepton number is not a good instrument anymore to separate neutrinos from anti-neutrinos; and the distinction based on helicity does not hold anymore, in accordance with what discussed in Sec. 1.1, as neutrinos are not massless in this picture. If neutrinos are Majorana particles, then they coincide with their anti-particles.

Let's focus on lepton number. The $\mathscr{L}_D$ term conserves L, in accordance to the rest of the SM, and each neutrino differs from its antiparticle by condition (1.5). The ν_l-$\overline{\nu_l}$ complex is referred to as a *Dirac neutrino*. The situation is different as far as $\mathscr{L}_M$ is concerned, because, as seen, it mixes ν and $\overline{\nu}$ and thus does not conserve L. However, the conservation of L is not considered inviolable, as it is an accidental symmetry of the SM: it is not required in the construction of the model; it is obtained naturally from gauge invariance and renormalization, and it doesn't have the strength of the gauge symmetry which determines an interaction. Summing up: the introduction of ν_R in the picture implies that a Majorana mass term can be written, which in turn means that helicity cannot be used as distinctive quantum number, that lepton number is not conserved and that neutrinos coincide with anti-neutrinos.

Getting back to Eq. (1.15), the mass-eigenstate neutrinos are Majorana particles, whereas they are of the Dirac type if M_R=0. Now, the orders of magnitude difference that neutrino masses show in respect to the other particles can be explained: it the so-called Seesaw mechanism that allows this [10], [11]. It depends by the fact that the Majorana mass can assume arbitrarily large values as opposed to m_D, which is expected to be of the same order of magnitude as the other fermions because it is generated by the Higgs process. When $M_R \gg m_D$, the mass eigenstates of the Lagrangian are $m_1 \sim m_D^2/M_R$ and $m_2 \sim M_R$, with $\nu_1 \sim \nu_L$ and $\nu_2 \sim \nu_R^C$. Therefore, it is the large mass of the unobserved particle ν_R to determine the small mass of the observed particle ν_L.

1.1.2 Oscillating flavours

Let's imagine a W^+ decay in which a lepton and a neutrino of defined flavour are produced:

$$W^+ \rightarrow l + \nu_l\,, \qquad l = e, \mu, \tau \tag{1.17}$$

Suppose that ν_l travels a distance L and eventually interacts with matter producing a lepton in the final state. According to SM, the resulting charged lepton will be l again; however, it is possible to imagine a beyond-SM picture where the produced lepton has a different flavour l'. This change of properties involved in the interaction of neutrinos with matter is called *flavour oscillation* and has been observed clearly by various experiments during the last years. The reason underlying neutrino flavour oscillations can be found by first considering that the three weakly-interacting neutrinos are linear combinations of the neutrinos with definite mass, which can be expressed in terms of states by:

$$|\nu_l\rangle = \sum_{i=1}^{n} U_{li}^* |\nu_i\rangle \tag{1.18}$$

In other words, a flavour eigenstate is a linear combination of mass eigenstates [12]. In the previous equation, U is a unitary matrix called the Pontecorvo-Maki-Nakagawa-Sakata (PMNS) matrix [13], [14]. The PMNS matrix is the leptonic counterpart of the CKM matrix that acts in the hadronic environment. It should be noted that if "sterile" neutrinos are considered, which don't participate in the SM weak interactions, then the number of neutrinos of definite mass can be more than three; in accordance with experimental results, however, the subset of U with n=3 can be considered: it is approximately unitary and it can be parametrized by introducing three mixing angles θ_{12}, θ_{13}, θ_{23}, the phase δ to account for CP violation and two Majorana phases α_1 and α_2, which have observable consequences only if neutrinos are Majorana particles. The resulting standard parametrization of U is

$$U = \begin{pmatrix} c_{12}c_{13} & s_{12}c_{13} & s_{13}e^{-i\delta} \\ -s_{12}c_{23} - c_{12}s_{23}s_{13}e^{i\delta} & c_{12}c23 - s_{12}s_{23}s_{13}e^{i\delta} & s_{23}c_{13} \\ s_{12}c_{23} - c_{12}c_{23}s_{13}e^{i\delta} & -c_{12}s23 - s_{12}c_{23}s_{13}e^{i\delta} & c_{23}c_{13} \end{pmatrix} \times \begin{pmatrix} e^{i\alpha 1/2} & 0 & 0 \\ 0 & e^{i\alpha 2/2} & 0 \\ 0 & 0 & 1 \end{pmatrix} \tag{1.19}$$

In the previous notation, c_{ij} and s_{ij} are used for convenience in place of $\cos\theta_{ij}$ and $\sin\theta_{ij}$. Flavour oscillations arise because neutrinos are produced and absorbed in weak interactions as mixtures of states with different masses. Experiments designed to observe neutrino oscillations are not able to give information on the absolute value of neutrino masses, but only on the difference between the squares of neutrino mass eigenvalues. This is proved by computing the probability that a neutrino ν_l, with initial energy E, interacts with a target after travelling a length L producing a charged lepton with different flavour l'. In order to do so, the general case of three generations can be restricted to the subset of two neutrino flavors ν_l and $\nu_{l'}$, and two mass eigenstates ν_1 and ν_2: two-neutrino mixing is a good approximation allowed by current experiments, as will be seen later in this section. Given this approximation, the probability of detecting a neutrino with flavour l' when the initial particle is ν_l is

$$P(\nu_l \to \nu_{l'}) = \sin^2(2\theta)\sin^2\left(\frac{\delta m^2}{4E}\cdot L\right) \tag{1.20}$$

The probability $P(\nu_l \to \nu_{l'})$ oscillates as a function of L/E. The oscillating behaviour is due to the interference between two different mass eigenstates; the phase of the interference is proportional to the term $\delta m^2 = m_2^2 - m_1^2$, which confirms the previous note about oscillation experiments being able to provide information only on squared-mass differences but not on their absolute values. Fig. 1.1 shows a representation of the mass states of ν_μ with oscillating amplitudes.

Historically, the first experiment that gave evidence of neutrino flavour oscillations was the Homestake experiment, proposed by R. Davis and started in 1968. Homestake [6] observed a deficit of approximately 2/3 in the flux of solar electron neutrinos expected according to the Standard Solar Model (SSM), and was followed by other experiments (Gallex, SAGE and GNO) [19]. Their results suggested to B. Pontecorvo the idea of oscillating solar neutrinos. The Subdury Neutrino Observatory (SNO) experiment [20] confirmed that electron neutrinos were converted into other flavours by comparing charged current reactions, sensitive only to ν_e, to neutral current reactions, sensitive to all flavours. A summary of data on solar neutrinos compared to the SSM, with and without neutrino oscillations, is shown in Fig. 1.2. Experiments on other neutrino sources also gave evidence of oscillations. Among the most remarkable examples,

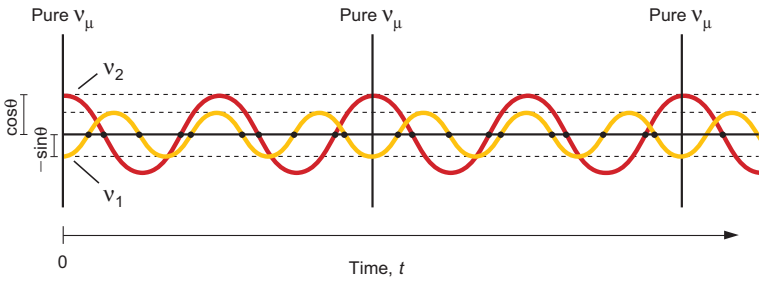

Figure 1.1: The amplitudes of the mass states of a ν_μ produced at $t = 0$ are shown oscillating in time: according to their phase relationship, they compose a pure ν_μ or a mixture of ν_μ and ν_e [15].

Super-Kamiokande investigated atmospheric neutrinos and observed a difference between the flux of downward-going and the flux of upward-going ν_μ, which has been explained by their oscillation into ν_τ; KamLAND observed the oscillations of anti-electron neutrinos emitted by nuclear reactors for the first time in 2002, and reconstructed a clear pattern which is shown in Fig. 1.3. The following values summarize the current status in the experimental research on neutrino oscillations, in terms of mixing angles and square masses differences [21]:

- $\delta m^2_{\text{sol}} = \delta m^2_{21} = 7.65^{+0.23}_{-0.20} \times 10^{-5}\text{eV}^2$
- $\delta m^2_{\text{atm}} = \left|\delta m^2_{23}\right| = 2.40^{+0.12}_{-0.11} \times 10^{-3}\text{eV}^2$
- $\sin^2\theta_{\text{sol}} = \sin^2\theta_{12} = 0.304^{+0.022}_{-0.016}$
- $\sin^2\theta_{\text{atm}} = \sin^2\theta_{23} = 0.50^{+0.07}_{-0.06}$
- $\sin^2\theta_{13} = 0.010^{+0.016}_{-0.011}$

Two-neutrino mixing is a good approximation for existing experiments because the value of θ_{13} turns out to be small, and δm^2_{sol} is very different from δm^2_{atm}. Various scenarios on neutrino masses are compatible with the results provided here. The relationship between m_1 and m_2 is known from the sign of the solar mass splitting, which leads to $m_2 > m_1$; on the other hand, the position of m_3 in respect to m_1, m_2 cannot be deduced because only the absolute value of the atmospheric mass splitting is measured by oscillation experiments. In this context, three scales of neutrino masses are allowed:

- *Quasi degenerate regime*: $m_1 \sim m_2 \sim m_3$, $m^2_{1,2,3} \gg \delta m^2_{\text{atm}}$
- *Normal hierarchy*: $m_1 \lesssim m_2 < m_3$
- *Inverted hierarchy*: $m_3 < m_2 \lesssim m_3$

The possible scales are summarized in Fig. 1.4 [18]. This picture adds to the questions that are still open in the field of neutrino physics. For example, the number of neutrino mass eigenstates is not known; the value of the masses m_i cannot be determined by oscillation experiments, and there is no clue on their hierarchy; the nature of the neutrino, whether it is a Majorana or Dirac particle, is yet to be cleared. Experimental alternatives to the investigation of flavour oscillations must be used.

As far the issue of absolute masses is concerned, three kinds of experimental researches provide information. One method consists in the study of the endpoint of the Beta Decay spectrum, whose shape is modified by the finite mass of the neutrino. The parameter measured by this kind of experiments is

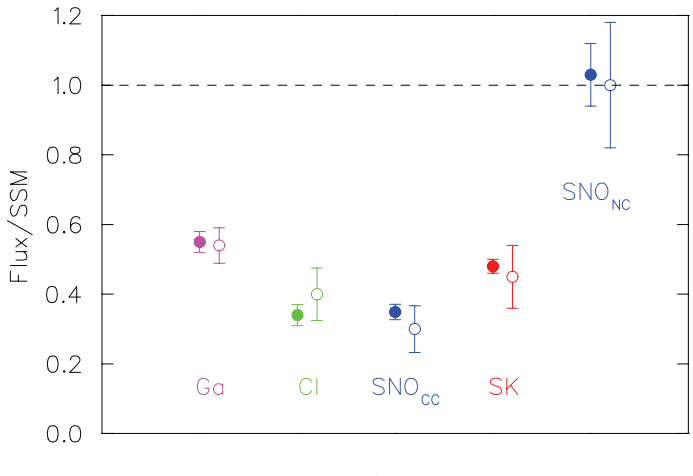

Figure 1.2: Ratio of solar neutrino flux to SSM (without neutrino oscillations) for various experiments. Filled circles are experimental data (with experimental uncertainties only) and open circles are theoretical expectations based on SSM with best fit parameters to KamLAND and solar-ν data. The two fluxes of CC and NC reactions measured by SNO are reported. [16]

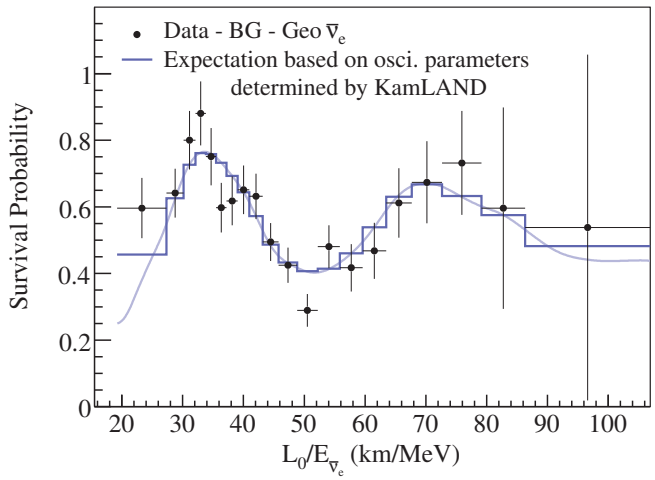

Figure 1.3: Observation of neutrino oscillations by KamLAND. Results are in good agreement with the expected survival probability of $\overline{\nu_e}$ [17].

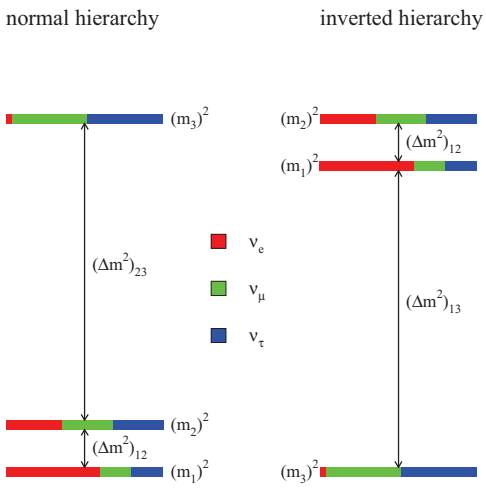

Figure 1.4: Hierarchy scenarios for neutrino masses, as depictable by taking into account results of oscillation experiments [18].

$$m_\beta^2 = \sum_{i=1}^{3} |U_{ei}|^2 m_i^2 \tag{1.21}$$

The main constraint on absolute neutrino masses in this field comes from the Mainz and Troitsk experiment and fixes an upper limit of 2.5 eV (95% C.L.) [22]. A stronger bound, although affected by being model-dependant, is given by cosmological constraints, which come from the observation of the Cosmic Microwave Background anisotropies and from the study of large scale structures; the constrained parameter is the sum of the three neutrino masses and it results $\sum m_i$ <0.67 eV (95% C.L.) [23]. The last kind of experimental investigation able to determine the values of absolute neutrino masses, but only if certain preliminary conditions are met, is the search for Neutrinoless Double Beta Decay (0ν-DBD), which defines the subset of neutrino physics where the work presented in this thesis has been performed. An observation of this rare decay would provide information not only on the absolute neutrino masses, but also on the unsolved puzzle of the Majorana or Dirac nature of this particle.

1.2 0ν-DBD: the needle in the haystack

Double Beta Decay (DBD) is a rare spontaneous nuclear transition, whose existence was first proposed by Maria Goeppert–Mayer in 1935 [24]. In this transition, a nucleus (A,Z) changes the nuclear charge of two units maintaining the same mass number, becoming therefore a (A,$Z\pm2$) nucleus. Suppose that an (A,Z+2) nuclide appears in the final state. Normally DBD is not favored in respect to single β-decay: the transition is observable only when the nuclide has single β-decay either energetically forbidden (which occurs when the intermediate (A,Z+1) nucleus has a binding energy greater than the (A,Z) and (A,Z+2) nuclei) or suppressed by a large change of the nuclear spin–parity state.

This situation can be understood by looking at the Weizsäker expression for the atomic mass as a function of the mass number A and the number of neutrons N and protons Z. In particular, the Weizsäker formula contains the “pairing” term that takes

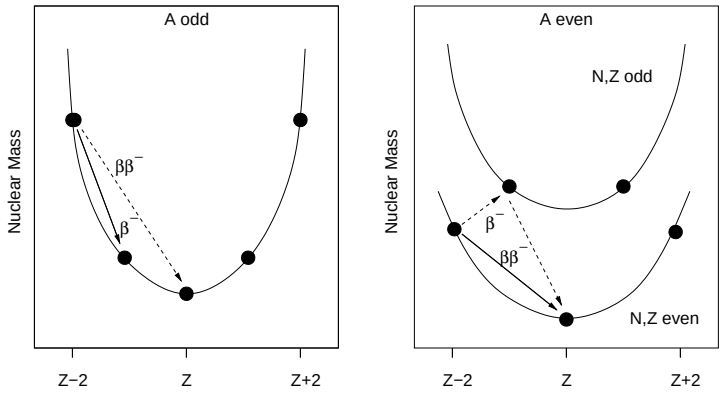

Figure 1.5: Nuclear mass as function of the proton number.

into account the increase in binding energy of the nucleus when protons or neutrons are coupled to give an angular momentum equal to zero:

$$\delta = \begin{cases} +12/A^{1/2} & \text{for even A and odd Z,N} \\ -12/A^{1/2} & \text{for even A and even Z,N} \\ 0 & \text{for odd A} \end{cases} \tag{1.22}$$

If isobaric nuclei are considered and their atomic masses are plotted as a function of Z it is easy to find that, for odd A, the nuclei are positioned as described on the left side of Fig. 1.5. If even A nuclei are considered, it is found that the nuclear masses are disposed as shown in the right part of Fig. 1.5.

Two different DBD modes are usually considered. First, the decay with two neutrinos (2ν-DBD). Lepton number is conserved by this decay, which is allowed by the SM:

$$2\nu\text{−DBD}: \quad (A, Z) \rightarrow (A, Z+2) + 2e^- + 2\bar{\nu}_e \tag{1.23}$$

Second, the decay without emission of neutrinos (0ν-DBD), given by

$$0\nu\text{−DBD}: \quad (A, Z) \rightarrow (A, Z+2) + 2e^- \tag{1.24}$$

A brief look at the reaction above makes it evident that lepton number conservation is violated; obviously, lepton number conservation is broken anyway if neutrinos are Majorana particles. An experimental confirmation of this decay mode will thus constitute an important step in the study of elementary particle physics beyond the SM. The Feynman diagrams for both decay modes are shown in Fig. 1.6. While the 2ν-DBD diagram contains only SM interactions, the 0ν-DBD requires the known $V - A$ interactions in addition to a massive Majorana neutrino. The virtual neutrino in the diagram can be thought of as produced as an anti-neutrino at one vertex and absorbed as a neutrino, which is equal to the anti-particle thanks to the Majorana nature, at the other vertex; moreover, a non-zero neutrino mass is required to flip the helicity, since the neutrino emitted with the electron at vertex 1 is right-handed and the one absorbed at the other vertex is left-handed. Should 0ν-DBD occur, its rate would be much lower than the one of 2ν-DBD because of the helicity flip and the smallness of the neutrino mass.

The discrimination between these decay modes is, in principle, very simple and is based on the shape of the spectrum obtained by summing on the energies of the two emitted electrons. In fact, this spectrum is determined by the phase space of the other emitted particles. As shown in Fig. 1.7, 2ν-DBD is a four body decay, with a continuous

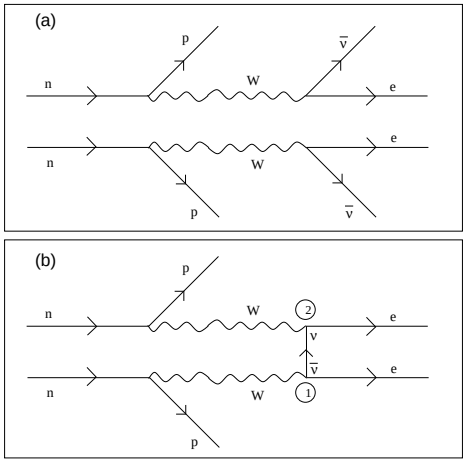

Figure 1.6: Feynman diagrams for the two Double Beta Decay channels: (a) 2ν. (b) 0ν: an anti-neutrino is produced at vertex 1 and a neutrino is absorbed at vertex 2; this process is allowed only for Majorana neutrinos.

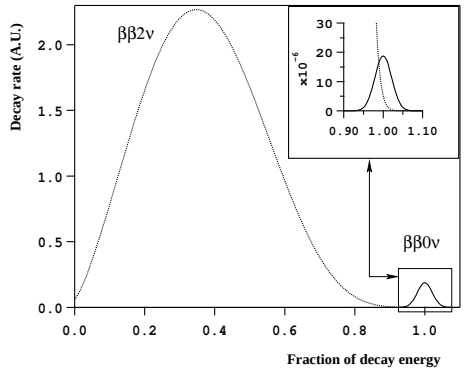

Figure 1.7: Schematic representation of the spectra obtained by summing on the two electrons energies for 2ν-DBD (dashed line) and 0ν-DBD. In the inset, the relative intensity of the 2ν-channel is overestimated in order to underline its contribution to the 0ν background. Spectra are obtained with the convolution of a 5% energy resolution, common to many experiments.

spectrum featuring a maximum value around one third of the Q-value. On the contrary, the two electrons retain all the available kinetic energy in 0ν-DBD (neglecting nuclear recoil). For this reason, the spectrum is just a spike at the transition energy.

In both cases, DBD is a semi-leptonic second-order weak interaction, and thus is characterized by a very long lifetime: $T^{2\nu}_{1/2} \sim 10^{18} - 10^{22}$ years for the 2ν-channel. This remarks that the experimental observation of this decay turns out to be a great challenge: very rare events have to be detected and disentangled from the traces of other radioisotopes, which have similar transition energies but decay times even 10 orders of magnitude shorter. Presently, 2ν-DBD has been observed for $\sim$ 10 nuclides.

The probability for 0ν-DBD to occur is usually expressed using the general relation derived from Fermi's golden rule:

$$\left[T^{0\nu}_{1/2}\right]^{-1} = G^{0\nu}|M^{0\nu}|^2\langle {m_{\beta\beta}}^2\rangle \tag{1.25}$$

In the previous equation, $G_{0\nu}$ is the phase space integral, approximately proportional

to $\left[Q_{\beta\beta}^{0\nu}\right]^5$ and determined exactly, $\left|M^{0\nu}\right|^2$ is the decay matrix element and $\langle m_{\beta\beta}\rangle$ the effective Majorana mass, defined by

$$\langle m_{\beta\beta}\rangle \equiv \sum_i \phi_i m_i |U_{ei}|^2 \qquad (i = 1,2,3) \tag{1.26}$$

The ϕ_i phases that appear in the last equation are the CP intrinsic neutrino parities, which are connected to the α_1 and α_2 phases that have already been introduced in Eq. (1.19). Their presence implies that cancellations are possible, and if the neutrino is a Dirac particle the cancellation is total (it is equivalent to a couple of degenerate Majorana neutrinos with opposite phases), so that the decay doesn't take place. It is true, however, that mechanisms other than the exchange of a light Majorana neutrino cannot be excluded for 0ν-DBD. However, it has been shown [25] that if 0ν-DBD occurs, then neutrinos are Majorana particles even if the decay is dominated by a different process: the dominant mechanism that drives 0ν-DBD is inserted into the *black-box* shown in Fig. 1.8, and by connecting the external lines appropriately, a contribution to the neutrino propagator that turns ν into $\overline{\nu}$ induces always a Majorana mass term. The conclusion is that the experiments looking for 0ν-DBD provide a model-independent determination of the neutrino nature, no matter which is the dominant mechanism driving the decay: additional information on this regard could be provided by measurements on different nuclides.

The importance of 0ν-DBD in the field on neutrino physics does not end here: Eq. (1.26) points out also its importance in mass hierarchy discovery. In fact, even if $\langle m_{\beta\beta}\rangle$ has a dependence on ϕ_i, its upper and lower limits depend on the absolute values of the mixing matrix elements. There is a relationship between the effective Majorana mass and the lightest neutrino mass: it depends on the valid hierarchy, according to which the lightest mass eigenstates is determined. The $\langle m_{\beta\beta}\rangle$ vs. m_{light} relationship can be determined easily for both the normal and the inverted hierarchy. The result in the case of normal hierarchy, where $m_{\text{light}} = m_1$, is reported as an example:

$$m_{\beta\beta} = |cos^2\theta_{12}cos^2\theta_{13}e^{i\alpha 1}m_1 \tag{1.27}$$
$$+sin^2\theta_{12}cos^2\theta_{13}e^{i\alpha 2}\sqrt{\Delta m_{12}^2 + m_1^2} + sin^2\theta_{13}e^{-2i\delta}\sqrt{|\Delta m_{13}^2| + m_1^2}|$$

Incorporating the values of mixing angles and squared-mass differences measured by oscillation experiments gives m_ν in function of m_1 for the normal hierarchy and m_3 for the inverted hierarchy, for a given set of phases. Fig. 1.9 shows the plot of m_ν in the two cases, allowing phases to vary from 0 to 2π. Thus, an observation of 0ν-DBD, together with data provided by oscillation experiments, would define a range for the absolute neutrino mass and disentangle the hierarchy scheme of the neutrino mass eigenvalues. Experiments on 0ν-DBD search give an upper limit to the effective Majorana mass and rule out regions of the plot 1.9. In particular, a sensitivity of $\sim 10 - 50$ meV on $\langle m_{\beta\beta}\rangle$ could definitely exclude the inverse and quasi–degenerate hierarchy.

Eq. (1.25) shows clearly that the evaluation of $\langle m_{\beta\beta}\rangle$ from an experimental measurement of $T_{1/2}^{0\nu}$ requires the exact knowledge of the Nuclear Matrix Elements $\langle M^{0\nu}\rangle$. From a theoretical point of view, this is the main limit when describing 0ν-DBD. Several models have been proposed (for example [26], [27]), and it is not simple to evaluate their correctness and accuracy: this is mainly because they are not connected with other nuclear processes that allow a simple verification. Even the comparison with the 2ν-channel presents unclear points, mostly because of the different role played by neutrinos in the two processes. In this situation, one possibility is to consider the spread of the theoretical values of the NME as a measure of their uncertainty. The spread of NME for different nuclide candidate to 0ν-DBD will be mentioned again in Sec. 2.1.1.

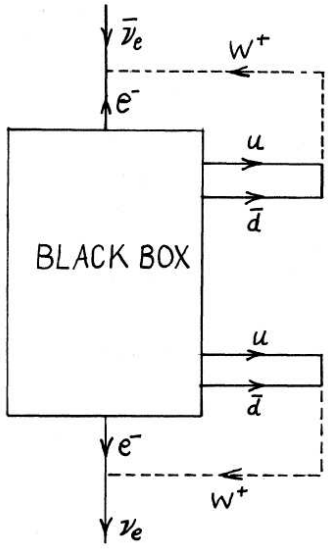

Figure 1.8: The "Black box" of 0ν-DBD: regardless of the physical mechanism that dominates the decay, this diagram shows that a modification in the neutrino propagator results in a Majorana mass term for neutrinos [25].

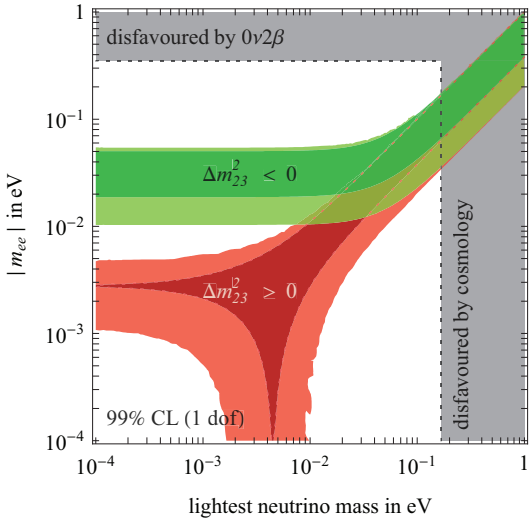

Figure 1.9: The Majorana effective mass in function of the lightest ν mass, in a parameter space constrained by previous experimental achievements. The green region corresponds to the inverted hierarchy and the red one to the normal hierarchy; the darker bands are the regions allowed if oscillation parameters were to be known with infinite precision [11].

Nuclide	$T^{0\nu}_{1/2}$ [y]	Nuclide	$T^{0\nu}_{1/2}$ [y]
^{48}Ca	$> 1.4 \times 10^{22}$ [28]	^{76}Ge	$> 1.9 \times 10^{25}$ [29]
^{76}Ge	$> 1.19 \times 10^{25}$ [30]	^{82}Se	$> 1.0 \times 10^{23}$ [31]
^{96}Zr	$> 1.0 \times 10^{21}$ [32]	^{100}Mo	$> 4.6 \times 10^{23}$ [31]
^{116}Cd	$> 1.7 \times 10^{23}$ [33]	^{130}Te	$> 3.0 \times 10^{24}$ [34]
^{136}Xe	$> 1.2 \times 10^{24}$ [35]	^{150}Nd	$> 1.8 \times 10^{22}$ [36]

Table 1.1: Experimental constraints on $T^{0\nu}_{1/2}$ for various nuclides candidate to the rare decay. References for the reported numbers are indicated next to each limit/value.

1.2.1 Current status of 0ν-DBD search

The experimental signature of 0ν-DBD is in principle very clear: a peak at the $Q^{0\nu}_{\beta\beta}$ value in the spectrum of the two electrons summed energies. In spite of such a simple mark, the search is very complex. The peak is superimposed on a continuum, therefore good energy resolution is a must; apart from improving the signal-to-background ratio in the peak search, this is required also to avoid that the 2ν-DBD tail, extending to the peak region, becomes a background source itself. Other general requests regard high radio-purity, with the control of natural radioactivity and of cosmogenic activities built up in materials through nuclear reactions of cosmic ray muons and their secondary products, especially neutrons: underground fabrication and operation of the detector reduces greatly this background. Specific criteria will be given in Chapter 2, focusing on the experiment connected to the Ph.D. work presented in this thesis.

The measurement of both 2ν-DBD and 0ν-DBD, three general approaches have been followed: geochemical, radiochemical, and direct counting measurements. In this context, only the last type will be reviewed.

Direct counting experiments are based on two different methods. In the source$\neq$ detector approach, a material containing the nuclide candidate to 0ν-DBD is inserted, normally in form of thin sheets, in a suitable detector. In the source=detector approach, also called *calorimetric*, the detector itself is the material containing the 0ν-DDB active nuclide. Several types of conventional devices have been used in 0ν-DBD direct searches: solid state devices (germanium spectrometers and silicon detector stacks), gas counters (time projection chambers, ionization and multi-wire drift chambers) and scintillators (crystal scintillators and stacks of plastic scintillators). Tab. 1.1 reports the current experimental lower limits obtained on the $T^{0\nu}_{1/2}$ of various candidate nuclides.

The Neutrino Ettore Majorana Observatory (NEMO-3) [37], operating at the Frejus underground laboratory (4800 m.w.e.), can be evidenced among the most sensitive researches in this field. NEMO-3 is an experiment of the source$\neq$detector approach, with the primary goal of studying different nuclides candidate to 0ν-DBD with big $Q^{0\nu}_{\beta\beta}$ values. Its detector can contain at least 10 kg of different decaying isotopes. The biggest effort has been dedicated to ^{100}Mo and ^{82}Se (both with $Q^{0\nu}_{\beta\beta} \sim 3$ MeV). The experiment is based on the direct detection, by a tracking set–up, of the two electrons resulting from the decay and on the direct measurement of their energy with a calorimeter. The detector has a cylindrical shape and is divided in 20 identical parts. The source consists of thin layers ($\sim 50\mu$m thick) vertically fixed that separate the tracking volume made of Geiger counters cells. In order to minimize multiple scattering effects, the tracking element is filled with helium and ethyl alcohol. The cells give a 3D tracking

of the particles recording for each cell both drift time and the two propagation times of the plasma. The tracking volume is covered by very low activity scintillators coupled to photo-multipliers. In total the final detector is made of 6180 counters and 1940 scintillators, and is surrounded by a solenoid producing a 30 Gauss magnetic field to separate (e^+e^-) couples produced in the thin source foils. An external 20 cm thick shield of low activity iron reduces the thermal neutrons and the γ ray flux. The values obtained for the 2ν-DBD half-lives are $T^{2\nu}_{1/2}(^{100}\text{Mo})=[7.11 \pm 0.02(\text{stat}) \pm 0.54(\text{syst})] \times 10^{18}$y and $T^{2\nu}_{1/2}(^{82}\text{Se})=[9.6 \pm 0.3(\text{stat}) \pm 1.0(\text{syst})] \times 10^{19}$y; the 2ν-DBD spectra are reported in Fig. 1.10. Lower limits on 0ν-DBD have also been provided: $T^{0\nu}_{1/2}(^{100}\text{Mo}) > 4.6 \times 10^{23}$y and $T^{0\nu}_{1/2}(^{82}\text{Se}) > 1.0 \times 10^{23}$y. The corresponding upper limits on the effective Majorana mass range from 0.7 to 2.8 eV for ^{100}Mo and from 1.7 to 4.9 eV for ^{82}Se, according to the NME used [31].

The best limit so far on 0ν-DBD comes from the Heidelberg–Moscow (HM) experiment, which aims at detecting the decay of the nuclide ^{76}Ge: $^{76}Ge \rightarrow ^{76}Se + 2e^-$ by the detector=source approach. The experiment, now closed, operated five high–purity ^{76}Ge detectors enriched to 86%, with a total mass of 11.5 kg, the active mass of 10.96 kg being equivalent to a source strength of 125.5 mol of ^{76}Ge nuclides. The experiment was installed in the Gran Sasso underground laboratory under heavy shields for gamma and neutron environmental radiation. Extremely low background levels were achieved thanks to a careful selection of the setup materials, and were further improved by the use of Pulse Shape Discrimination (PSD) techniques. A background level of $\sim$0.12 c/(keV $\cdot$ kg $\cdot$ y) in the 0ν-DBD region was obtained. With a statistics of 35.5 kg·y in ^{76}Ge, the half-life limit obtained by the HM collaboration is $T^{0\nu}_{1/2}(^{76}\text{Ge}) > 1.9 \times 10^{25}$y at 90% C.L. [29], which corresponds to a limit on the effective Majorana mass $m_{\beta\beta} < 0.35$ eV (using NME from [38]). In January 2002, a few members of the HM collaboration claimed evidence for a 0ν-DBD peak with $T^{0\nu}_{1/2}$ in the range 0.7-4.2$\times$ 10^{25} y (3σ) [30],[39]: this would translate in $m_{\beta\beta}$ =0.2-0.6 eV [38]. The energy spectrum is reported in Fig. 1.11. The claim raised skepticism and a controversy followed; in particular, a strong criticism is due to the fact that the identification of the background in the region of the peak is not clear. It is probable therefore that a definite answer to the correctness of the claim will be given only by the very sensitive next generation 0ν-DBD projects: in particular, the first phase of the GERDA experiment [40], whose construction at the Gran Sasso National Laboratory is complete, is starting taking data on ^{76}Ge and will be able to verify the claim.

The last experiment to be mentioned as provider of one of the best limits on 0ν-DBD is Cuoricino [34]. Cuoricino closed two years ago and searched for the decay using low temperature detectors. As the Ph.D. work presented in this thesis was developed in the framework of the next-generation evolution of Cuoricino, the presentation of its results, which will take place in Sec. 1.5, will be anticipated by a thorough discussion of its detection technique.

1.3 The bolometric technique as an instrument for 0ν-DBD search

Bolometers are Low Temperature Detectors (LTD) sensitive to single particle interactions. Their first appearance can be traced back to the work of F. E. Simon, who in 1934 proposed the use of low-temperature calorimeters in the field of nuclear physics research and radioactivity measurements; the first detection of α-particles dates back to 1949. Thirty years were needed to make the following important step. Two fundamental articles on the use of cryogenic detectors for particle physics experiments were

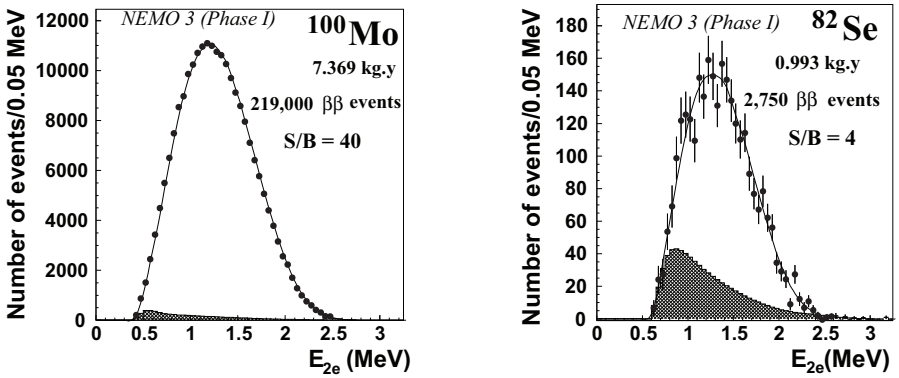

Figure 1.10: Energy spectra measured by NEMO-3 for the 2ν-DBD, from left to right, of ^{100}Mo and ^{82}Se. Black dots are for data, the solid line is the simulated DBD-spectrum and the shaded histogram is the subtracted background [31].

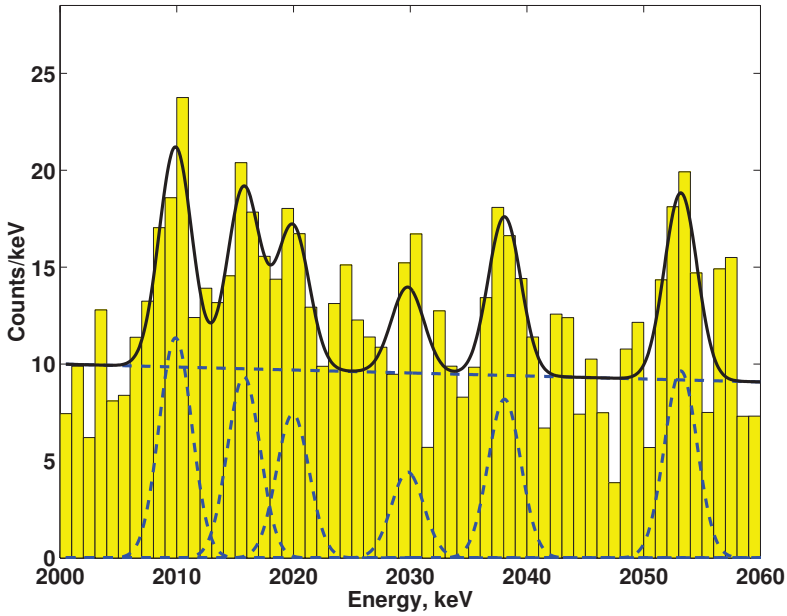

Figure 1.11: Energy spectrum measured by the Heidelberg-Moscow experiment in the $Q^{0\nu}_{\beta\beta}(^{76}\text{Ge})$ region [30].

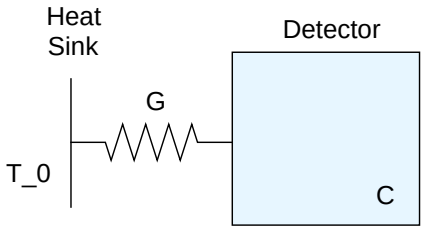

Figure 1.12: Monolithic thermal model for a bolometric detector: the sensor and the absorber form a unique element weakly coupled to a heat sink.

published in 1984: Fiorini and Niinikoski [41] proposed the application of the bolometric technique in the field of Double Beta Decay and neutrino mass determination; McCammon, Mather and Moseley [42] suggested their impact in X-rays astrophysics. The bolometric technique can therefore be considered young, with only twenty-six years of activity in fundamental physics research; its potentialities have not been fully explored yet, and there is room for the improvement of current performances. Cryogenic methods can be applied to many fields of application. The high energy resolution of microcalorimeters can be implied for direct measurements of the neutrino mass by β-decay study (quoted at the end of Sec. 1.1.2) and X-spectroscopy; the low energy thresholds and the high efficiencies in respect to nuclear recoils make bolometers suitable for dark matter detection; again, the high energy resolution combined to the versatility in the choice of materials are a great advantage in the field of 0ν-DBD search, which is the context of this thesis.

1.3.1 Principles of operation

In a generic detector, particles lose their energy producing elementary excitations which are afterwards converted into an electric signal; in a bolometer, the order of magnitude of excitations is such that detection is impossible unless cryogenic temperatures are reached. Different typologies of detectors can be identified according to the kind of elementary excitations that mediate energy depositions: phonons, quasi-particles or other exotic excitations. In the case under discussion, phonons are the mediators. When the mass of the detector does not exceed 1 mg and its linear dimensions are at maximum $\sim$100μm, one speaks about *micro-calorimeters*. However, they will be neglected here and explicit reference will be made to *macro-bolometers*, which exceed their mass and size. These detectors are designed to work as perfect calorimeters: devices where the energy deposited by the impinging particle is thoroughly thermalized by phononic mediation and read by an appropriate sensor in the form of a rise in temperature. The bolometer, in first approximation, can therefore be sketched as formed by an *absorber*, where the impinging particle transmits its energy to phonons, and the *sensor*, which is sensitive to the resulting rise in temperature and converts it in another physical quantity, such as a current or a voltage signal.

The bolometric detector's behaviour can be described in first approximation by modelling the previous rough sketch as a heat capacity C linked by means of a thermal conductance G to a heat bath at the constant temperature T_0 (Fig. 1.12). As C gathers in one element the contributions of both the absorber and the sensor, this simple model is called *monolithic*; its expansion in the form of a more complex *composite* model will be treated in Sec. 1.4. The heat bath's capacity is considered as infinite. If $T(t)$ is the absorber's temperature at the time t, the assumption that the dependency of C and G on T can be neglected translates into the relation $\Delta T = |T(t) - T_0| \ll T_0$, true at every t.

As a consequence, the temporal evolution of a temperature pulse due to instantaneous absorption of an energy E is given by, in first approximation:

$$\Delta T(t) = \frac{E}{C} e^{-t/\tau}, \qquad \tau = \frac{C}{G} \tag{1.28}$$

According to the approximation, the maximum value T_{max} of the variation in temperature is the E/C ratio: for energy depositions in the kev-MeV range to generate appreciable signals, C must be minimized. This is allowed by temperatures lower than 1 K (10-10^2 mK), which change according to the size of the bolometer, its constitutive materials and the energy of the particles to be observed. Heat capacity is also relevant for the thermal relaxation time τ and its reduction leads to fast signals. At the same time, however, τ should be long compared to the time scale of the trasmission of the signal to the sensor, which is of order a few ms for the macro-bolometers considered here: for this reason, bolometers cannot stand counting rates higher than Hz. Heat capacity plays a fundamental role in shaping energy resolution, too, as Sec. 1.4.3 will point out. The first constraints on the design of a bolometric detector arise, hence, from the previous discussion: the operation at low temperatures and the selection of materials with low capacity are a must.

Reminding that the monolithic model is a rough, introductive approximation, and that a more sophisticated picture is reserved to the final part of this same chapter, the constitutive elements of a bolometric detector will be presented in the next sections. The discussion will be general, and will be related to its specific application in the Cuoricino and CUORE experiments only in Chapter 2.

1.3.2 The crystal absorber

The most important parameter of the detector is the overall heat capacity, that has to be small enough to obtain big and fast signals in response to an energy deposition. A wide choice of materials that meet this condition are available for the energy absorber. The specific heat of a crystal at low temperature can be expressed as:

$$c(T) = c_r(T) + c_e(T)\,, \tag{1.29}$$

where c_r represents the lattice contribution to the specific heat and c_e the electronic one. Dielectric diamagnetic materials are preferred as energy absorbers, as only the lattice contribution is present; furthermore, it is proportional to the cube of the temperature over the Debye temperature T_D at low temperatures, according to the Debye law:

$$c_r(T) = \frac{12}{5}\pi^4 k_B N_A \left(\frac{T}{T_D}\right)^3 \tag{1.30}$$

The Boltzmann constant k_B and the Avogadro number N_A appear in the previous formula. This contribution can be written in terms of heat capacity as

$$C(T) = \beta \frac{m}{M} \left(\frac{T}{T_D}\right)^3 \tag{1.31}$$

The constant β is equal to 1944 J/(K·mol), m is the absorber mass and M is the molecular weight. In the case of metals, the specific heat is dominated by the electron contribution

$$c_e(T) = \frac{\pi^2}{T_D} ZR \frac{T}{\Theta_F}\,, \tag{1.32}$$

where Z, R and Θ_F are the conduction electron number for each atom, the gas constant and the Fermi temperature respectively. The last case is that of a metal in superconductive state, for which the electron contribution to the specific heat at $T \ll T_c$ is

$$c_e(T) = K_s e^{-2(\frac{T_c}{T})} \tag{1.33}$$

K_s is a constant depending on the material's characteristics.

The above considerations lead to prefer diamagnetic or superconductors as energy absorber materials.

As for the processes of energy conversion, the interaction of an elementary particle with a solid medium produces excitations of its elastic field, so that the energy spectrum of the target phonon system is modified and the starting equilibrium condition is broken. The energy deposited in the absorber is first converted into high energy phonons, thus modifying the system thermal equilibrium (non-thermal phonons). When enough time is elapsed ($\sim 1\mu$s) the phonon system relaxes to a new equilibrium distribution, corresponding to an higher temperature (thermal phonons). The detector works as a true calorimeter only when it is not too fast in response, so that a complete thermalization of the deposited energy is guaranteed. In order to give a correct interpretation of the behaviour of calorimeters, it is necessary to give a description in terms of thermodinamic systems with a well defined temperature while operated. This is only possible if, after the particle interaction, the equilibrium condition is restored before the complete formation of the thermal signal (which typically requires $\sim$100 μs time). The processes involved in the restoration of the thermal equilibrium condition are very complex and depend on the material. First of all, when ionizing particles interact with a dielectric material there can be two different channels for the transmission of the energy E. Nuclear scattering is most probable in the case of heavy particles such as αs, when the energy transfer to the absorber is by direct excitation of the lattice: the propagation of this excitation can be delayed by damages or irregularities in the lattice, and also by subsequent electromagnetic interactions, so that signals develop in longer times and energy resolution gets worse. Electronic interactions are the second channel: the particle is stopped inside the absorber and loses energy along the path by forming electron-hole pairs, which diffuse in the crystal generating phonons by recombination or interaction with lattice impurities. In both cases, however, highly energetic phonons, out of equilibrium, are produced. Let's suppose that a number of electron-hole pairs $N_{eh} = E/\epsilon_{eh}$ is available, where ϵ_{eh} is the average energy of the electron-hole pairs. These pairs release their energy excess by emitting high energy optical phonons, with time scale of order $\sim$ps. Optical phonons subsequently decay in a few ns into longitudinal acoustic phonons, with frequency about half the Debye frequency ν_D. The effect of the interaction of a ionizing particle into the absorber is, eventually, the production of acoustic phonons with energy $\sim h n_D$ after a few ns. At the typical operating cryogenic temperatures, $h n_D$ is $\gg k_B T_p$, which is the energy carried by the reticular thermal phonons: this situation does not yet correspond to an equilibrium condition. In order to get to the new thermal equilibrium, the acoustic phonons must degrade their energy through decay of longitudinal acoustic phonons, thanks to the anarmonic terms of the lattice potential; or isotopic scattering of phonons, which allows also the conversion between longitudinal and transversal acoustic phonons. In the end, the phonons to be detected and converted in an electric signal are those transmitted to the temperature sensor.

1.3.3 The temperature sensor

In order to achieve good signal-to-noise ratio, a bolometer needs a sensor: a device that collects the phonons produced in the absorber and generates an electrical signal,

usually proportional to the energy contained in the collected phonons. A simple realization of this device is a thermistor whose resistance, as a function of temperature, has a steep slope. A characterizing parameter of thermistor performance is the *logarithmic sensitivity* A, defined as

$$A = \left| \frac{d \log R(T)}{d \log T} \right| \tag{1.34}$$

The parameter measures the ability of the sensor to convert small variation in temperature (fractions of mK) in appreciable resistance variations. In practical devices, two main classes of thermistors give the best results: Transition Edge Sensors (TES), which are super-conductive films operated at the critical temperature T_c and whose sensitivity lies in the range $10^2 < A < 10^3$; and Semiconductor Thermistors (ST), with $1 < A < 10$. The attention from now on will be focused on STs.

Semiconductor thermistors are intrinsically slow and are sensitive mainly to thermal phonons in a bolometer. They give information about systems in thermal equilibrium, and can be thought of as temperature sensors. However, hints have been observed about the fact that also athermal phonons can be detected by STs; in this case the collected pulses contain non thermal components. STs consist normally of Ge or Si small crystals with a doped region. For both, doping is performed so that a strong dependence of the sensor's resistance on temperature results:

$$\rho(T) \simeq \rho_0 \cdot \exp\left(\frac{\epsilon T}{k_B T}\right)^{1/2} \tag{1.35}$$

$\epsilon(T)$ is the activation energy and ρ_0 is a parameter depending on the doping conditions. Semiconductors are covalent solids that may be regarded as insulators because the valence band is completely full and the conduction band is completely empty at the absolute zero. They present an energy gap between the valence and conduction bands of no more than 2 eV. In an intrinsic semiconductor conduction can happen only with an activation energy equal or larger than the energy gap. This mechanism is possible if the working temperature is $T \ll T_{amb}$, since $k_B T \simeq 0.025$ eV at room temperature.

Electronic conduction at low temperatures is allowed by the introduction of energy levels of impurities localized above the top of the valence band or under the bottom of the conduction band, according on the doping type. Depending on the number of dopant atoms, the semiconductor, even when near the zero temperature, can behave as an insulator or a metal; in particular, the critical concentration N_c characterizes the transition of the semiconductor from insulating to metallic behavior. The region near this concentration is named metal-insulator transition region (MIT) [43].

At temperatures lower than 10 K, conduction is due to the migration of charge carriers between impurity sites. When the concentration of donors is increased, the wave function of the external electron of donor atoms overlaps with the external electron wave function of the neighboring atoms: in this situation the electrons are not localized, and the conduction can be described as electrons jumping from a donor site to the other in the so-called *hopping* mechanism, without using the conduction band [44]. This migration, which is represented schematically in Fig. 1.13, is due to quantum-mechanical tunneling through the potential barrier that separates the two dopant sites. Conduction is activated by phonon mediation.

When $T \ll 10$ K and if the net doping atom concentration is slightly lower than N_c, the resistivity is strongly dependent on the temperature. This is the reason that pushes to operate STs slightly below the MIT region. The dominant conduction mechanism in these conditions of temperature and dopant level is named *Variable Range Hopping*

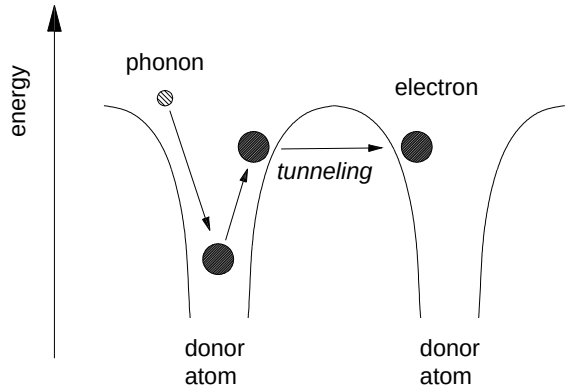

Figure 1.13: The mechanism of tunneling-assisted hopping conduction in semiconductor thermistors.

(VRH), which implies that carriers can migrate also on far sites if their energy levels are located in a narrow range around E_F [45]. The compensation level $K=N_A/N_D$, where N_A N_D are the acceptor and donor concentrations, plays a fundamental role in the VRH process, as it determines the density of states near the Fermi energy. When VRH holds, the resistivity depends on the temperature as

$$\rho(T) = \rho_0 \exp(T_0/T)^{\gamma} \tag{1.36}$$

ρ_0 and T_0 are parameters depending on the doping and compensation levels: they will be mentioned and discussed various times in chapters 2 and 5. The exponent γ is 1/2 for high compensation levels, which corresponds to the formation of a gap in the electron density of states near E_F due to the Coulombian repulsion among electrons [46].

Given the strong dependence of conduction mechanisms on doping density, the production of thermistors must guarantee control on this matter: a good candidate is the Neutron Transmutation Doping technique (see Chapter 5). The processes described previously do not describe entirely the behaviour of a real sensor. In particular, the introduction of a phenomenological model known as *Hot Electron Model* (HEM) [47] helps to understand the non-linearities of VRH. The basic idea of HEM is that, at low temperatures, the thermal coupling between electrons and the lattice in the thermistor is weakened. This implies the introduction of an electronic temperature T_e and of a phononic temperature T_{ph}: when a power P is injected into the system, T_e results larger than T_{ph}. The HEM answers the question about which temperature should be considered in Eq. 1.36. For example, the temperature of metals is defined through their conduction electrons; in semiconductor thermistors, where conduction electrons and phonons of the lattice form two separate systems connected by a finite thermal conductance, resistance will depend on T_e.

The last question to be answered about the general behaviour of the phonon sensor regards the mechanism by which it converts the thermal pulses due to energy depositions into electrical signals. In order to obtain a voltage signal, a bias current I is sent trough the thermistor by means of the bias circuit shown in Fig. 1.14(a). In the conditions pictured, a voltage $V(T) = I \cdot R(T)$ appears across the sensor. This produces a power dissipation P which increases the temperature and acts back on the resistance $R(T)$, until an equilibrium is reached. In static conditions, the absorber's temperature T_b is equal to $T_0 + P/G$, where G is the conductance to the heat bath and T_0 its temperature. This phenomenon, which makes the V-I relation deviate from linearity and leads to a non-ohmic behavior, is often referred to as *electro-thermal feedback*. The static resis-

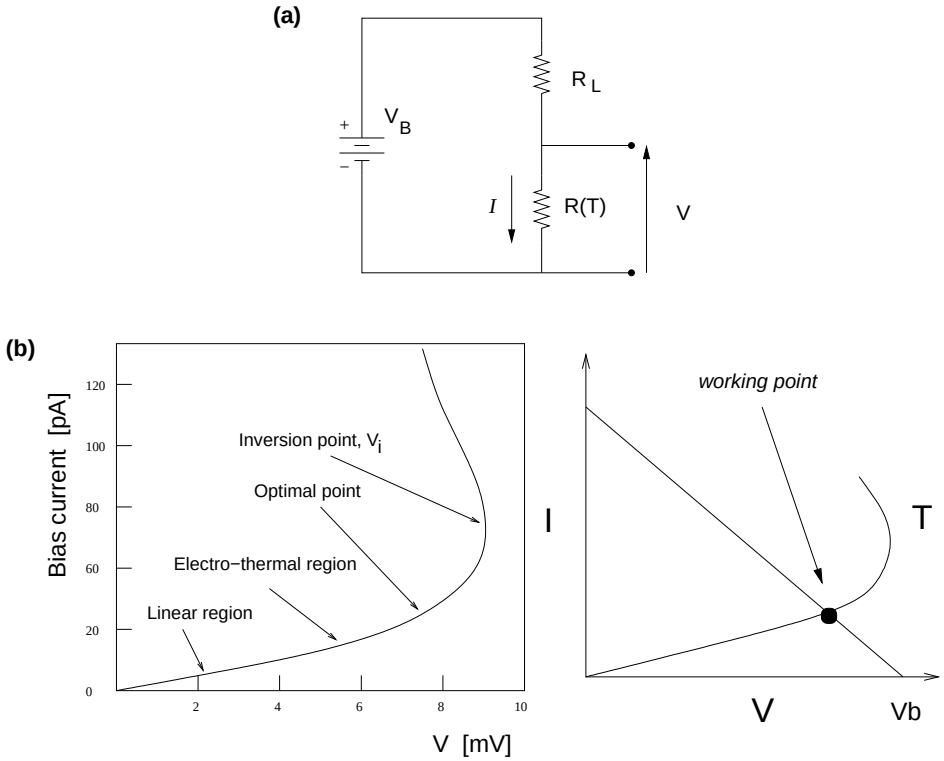

Figure 1.14: The polarization of a semiconductor thermistor. (a) Electric scheme of the bias current circuit, described in the text, used to read-out a bolometer. (b) Typical current-voltage characteristics (load curve) of a thermistor polarized by means of the circuit (a).

tance is simply the ratio V/I while the dynamic resistance is the tangent at the V-I: by further increasing the bias current, the dynamic resistance becomes 0 at the inversion point and then negative. A typical V-I curve for a ST, called *load curve*, is represented in Fig. 1.14(b). In static conditions, the thermistor's electric and thermal parameters are described by a point on the load curve. The intersection of the straight line of equation $V = V_b - IR_L$ and the load curve $I = I(V)$ determines the working point of the sensor, as described in Fig, 1.14(b). Usually an optimal working point is chosen so that the signal amplitude or the signal-to-noise ratio is maximum.

Following an energy deposition, the thermal pulse in Eq. (1.28), given by the rough monolithic approximation, is converted into an electric signal by means of the thermistor bias circuit; optimizing the detector means finding the best configuration for maximum pulse amplitude. Considering the basic circuit shown in Fig. 1.14(a), it is straightforward to obtain the relationship between the voltage signal ΔV, the parameters of the thermistor and the deposited energy E:

$$\Delta V = \frac{R_L}{R_L + R} \cdot V \cdot A \cdot \frac{\Delta T_b}{T_b} \sim \frac{E}{C \cdot T_b} \cdot A \cdot \sqrt{P \cdot R} \tag{1.37}$$

All the terms included in the previous formula have already been defined, apart from the increase in the detector's temperature ΔT_b. This expression vanishes both in the limit $P \to 0$ and $P \to \infty$. One could switch to higher voltage operation points to increase signal amplitude, but typically not above the inversion point V_i on the load curve. Usually the best working point doesn't correspond to the V_i voltage, as the increase in the applied voltages determines lower $\Delta T/T$ ratios. The optimal working point must be determined experimentally for each detector.

1.4 Modeling the TeO_2 macro-bolometer

Now that the basic principles of the energy absorber and of the temperature sensor are known, a more refined bolometric model can be presented. The aim of this section is to provide a basic understanding of the static and dynamic behaviour of macro-bolometers, aiming at the explanation of their use in experiments on 0ν-DBD. Also, the instruments will be given to face the optimization work that will be detailed in this thesis, from Chapter 3 to Chapter 6. The thermal model presented here will be described in its main aspects for the sake of a better comprehension of the next topics; a detailed treatment is found in [48].

The simplified monolithic model has just been presented in Sec. 1.3 to support a general introduction to the bolometric technique: in that thermal picture, the detector is seen as a single heat capacity C connected to the heat bath by means of a conductance G. The monolithic model has already been labeled as limited and incapable of accounting for the real signal structure. The first adjustment to the real case consists in separating the detector in its two main components, the absorber and the thermistor; each of them will be described by means of a heat capacity and will be linked to the other elements of the system through a heat conductance. This evolution of the model is still not sufficient, however, as it neglects any non-linearities in the thermistor's behaviour. For example, the HEM (Sec. 1.3.3) separates the phonon system from the electron system inside the temperature sensor: as mentioned, the two systems are connected by a thermal conductance weaker than the one among the electrons, and therefore they reach distinct temperatures following power injection. Summing up, the bolometric detector under discussion here can be described by an enhancement of the monolithic model that takes into account, at least, the following terms:

- the heat bath, which is the thermal reference point;
- the absorber, connected by means of distinct conductances to the heat bath and to the thermistor's phonon system;
- the thermistor's phonon system, connected by means of distinct conductances to the heat bath and to the thermistor's electronic system, which is uncoupled due to the HEM picture;
- the thermistor's electron system, connected to the thermistor's phonon system by a conductance.

The three-nodes system just sketched constitutes a *composite model* and is integrated by taking into account the characteristics of the electric circuit for thermistor polarization, already pictured in Fig. 1.14(a), which allows temperature read-out by measuring the resistance at its terminals. The behaviour of a similarly structured macro-bolometer will be analyzed now in both its static and dynamic behaviour.

1.4.1 Static behaviour

In ideal static conditions, when no electric power is injected in the system, all the nodes are expected to reach the same temperature T_0 of the heat bath; in the real case, localized background powers are always present and generate a thermal flow among the model's nodes, even when no energy is released in the absorber and the thermistor is not polarized. At least two parasitic powers, P_a^b and P_{el}^b, should be considered: the first one is dissipated in the crystal absorber because of unavoidable micro-vibrations, while the second one can be correlated to parasitic currents induced by electromagnetic interferences. When the thermistor is polarized by the passage of an electric current I

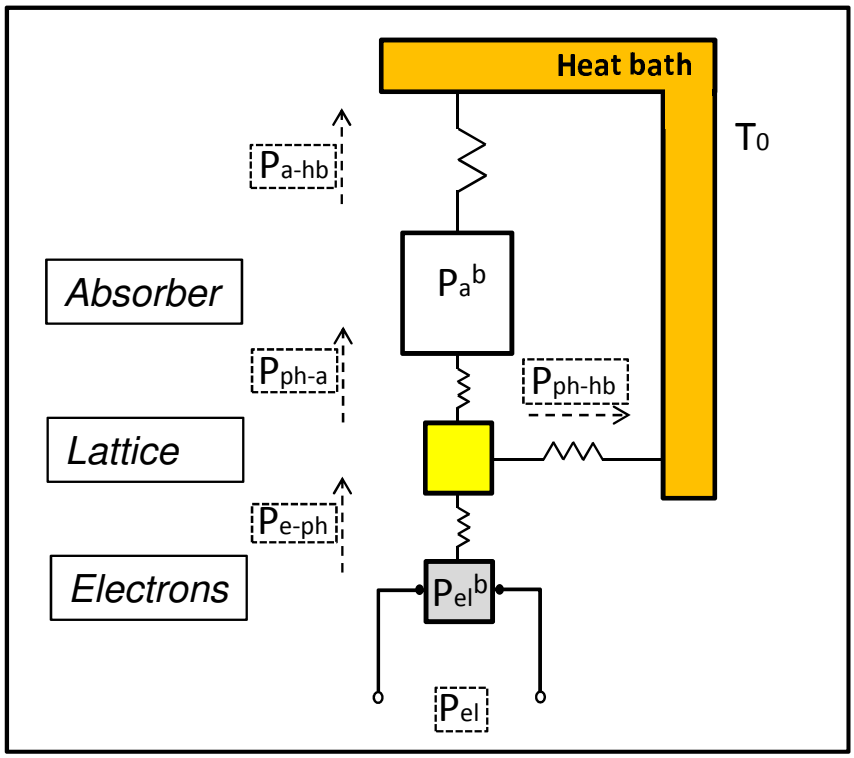

Figure 1.15: Composite thermal model with three nodes. The sign of powers flowing in the system is not known in principle, and they are fixed by convention.

for signal read-out, Joule heating by means of an electric power P_{el} takes place in its electron system. In such conditions, describing the static behaviour of the modeled macro-bolometer means finding the thermal equilibrium configuration reached by the network sketched in Fig. 1.15. The power balance for the three nodes of the thermal system under discussion is

$$\begin{cases} P_{el} + P_{el}^{b} &= P_{e-ph} \\ P_{e-ph} &= P_{ph-hb} + P_{ph-a} \\ P_{ph-a} + P_{a}^{b} &= P_{a-hb} \end{cases} \tag{1.38}$$

where P_{el} can be expressed in terms of the elements in the polarization circuit pictured in Fig. 1.14(a):

$$P_{el} = R(T_{el}) \cdot \left(\frac{V_{bias}}{R(T_{el}) + R_L} \right) \tag{1.39}$$

In the set of equations (1.38), the dependence on the nodes' different temperatures can be made explicit by expressing the power P_{12} flowing between nodes 1 and 2 in function of T_1 and T_2, with $T_1 > T_2$. As confirmed by experimental measurements that will be reported in 2.1.6, the thermal conductances used in the model are expressed by a law of power in function of T:

$$G(T) = g_0 \cdot T^{\alpha} \tag{1.40}$$

The power flowing between the generic nodes 1 and 2 in the depicted thermal network can therefore be written as

$$P_{12} = \int_{T_1}^{T_2} G(T)\,\mathrm{d}T = \frac{g_0^{12}}{\alpha_{12}+1}\left[T_1^{\alpha_{12}+1} - T_2^{\alpha_{12}+1}\right] \tag{1.41}$$

The thermal balance system (1.38), rewritten in terms of Eq. (1.41), is non-linear and cannot be solved analytically. Its solution by means of numerical methods gives the temperature of each node, and both the thermistor's resistance $R(T_{el})$ and the current flowing through it, then, can be calculated from the value T_{el}. Eventually, the load-curves $I-V$ and $R-P$, whose shapes have already been presented in Sec. 1.3.3, are drawn.

1.4.2 Dynamic behaviour

Once static conditions are known, the dynamic problem can be approached. It consists in finding the temporal evolution of a pulse generated by an energy deposition in the crystal absorber. When the monolithic model was presented in Sec. 1.3.2, a first-order approximation for the evolution in time of pulses was found in the case of a capacity C linked to the heat bath by a conductance G. Although the composite model is more complex and should be treated independently, some considerations on the general signal structure can be drawn. The temperature variation generated by the particle interaction is defined starting from the static equilibrium configuration of the network, which is regained when the whole evolution of the thermal pulse is over; although approximate, this first picture shows that the characteristic times of a thermal pulse, linked to the constant $\tau = C/G$, are those of the thermal relaxation towards equilibrium, and that such relaxation is described by exponential functions.

The previous general view can be refined by specific reference to temperature variations in the composite model. Energy conservation in the time interval $\mathrm{d}t$ can be applied to the three nodes of the thermal network in Fig. 1.15, obtaining the set of differential equations

$$\begin{cases} -C_{el}\cdot\dfrac{\mathrm{d}T_{el}}{\mathrm{d}t} &= -P_{el} - P_{el}^{b} + P_{e-ph} \\ -C_{ph}\cdot\dfrac{\mathrm{d}T_{ph}}{\mathrm{d}t} &= -P_{e-ph} + P_{ph-hb} + P_{ph-a} \\ -C_{a}\cdot\dfrac{\mathrm{d}T_{a}}{\mathrm{d}t} &= -P_{ph-a} - P_{a}^{b} + P_{a-hb} \end{cases} \tag{1.42}$$

$T_{el}(t)$, $T_{ph}(t)$ and $T_a(t)$ are the unknown temperatures of the thermistor's electron, thermistor's phonon and crystal absorber nodes; C_{el}, C_{ph} and C_a are their heat capacities, respectively, and depend on temperature with the general form

$$C(T) = c\cdot T^{\beta}, \tag{1.43}$$

where c is a coefficient experimentally measured; the exponent β is equal to 3 for the absorber due to the Debye law and 1 for the thermistor's electron system. The powers P_{12} flowing in the system still have the form (1.41). At time $t = 0$, the power $P_a = E\cdot\delta(0)$ is released instantaneously in the absorber, which implies the following conditions hold:

$$\begin{cases} T_{el}(0) &= T_{el}^{s} \\ T_{ph}(0) &= T_{ph}^{s} \\ T_{a}(0) &= T_{a}^{s} + \dfrac{E}{C_a} \end{cases} \tag{1.44}$$

The superscripts s refer to the static equilibrium temperatures of the three nodes. A necessary remark is that the third equation, more specifically the initial condition $\Delta T_a =$

E/C_a, is valid provided that the variation with temperature in the absorber's heat capacity is negligible, and then $\Delta T \ll T$: the approximation is valid in the case under study but does not hold for absorbers with very small heat capacities or large energy depositions. The set of equations (1.42), completed by the initial conditions (1.44) that correspond to an instantaneous release of energy E, can be solved only in a numerical way. However, opportune approximations can be made in order to linearize it:

1. the thermal pulse generated in the crystal absorber is treated as a small perturbation of the work point determined by the static problem. In other words, the power flowing from the heat bath to the generic node j in dynamic conditions can be written as

$$\int_{T_{hb}}^{T_j} G(T)\,\mathrm{d}T = \int_{T_{hb}}^{T_j^s+\Delta T} G(T)\,\mathrm{d}T = \\ = \int_{T_{hb}}^{T_j^s} G(T)\,\mathrm{d}T + \int_{T_j^s}^{T_j^s+\Delta T} G(T)\,\mathrm{d}T \sim \int_{T_{hb}}^{T_j^s} G(T)\,\mathrm{d}T + G(T_j)\cdot\Delta T \quad (1.45)$$

   In the previous equation, T_j^s is the temperature of the generic node j determined in static equilibrium conditions, and ΔT is the temperature variation during pulse evolution. The "small perturbation" approximation relies on the assumption that heat conductances and capacities do not change within the variation range of the pulses. In this way, the equations that describe the composite model's dynamic behaviour are rewritten in terms of heat capacities and thermal conductances evaluated at the temperatures in the operation point;

2. the heat capacity C_{ph} of the phonon system in the thermistor is considered negligible compared with the other ones; as will be evidenced in Sec. 2.1.6, the inequality $C_{ph} \ll C_{el} \ll C_a$ holds true for the Cuoricino detector.

These approximations allow to solve analytically the dynamic problem and the resulting solution has the form

$$T_{el}(T) = \frac{E}{C_a}\cdot K\cdot\left(e^{\lambda_1 t} - e^{\lambda_2 t}\right) + T_{el}^s \quad (1.46)$$

The constants K, λ_1 and λ_2 depend from the values of the heat capacities and conductances in the system evaluated at the temperatures T_j^s obtained from the solution of the static problem.

However, the description of the composite model given in this section must be completed by incorporating some additional features.

Electro-thermal feedback: the effect has already been described qualitatively in Sec. 1.3.3. As depicted by the first equation in the set (1.38), the power in the electron system is given by the sum of two terms: a static parasitic power and a Joule power $I^2\cdot R(T_{el})$. The latter becomes smaller during the time-evolution of a thermal pulse because the rise in temperature due to particle interaction in the absorber leads to a decrease in the thermistor's resistance: the lower the Joule power dissipated, the faster is the relaxation of T_{el} to its static equilibrium value T_{el}^s. This effect is relevant unless the power in the electron system is dominated by the parasitic term. Electro-thermal feedback is integrated in the model by introducing an effective thermal conductance between the electron and the phonon systems, which substitutes the G_{ph-el} used in the previous discussion:

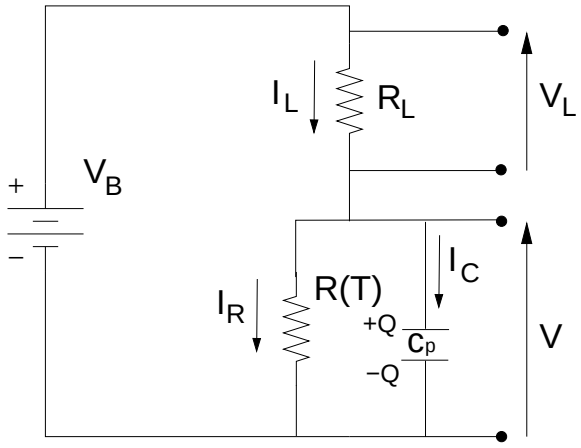

Figure 1.16: Bias circuit for the voltage read-out of the thermistor, corrected by the presence of a parasitic capacitance in parallel with the sensor's resistance.

$$G^{*}_{ph-el}(T^{s}_{el}) = G_{ph-el}(T^{s}_{el}) - \frac{I^2 \cdot R(T^{s}_{el}) \cdot A(T^{s}_{el})}{T^{s}_{el}} \tag{1.47}$$

A is the logarithmic sensitivity of the thermistor used. The use of the substitution (1.47) incorporates the electro-thermal feedback effect in the system without altering the structure of the solution (1.46).

Presence of parasitic capacitances in the bias circuit: since bolometric detectors are operated in a cryogenic environment, the electric read-out of each thermistor requires that a pair of wires is brought up to the room temperature electronics stage. Experimentally, parasitic capacitances are observed between the wires and between the wires and the ground. The second refinement of the composite thermal model consists therefore in integrating similar effects: this is done by including the presence of a capacitance-to-thermistor's resistance parallel configuration in the bias circuit (see Fig. 1.16). Given a parasitic capacitance c_p, the differential equation that describes the variation in time of the voltage pulse at the terminals of the thermistor is given by

$$\frac{\mathrm{d}V}{\mathrm{d}t} = \frac{1}{c_p R_L}\left[V_{bias} - \frac{R + R_L}{R} \cdot V\right] \tag{1.48}$$

This expression completes the set of equations (1.42) that describes the time evolution of the thermal pulse in the three nodes of the composite system. Summing up, the presence of a parasitic capacitance introduces in the system a new time constant $\tau_p = c_p R_L$, which cannot be neglected in the application under discussion: in the Cuoricino case, the typical operational values $c_p \sim 20 - 500$ pF and $R_L \sim 10$ GΩ lead to τ_p of even a few seconds, therefore comparable to the evolution times of thermal pulses.

Contribution of athermal phonons: the last refinement of the proposed composite model regards the contribution of phonons with high energy (of order $\hbar\omega_D$); they can degrade in thermal phonons by scattering with the absorber's surfaces or lattice impurities, but they can also reach directly the thermistor where they thermalize by interaction with conductance electrons. In this case, the initial condition $T_a(0) = T^{s}_{a} + E/C_a$ should be modified because the energy transfer of the interacting particle is now split in two contributions to both thermal and athermal phonons.

Due to this effect, a time constant τ_{ph} is introduced in the system to characterize the energy deposition in the thermistor by the athermal component of phonons. The time constant depends on the linear dimensions of the absorber, the propagation velocity of phonons and the absorber surface-to-thermistor surface ratio; it is, for typical values of the Cuoricino standard detector, of order $\sim$750 ms, comparable with the characteristic times of thermal pulses.

The general picture of bolometric performances will be now completed with a brief summary of the energy resolution obtained by this category of detectors and of the main noise sources that can deteriorate it.

1.4.3 Energy resolution

By thermodynamic considerations that will be explained in Sec. 1.4.4, the intrinsic energy resolution ΔE for a bolometric detector sensitive to thermal phonons is

$$\Delta E = \sqrt{k_B C(T) T^2} \tag{1.49}$$

Again, the Debye temperature T_D is confirmed as a crucial parameter of the energy absorber. It should be stressed that, according to Eq. (1.49), ΔE is does not depend on E. Even in the case of athermal phonons, it is possible to see the advantage of bolometers over conventional devices for radiation spectroscopy as the energy resolution is concerned. In fact the energy interaction generates a number N of elementary excitations equal to E/ϵ, where ϵ is the energy required to produce an elementary excitation. The intrinsic energy resolution is limited by the statistic fluctuation of the produced elementary excitation number. So the theoretic energy resolution ΔE is

$$\frac{\Delta E}{E} = 2.35 \cdot \frac{\Delta N}{N}, \tag{1.50}$$

which is proportional to $\sqrt{\epsilon}$. In a scintillator ϵ is about 100 eV, in a gas detector $\epsilon \sim$30 eV whereas in a solid state detector $\epsilon \sim$3 eV. In a detector based on phonon mediation, the energy of an elementary excitation is less than 0.01 eV even in the case of athermal phonons. So, at least in principle, energy resolutions more than an order of magnitude better than conventional devices are possible.

1.4.4 Noise sources

The noise sources of a bolometric detector equipped with a ST sensor can be classified as sources of intrinsic and extrinsic noise.

Intrinsic noise, which cannot be eliminated totally, limits the nominal energy resolution of the detector; its sources depend on some parameters of the detector, and optimizing the energy resolution means analyzing them to achieve the optimal experimental configuration. The main sources of intrinsic noise produce Johnson noise and thermodynamic noise.

Johnson noise is the white noise generated by every resistance R working at a temperature T_b, and has power spectrum equal to $e_R = \sqrt{4k_B R T_b}$. If the monolithic model is used, it is possible to demonstrate that the Johnson noise at low frequency is reduced by the electro-thermal effect.

Thermodynamic noise limits the intrinsic energy resolution in the case of complete energy thermalization. The cause is the fluctuations of the number of thermal phonons exchanged with the heat bath through the conductance G (in fact it is

also called *phonon noise*). This leads to random fluctuations in the temperature of the absorber. An estimation of this noise can be obtained by the following simplified argument. The number of phonons contained in the absorber at thermal equilibrium can be estimated as

$$N = \frac{E}{\epsilon_a} = \frac{C(T) \cdot T}{k_B \cdot T} = \frac{C(T)}{k_B}, \tag{1.51}$$

where the mean phonon energy ϵ_a is expressed as equal to $k_B \cdot T$ and E is the internal energy of the absorber. If Poisson statistics is assumed, then it is possible to estimate the fluctuations of the internal energy of the absorber in the following way:

$$\Delta E = \Delta N \cdot k_B T = \sqrt{N} \cdot k_B T = \sqrt{\frac{C(T)}{k_B}} \cdot k_B T = \sqrt{k_B C(T) T^2}, \tag{1.52}$$

which is the expression already presented in sec. 1.4.3. In the monolithic bolometer model case, a detailed calculation of noise due to intrinsic sources shows that a dimensionless factor ξ has to be introduced as a multiplier for Eq. (1.52) [49]. The ξ value depends on the details of the temperature sensor, and of the temperature dependencies of the thermal conductance and of the heat capacity; it can be made of the order of unity with a proper optimization work.

On the other hand, the extrinsic noise sources usually depend on the cryogenic, electronic and read-out set-ups. In the bolometers described in this thesis they dominate the intrinsic noise source, so they are the real limits to the energy resolution. Other sources of noise can be included in this category, such as a electric microphonic noise, electromagnetic interferences, and mechanical microphonic noise. These aren't classifiable as intrinsic noise of the detectors or as consequence of the electronic read-out of bolometers but can seriously impact detector performance. The extrinsic noise sources are characteristic of different experimental set-ups.

1.5 The Cuoricino experiment and its results

The bolometric technique described in Sec. 1.3 is the instrument used by the Cuoricino experiment in its research of 0ν-DBD. The Cuoricino experiment looks for the rare decay of the isotope ^{130}Te, whose 0ν-decay is

$$^{130}\mathrm{Te} \longrightarrow ^{130}\mathrm{Xe} + 2e^- \tag{1.53}$$

The $Q^{0\nu}_{\beta\beta}$ of the decay is $\sim$2.5 Mev (the precise value will be given in Sec 2.1.1). The isotope under investigation is contained in the bolometer itself, Cuoricino being an experiment of the kind source=detector: the material chosen for the energy absorber is the dielectric Tellurium dioxide, also known as paratellurite (TeO_2). Before Cuoricino started, its collaboration had already gathered years of experience in the use of TeO_2. The Milano group led by E. Fiorini succeeded first in operating a 340 g crystal, and then replied the result increasing the number of detectors up to 20, for a total mass of 6.8 kg of Tellurium dioxide. The measurement of the array is known as the MiDBD experiment.

Cuoricino, which was operated at the Gran Sasso National Laboratory (LNGS) in L'Aquila, Italy, constituted a further mass increase. The experiment started in 2003 and was concluded in June 2008. Currently, the constraint set by Cuoricino on the $T^{0\nu}_{1/2}$ of

^{130}Te gives one of the most competitive limits for the effective Majorana mass, comparable with the ones obtained with Ge detectors presented in Sec. 1.2.1. The importance of Cuoricino extends far from its results, as it has been the test bench for one of the most promising next-generation searches for 0ν-DBD: the future CUORE experiment, which will be presented in Sec. 1.6.1 and whose R&D provides the framework for this Ph.D. thesis. This section will give basic information about Cuoricino results, without giving details on its single-module of detection. A thorough analysis of this subject will be pursued in Section 2, and the rest of this thesis will be devoted to investigate its advancement in view of CUORE.

Cuoricino is an array of 62 TeO_2 bolometers arranged in a thirteen-floors tower (see Fig. 1.17). Eleven floors are made each of four bolometers with $5\times5\times5$ cm^3 absorbers, while the other two are composed each by six $3\times3\times6$ cm^3 detectors. Crystals have the natural abundance of ^{130}Te (34%), apart for four *small* absorbers: two of them are enriched in ^{130}Te at 82% and the other two are enriched in ^{128}Te at 75%. The total detector mass is $\sim$40.8 kg, equivalent to 11.8 kg in ^{130}Te. The tower was located in the Hall A facility at LNGS, under a mountain that provides $\sim$3400 m.w.e. shielding against cosmic rays: this, as will be explained in Sec. 2.3.1.4, is a fundamental request for the experiment. The mechanical structure of tower is made of OFHC copper, to which bolometers are connected by means of PTFE holders. Thermal pulses are read by Neutron Transmutation Doped Ge thermistors. The Cuoricino tower was hosted in a dilution refrigerator that allowed to operate the detectors at a temperature of $\sim$8 mK and was shielded by layers of lead and borated polyethylene to provide protection from the radioactive background and neutrons; details regarding cryogenic systems can be found in Appendix A. The cryostat was also surrounded by a box continuously flushed with clean N_2 to reduce Rn contaminations and it was enclosed in a Faraday cage to avoid electromagnetic interference. About once in a month, energy calibration was performed by inserting ^{232}Th sources between the cryostat and the external lead shields. Typical sum energy spectra obtained in a calibration are reported in Fig. 1.18.

The data taking of Cuoricino started in March 2003 and was interrupted in November 2003 to recover electric connections lost during the cool-down; it started again in May 2004 and continued until June 2008. The interruption divides the data taking of Cuoricino in two distinct runs. The performance of the detectors in both runs can be considered excellent, for the application under discussion: respectively 7 keV and 9 keV of energy resolution were obtained in average by the *large* and small bolometers, with highlights of $\sim$5 keV. Energy resolution is evaluated as the FWHM of the 2615 keV ^{208}Tl γ-peak observed in calibration measurements; this is also compatible with the resolution visible on the same line over long time periods. The background of the experiment and the detector's specific performances will not be discussed here, as they will be analyzed in other points of this thesis. For example, a treatment of the single detection module can be found, as already mentioned, in Sec. 2.1, and the main contributions to the background will be summarized in Sec. 3.1.1.

The single-hit energy spectrum collected by Cuoricino in the 0ν-DBD region, that is, the spectrum selecting events in which only one crystal is hit within a time window of $\sim$100 ms, is presented in Fig. 1.19. All detectors are summed. The spectrum corresponds to a total statistics of 11.83 kg·y in ^{130}Te. It must be stressed that a thorough re-analysis of the experiment is currently (June 2010) going on which will lead to an update of the statistics and to the final result of the experiment. The limits reported here are, therefore, partial.

The background in the energy spectrum in the 0ν-DBD region is

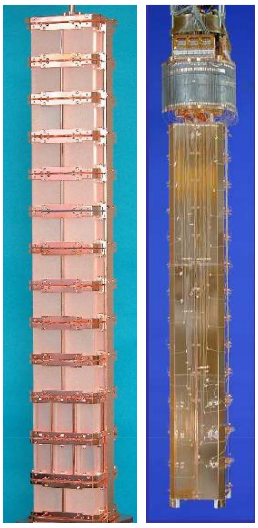

Figure 1.17: Picture of the Cuoricino tower, after the assembly (left) and suspended to the cryostat's dilution unit (right).

$$0.18 \pm 0.01 \text{ c/(keV·kg·y)}$$

The lower limit on the half-life of the decay for ^{130}Te is

$$T^{0\nu}_{1/2}(^{130}\text{Te}) \geq 3.0 \times 10^{24}\text{y} \qquad (90\%\ \text{C.L.}) \tag{1.54}$$

In order to evaluate the limit, the peaks and the continuum in the 0ν-DBD region are analyzed using a maximum likelihood method. The six spectra from the two runs and from the three different kind of crystals ($5\times5\times5$ cm^3, $3\times3\times6$ cm^3 natural and $3\times3\times6$ cm^3 enriched) are combined allowing a different background level, a different intensity of the 2505 keV ^{60}Co peak (which is inside the Region Of Interest (ROI), as will be cleared in 3.1.1) and other free parameters (the position of the ^{60}Co line and the number of counts under the 0ν-DBD peak). The response function for each spectrum is assumed to be a sum of symmetric Gaussian functions, each having the typical energy resolution of one of the detectors summed in that spectrum. The limit comes from the sum spectrum of the entire statistical data set in which each of the six spectra is weighted, based on the corresponding live time, geometric efficiency, and number of ^{130}Te nuclides. The determination of an upper limit for the effective Majorana mass is then mainly a problem of Nuclear Matrix Elements for the transition under study. It has already been mentioned that the task of their determination is quite complex, as nuclides candidate to the decay are heavy and many nucleons are involved in the calculations. Computations depend on the selection of a number of parameters, and the results from different authors give a significant spread, even for the same nucleus. Using the worse and the best case obtained by NME reported in [50],[51], [52], [53], [54], [55], [56], [57], [58], [59], [60], [61], [62], [63], [64], the lower limit on the effective Majorana mass fixed by Cuoricino is

$$m_{\beta\beta} < 0.19 - 0.68\text{eV} \tag{1.55}$$

Currently, and also considering that the full review of its analysis has not been concluded yet, Cuoricino is the only 0ν-DBD experiment with enough sensitivity to probe the claim of discovery on the decay of ^{76}Ge, briefly commented in Sec. 1.2.1. The assessment is proved by converting the half-life for ^{76}Ge, obtained from the claim, in an estimation of the half-life of ^{130}Te. For this reason, it is useful to introduce the *nuclear factor of merit* F_N defined as

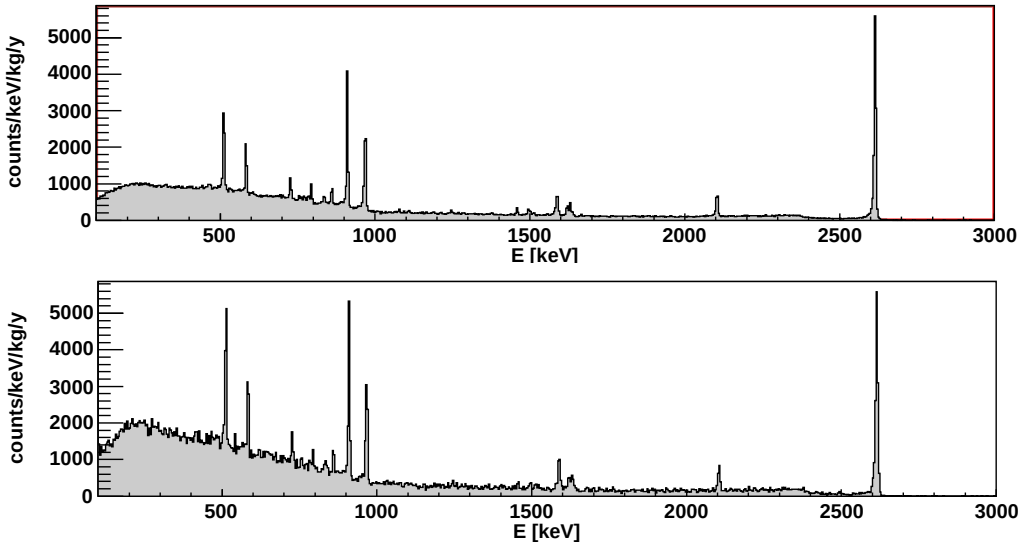

Figure 1.18: Energy spectra obtained in a common calibration of few days by the Cuoricino bolometers. The top spectrum sums over all the large crystals, while the bottom spectra sums over the small ones.

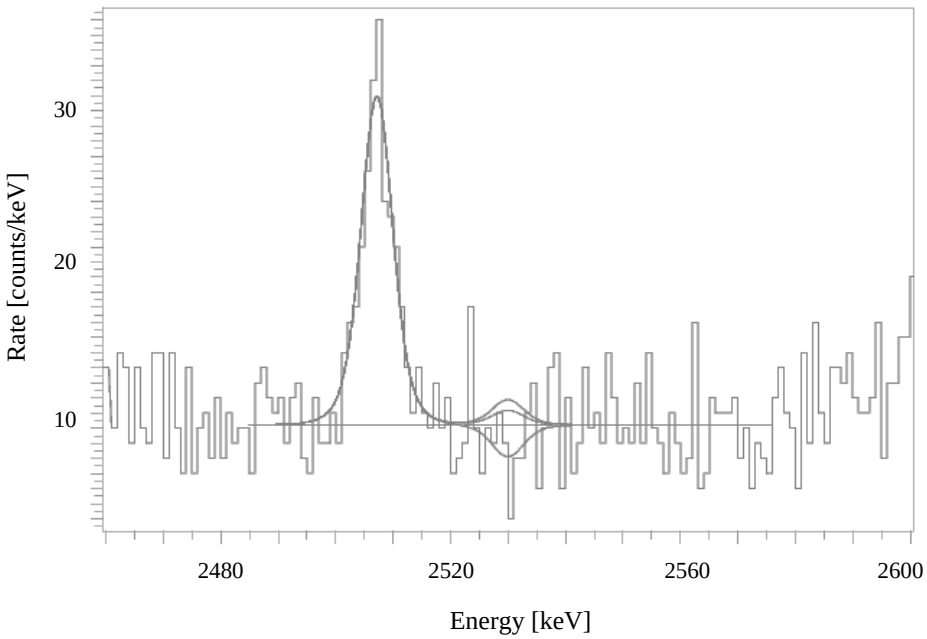

Figure 1.19: Single hit background spectrum obtained by summing over all the bolometers in the Cuoricino tower. The contribution of the observed peak at 1505 keV is negligible and will be discussed in Sec. 3.1.1. The red lines mark the best-fit, 68% and 90% C.L. on the number of events under the 0ν-DBD peak.

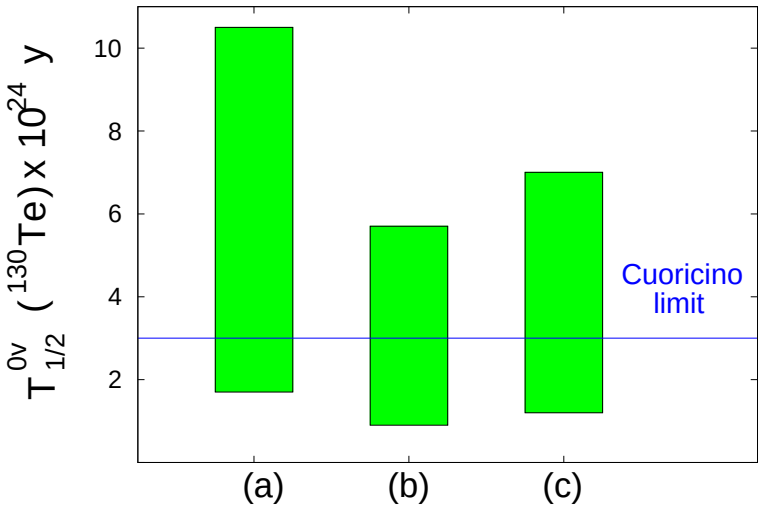

Figure 1.20: Comparison between the Cuoricino limit and the ^{76}Ge claim. The blue line represents the Cuoricino limit for ^{130}Te, while the green bands are the range of the ^{76}Ge claim [30] expressed in terms of $T^{0\nu}_{1/2}(^{130}\text{Te})$ as stated by Eq. (1.58). The F_N used to compute the three bands derive from the NME reported in (a) [50] (b) [51] (c) [52].

$$F_N \equiv G^{0\nu}|M^{0\nu}|^2\,, \tag{1.56}$$

so that, in accordance to Eq. (1.25), the effective Majorana mass can be written as

$$\langle m_{\beta\beta}\rangle = \frac{1}{\sqrt{T^{0\nu}_{1/2}\cdot F_N}} \tag{1.57}$$

When comparing germanium to tellurium, the previous definition translates into

$$T^{0\nu}_{1/2}(^{130}\text{Te}) = T^{0\nu}_{1/2}(^{76}\text{Ge})\cdot\frac{F_N(^{76}\text{Ge})}{F_N(^{130}\text{Te})} \tag{1.58}$$

In order to compare $T^{0\nu}_{1/2}(^{76}\text{Ge})$, written in terms of $T^{0\nu}_{1/2}(^{130}\text{Te})$, to the limit obtained by Cuoricino, NME must be selected. Fig. 1.20 plots the results based on three different calculations ([50], [51], [52]) and shows that, although Cuoricino has explored part of the $m_{\beta\beta}$ range allowed by the claim on ^{76}Ge, it does not have enough sensitivity to refute it.

1.6 Upcoming developments of 0ν-DBD search

According to the motivations and data presented in Sec. 1.2, united to the limit obtained by Cuoricino, the next experimental goal in the field of 0ν-DBD search is pushing the investigation down to the region of the effective neutrino Majorana mass corresponding to the inverted hierarchy. This means increasing of an order of magnitude the current sensitivities on $m_{\beta\beta}$. Many strategies, according to the technique, can be adopted to reach the goal, and the second part of Chapter 2 will present some possibilities regarding mainly the framework of bolometric detection; the general trend, however, is an increase in the source mass and a strong reduction of the background. Tab. 1.2 indicates the future experiments that are foreseen to reach the highest sensitivities in the next-generation. Experiments in the list are currently in R&D, apart from the first phase

of GERDA, the first phase of EXO and CUORE, which are in progress. The CUORE experiment, the next-generation of Cuoricino, will be now introduced: the work presented in this thesis has been developed in the framework of its R&D activity.

1.6.1 The near and the next future: CUORE-0 and CUORE

The CUORE detector is the future of the bolometric technique applied to 0ν-DBD search. Its principle of operation is very close to that of Cuoricino. It will comprise 988 TeO_2 bolometers arranged in 19 towers of 52 crystals each; each tower will be composed by 13 floors holding 4 bolometers. The towers will be assembled in a cylindrical structure, as shown in Fig. 1.21. The single module of detection of the CUORE experiment is basically an evolution of the Cuoricino bolometer: for this reason, before introducing the R&D work developed for CUORE, a detailed presentation of the Cuoricino Single Module will be given in Chapter 2. The closely-packed configuration, with high granularity, of CUORE bolometers will allow to operate the array in anti-coincidence, providing a powerful instrument for the reduction of certain contributions to the background.

The total mass of CUORE will be $\sim$740 kg in TeO_2, and $\sim$200 kg in ^{130}Te: this, compared to Cuoricino, corresponds to an increase in mass of order 20. Also, the background in the range of the $Q^{0\nu}_{\beta\beta}(^{130}\text{Te})$ will be reduced of approximately the same amount, although this is one of the most delicate points in the design of the experiment. CUORE will start taking data in 2013 and will operate for five years. No further appreciable gain in sensitivity, as Sec. 2.3.1 will demonstrate, is expected by operating beyond this amount of time.

The experiment will be located in the underground Hall A facility at LNGS, as Cuoricino. The cryogenic system will be LHe-free and will be operated at $\sim$10 mK, shielded by a structure thoroughly revised, in respect to that used for the Cuoricino tower. Several other aspects of the detector have been revised, apart from the increase of mass and the reduction of the background: the mechanical structure of the towers, the calibration system, the data acquisition system and the analysis software tools are only a few examples of the many requirements necessary for CUORE to live up to its expectations.

The R&D phase is now over, and the experiment is under construction. However, an intermediate phase is planned before CUORE starts. The first tower of CUORE will be, in fact, assembled and cooled-down in the same cryostat that has been hosting Cuoricino until Summer 2008 and will start taking data at the beginning of 2011. The necessity for a step between the last and the next-generation is justified by the many innovations introduced, for example, in the assembly, in the structure of the detector, in the surface treatments of the materials. CUORE-0 will provide validation for the protocols and the elements introduced in the setup. Moreover, it will be a stand-alone experiment that will increase the current sensitivity on the effective Majorana mass gained by Cuoricino: this will be explained in Sec. 2.4.1.

As the future performances of CUORE stand on the shoulders of the Cuoricino detector, the next chapter will be devoted to describing its features, as well as the characteristics to focus on when planning an optimization work.

Isotope	Experiment	Nuclide mass [kg]	Technique	$T^{0\nu}_{1/2} \geq \times 10^{26}$ [y]	$\langle m_{\beta\beta} \rangle$ [eV]
^{76}Ge	GERDA [40]	40	HPGe	2	0.07-0.3
”	”	1000	”	60	0.01-0.04
^{76}Ge	Majorana [65]	40	HPGe	2	0.07-0.3
”	”	1000	”	60	0.01-0.04
^{130}Te	CUORE [66]	200	Bolometric	2	0.02-0.09
^{136}Xe	EXO [67]	200	TPC	0.6	0.1-0.2
”	”	1000	”	20	0.02-0.03
^{82}Se	Super-NEMO [68]	200	Tracking	2	0.05-0.1

Table 1.2: Next-generation experiments for 0ν-DBD search.

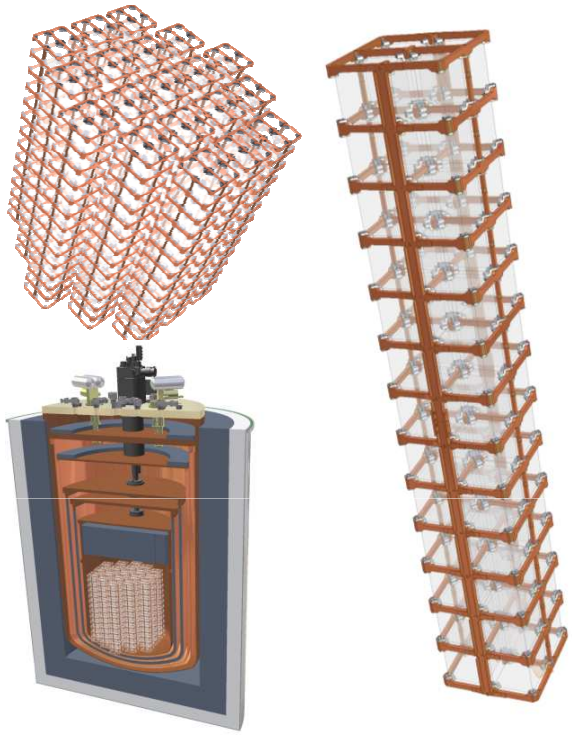

Figure 1.21: Pictures of the future CUORE detector. Top left: the closely-packed structure of the 19-towers array; bottom left: simulation of the detector suspended in the L-He free cryostat; right: the 52-crystals single CUORE tower: the first tower constructed will serve as the detection unit of the independent experiment CUORE-0.

Chapter 2

Overcoming the Single Module of the Cuoricino detector

Chapter 1 provided an overview on the currently hot topics in neutrino physics and introduced 0ν-DBD search as a powerful instrument to answer the open questions on this particle's nature and mass. Moreover, a description of the bolometric technique applied to this field of research allowed to present the results from the Cuoricino experiment, which in turn motivated the drive towards the next generation of macro-bolometers based investigations. CUORE, preceded by its *test bed* CUORE-0, is the future of the bolometric technique in 0ν-DBD search. The design of the new experiment is based on a review of the Cuoricino basic element, which has been subjected to a radical R&D. The goal of this thesis is to present the advancements obtained on the *Single Module* of the Cuoricino detector, and this chapter will give the elements to motivate and understand the optimization work performed. For this reason, the following sections will detail the elements of the basic Cuoricino detector, apply the composite model described in the previous chapter to its characteristics, and introduce the components whose tuning contributes to increasing the sensitivity of the final experiment.

2.1 The Single Module of the Cuoricino detector

In this section, a picture of the components that constitute the Cuoricino Single Module (SM) will be provided, basing on the main concepts of the bolometric technique described in Sec. 1.3. Although the optimization work presented in Chapters 4 to 6 will focus on just a subset of the elements listed hereafter, a thorough comprehension of the R&D performed requires the overview to be complete. The devices of the full SM that will be introduced are the TeO_2 crystal absorber, the Ge temperature sensor doped by neutron transmutation, the detector holding structure and the Si heater; moreover, the thermal connections between pairs of components will be mentioned.

2.1.1 The TeO_2 crystal absorber

As already explained in Sec. 1.3, the use of bolometric detectors can be successfully applied to the search for 0ν-DBD, due to the good energy resolutions and the consequent increase of the signal-to-background ratio offered by this technique [69], [70]. It was also pointed out that the CUORE collaboration, and the Milano group led by E. Fiorni before it, have been developing for years large mass bolometers based on TeO_2 crystals as energy absorbers [71]. This design strategy relies on two motivations that

involve the choice of an advantageous nuclide for the investigation on one hand, and of a material suitable for detector assembly and operation on the other hand.

2.1.1.1 The choice of the nuclide: ^{130}Te

When introducing Cuoricino in Sec. 1.5, the rare event searched for by this experiment was mentioned to be the 0ν-DBD decay of ^{130}Te in ^{130}Xe with the emission of two electrons, quoted in Eq. (1.53). Various properties of ^{130}Te confirm it as a good choice of 0ν-DBD source.

High natural isotopic abundance - This property is particularly important in the field of investigation discussed here. Later in this chapter, in Sec. 2.3, the sensitivity of a 0ν-DBD bolometric experiment will be introduced as a measure of the impact that a specific detector property has on the experiment's capability to detect 0ν-DBD. A simple estimation, based on a calculation that will become clear later on, can nonetheless be anticipated to understand the importance for a nuclide to have a high natural isotopic abundance. Should the experiment have a radioactive background level b equal to 1 c/(keV·kg·y), an energy resolution ΔE=10 keV and a detector efficiency ϵ equal to 1, a minimum number of 5×10^{27} nuclei must be investigated for one year to detect half-lives higher than 10^{26} years. For this reason, natural isotopic abundances of a few per cent are insufficient. Another aspect that makes high isotopic abundance a desirable property is the lack of experimental space in certain kind of experiments, which limits the total usable mass: this is the case of the cryogenic detectors under discussion here. The natural i.a. of ^{130}Te, 33.8% [73], is strikingly higher than that of all the investigated nuclides. The property is a definite advantage: it means that no isotopic enrichment is necessary to perform an experiment highly sensitive to 0ν-DBD; enrichment is an expensive and complex procedure, and it can also introduce radioactive impurities in the crystals, as it will be remarked in Sec. 2.3.1.5. Fig. 2.1a shows a comparison in natural isotopic abundance among the set of candidates to be 0ν-DBD sources.

Transition energy $Q_{\beta\beta}$ - A second reason to choose ^{130}Te as 0ν-DBD source regards the energy transition of the decay, the latest measurement of which gave the result [74]

$$Q^{0\nu}_{\beta\beta} = 2527.01 \pm 0.32\,[\text{keV}] \tag{2.1}$$

The value is considerably high, in respect to the other candidate nuclides, although it is not the highest. A larger $Q^{0\nu}_{\beta\beta}$ is preferred because it corresponds to a larger phase space $G_{0\nu}$, as determined by the Q^5 dependence; the higher the Q-value, the bigger is the probability for the decay to occur.

Energy window - Even though the $Q^{0\nu}_{\beta\beta}$ of ^{130}Te is not the largest among the nuclides candidate for 0ν-DBD search, it leads to a striking advantage when considering its position in respect to the natural radioactive background: it is, in fact, situated in a window of the spectrum characterized by low radioactivity, between the full energy and the Compton edge of the 2615 keV photon peak (^{208}Tl due to the Th chain), and out of the ^{238}U background. Fig. 2.1b shows the position of the $Q_{\beta\beta}$ value among the other nuclides candidate to the decay; the 2.6 MeV γ of ^{208}Tl is marked for convenience.

Nuclear dynamics - As shown in the previous chapters, the 0ν-DBD half-life is inversely proportional to the Nuclear Matrix Elements $|M^{0\nu}|^2$ by means of the nuclear structure factor F_N. F_N has already been defined in Eq. (1.56) as the product of $|M^{0\nu}|^2$ to the phase space $G^{0\nu}$, and its relationship of inverse proportionality

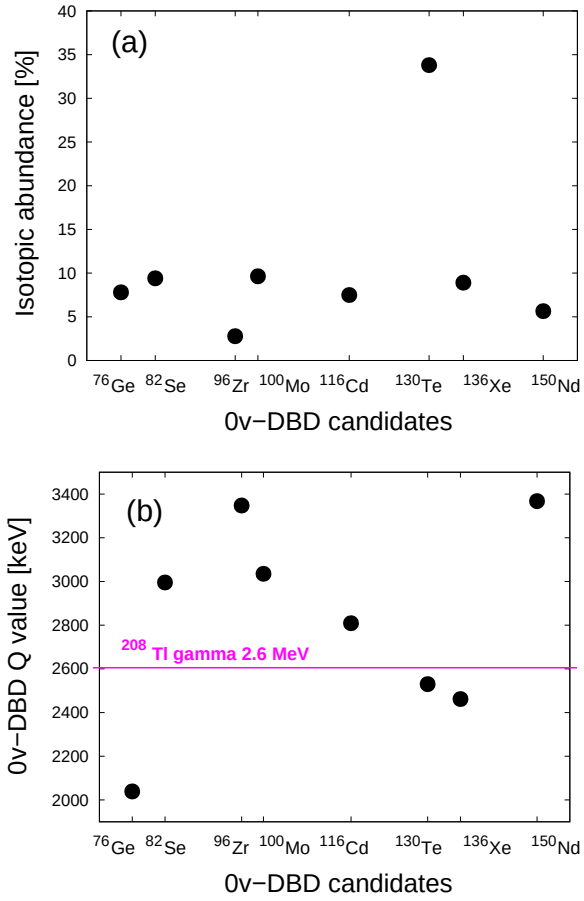

Figure 2.1: Properties of the nuclides candidate to 0ν-DBD: (a) isotopic abundance and (b) Q-value of the decay. In plot (b), the 2.6 MeV γ-peak of 208Tl, which is the end-point of natural radioactivity, is evidenced.

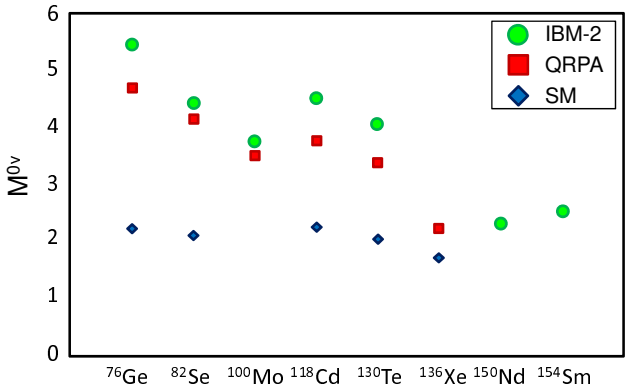

Figure 2.2: Comparison among the average nuclear matrix elements $< M^{0\nu} >$ by IBM-2, QRPA and SM of candidate nuclides, extracted from [72].

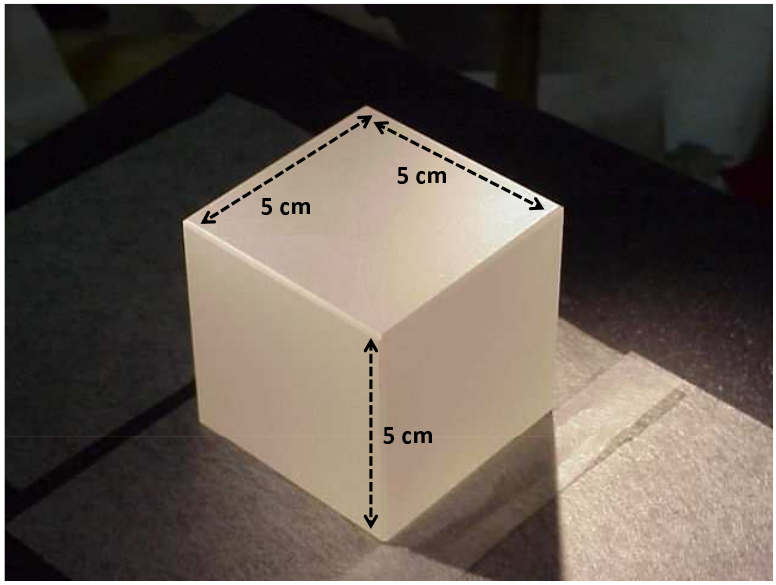

Figure 2.3: 5×5×5 cm^3 TeO_2 crystal absorber used in the Cuoricino experiment.

with $T^{0\nu}_{1/2}$ has been made explicit in Eq. (1.57). The NME are dominated by the nuclear dynamics, and their values are model dependent and different from one nuclide to another (see, for example, the comparison in Fig. 2.2 among the Interacting Boson, QRPA and Shell models [72]). In most of the nuclear models used to compute the matrix elements, the final F_N obtained by their product with the phase space is more favorable for ^{130}Te than for ^{76}Ge.

2.1.1.2 The choice of the material: TeO_2

The choice of ^{130}Te is supported by the selection of a material which contains the nuclide under investigation and features, at the same time, properties compatible with its use in cryogenics. The compound known as paratellurite (TeO_2) satisfies the characteristics requested. More specifically, it brings the following advantages.

Good mechanical properties - TeO_2 resists subsequent thermal cycles down to a few mK, in opposition to pure metallic tellurium whose crystals do not stand easily cool-downs at similar temperatures and crack after a few cycles; with TeO_2, large single crystals with excellent thermal and mechanical properties can be grown;

Debye temperature - T_D is higher for TeO_2 than that for pure Te and so, at the same temperature, paratellurite crystals have a lower specific heat: higher pulses can be achieved;

Compound composition - Te dominates the paratellurite compound with respect to the mass (about 80%), permitting to work with large quantities of this material;

Radio-purity - Crystals can be grown with high radio-purity ($<$1 pg/g in ^{232}Th and ^{238}U): the importance of this characteristic will be evidenced by Sec. 2.3 and described to a large extent by Chapter 4.

Fig. 2.3 shows the picture of a typical 5×5×5 cm^3 TeO_2 crystal used in the Cuoricino experiment.

2.1.2 The NTD Ge thermistor

In the Cuoricino experiment, Ge thermistors doped by the neutron transmutation technique are used as temperature sensors: this choice has been pursued by the Milano *Weak Interaction Group* (WIG) since the beginning of its research on the bolometric technique applied to the search of 0ν-DBD. In the operational mode valid for this thesis, NTD-Ge thermistors work in the VRH conduction regime with Coulomb gap. Sec. 1.3.3 has already pointed out that this kind of sensors behave as perfect thermometers; they convert each thermal pulse into an electrical signal, thanks to the dependence of resistivity on temperature

$$R(T) = \rho(T) \cdot \frac{l}{S} = R_0 \cdot e^{(T_0/T)^\gamma}. \tag{2.2}$$

The γ parameter's value is 0.5 in the MIT region and at a working temperature lower than 1 K; T_0 is a function of doping; R_0 depends on the sensor's geometry and is obtained by multiplying the ratio of l (the distance between the electrical contacts) to S (the area of each pad) with the electric resistivity ρ_0, already described by Eq. (1.36). This is assumed when the pads for electric contact are situated on the sides of the thermistor, opposed to each other; other configurations will be discussed in Chapter 5.

The thermistors of the Cuoricino experiment were designed and produced by a conjunct group led by E. E. Haller and composed by researchers of both the Lawrence Berkeley National Laboratory (LBNL) and the Department of Material Sciences at the University of California-Berkeley. The Neutron Transmutation technique used for material doping consists in placing wafers of ultra-pure Ge in a nuclear reactor to obtain the characteristics required for the resistance and its variation with temperature. Only the NTD technique is capable of producing doping at the uniformity levels required for the application under discussion; for example, melt-doped Ge crystals cannot achieve the necessary uniformity due to a variety of dopant segregation effects. In typical applications, the neutron absorption probability for a 3 mm thick wafer of Ge is small, on the order of 3 %, leading to a very homogeneous, uniform absorption process.

The reactions that take place when a Ge wafer is inserted into a nuclear reactor are listed in Tab. 2.1: in the process, ^{70}Ge transmutes into the acceptor atom Ga and ^{74}Ge transmutes into the donor As, which is the primary active dopant in NTD-Ge. The concentration of dopant atoms is expressed by

$$N_{\text{dopant}} = m \cdot \text{i.a.} \cdot \frac{N_A(\sigma_T \Phi_T + \sigma_E \Phi_E)}{M} \cdot t. \tag{2.3}$$

Figure 2.4: $3\times3\times1$ mm^3 NTD-Ge thermistor used in the Cuoricino experiment: the sensor is connected to the crystal absorber; gold wires for signal read-out are visible.

^{70}Ge (21%) + n $\rightarrow$ ^{71}Ge + γ	σ_T=(3.43$\pm$0.17) b	
	σ_E=1.5 b	Acceptor
^{71}Ge + e$^-$ $\rightarrow$ ^{71}Ga + ν_e	$\tau_{1/2}$=11.4 days	
^{74}Ge (36%) + n $\rightarrow$ ^{75}Ge + γ	σ_T=(0.51$\pm$0.08) b	
	σ_E=(1.0$\pm$0.2) b	Donor
^{75}Ge $\rightarrow$ ^{75}As + e$^-$ + $\bar{\nu_e}$	$\tau_{1/2}$=83 minutes	
^{76}Ge (7.4%) + n $\rightarrow$ ^{77}Ge + γ	σ_T=(0.160$\pm$0.0014) b	
	σ_E=(2.00$\pm$0.35) b	Double
^{77}Ge $\rightarrow$ ^{77}As + e$^-$ + $\bar{\nu_e}$	$\tau_{1/2}$=11.33 hours	donor
^{77}As $\rightarrow$ ^{77}Se + e$^-$ + $\bar{\nu_e}$	$\tau_{1/2}$=38.8 hours	

Table 2.1: Reactions in the Neutron Transmutation Doping of a Ge wafer. Here, σ_T and σ_E are the thermal and epithermal neutron capture cross sections, respectively.

In Eq. (2.3), m is the wafer mass, i.a. the isotopic abundance, M the molar mass of the target isotope, σ_T and Φ_T the cross section and flux of the thermal neutrons, σ_E and Φ_E the cross section and flux of the epithermal neutrons, t the irradiation time. The NTD procedure allows to obtain a concentration of dopants per neutron unity flux equal to 2.94×10^{-2} cm^3 per neutron/(cm^2·s) for Ga and 8.37×10^{-3} cm^3 per neutron/(cm^2·s) for As [75]. Since the doping level of Ge needs to be on the order of 1×10^{17} atoms/cm^3, a very high flux reactor, such as the ones at the University of Missouri-Columbia and at the Massachusetts Institute of Technology, is necessary to perform the doping in a reasonable time; even more relevant factors are stability in the flux and stability in the neutron energy distribution as measured by the Cd ratio. It is very important to optimize the neutron irradiation exposure and to make the exposures as uniform as possible. The significant quantity involved in thermistor performance is the net dopant concentration, which is equal to the difference in concentrations N_{Ga}-N_{As}-2N_{Se}. Unfortunately, the evaluation of the doped material's quality is possible only after the decay of the activation product ^{71}Ge (11.4 day), and about one year is necessary before the samples can be handled; a delay is required before understanding if the wafers need more exposure. To overcome this difficulty, the Ge samples are always accompanied by foils of metal with long-lived (n,γ) radioactive daughter nuclei; the neutron exposure of Ge can be determined accordingly with accuracy and uniformity of exposure is achieved. Previous measurements performed at LNGS also show that the residual activity of the NTD thermistors become fully tolerable in an experiment with thermal detectors already a few months after irradiation [76]. Following neutron exposure and the radioactive decay period, the NTD germanium is first heat treated to repair the crystal structure and then cut to obtain pieces of the desired geometry. No details are now given on the processing and handling of the bare Ge material, because the topic will be discussed in Chapter 5.

The intrinsic parameters R_0, T_0 and γ introduced by Eq. (2.2) must be experimentally measured for each thermistor at its operating temperatures: in the case of Cuoricino, the characterization process was done at the cryogenics laboratories in the universities of Milan and Florence; the procedure is described in detail for Si thermistors in [77] and the same process is used for the Ge thermistors of this application. The logarith-

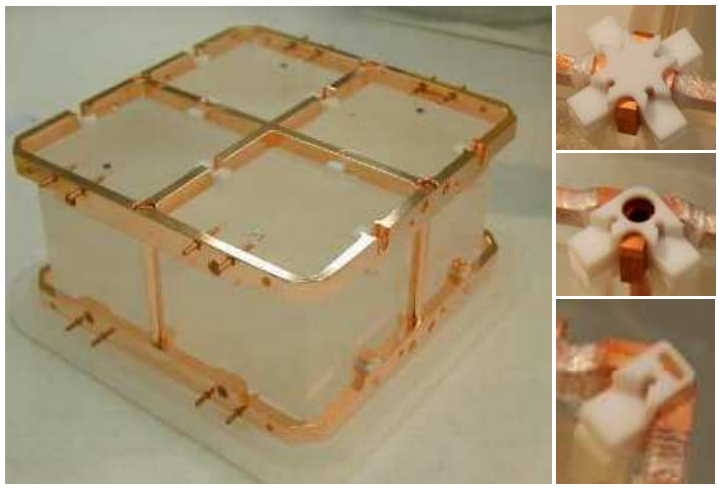

Figure 2.5: Left: the Cu frame for the four-crystals Cuoricino module. Right: examples of PTFE holders. The samples in the picture are a variation of the ones used in Cuoricino, and were designed during the CUORE R&D.

mic sensitivity A for semiconductor thermistors has also been defined in Sec. 1.3.3 as a parameter that depends on the neutron irradiation dose. Groups of thermistors are classified as belonging to numbered doping series, each described by the values measured in the characterization for R_0 and T_0. The NTD-Ge thermistors used in the Cuoricino experiment belong to the series numbered as #31 in the classification established by the Berkeley group: among the tested series, their parameters fit in the best way the requirements on detector performances made by the R&D previous to the realization of Cuoricino. Their T_0 is $\sim$4 K, and therefore A ranges from 7 to 10. Fig. 2.4 shows the picture of a Cuoricino thermistor connected to the absorber.

2.1.3 The support structure

The support structure of the Cuoricino detector's SM is designed to host four $5\times5\times5$ cm^3 TeO_2 crystals. Its role is to secure the bolometers in order to prevent power dissipation due to the friction caused by mechanical vibrations and to provide adequate thermal contact with the dilution refrigerator used for the cool-down at $\sim$10 mK temperature. The support structure is constituted by two components.

2.1.3.1 The heat bath

This part of the support structure is provided by metal frames connected to the *mixing chamber*, the coldest part of the dilution refrigerator: due to the specific application, and due to its good thermal properties, *Oxygen-Free High Conductivity* copper (OFHC Cu) was selected as a material. A strong constraint on the quality of the final Cu frames is the lack of radioactive contaminants on the surfaces that face directly the detectors: this will be motivated the end of this chapter and investigated in Chapter 3.

2.1.3.2 The mechanical holders

The contact between the four bolometers in the SM and the copper frames that enclose them is not direct because of thermal and mechanical motivations. First, crystal absorbers have to be held tightly enough to reduce the sensitivity to mechanical vibrations, but with sufficient elasticity to prevent them from cracking because of low-temperature

differential thermal contractions; then, the thermal conductance between the bolometers and the heat bath must not be too low, which would result in thermal pulses with excessive τ_d, neither too high, or the energy released by the particle in the absorber would flow through the thermal link to the bath producing a loss in pulse amplitude. Copper allows good thermal contact with the dilution refrigerator but cannot provide the aforementioned features. The solution used in Cuoricino consists in interposing PTFE holders between TeO_2 and Cu. In fact, the high thermal contractions of PTFE allow to hold crystals firmly in a down-to-10 mK cool down; at the same time, it remains elastic enough to touch the absorbers without breaking them. Moreover, PTFE holders can be easily dimensioned to obtain the desired bolometer-to-heat bath thermal conductance. Such conductance was measured directly in Milan: the obtained value, corresponding to the Cuoricino design, will be quoted in Sec. 2.1.6 and is deemed reasonable for the application.

2.1.4 The Si heater

When operating a long-running experiment like Cuoricino, one of the critical points is the necessity to maintain the bolometers in conditions as much stable as possible. Unfortunately, the complicated cryogenic set-up required for detector operation at low temperatures shows intrinsic instabilities. For example, temperature fluctuations can spoil the detector's energy resolution, because the small but unavoidable changes in the temperature of the heat sink produce correlated fluctuations in the detector operation temperature: since the operation voltage V_{bol} across the bolometer is equal to IR, where I is the applied constant bias current and R the thermistor resistance (see 1.3.3), and since R has a strong temperature dependence, the operation voltage changes with bath temperature fluctuations. As a consequence pulse amplitudes also change, thus originating a broadening of the energy resolution. A specific method for the stabilization of detector response is therefore required; the method is based on mechanisms acting directly on the detector followed by an off-line correction of pulse amplitude. The obvious approach to stabilize the response consists in the use of a pulser, able to deposit periodically in the bolometer's absorber a known amount of energy and to generate a pulse as similar as possible to the searched signals. The most efficient method for response correction requires that the ratio between the amplitude of a pulse and its baseline value is considered. A baseline segment is registered for a given time interval ($\sim$100 ms) preceding the signal's development, and the corresponding baseline level V_{BL} is determined. The baseline level is related to the operation voltage V_{bol} across the thermistor by the relationship

$$V_{BL} = G(-V_{bol} + V_{off}) \,, \tag{2.4}$$

where G is the total gain and V_{off} is the offset added to null the DC output. In the absence of temperature fluctuations and because the pulser delivers signals corresponding to a fixed energy, V_{bol} and V_{BL} are constant; in real cases, where instabilities are present, the relationship $V_{bol}(V_{BL})$ between the two can be often approximated with a negative slope straight line. It has been observed that during long run measurements the function $V_{bol}(V_{BL})$ can change, which leads to the necessity of keeping continuously monitored the baseline dependence of pulse amplitude. Then, a reference value V_{BL}^{ref} is chosen and the multiplicative factor $\alpha(V_{BL})=V_{bol}(V_{BL}^{ref})/V_{bol}(V_{BL})$ is defined; in the off-line analysis, $\alpha(V_{BL})$ is used to bring back to the reference level V_{BL}^{ref} the amplitude V_{bol} of a pulse acquired in correspondence to the baseline level V_{BL}. The same procedure is used to correct the amplitude of each pulse acquired, provided that the corresponding baseline level is known. The final result of the stabilization process is that energy spectrum peaks that had been removed or broadened by system instabilities are recompacted (Fig. 2.6). Heater operation also allows to determine the optimum point in

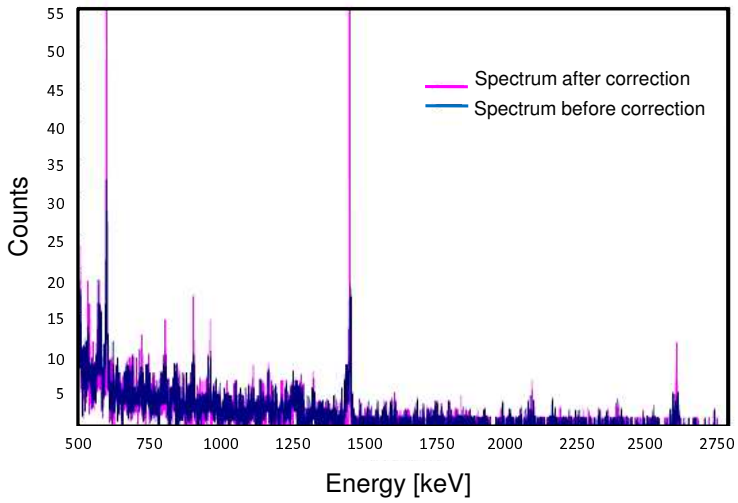

Figure 2.6: Example of energy spectrum stabilization.

the thermistor's *IV* curve, which has already been introduced in Sec. 1.3.3: by injecting a constant amount of power, it is possible to determine the voltage at the thermistor's terminals corresponding to the maximum detector response.

In the Cuoricino experiment, for these aims a heating element that delivers Joule pulses is thermally coupled to the crystal. This resistive device is called *heater* and allows to have full control on calibration mechanisms, as the produced pulses are equally spaced in time, the rate and amplitudes are easily tunable with the experimental requirements, and pulser signals can be recognized by software. In order for the heater to inject a stable, almost instantaneous, reference amount of Joule power in the detector, some basic requirements are made: its resistance must be reasonably independent of temperature and applied voltage, and it must be higher than the one of connection wires; its heat capacity must be negligible compared to that of the detector; the relaxation time of the heat pulse delivered into the crystal must be much shorter than all the other typical thermal constants; and the signal formation due to Joule heating must simulate as much as possible a particle interaction, to assure that the pulse amplitude dependencies on time, baseline level and other operation conditions are the same for the two processes. Heaters fabricated from heavily doped Si satisfy the previous requests. They are glued on crystal absorbers and once detectors are cooled down, square voltage pulses are injected into the devices with a programmable pulse generator; the amplitude (of order

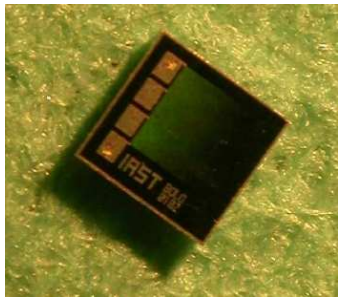

Figure 2.7: One of the Si heaters used in the Cuoricino experiment.

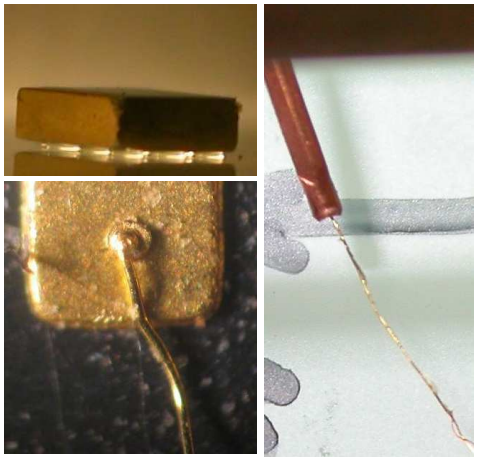

Figure 2.8: From upper left, counterclockwise: the connection of the thermistor to the TeO_2 crystal by means of glue spots; detail of a wire ball-bonded to a gold pad; wire inserted in the apposite copper pin for signal read-out.

1 V) and time width (of order 1 ms) are tuned to develop a few MeV thermal energy in the pulser.

Si heaters based on the same principle of those used in Cuoricino and produced by the Italian research center on semiconductors ITC-irst will also be used in CUORE-0 and CUORE: heater batches for use in the two next experiments have been characterized at low temperatures, of order 1 keV, at the Cryogenics Laboratory in Como [78]. The Si heater is shown in Fig 2.7.

2.1.5 Other sensor couplings

The description of two kinds of connection for the mechanical, thermal and electric coupling of the Ge thermistor and the Si heater completes the picture of the Cuoricino SM. Examples of these couplings are shown in Fig. 2.8.

2.1.5.1 The sensor-to-crystal coupling

Both the Ge thermistor and the Si heater are connected to their crystal absorber by means of the bi-component epoxy Araldite Rapid; the glue is distributed in matrices of dots with diameter ranging from 0.5 to 0.8 mm, and 50 μm height. A matrix of nine dots is used for the thermistor, while five dots are used for the heater. The distribution in separate dots compensates the differential thermal contractions between the material of each sensor and TeO_2, so that no fractures or detachment of the elements happen at low temperatures. A thorough review of the motivations and the characteristics of this connection will be provided in Chapter 6.

2.1.5.2 Electric connections

The electric contacts are obtained with gold wires with diameter 50μm ball-bonded on the lateral gold sides of the thermistors and on the aluminum pads of the heater. These connections are also thermal links to the heat bath, as the wires are inserted inside small Cu tubes and crimped for electric read-out. The ball-bonding procedure and the difficulties it brings to the detector assembly process will be detailed in Chapter 5.

All the materials used in the construction of the complete four-crystals SM used in the experiment must be certified from the point of view of radio-purity. Copper has the advantage to have a good heat conductance and that it is relatively easy to obtain batches of material complaint with the radio-purity requests; in the same way, PTFE is available at good radio-purity levels. However, all this issues will be discussed later in this same chapter.

2.1.6 Composite modeling: application to the Cuoricino detector

The second part of the previous chapter was focused on an overview of the bolometric technique with large-size absorbers. The behaviour of macro-bolometers was treated first by means of the simplified monolithic picture, and then by introducing a more detailed composite thermal model from both the static and the dynamic point of view (Sec. 1.4). Now that the characteristics of the Cuoricino detector have been introduced, the composite modeling can be referred to this specific application. The thermal network corresponding to the composite picture and updated to the elements of the Cuoricino basic macro-bolometer is sketched in Fig. 2.9. The reference node of the model is the heat bath, which, in the practical case considered here, is constituted by the bolometer's copper holder: the real experimental set-up is operated at bath temperatures of order $\sim$10 mK. The quantities required for a full definition of the Cuoricino basic bolometer in the composite thermal model are listed hereafter. Thermal conductances G_j and heat capacities C_j all have the forms described in the previous chapter by Eqs. (1.40) and (1.43): power laws in T, with experimentally determined coefficients g_j and c_j.

- The thermistor's characteristic curve, expressed in terms of the VRH parameters R_0, T_0 and γ quoted in equation 2.2. The measurement of this values relies strongly on the temperature scale used in the characterization and is a delicate experimental issue. For example, two different temperature scales have coexisted in the CUORE collaboration, which came from measurements performed at either Milan or Florence University and gave slightly different values of T_0 for thermistors used in Cuoricino. However, a specific characterization has recently been performed at the Cryogenics Laboratory in Como, taking particular care to solving the issue of defining a reliable temperature scale. The values used for the R_0 and T_0 parameters in this thesis come from that characterization [79]: they are 0.92 Ω and 4.11 K for the Cuoricino thermistors of the #31 series. Another doping series, #34, will be introduced in Chapter 5 and a few more details about characterization issues will be given.

- The TeO_2 crystal's specific heat (C_{abs}). Dedicated measurements [80], once again performed in Florence, confirmed the good agreement of its temperature dependence with Debye's law, and determined the Debye temperature as T_D=232 K.

- The crystal-to-heat bath thermal coupling ($G_{abs-bath}$), provided by the set of PTFE holders screwed to the Cu support structure. The measurement made in Milan [81], and specific to the Cuoricino design in terms of contact surface, gave the result

$$G_{abs-bath}\,[\mathrm{W/K}] = 4 \times 10^{-5} \cdot T\,[\mathrm{K}]^2 \tag{2.5}$$

- The thermal conductance of the glue spots in the thermistor/absorber interface (G_{th-abs}). The conductance measured for the bi-component epoxy used and for the peculiar geometry of its deposition is [81]

$$G_{th-abs}\,[\mathrm{W/(K{\cdot}spot)}] = 2.6 \times 10^{-4} \cdot T\,[\mathrm{K}]^3 \tag{2.6}$$

- The specific heat of the thermistor's lattice (C_{lat}). It corresponds to the Ge specific heat

$$C_{lat}\,[\mathrm{J/K{\cdot}mm^3}] = 3 \times 10^{-9} \cdot T\,[\mathrm{K}]^3, \tag{2.7}$$

- The thermistor's lattice-to-heat sink thermal coupling. It is due to the interface between Ge, which constitutes the sensor's bulk material, and Au, in form of side pads for signal read-out. The conductance is proportional to the single pad area:

$$G_{pad}\,[\mathrm{W/K{\cdot}mm^2}] = 0.8 \times 10^{-5} \cdot T\,[\mathrm{K}]^{2.4} \tag{2.8}$$

- The thermal conductance in the electron-phonon uncoupled systems (G_{ph-el}). It is internal to the thermistor itself and its estimation is [81]

$$G_{ph-el}\,[\mathrm{W/K{\cdot}mm^3}] = 7.8 \times 10^{-2} \cdot T\,[\mathrm{K}]^{4.37} \tag{2.9}$$

- The specific heat of the thermistor's electron system (C_{el}), chosen to account for the observed rise times of thermal pulses and not measured directly:

$$C_{el}\,[\mathrm{J/K{\cdot}mm^3}] = 1.1 \times 10^{-9} \cdot T\,[\mathrm{K}] \tag{2.10}$$

- The background power acting on the crystal and on the thermistor's electron system. No direct experimental measurements on these parameters have been performed; however, a few pW are deemed a reasonable value for the background power in the absorber, while fractions of pW are assumed for the thermistor's electron system (the simulations that will be shown in the course of this dissertation are based, respectively, on the values of 6.5 pW and 0.1 pW).

Calculations referred to the specific case of the single Cuoricino macro-bolometer are reported in Tab. 2.2. The values in the table are obtained from the parameters listed above, assuming crystal absorber with $5\times5\times5$ cm^3 volume and Ge thermistor with $3\times3\times1$ mm^3 size. A comparison among the heat capacities reported in the table confirms the approximation made in Sec. 1.4.2 to obtain an analytic solution for the dynamic behaviour of the modeled bolometer: the term C_{lat} is negligible, in respect to C_{el} and C_{abs}, at the operating temperature of the Cuoricino detector. There is no need to include the Si heater in the picture, as its heat capacity is properly designed to give a negligible contribution. The composite model described in Sec. 1.4, completed with the considerations made in this section, allows to simulate the behaviour of the Cuoricino basic bolometer; examples of similar simulations, implemented using the C language under the Linux-i386 operating system, will be reported in the course of this thesis, to support some steps of the optimization work performed. Moreover, the composite model applied to the detectors discussed here will be also used in chapters 4, 5 and 6 for a qualitative evaluation of bolometric performances, as well as to make assumptions about the contributions brought in this regard by the single parameters.

2.2 Running a large-mass bolometric experiment

A general description of the Cuoricino experiment and the results obtained on ^{130}Te 0ν-DBD have already been given in Chapter 1. The Cuoricino tower is an array of 62 TeO_2 crystals. Eleven planes of the tower are constituted by four-crystals modules with the characteristics provided in the first part of this chapter; two planes are special nine-crystals modules: the enclosed bolometers have absorbers with $3\times3\times6$ cm^3 volumes each, which have not been considered in the previous discussion because their

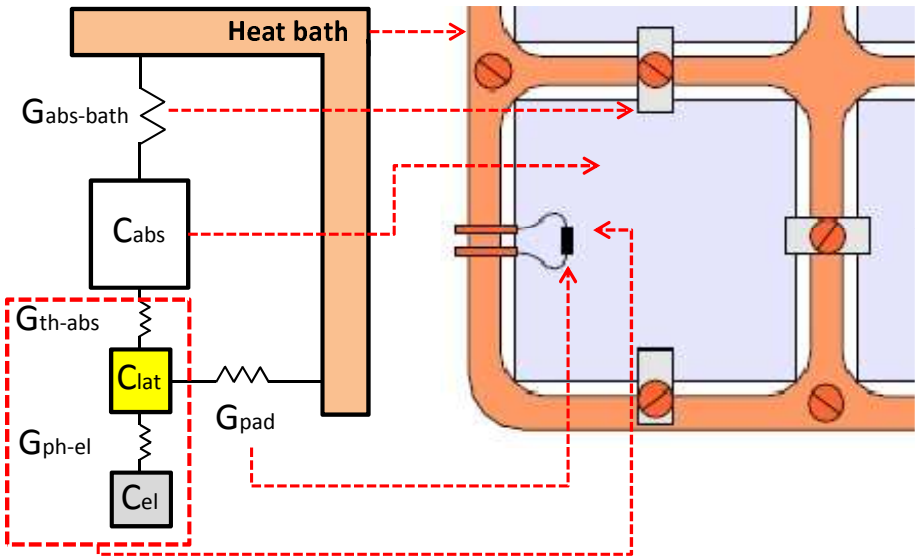

Figure 2.9: Composite model application to the Cuoricino basic macro-bolometer. On the right, sketch of the thermal network with the corresponding parameter names; on the left, part of the Cuoricino SM for immediate reference to the model.

Model parameter	Value
C_{abs}	$2.3\times10^{-3}\cdot T^3$ [J/K]
C_{lat}	$2.7\times10^{-8}\cdot T^3$ [J/K]
C_{el}	$9.9\times10^{-9}\cdot T$ [J/K]
G_{pad}	$4.8\times10^{-5}\cdot T^{2.4}$ [W/K]
$G_{abs-bath}$	$4.0\times10^{-5}\cdot T^2$ [W/K]
G_{ph-el}	$7.0\times10^{-1}\cdot T^{4.37}$ [W/K]
G_{th-abs}	$1.6\times10^{-3}\cdot T^3$ [W/K]

Table 2.2: Values of the parameters in the composite model applied to the Cuoricino basic detector, with $5\times5\times5$ cm^3 absorber and $3\times3\times1$ mm^3 thermistor.

design will not be included in CUORE-0 and CUORE. Data regarding the total mass of the experiment, the amount of investigated nuclides, the final resulting limits have already been given in Sec. 1.5 and will not be repeated here. In order to complete the experiment's review, information on the cryogenic system for detector's cool down and operation at $\sim$10 mK, the data acquisition system and the data analysis process should be given: however, no optimization work on these important aspects of the experiment has been performed in this thesis, and their description here would just be of technical support. The choice is therefore to provide the useful information on these three topics in the final appendixes, adding details on the different experimental setups used in the course of my Ph.D. work.

2.3 Beyond the Cuoricino single module detector

Chapter 1 ended with a consideration about the necessity to explore the inverted hierarchy mass region, which corresponds to designing experiments for 0ν-DBD search capable to detect the rare decay in the case of effective neutrino Majorana mass lower than $\sim$50 meV. When ^{130}Te is considered, this translates in a half-life $T^{0\nu}_{1/2}$ above a few 10^{26} years. The achievements in cryogenic spectroscopy obtained by the Cuoricino experiment show that its technology is, in line of principle, able to run for such a goal in fundamental physics research; once the general aspects of the detection mechanism are fixed, however, the jump from Cuoricino to its next-generation evolution requires a huge R&D effort to tune the most delicate contributions in the experimental setup, which could limit the final sensitivity and performance. This is the starting point for the CUORE project, whose imminent first step is the construction and operation of the CUORE-0 single tower. Both the CUORE-0 and CUORE detectors in their latest designs have already been described in Chapter 1. Their basic element will be the four-bolometers SM with $5\times5\times5$ cm^3 crystals, and each SM will constitute a tower plane. The passage from the Cuoricino experiment to the final goal of CUORE is made possible by focusing the R&D work on two directions.

- An improvement of the overall experimental *sensitivity to 0ν-DBD* in respect to the potentialities shown by Cuoricino. The mathematical expression of sensitivity for a calorimetric experiment affected by the presence of background counts will be defined in the following section; it gives a measure of the investigation range available for the designed experiment. By analyzing its main dependencies, one can select the parameters whose tuning has a stronger impact, and design consequently the R&D activity.
- An improvement of the *detector's reliability, performance and overall comprehension*. Uniformity in terms of pulse heights and energy resolution is a must for the bolometers that will constitute CUORE, for reasons that will be cleared in the course of this Ph.D. thesis. In this case, the main guidelines of the R&D activity are provided by the experience on the bolometric behaviour observed in the Cuoricino experiment.

This aspects will be examined separately in the following sections.

2.3.1 The how-to of sensitivity improvement

A useful way to introduce part of the guidelines of a CUORE and CUORE-0 oriented R&D activity is to define the sensitivity of a calorimetric experiment for 0ν-DBD search, and to see which parameters have the strongest influence on it. The sensitivity $S^{0\nu}$ to 0ν-DBD is defined as the half-life corresponding to the maximum number of decays $N_{\beta\beta}$

that can be hidden by background fluctuations at a given confidence level. First of all, the radioactive decay law for the process under investigation can be written as

$$N(t) \sim N_0 \left(1 - \ln 2 \cdot \frac{t}{T_{1/2}^{0\nu}}\right) , \tag{2.11}$$

where N_0 is the number of nuclei under control at t=0; the equation is obtained in an approximated form by considering the inequality $T_{1/2}^{0\nu} \ll t$, which is allowed by the current limits on 0ν-DBD half-lives of order 10^{24} or greater. As a consequence, the number of 0ν-DBD decays $N_{\beta\beta}$ expected during the measurement time t is

$$N_{\beta\beta} = \frac{M \cdot N_A \cdot \eta \cdot a}{W} \cdot \ln 2 \cdot \frac{t}{T_{1/2}^{0\nu}} \cdot \epsilon \tag{2.12}$$

In the previous formula, M is the total absorber mass, N_A is the Avogadro number, η is the number of nuclides candidate to 0ν-DBD for absorber molecule, W is the molecular weight of the absorber, a is the isotopic abundance and ϵ is the detector's efficiency. When no decays are observed in the measurement time, $N_{\beta\beta}$ represents the background fluctuation in the energy region under investigation, and the $T_{1/2}^{0\nu}$ written in the previous equation becomes the limit on the half-life of the decay. In order to detect $N_{\beta\beta}$ in an energy window ΔE, which corresponds to the energy resolution of the detector, the presence of radioactive background counts is a severe limitation. The calculation of sensitivity can be performed in the case both of a zero-background experiment, and of background fluctuations that can cover the expected peak: only the second option will be considered, as it is suitable to the Cuoricino experiment and its next-generation evolutions. Let's assume that the background level is b, measured in c/(kg·keV·y): for a detector with mass M, the number of background events B in a time t and in an interval equal to the energy resolution FWHM ΔE, centered around the Q-value of the decay, is given by

$$B = b \cdot t \cdot M \cdot \Delta E \tag{2.13}$$

Two assumptions are made: the number of background events scales with the absorber mass of the detector and b is measured independently and precisely, as it commonly happens in bolometric experiments; the background events in the region of interest will follow a Poissonian distribution, with standard deviation equal to the square root of the number of events. The minimum number of events that are needed to reach a certain significance of the peak, for example at a ξ% Confidence Level, is given by the probability that the fluctuation of background events is equal to the peak. In other words,

$$N_{\beta\beta} = n_\sigma \cdot \sqrt{B} , \tag{2.14}$$

with n_σ equal to the number of deviations corresponding to a probability of (1-ξ)%. The combination of Eq. 2.12 and Eq. 2.14 defines the sensitivity of a calorimetric experiment for 0ν-DBD search with non-zero background rate:

$$S^{0\nu} = 4.174 \times 10^{26} \left(\frac{a}{A}\right) \sqrt{\frac{M \cdot t}{b \cdot \Delta E}} \cdot \epsilon_{\Delta E} \tag{2.15}$$

The previous expression is valid for 1σ. It is evident by looking at the formula that action on the parameters M, t, b, ΔE and possibly a is required to increase the sensitivity of the experiment. In the following sections, the possible tuning of parameters will be discussed.

2.3.1.1 Detector mass

The easiest way to increase $S^{0\nu}$ is rising the detector's mass. Nonetheless, the present mass scale of experiments based on TeO_2 does not allow a strong enlargement of this factor. Since the Cuoricino mass is $\sim$41 kg, an increase of at least one order of magnitude is needed to make a non-negligible gain in sensitivity. The solution chosen for CUORE is to include 988 bolometers, with a total mass of about 741 kg: the growth in sensitivity gained from this factor is

$$\sqrt{\frac{M^{CUORE}}{M^{Cuoricino}}} \sim 4.25 \tag{2.16}$$

A further increase of the CUORE mass magnitude by the same factor, $(4.25)^2 \sim 18$, is beyond the possibilities of the present cryogenic techniques for the cool-down of a large mass: M^{CUORE} represents therefore the technical limit for current cryogenic capabilities. Any possible modification in the M factor follows two paths.

- *Increasing the single absorber's mass*. The inconvenient is having larger C_{abs}, which grows with the volume, with the consequent risk of lower thermal pulses. The first solution has been tried in the R&D activity of the past years with crystals as big as $6\times6\times6$ cm^3, but has been discarded both because the indications on the tested detectors' behaviour were not conclusive, both because a full research activity on them, inclusive of a dramatic modification of the setup, would not have been compatible with the CUORE time schedule [82].
- *Building an array with a higher total number of bolometers*. This path, on the other hand, has no consequences on the individual behavior of each bolometer but leads to major technical issues. For example, the increase in the number of channels implies more power dissipated through the read-out wires in the coldest parts of the cryostat.

2.3.1.2 Energy resolution

The energy resolution in the 0ν-DBD region is evaluated as the FWHM of the γ peak of ^{208}Tl at 2615 keV. The average resolution in Cuoricino, about 8 keV and corresponding to a few ‰ with a small spread from the mean value, can be considered good for the application under discussion as far as sensitivity is concerned. However, a further reduction to 5 keV is planned to be obtained for CUORE. The main strategies for energy resolution improvement are two.

- The first is the *reduction of noise sources*. In this case, the important sources, such as the pumps and compressors of the cryogenic set-up, cannot be eliminated: the solution is to prevent the transfer of vibrations to the detector. This is achieved by using damping system to decouple the vibrating device, or by using mechanical filters to decouple directly the detector from any vibration sources [83].
- The second strategy for ΔE improvement is the *reduction of the single detector's sensitivity to noise*, which is the response of the detector to some external or internal perturbation of the apparatus (mechanical noise from cooling pumps and compressors, vibrations from 1K Pot filling, and so on): the aim is achieved by studying baseline stability and N_{rms}. The topic will not be treated in this thesis; more information on the work performed by the CUORE collaboration at LNGS about this issue is found in [84].

Besides from the previous summary, it should however be noted that a reduction of the spread in energy resolutions is required for reasons other than sensitivity considerations. The problem will be discussed in Sec. 2.3.2.

2.3.1.3 Measurement time and duty cicle

The modification of measurement time from the Cuoricino experiment does not contribute relevantly to the increase in sensitivity. As a matter of fact, the typical life of a TeO_2 bolometric experiment is a few years, which allows to gain a factor $\sim$2: after that, any further contributions are approximately negligible. For example,

$$\frac{S^{0\nu}(20 \text{ years})}{S^{0\nu}(5 \text{ years})} = 2\,, \tag{2.17}$$

which means that an increase of a factor 4 in the live time is necessary to increase the statistics of a factor 2. The only aspect to work on is the improvement of the duty cycle, which is affected by the following categories of limitations.

- *Calibration and DAQ operations*. The first category, corresponding to a live time loss from 6% to 10% in Cuoricino, is a necessary trade-off for achieving good quality in measurements and is not going to be reduced significantly in CUORE-0 and CUORE. Due to the increased size of CUORE, a more complex calibration system is needed; a single calibration will take longer than in Cuoricino but, thanks to the improvements in detector and electronics stability, it is likely to be required less often [85].

- *Apparatus maintenance and failures*. This category is highly affected by the necessity for LHe refills of the dilution refrigerator, which is a $\sim$10% contribution to dead time in Cuoricino; moreover, apparatus failures due to the common and unavoidable critical state of all 10 mK-operated devices add another 15% to the count of time loss. Both aspects will be possibly improved by the use in CUORE of a *Pulse Tube*, LHe-free refrigerator [86] (see Appendix A for some information on cryogenic systems). CUORE-0 will be cooled down in the same cryostat used for Cuoricino, and therefore is not affected by the new solution.

Summing up, the duty cycle in Cuoricino is estimated as the $\sim$65% of the total time; the improvement for CUORE is expected to be $\sim$75%, and better results are unlikely.

2.3.1.4 Background level

In principle, 0ν-DBD events can be identified by their energy spectrum. However, in practice, the capability of the experiment to identify the DBD signal is limited by the presence of environmental radioactivity and radioactive contaminants in the detector. Once the total mass is fixed, the only parameter that can be tuned to achieve an effective increase in sensitivity is the background level, whose reduction is therefore the main goal of the CUORE-oriented R&D. The work is strongly connected to the interpretation of Cuoricino data and to the comprehension of how the dangerous background in the surroundings of the $Q^{0\nu}_{\beta\beta}$ of ^{130}Te is originated. The puzzle constituted by the disentanglement of contributions to the Cuoricino background in the 0ν-DBD region will be dealt with in Sec. 3.1.1), because it will serve as starting point for the part of the Ph.D. work presented in Chapter 3. Therefore, the most sensitive points in the CUORE-oriented background reduction program will be listed in this chapter, and their full presentation assisted by the interpretation of Cuoricino data is postponed.

A useful approach to understanding the problem of the radioactive background in 0ν-DBD experiments is the classification of all the possible elements that contribute to it in the energy Region Of Interest of the spectra (ROI), where the $Q^{0\nu}_{\beta\beta}$ of the chosen nuclide lies.

- *Natural radioactivity.* Environmental γs arise mainly from the natural contamination in ^{238}U and ^{232}Th. The highest relevant γ-line in natural radioactivity is the ^{208}Tl at 2615 keV, whose total *branching ratio* (BR) in the ^{232}Th decay chain is 36%. Above this energy, only extremely rare high energy γ-rays from ^{214}Bi can be found, with just a 0.15% BR in the 2615 to 3270 keV window. As the $Q^{0\nu}_{\beta\beta}$ of ^{130}Te is located between 2 and 3 MeV, most part of natural radioactivity does not offer significant contributions to its background. However, the half-lives of U and Th ($\sim 10^{10}$ years) are very short if compared to those of 0ν-DBD decaying isotopes, and the minimum activity by them can therefore contaminate the Q-value region. Materials with low concentrations of U and Th contaminants and/or purification techniques must be used to prevent problems of this kind. Moreover, ^{208}Tl and ^{214}Bi are daughters to the gaseous isotopes of Rn, which constitutes a peculiar issue and can be controlled by flushing nitrogen in the detector's surroundings; specific studies have been conducted, in view of CUORE, about radon diffusion and implantation on the surfaces of materials facing the detector and on TeO_2 itself [87].

- *Cosmogenic radioactivity.* Because of the high rate of cosmic rays on the planet's surface, it is mandatory that experiments for 0ν-DBD search are performed underground. The natural 1500 m-rock shield above the experimental site at LNGS (3500 m.w.e.) reduces the external muon flux of a factor 10^5-10^6, so that the value around the detector is $\Phi \sim 1.1\ \mu/(m^2 \cdot h)$ [88]. Recent measurements, aimed at understanding the contribution of cosmic ray muons to the Cuoricino background, fixed an upper limit of 0.0021 counts/(keV·kg·y) at 95% C.L.in the ROI [89]. The muon induced contribution is therefore expected to be negligible, as the numbers that will be given in Sec. 3.1.1, dedicated to the interpretation of the Cuoricino background, will evidence; the same is expected for CUORE, apart from subtle changes due to to differences in the detector and shield geometry, materials, and anti-coincidence efficiency. Nonetheless, cosmic rays can induce radioactive effects by means of various nuclear reactions as long as the materials for detector assembly are site aboveground. The most worrying isotope for the detection under investigation is ^{60}Co, which is present, as a common contaminant of Cu, both internally to the detector (in the supporting frames that face the absorbers) and externally (in the outer shielding). As far as internal contaminations are concerned, the β-decay of this isotope can contribute to the background spectrum with the total Q-value of 2823 keV, given by the β emission (Q=318 keV) together with the two cascade γs at 1173 keV and 1332 keV; on the other hand, the two cascade γs at 2505 keV remain the dominant background source in the case of external contaminations. The cosmogenic activation of ^{60}Co is controlled by minimizing the times for both aboveground storage and shipping; later in this same section, the influence of the remaining cosmogenic activation on the Cuoricino background in the region of interest will defined negligible. Specific studies on the cosmogenic induced activity of the relevant materials for TeO_2 macro-bolometers (Cu, Ge and Te) have been performed in the framework of the ILIAS project [90], [91].

- *2ν-DBD.* As opposed to the case of 0ν-DBD, since in 2ν-DBD the two electrons emitted share their energy with two neutrinos, the sum spectrum of their energies is a continuous distribution up to the end-point $Q^{2\nu}_{\beta\beta}$. Because $T^{2\nu}_{1/2} \ll T^{0\nu}_{1/2}$, the detector's finite resolution could lead the 2ν distribution to enter the 0ν region. The fraction F of the 2ν-DBD counts that enter the 0ν-DBD peak, centered in Q and large ΔE, is approximated by the expression

$$F \sim \frac{\alpha Q \delta^6}{m_e}\,, \tag{2.18}$$

where m_e is the electron mass, δ is the width ΔE of the peak divided by Q, and α is a coefficient that depends weakly on resolution (some values are α=7 for a 5% resolution and α=5 for 10%). Once again in approximation, a formula can be written for the limit to the $< m_{\beta\beta} >$ mass sensitivity due to this kind of background [92]:

$$< m_{\beta\beta} >^2 \sim \frac{7Q\delta^6}{m_e} \frac{T_{1/2}^{0\nu}}{T_{1/2}^{2\nu}} \tag{2.19}$$

In the previous expression, $T_{1/2}^{0\nu}$ and $T_{1/2}^{2\nu}$ are the half-lives of 0ν-DBD and 2ν-DBD. Using the current limits on $T_{1/2}^{2\nu}$ for tellurium, the contribution is completely negligible in the region enclosing the $Q_{\beta\beta}^{0\nu}$ of ^{130}Te thanks to the good energy resolution of TeO_2 bolometers.

- *Neutrons.* Low energy neutrons can induce (n,γ) reactions in materials close or internal to the detectors with γ energies up to 10 MeV; furthermore, high energy neutrons generated by μ-induced spallation reactions can release several MeV by direct interaction in the detectors. The flux of external neutrons can be limited by a borated polyethylene shielding, which makes their contribution to the background between 2 and 3 MeV negligible [93].

According to dedicated measurements and simulations that will be summarized in Sec. 3.2, a particularly large contribution to the radioactive background in the ROI of Cuoricino energy spectra is currently identified as degraded α particles emitted close to the surface of the bolometers or from the materials that surround them. Since these particles release only a fraction of their energy in the crystals, they contribute with a continuous spectrum which extends down to the range where the $Q_{\beta\beta}^{0\nu}$ of ^{130}Te lies. There is also a relevant contribution given by the 2615 KeV ^{208}Tl line, which is due to ^{232}Th contaminations in the cryostat's radiation shields: however, this is not a worrisome factor for the final experiment, as a dedicated lead shielding inserted in the CUORE cryostat will provide sufficient reduction. As a consequence, gaining control over surface contaminations is seen as one of the most demanding challenges in view of the sensitivity desired for the final experiment. Specific R&D activities aimed at the CUORE-oriented reduction of the unwanted background have been pursued both previously and during the years of the Ph.D. work presented in this thesis: they will be dealt with in Chapter 3.

Although the full approach to this topic will be developed later on, the target of CUORE for the background reduction in the ROI can be anticipated: b=0.01 c/(keV·kg·y), which, if combined with the expected values for the other experimental parameters discussed previously, allows to reach the desired final sensitivity.

2.3.1.5 Isotopic enrichment

The direct proportionality of the sensitivity $S^{0\nu}$ to the isotopic abundance a, expressed by Eq. (2.15), makes the possibility of isotopic enrichment an appealing solution to increase the potentialities of a next-generation experiment designed to investigate the inverted hierarchy region of neutrino masses. ^{130}Te, however, is the only candidate to 0ν-DBD detection that can be studied with no enrichment and, at the same time, no significant loss in $S^{0\nu}$: as already mentioned in Sec. 2.1.1, this is possible because of the high natural abundance of the nuclide ($\sim$34%). The option is nevertheless considered with interest by the CUORE collaboration, since it could double the sensitivity with a relatively sustainable technical effort. No specific R&D has been performed in this regard up to now (year 2010); a future phase of CUORE could, however, include the enrichment option, provided that a dedicated R&D is performed on the levels of radioactive contaminants in the enriched tellurium powders and on the bolometric performances of

the final absorbers. Some hints about possible developments in this field will be given at the end of Chapter 4.

As a final summary of the discussion regarding sensitivity and its dependencies, Fig. 2.10 reports the behaviour of $S^{0\nu}$ in function of the main variables affecting it: the plots allow to appreciate the different impacts of specific experimental configurations, related to the Cuoricino and CUORE cases. The final configuration of the CUORE experiment includes total mass 741 kg, energy resolution equal to 5 keV, no isotopic enrichment, target background b=0.01$\times 10^{-2}$ c/(kev·kg·y) and measuring time 5 years. The foreseen sensitivity is

$$S^{0\nu} = 2.1 \times 10^{26}\,\text{y} \tag{2.20}$$

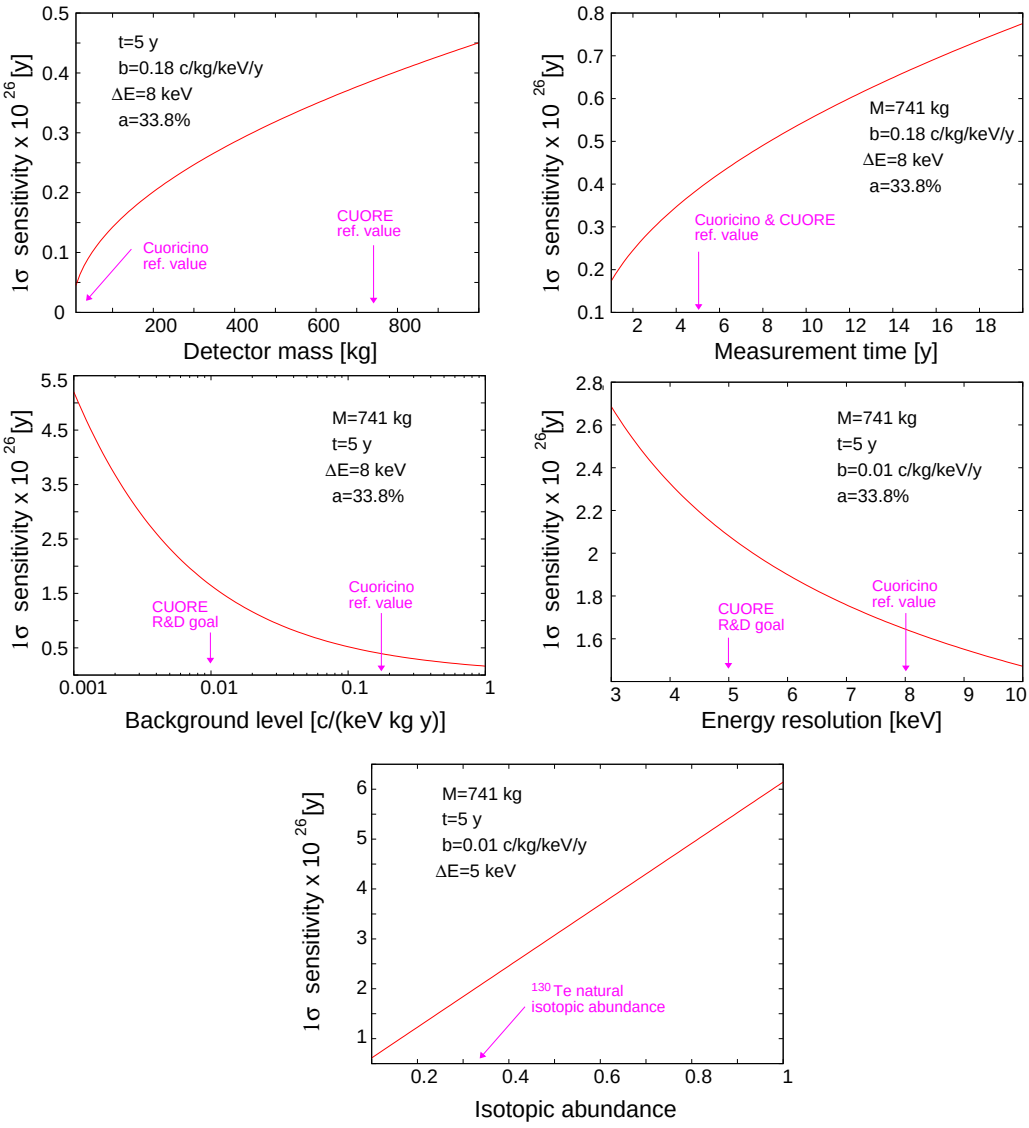

Figure 2.10: Behaviour of $S^{0\nu}$ in function of different experimental configurations. The sensitivity value reported in the last plot and corresponding to the natural isotopic abundance of ^{130}Te (a=33.8%) is the estimation foreseen for CUORE if the background level goal is reached.

2.3.2 Towards uniform and optimal bolometric performances

The discussion on the sensitivity of a calorimetric experiment for 0ν-DBD search with non-zero background counts, tailored on the evolution of the Cuoricino experiment, resulted in a list of parameters whose tuning is mandatory to push the observation window down to the inverted hierarchy range. The points of the previous section do not cover, however, the full set of requirements. In order to disentangle the other contributions that could improve the capability of the experiment to be competitive in the next-generation of 0ν-DBD search, another point of view has to be considered. In this case, the discussion does not start from an equation, but from the experience gathered on the behaviour of arrays of TeO_2 macro-bolometers.

The Cuoricino experiment obtained outstanding performances on a set of more than 40 large bolometers; however, there are still notable differences of behaviour from one detector to another. This is witnessed by different factors: the detectors' response, pulse shape and energy resolution. The response is the outcome in voltage obtained by a bolometer following a given energy excitation; it is measured in μV/MeV and in the course of this thesis will be also called, more generally, *pulse height*. Among the quoted factors, pulse height is the most varying performance indicator in the set of $5\times5\times5$ cm^3 Cuoricino bolometers. As an example, Fig. 2.11 reports the plot of the energy resolutions at the 2615 keV γ-line versus the corresponding response for the large bolometers in the Cuoricino experiment; the plot uses data taken during Run II. The spread in pulse heights is 167 ± 99 μV/MeV: this number has relative statistical significance, although the bolometers are supposed to be assembled in identical conditions, and is reported only as a measure of the large variability in the response. On the other hand, the spread in energy resolutions computed from this example is 8.5 ± 3.8 keV: although less evident than in the case of pulse heights, it motivates strongly the request for reproducible bolometers for reasons that will be cleared soon.

The underlying motivation to push on the aspect of reproducibility is the data analysis of a large number of channels, which will be of order 1000 in the case of CUORE: the more the behaviour of detectors is similar, the easier is the application of automatic procedures or standard software algorithms. Moreover, a reproducible behaviour helps the overall understanding of the physics of the detector, leading to better data control. The previous aspects will be explained in depth in Chapter 6, whose content is related closely to the issue of reproducibility. This section will be limited to presenting the three aspects on which the CUORE-oriented optimization work for the improvement of performance homogeneity is concentrated on.

2.3.2.1 Pulse shape and response

Although examples of such behaviour will be given at the beginning of Chapter 6, it must be anticipated that, along with the mentioned responses, pulse shapes feature a large variability in terms of rise and decay times from one bolometer to the other in the Cuoricino experiment. The reason of this peculiarity has not been cleared yet, although an answer will be tried at the end of this thesis. As a matter of fact, the composite model described in Sec. 1.4 and adapted to the specific Cuoricino case in Sec. 2.1.6, is not able to reproduce in detail the dynamic behaviour of a single macro-bolometer and cannot be considered complete; nevertheless, if the modeling is combined with the experimental experience gathered by operating real detectors, some components emerge as candidates to be responsible for shape and response variations. As a consequence, one of the guidelines of the R&D work aimed at the realization of CUORE is optimizing separately the single detector components: the design of both Cu frames and PTFE holders, the performances of thermistors and their coupling to the absorbers,

the dimensions and purity of the TeO_2 crystals, and so on.

2.3.2.2 Energy resolution

The lowering of ΔE has already been discussed briefly in Sec. 2.3.1 as one of the desirable achievements to rise $S^{0\nu}$. The problem analyzed here is different, as it regards its uniforming among separate bolometers belonging to the same array. Appendix C gives some details on first-level data analysis, and Sec. 1.5 explained briefly how to extract the useful 0ν-DBD information from data: as already pointed out, the exploration of these topics in depth exceeds the focus of this thesis. However, the important point in this discussion regards the necessity of summing the energy spectra from different bolometers to achieve a collective dataset. The peak searched for is almost of Gaussian shape, due to resolution effects of the detector, but when spectra are summed the result can differ from a Gaussian distribution, because data is acquired with distinct energy resolutions: the problem is avoided by fitting the peak with a distribution sum of different Gaussians, each with its own FWHM. The $\sim$1000 future bolometers in CUORE imply $\sim$1000 FWHMs for the whole set of Gaussian distributions fitting the peak, and even a minimal spread in energy resolutions can affect global analysis.

2.3.2.3 Detector modularity

This is a very technical aspect, required by the large number of bolometers to be constructed for CUORE. The six months required for the assembly of Cuoricino, scaled to the size of CUORE, give an increase factor of order $\sim$16, which is incompatible with any reasonable experimental time schedule. The introduction of automated steps in the construction phase, as well as the reduction of the variability brought by human operations, help in achieving this goal; the not-so-side effect is, once again, an improvement in reproducibility. For example, the Cu holding structure can be redesigned with specific requirements on shapes and dimensions to allow easier and rapid construction in respect to the Cuoricino standards: this work can bring at the same time a reduction in *thermophononic noise* [1], which increases uniformity in the distribution of energy resolutions, and similar thermal contacts in different points of the SM, which means a more uniform distribution of thermal conductances and, possibly, of pulse shapes. Chapters 5 and 6 will report two specific optimization works (on Ge thermistors and on their coupling to the crystals) that are motivated by modularity requirements but exceed this trivial motivation.

2.4 Designing a CUORE-oriented specific R&D activity

The previous section gave the instruments necessary to understand that the optimization of TeO_2 macro-bolometers for the next-generation of 0ν-DBD experiments is a wide and varied subject; although the main guidelines are two, increasing the $S^{0\nu}$ sensitivity and improving the reproducibility among separate bolometers, once they are analyzed in detail a multiplication of sensitive aspects occurs. The optimization of one SM component often involves more than just one of these aspects.

The Ph.D. work presented in this thesis focused on four detector components in particular (summarized also by Fig. 2.12).

[1] Thermophononic (TP) noise is the result of heat dissipation in the detector converting it into phonons. Its main source is vibrations being converted into heat via frictions between the crystal and the holder (PTFE and Cu); this determines sudden heat releases or base T fluctuations. The large spread of harmonic frequencies involved in this phenomenon implies a noise spectrum that has a $1/f$ roll-off and is particularly annoying for bolometers, which have very low characteristic frequencies.

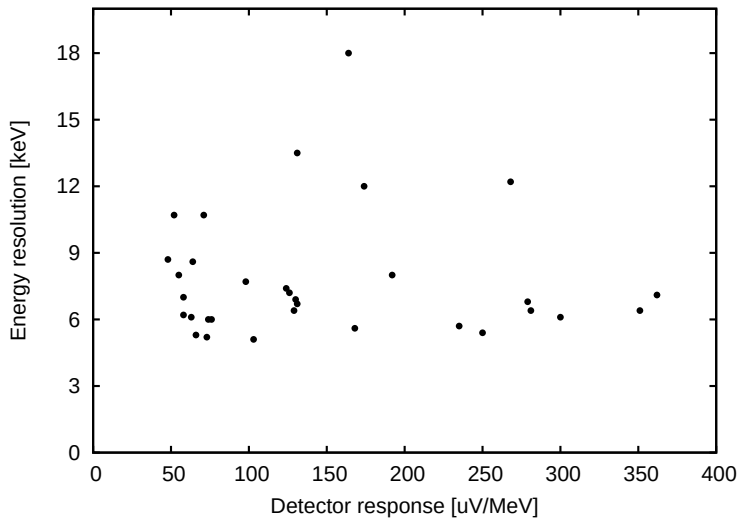

Figure 2.11: Energy resolution at 2615 keV vs. detector response for the $5\times5\times5$ cm^3 bolometers in the Cuoricino experiment. Data is extracted from measurements taken in Run II.

1. **R&D on the support structure.**

   Specific work on this component has involved the issue of radioactive contaminations in the surfaces of the materials facing the bolometers: as already explained in Sec. 2.3.1, the reduction of the contribution to the background in the 0ν-DBD region originated by surface radioactivity is one of the most important R&D efforts in the CUORE collaboration. Chapter 3 will deal with the different strategies to control the undesired counts that contaminate the region of interest in the sum energy spectra of the detector, and with a dedicated cryogenic run at LNGS designed to choose the final strategy for the treatment of Cu surfaces. Other optimization works have been performed by the collaboration on the four-crystals SM holding structure, but they are beyond the aim of this thesis: both the Cu frames and the PTFE holders used in the Cuoricino SM have been redesigned in order to control the variability of thermal conductances in time following stress at low temperature, to reduce the sensitivity to noise of the detector, to limit the amount of Cu facing directly the absorbers and to increase the overall modularity; results from the dedicated cryogenics tests, the CAW runs (from CUORE Assembling Working group, the R&D group in charge of this development), are presented along with detailed motivations in [82],[84].

2. **R&D on the absorber.**

   When considering the possible optimization aspects in the R&D dedicated to TeO_2 crystals, a variety of connections flourishes. This reflects the consideration that energy absorbers are the source of the searched decay as well as the heart of detectors. The lowering and reproducibility of energy resolution, the reduction of pulse shape variations, together with the increase of control on bulk and surface contaminations are all hot topics when considering possible improvements in the quality of crystal absorbers. The growth phase and the surface treatment of TeO_2 crystals are investigated with specific cryogenic tests performed at LNGS to individuate flaws that could limit the desired goal for CUORE. Considerations and results are reported in Chapter 4, supported by cryogenic tests performed both at LNGS and in Como.

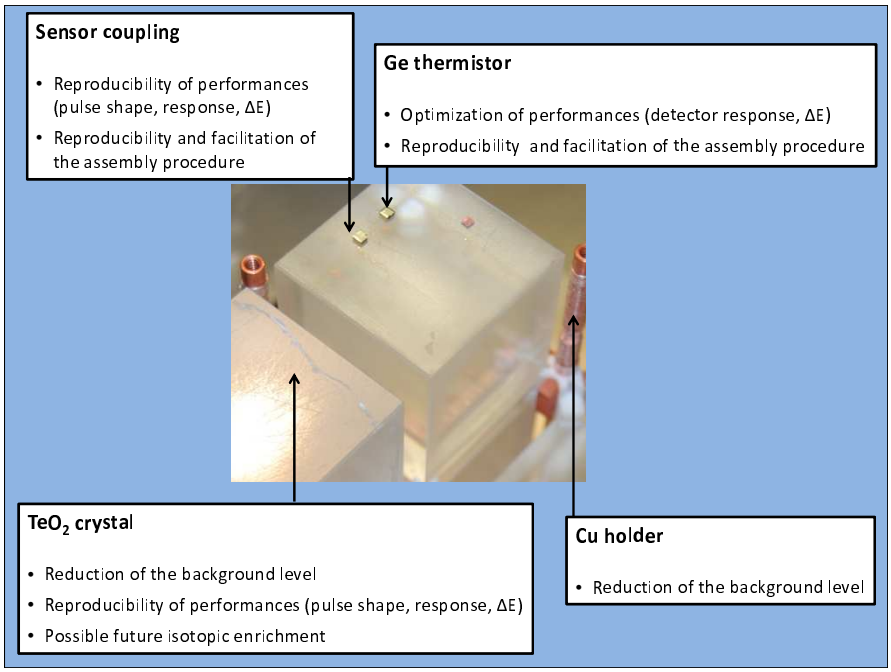

Figure 2.12: Graphic summary of the SM components subjected to a specific R&D activity in the course of this Ph.D. thesis. For each bolometric element, a brief list of the main sensitive aspects connected to its optimization is reported for convenience.

3. **R&D on the Ge thermistor**

   The size and doping characteristics of Ge thermistors for use in TeO_2 macro-bolometers had already been optimized in the course of the R&D preliminary to the realization of Cuoricino. However, the strive for an improved modularity of the future CUORE detector in respect to the Cuoricino one leads to a redesign of the thermistors' contact geometry. The specific reasons behind this request will be cleared in Chapter 5. The starting motivation for the optimization work is very practical: moving the position of the pads for electric read-out from the sides of the thermistor to the upper surface, with a notable simplification of various assembly procedures. However, it will be seen that it introduces a series of technological complexities and involves the physics of the NTD-Ge sensors. Tests on this topic have been performed at LNGS as well as at the aboveground cryogenics laboratory in Como, where the high cosmic ray rates force the use of smaller energy absorbers to avoid detector saturation.

4. **R&D on the thermistor-to-absorber coupling**

   The final aspect treated in this Ph.D. work concerns the thermal and mechanical coupling between the sensors and the TeO_2 energy absorbers they are attached to. In Chapter 6 some assumptions will be made on the importance of this coupling, performed by means of a matrix of epoxy dots, in regard of bolometric performances: the experience gathered from Cuoricino and R&D tests previous to this thesis, together with qualitative considerations derived from the analysis of the composite thermal model, will support the request for pushing on the uniformity of the thermistor-to-absorber coupling among different detectors. Its optimization aims at the final goals of both increasing the reproducibility of bolometric performances in an array and introducing automated procedures in the assembly process. The R&D work on this coupling is far from being trivial, as it is limited

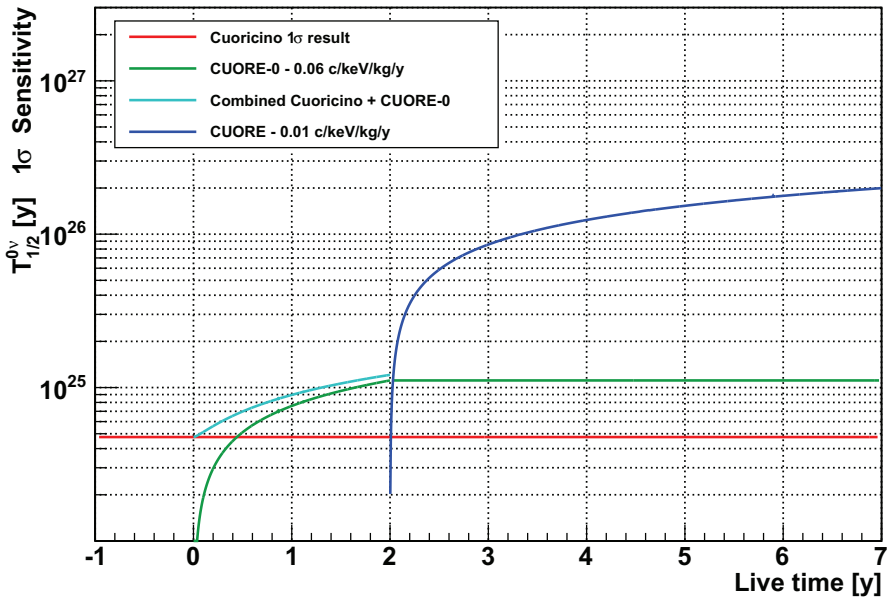

Figure 2.13: Comparison between the limit on the $T^{0\nu}_{1/2}$ of ^{130}Te set by Cuoricino and the 1σ sensitivities on the half-life foreseen for CUORE-0 and CUORE. The assumptions for the background levels *b* in the 0ν-DBD energy region are 1/3 of the Cuoricino level for CUORE-0 and the upper limit of the R&D goal for CUORE.

by a set of unavoidable constrains fixed by other requests on the detector. The research has been conducted in both Como and LNGS.

2.4.1 CUORE-0 as CUORE's test bed

Chapter 1 introduced CUORE-0 as the first phase in the road towards CUORE, but did not gave any details on its aims: the only information given is that CUORE-0 will be the first of the nineteen towers in the CUORE array, that it will be assembled starting from October 2010 and that it will be operated for two years, until the actual start of CUORE, in the refurbished cryogenics facility that housed Cuoricino. One could question about the relevance of an intermediate, partial step that seems to steal some efforts from the beginning of the final phase. However, the discussion developed in this chapter gives the elements to understand the importance of a stage preliminary to the construction of the whole CUORE detector. CUORE-0 is the main rehearsal for CUORE. The R&D to overcome the Cuoricino SM has been shown to be a complex and wide activity, and some of its goals, such as the background level in the 0ν-DBD region, have no prove of being reached until the final experiment is performed: CUORE-0 will be the ultimate test for this kind of uncertainties, thanks to the high statistics that it will collect, given the total TeO_2 mass comparable to Cuoricino and the two years of foreseen data-taking. There are three main reasons that motivate CUORE-0 as a fundamental step in the road towards CUORE.

- Testing the assembly procedure, which has been largely improved during the last R&D years by pushing on the zero-contact approach and by introducing modularity innovations in the gluing procedure, the holder design, the system of wires for signal read-out.
- Verifying the background reduction expected from the dedicated R&D work efforts, which is approximately 1/3 of the Cuoricino background in the 0ν-DBD region

and should be close to the CUORE target in the energy range corresponding to degraded αs. The part of background reduction expected for CUORE due to the new design of shields does not hold for CUORE-0, because it will be mounted in the same facility used to operate Cuoricino: the background value will be limited by contaminations in the cryostat.

- Improving the limit on the 0ν-DBD's half-life for ^{130}Te set by Cuoricino. In fact, CUORE-0 will be more than an ultimate test for CUORE; it will also be a powerful experiment, capable of overtaking soon the sensitivity of Cuoricino. The plot for sensitivity comparison presented in Fig. 2.13 supports this assessment.

The R&D activities presented in the next chapters must therefore be intended as aimed at the imminent realization of CUORE-0, which will be then capable of validating them, both in the technical aspects of assembly procedures and in the results of bolometric performances, as viable options for the CUORE array.

Chapter 3

The chase for background reduction

As anticipated in Chapter 2, this thesis work starts from the benchmark constituted by the Single Module of the Cuoricino experiment's detector. The standard Cuoricino bolometer is the focus of an optimization process which aims both at the short-term use in the CUORE-0 tower as well as at the subsequent integration in the one thousand-elements array of the future CUORE experiment. Four issues were introduced in Sec. 2.4 which affect strongly, in terms of bolometric performance and radioactive background, the sensitivity required to any experiments designed to succeed Cuoricino: the next chapters will be concerned each with one of the aforementioned topics. The first aspect to be treated is the issue of background reduction, focused on one peculiar contribution. Lowering the rate of counts in the 0ν-DBD region of the energy spectrum down to the value b=0.01 c/(keV·kg·y) is a fundamental goal to allow the final experiment to reach the sensitivity required for exploring the inverted hierarchy range of neutrino masses. As the first sections of this chapter will clear, the most dangerous contribution to the background in the ROI is constituted by U and Th contaminations in the surfaces of the passive materials facing the detector. Gaining control on this problem is far from being trivial, as long as bolometric detectors are concerned. The following discussion will explain the reason of such difficulty and deal with the strategies adopted by the CUORE collaboration to reduce the unwanted counting rate in the 0ν-DBD energy region.

3.1 The identification of relevant background sources

The first part of this chapter is devoted to identifying the sources of the background level in the ROI, by relying on the experience gathered with the Cuoricino experiment and with the years of R&D activity previous to the Ph.D. work presented here.

3.1.1 An investigation on the Cuoricino background

Several works on the analysis of the Cuoricino background have been performed, and only the main results will be used in the following discussion [94].

The background counting rate in the 0ν-DBD region seen by the $5\times5\times5$ cm^3 detectors in Cuoricino is (0.18$\pm$0.01) c/(keV·kg·y). In order to understand its origin, the Cuoricino energy spectrum obtained by summing on the single spectra collected by each independent detector is analyzed, and the 2615 KeV ^{208}Tl line can be used as a

reference point to split the measured background in two regions.

The ^{208}Tl line appears as one possible contribution, through Compton events, to the background in the $Q^{0\nu}_{\beta\beta}$ region, whose plot is reported in Fig. 3.1. This peak is due to contaminations which are relatively far from the detector, as proved by comparing the intensity of the ^{208}Tl γ-line with other low energy γs coming from the ^{232}Th chain: their position is assumed to be in the cryogenic setup, coming from the thermal shields. Below 2615 keV, other two peaks can be identified in correspondence of 2448 keV, due to ^{214}Bi, and of 2505 keV, which is the sum line due to the interaction, in the same crystal, of the two cascade γs emitted by ^{60}Co in its β-decay. The energy of both peaks is too low to contribute to the background in the investigated region of the spectrum.

On the other hand, the interpretation of the background measured above 2615 keV is the key to understanding the part of the CUORE R&D presented in this chapter. It will be cleared later on, although the assertion has already been made in Sec. 2.3.1, that the background which is reputed dangerous in the bolometric search for the 0ν-DBD of ^{130}Te is ascribed mainly to αs coming from the ^{238}U and ^{232}Th radioactive chains: these particles are degraded in energy because of the deposition mechanisms connected to their origin from surface contaminations of either the crystals or the inert materials facing them, and their continuum extends below the ^{208}Tl line down to the ROI. This assessment is supported by the specific analysis of the α-peaks seen in the energy range of the Cuoricino sum spectrum above 3 MeV, whose position and shape are neat clues to their origin. As a matter of fact, contaminations can be located with reasonable confidence according to the characteristics of the relative α-lines:

- when the contamination is inside the bulk of the TeO_2 crystal, both the α-particle and the nuclear recoil deposit their energy inside the absorber and a sharp Gaussian peak is produced in the spectrum;

- a Gaussian peak at just the α energy, with no recoil, is generated if the contamination is site in a thin surface layer, either on the crystal or on the inert materials facing it: in this case, the α can escape retaining almost all of its energy and hit another crystal;

- in case of a deeper surface contamination, a part of the α energy is released in the material where the decay occurs and in case it is a crystal, an asymmetric, long-tailed peak is seen in the spectrum;

- if, on the other hand, the thicker surface contamination is in an inert material facing the detector, a flat continuum is seen.

More details on the processes of energy deposition connected to degraded α particles will be given in Sec. 3.2, while the listed considerations aim at reaching a quick understanding of the Cuoricino background. Besides the shape of structures observed in the energy spectrum, another instrument is used to trace back the origin of contaminations: the analysis of coincidences between neighbouring pair of bolometers. When the contaminant is site on the crystal's surface, there is a non-negligible probability that the α-particle hits a bolometer next to the one it has escaped from: in this case, a signal is recorded in both crystals within a time window defined as $\sim$100 ms, and the sum energy will be equal to the total transition energy of the decay (the rise times 10%-90% of a Cuoricino large macro-bolometer lie in the approximate range 50-100 ms). The coincidence spectrum, which corresponds to collecting events where two crystals are hit at within the same time coincidence window, is therefore compared to the anti-coincidence spectrum, obtained by selecting events where just one absorber is hit. Needless to say,

no coincident signals are observed when the unwanted decay source is site in the passive materials surrounding the detector.

Most of the peaks that appear in the energy region above 4 MeV, which is depicted in Fig. 3.2, are found in both coincidence and anti-coincidence spectra, and are characterized by a large low energy tail: they are therefore assumed to be related to ^{238}U and ^{232}Th surface contaminations of the crystals. With the aid of dedicated Monte Carlo simulations, the general shape of the structures featured by background spectra appear to depend strongly on the depth and density profile assumed for the contamination, and the best fitting results are obtained with an exponentially decreasing function $\rho(x) = Ae^{-\lambda x}$, where λ is the depth. However, four peaks above 4 MeV cannot be attributed to U and Th surface contaminations of the crystals: the α-line at 3249 keV, ascribed to an internal ^{190}Pt contamination of the absorbers, probably due to the inclusion of Pt fragments from the crucibles for TeO_2 crystal growth (see Chapter 4); the α-peak centered at 4080 keV, which was demonstrated by dedicated tests to come from a bulk contamination in ^{232}Th; the 5304 keV line, which corresponds to the α energy emitted by ^{210}Po with no recoil, and which is ascribed, because of considerations regarding its stability in time and its position, to a contamination of ^{210}Pb located in a thin layer of the surfaces of the crystal or the surrounding materials; and the α+recoil 5407 keV peak, given by a ^{210}Po bulk contamination in the crystals. The isotope ^{210}Pb, daughter of ^{222}Rn, must be taken care of because its long half life of 22.3 years makes it a radioactive source constant in time: although its main decay channel, β decay with Q-value $\sim$0.06 MeV, is not a direct background source for the case under study, ^{210}Pb becomes relevant through the β decay of ^{210}Bi, which in turn generates the α-decaying ^{210}Po: the final result is the 5.3 MeV signature mentioned above. Polonium is constantly generated by ^{210}Pb but can also be present independently, and its chemical characteristics similar to those of Te make its removal difficult [95].

This said about the α-peaks observed in the Cuoricino spectrum, which are largely identified and understood, the origin of the continuous background that populates the 0ν-DBD region is quite a puzzle. It is not straightforward, in fact, to associate the continuum to a specific α-peak and contaminant. Nevertheless, the small amount of coincidences in the 3 MeV to 4 MeV energy window, supported by dedicated Monte Carlo simulations, suggests that a large fraction of the flat continuum in that region is originated by a contamination source external to the crystals. Some contributions are excluded: ^{238}U and ^{232}Th contaminants in the bulk of the Cu holding structure, because of the reduced rate of low energy γ-peaks; bulk contaminations in the small components of the detector (thermistors, heaters, PTFE holders, glue, Au wires), because of independent radioactive measurements; neutrons, because of both Monte Carlo simulations and experimental considerations coming from the MiDBD experiment. All the hints collected and the considerations exposed allow to attribute great part of the background rate in the $Q^{0\nu}_{\beta\beta}$ region of ^{130}Te to contaminations in the surfaces of both crystals and the copper material surrounding them. Tab. 3.1 summarizes the relative contributions of the discussed sources to the radioactive background in three regions of the Cuoricino sum energy spectra [34].

3.1.2 Past R&D activity on background issues

Following the proposed interpretation of the Cuoricino background, one can conclude that the main contributions in the 0ν-DBD region are due to ^{232}Th contaminations in the cryostat's shields, surface contaminations in the crystals and surface contaminations in the Cu holding structure of the detector. The first contribution has been identified

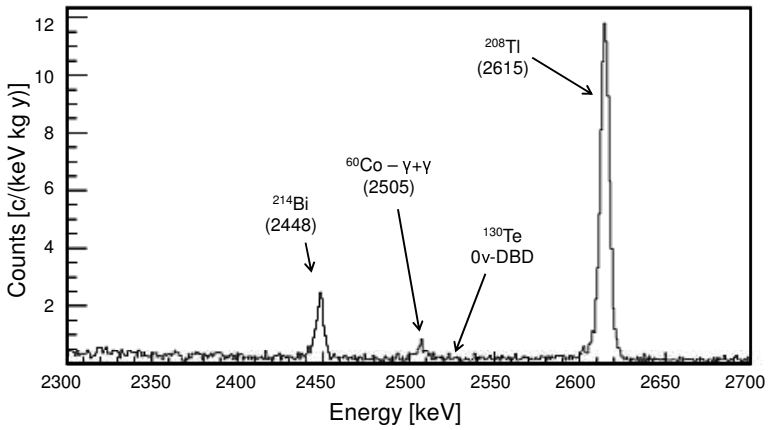

Figure 3.1: Spectrum of the sum of the two electron energies in the region of the 0ν-DBD of ^{130}Te obtained from the $5\times5\times5$ cm^3 bolometers in the Cuoricino detector. The lines due to the decays of ^{214}Bi (2447 keV) and ^{208}Tl (2615 KeV) are clearly visible, together with the small peak at 2505 keV, given by the sum of the two γs of ^{60}Co. The background counting rate in the double-beta decay region for the set of Cuoricino large bolometers is 0.18 ± 0.01 c/(keV·keV·y).

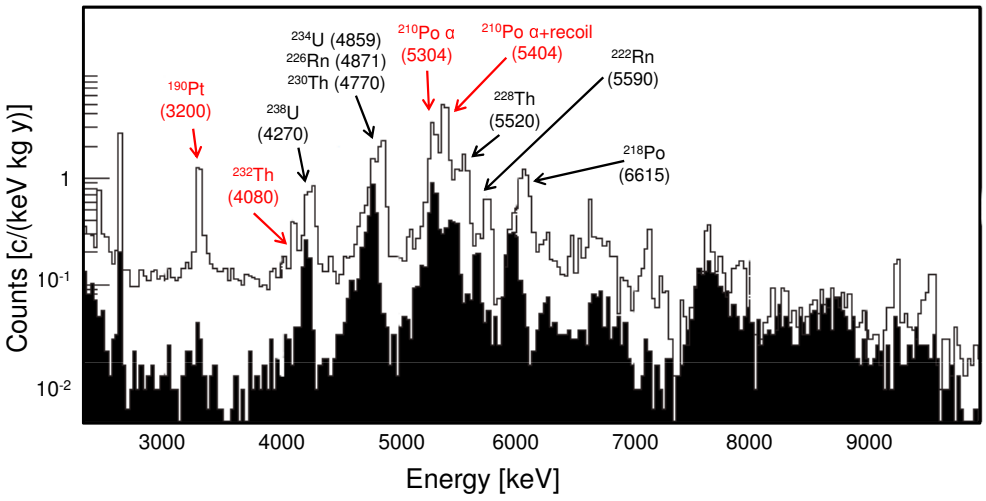

Figure 3.2: Cuoricino background in the α region. The line refers to the anti-coincidence events spectrum, where only one bolometer is hit within the time coincidence window; the filled plot refers instead to the coincidence events, where two detectors are hit. The recognized peaks are labeled, and those not ascribed to surface contaminations in ^{238}U and ^{232}Th (see text) are evidenced in red.

Site	Contamination type	Energy range		
		^{208}Tl	$Q^{0\nu}_{\beta\beta}$	3-4 MeV
TeO_2 surface	^{238}U and ^{232}Th	–	10±5%	20±10%
Cu surface	^{238}U and ^{232}Th	∼15%	50±20%	80±10%
Cryostat Cu shields	^{232}Th	∼85%	30±10%	–

Table 3.1: Summary of the relative contributions due to the different sources responsible for the background measured in Cuoricino.

with good confidence and will be reduced by an apposite lead shielding in the CUORE cryostat. The problem of surface contaminations is, on the other hand, still open and represents one of the most demanding challenges in view of the sensitivity desired for the final experiment. A specific R&D activity aimed at the CUORE-oriented reduction of the unwanted background has been pursued in the years previous to this Ph.D. work: its main results will be summarized briefly because they are a starting point to part of the topics presented in this thesis.

The campaign of measurements presented here was performed on a dedicated setup called *Radioactivity Array Detector* (RAD) and constituted by eight bolometers with 5×5×5 cm^3 absorbers, distributed in two four-crystals modules. The basic detector is shown in Fig. 3.3. The RAD campaign allowed a better understanding of the background as well as the development of a surface treatment for both TeO_2 crystals and the Cu elements facing them. Six RAD measurements were realized from 2004 to 2006 in the cryogenic Hall C facility at LNGS (see Appendix A), each with a specific goal.

RAD1: test of a dedicated procedure to clean the surfaces of TeO_2 crystals.

RAD2: test to disentangle possible radioactive contaminations due to the small components of the SM facing the absorber (NTD Ge thermistor, Si heater, Au wires for signal read-out, PTFE holders).

RAD3: test to control the surface contaminations of the Cu holding structure by coverage with thin layers of polyethylene film.

RAD4: test to identify contributions to the 3-4 MeV continuum other than surface contaminations, by operating the same RAD3 detector with an outer neutron shield.

RAD5 and RAD6: tests to identify peculiar exotic contributions to the 3-4 MeV continuum, by substituting the PTFE holders in the RAD3 detector with phosphorus-bronze, Cu-coated clamps.

An effective cleaning procedure for TeO_2 surfaces, leading to a reduction by a factor ∼4, was found in RAD1 (see Chapter 4). Then, contributions from small detector components were ruled out by RAD2. RAD3 was performed because no appreciable reduction in the 3-4 MeV continuum could be obtained during the first tests: assuming as origin of the main contribution the radioactive surface contaminations in the holding elements around the detector, all Cu pieces were covered by a 60 μm thick polyethylene layer (the exact role of polyethylene will be explained later in this chapter, Sec. 3.4.1.1). The addition of a neutron shield in RAD4 did not bring any appreciable improvement to the results of RAD3, and the spectra of the two measurements, given their compatibility, were summed to increase the total statistics available. The overall analysis on the polyethylene coverage showed a definite reduction of the continuum from 3 to 4 MeV by

a factor 2±0.4, in respect to both Cuoricino and RAD1.

As for RAD5 and RAD6, they were instruments to investigate a possible contribution to the 3-4 MeV background due to thermal relaxation processes in the PTFE supports: the assumption to be tested was the production of heat releases in the absorbers able to mimic the thermal pulses produced by particle interactions. The tests did not rule out possible contributions to the background from non-radioactive sources because of problems in excessive surface contaminations; however, they demonstrated as a side effect the good performance of bolometers even after the replacement of PTFE supports with Cu clamps: this result will be quoted again in Chapter 6 (Sec. 6.1). Extensive information on all the RAD tests performed at LNGS can be found in [84].

In conclusion, while the heavy cryostat shielding foreseen for CUORE will guarantee a deep reduction of the γ background due to the ^{208}Tl contribution, the control of the α background due to contaminations in the very inner part of the detector is possible only by means of a thorough, dedicated R&D activity. The campaign of RAD measurements showed that a proper surface cleaning of crystals could be achieved, but without any appreciable influence on the 3-4 MeV continuum; the latter, however, is reduced by half in respect to the Cuoricino background when surface contaminations in the materials of the holding structure are shielded (i.e., when the Cu elements are covered by polyethylene layers). It must also be noted that detector operation in anti-coincidence, which does not yield dramatic background reduction in Cuoricino, will play a fundamental role in CUORE because of its tightly-packed design. Tab. 3.2 reports the projections to the final background foreseen for CUORE, made by Monte Carlo simulations on the basis of the current R&D achievements. The target for CUORE, which is the reduction of the background level from the Cuoricino value to at least b=0.01 c/(keV·kg·y), is not far.

3.2 Getting to grips with the radioactive background

Both the analysis of the Cuoricino background and the results of the RAD campaign of measurements push the current efforts of the R&D towards the control of surface contaminations. The most critical source of unwanted counting rates in the 0ν-DBD energy region of ^{130}Te is α-radioactivity in the form of degraded α particles: they release only a variable fraction of their energy in the detector's absorber and generate events which cannot be traced back to a specific decay by their signature, as explained in Sec. 3.1.1. The outcome is a continuous background. As already seen, the dangerous degraded αs are generated by surface contaminations of two kinds. The possible patterns are summarized by the graphic representation in 3.4.

- The α-decaying nuclide can be implanted or site on the surface of a crystal. In this case, it becomes highly probable that only one of the decay products, the daughter nuclide or the α, releases all of its energy in the absorber: this was mentioned in Sec. 3.1.1 to generate a count in the spectrum located at energy lower than the peak of the corresponding decay. On the other hand, the remaining particle deposits a fraction of its energy in the crystal and leaves, retaining the rest of it. If the escaped particle encounters any inert elements of the detector, the surviving information on the decay is definitely lost; but if it hits a neighbouring crystal, the final signature will be constituted by coincident counts in two bolometers with sum energy corresponding to that of the original decay. The problem can be dealt with in two coexisting ways: a *passive* strategy, which consists in the careful surface treatment of crystals mentioned in Chapter 4 and first studied in the framework of the RAD campaign; and an *active* strategy, which asks for a specific design of the detector's geometry: the fraction of active volume should be maximized, at

Figure 3.3: The basic RAD detector, used in the R&D activity of the CUORE collaboration focused on background investigation.

Element	**Rate in the 0ν-DBD region** [$\times 10^{-3}$ c/(kev·kg·y)]
Crystal bulk	<1
Crystal surface	<3
Cu mounting bulk	<0.6
Cu mounting surface	20-40
Experimental setup	<10
Environmental γs [89]	<0.4
Environmental neutrons [89]	$(8.6\pm6.06)\times10^{-3}$
Environmental muons (with no veto) [89]	0.104 ± 0.022

Table 3.2: CUORE background projections made by Monte Carlo simulations based on the current R&D achievements (Summer 2010).

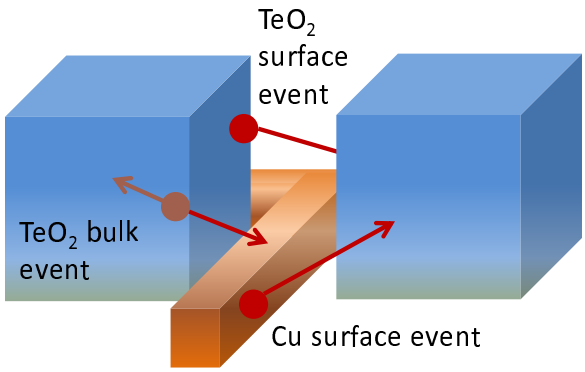

Figure 3.4: Possible α patterns in the setup of TeO_2 macro-bolometers

the same time reducing the probability for the second particle to travel in the free space among the bolometers without hitting on an active element.

- The α-decaying nuclide can be site on the surface of some inert material that faces the detector. In this case, the probability is higher for the α-particle to escape from the passive element and hit on a crystal. The result of such interaction is highly dangerous for the examined application: the originated count will occupy a random position in the spectrum, across the whole region that lies below the total energy of the initial decay. These kind of events cannot be dealt with easily as far as the bolometric technique is concerned. In fact, the use of low temperature calorimeters in particle detection implies information about the nature of events is lost. This is intrinsic to the detection mechanism because the energy deposited inside the device in calorimetric mode, where quasistatic equilibrium is implied, is completely transfered into the final state as heat. As a consequence, one measures the entire energy of the particle, losing additional details such as the location or type of the interaction. No spatial resolution is obtainable; the bolometer works like a single pixel the size of the detector itself.

The core of the CUORE-oriented R&D activity is therefore the development of strategies aimed at controlling the radioactive background in the ROI originated by degraded αs due to surface contaminations of the detector's passive elements. The inert material that crystals are most exposed to is Cu. A redesign of the bolometric array with the purpose of limiting the amount of Cu surface seen by each crystal is not sufficient. Other paths must be followed and will be described in the rest of this chapter: they can be classified as active or passive approaches.

3.3 Inert detector elements and surface contaminations: active approach

The starting point of this discussion is that the bolometric technique has no spatial resolution and is not capable, because of its intrinsic qualities, of dealing with the problem proposed here, caused by surface contaminations on Cu. This flaw of low temperature calorimeters can be partially overcome by utilizing a composite bolometer made of separate elements thermally coupled to each other, and exploiting the dynamics of the heat

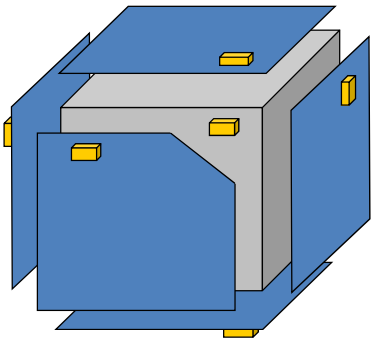

Figure 3.5: Graphic representation of a Surface Sensitive Bolometer. Full coverage is provided to the main TeO_2 crystal by the surrounding slabs, except for a free portion of surface hosting its thermistor.

flux in order to attain information on the origin of the particle interaction [96]. Composite bolometers of this kind are called Surface Sensitive Bolometers (SSB). The basic concept to realize a SSB is to shield each TeO_2 crystal with crystalline slabs, which may come in different materials selected for their availability, high purity and appropriate thermal properties. If a thermometer for temperature reading is applied to a slab, the slab behaves as an auxiliary bolometer and can be regarded as an active shield. Particles that release energy inside the slabs can thus be detected and rejected by common anti-coincidence methods. A representation of this kind of detector is given in Fig. 3.5.

3.3.1 Discrimination of surface events with TeO_2 macro-bolometers

The main crystal surrounded by the system of auxiliary bolometers is provided with almost a 4π coverage from external charged particles. When a particle, for example an α particle, coming from outside the detector interacts with one of the active shields, it deposits all of its energy in the slab. This raises the temperature of all the elements of the detector. Because of the small heat capacity of the slab, the signal read by its thermistor will have a higher amplitude and faster rise time than the signal read by the thermistor attached to the main energy absorber. On the other hand, if an event happens inside the main absorber, all the thermistors of the detector will read pulses with comparable amplitudes and rise times. It is therefore possible to separate events with distinct origins through a comparison in amplitude and shape (e.g. rise and decay times) of pulses among the different thermistors. Although the bolometer is split up in various parts, no degradation in energy resolution of the main absorber is expected since the device is still operating in calorimetric mode, where phonon thermalization is nearly complete.

Thanks to the aforementioned behavior, the SSB is able to isolate energy depositions occurring in the bulk of the main absorber from two other types of events: energy depositions by particles that originate outside of the entire detector and those by particles originating from contamination at the main absorber surface or at the shield surface facing the main absorber. The first ones are intercepted by the shields; the second ones can mimic the searched decay by depositing about 2.5 MeV in the main absorber. Since the energy of a natural α is approximately higher than 4 MeV, at least 1.5 MeV must be deposited in the active shield. These events are classified as mixed events and can be recognized by the large fast component associated to the energy deposited in the shields. Therefore, SSBs are also useful to recognize the background due to surface contaminations in the detector elements themselves. The scatter-plot of pulse ampli-

tudes is the most convenient instrument to apply the discrimination principle introduced by SSBs: in this kind of graphs, for all energy depositions, the amplitudes of pulses read by the main thermistor is reported on the X-axis, while those of each auxiliary thermistor are plotted on the Y-axis. Scatter-plots allow a clear reading of signatures. The curve resulting from energy depositions inside the sole main absorber is a line with approximately unitary slope, while it becomes steeper in the case of energy released inside the shield, sometimes even reaching saturation; events corresponding to energy released in both the main absorber and the slab within the time coincidence window are collocated in the middle region of the graph. Fig 3.6 shows the simulated behaviour of a SSB detector the size of a Cuoricino bolometer, useful to draw qualitative conclusions on the expected performance; simulations are based on an extension of the composite thermal model presented in Sec. 1.4 that includes the presence of at least one auxiliary bolometer equipped with a thermistor [97].

SSBs have been tested extensively in the past years in the shape of both small $2\times2\times0.5$ cm^3 prototypes at the Cryogenics Laboratory in Como and $5\times5\times5$ cm^3 detectors at LNGS [98], [99]. Fig. 3.7 shows a selection of the measured bolometers. Various materials have been tested as shields (Ge, Si, TeO_2 itself), together with different ways to couple them directly to the main absorber. The most effective results have been reached with TeO_2 slabs glued by epoxy dots on the six faces of the main absorber: TeO_2 is preferred as shield material to avoid mechanical problems due to differential thermal contractions at low temperatures, and because it can be subjected to the same production protocol, certified in terms of radio-purity, fixed for the $5\times5\times5$ cm^3 crystals.

3.3.2 Potentialities of SSBs in the search for the 0ν-DBD of ^{130}Te

Ideally, the composite bolometer for the identification of surface events in the CUORE setup has six auxiliary bolometric TeO_2 slabs working as active shields, one for each face of a main TeO_2 bolometer; all slabs have approximately the same area and shape as the corresponding absorber face, to which they are connected by epoxy glue spots with sub-millimeter height; each slab has its own semiconductor thermistor and a dedicated signal channel for temperature reading.

The most effective results in the course of the R&D campaign on SSBs were reached during a measurement on large size bolometers performed at LNGS using TeO_2 slabs. Four SSBs were assembled and operated. The coverage was not complete because an almost triangular area near each vertex was unshielded in order to host the PTFE holders for connection to the Cu frame. Not all of the shields were provided with a temperature sensor: for two SSBs, each slab had its own thermistor and they were read independently; for the other two, the slabs were without thermistor ("passive"). The choice of introducing passive slabs was done in order to test the possibility to discriminate surface events by using just the main thermistor read-out, exploiting the behaviour of shields, observed in prototypes, as shape modifiers of pulses deriving from interactions with external αs. The statistics collected was of 687 hours. For reasons that will be explained in Sec. 3.4.2, the background was not evaluated in the 0ν-DBD region but in the energy regions right above it. The resulting background level, obtained from discrimination performed by decay time and amplitude cuts, is (0.07 ± 0.02) c/(keV·kg·y) in the 2.8-3.2 MeV range and (0.04 ± 0.02) c/(keV·kg·y) in the 3.4-4.0 MeV range. The best values of the RAD tests described in Sec. 3.1.2, which are the highlight of the R&D background reduction programme through accurate cleaning of detector materials, are (0.06 ± 0.01) c/(keV·kg·y) in the 2.8-3.2 MeV range and (0.08 ± 0.02) c/(keV·kg·y) in the 3.4-4.0 MeV range. The count rate obtained with the SSB method is hence compatible

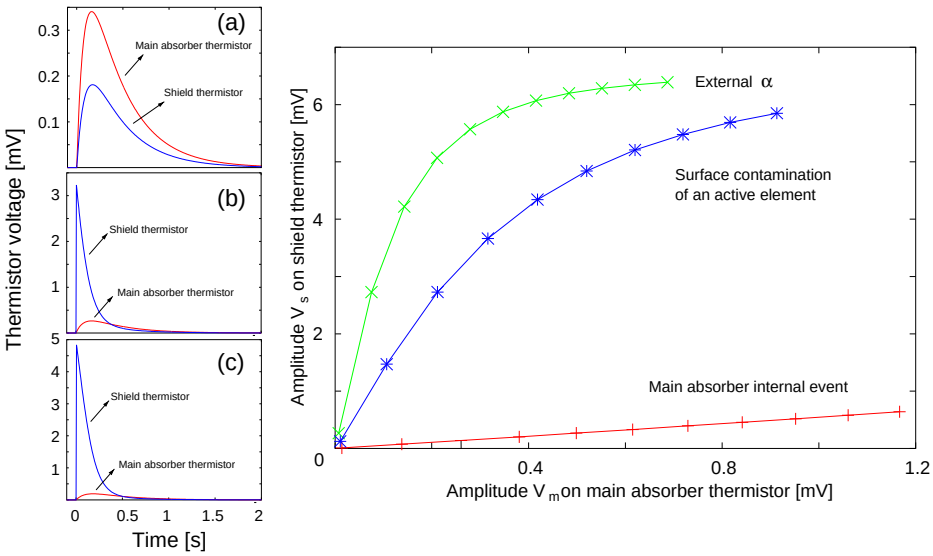

Figure 3.6: Simulation of a Surface Sensitive Bolometer, describing the qualitative behaviour expected from the detector. On the right, pair of simulated pulses generated by a total energy deposition of 2.5 MeV in the detector as seen, alternatively, by the thermistors on the main absorber and on one slab of the SSB. The position of the energy deposition is varied: (a) 2.5 MeV in the main absorber; (b) simultaneous deposition of 1.25 MeV inside of the shield and of 1.25 MeV inside of the main absorber; (c) 2.5 MeV inside of the shield. On the left, the simulated scatter-plot for total energy depositions ranging from 0.1 to 9 MeV is shown: the middle line corresponds to energy depositions simultaneously shared between the main absorber and the shield (as in the (b) pair of simulated pulses).

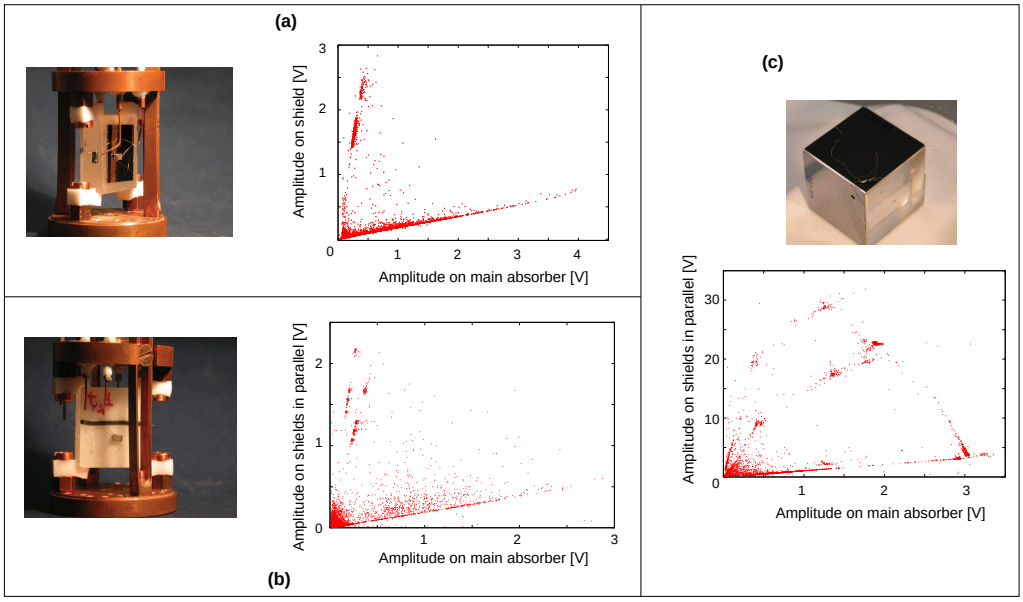

Figure 3.7: Pictures of SSB prototypes and examples of relative scatter-plots. (a) $2\times2\times0.5$ cm^3 prototype with Si shields measured in Como. (b) $2\times2\times0.5$ cm^3 prototype with TeO_2 shields measured in Como, with thermistors are read in parallel configuration. (c) $5\times5\times5$ cm^3 prototype with Si shields measured at LNGS, with thermistors read in parallel configuration.

with the benchmark results previously obtained by the R&D. However, the reduction was not as effective as expected, which can be easily explained by the various problems that afflicted the experimental run: first, one active slab channel was lost on each of the two fully-read SSBs affecting the procedure of event discrimination; then, TeO_2 slabs were eventually found to be contaminated because of the cutting procedure followed by the manufacturer; moreover, poor measurement quality due to cryogenic problems was a further complication.

Despite the problems witnessed in the presented experimental test (chose as a reference for the surface sensitivity technique described here), the effectiveness of the SSB as tool for background reduction and diagnosis can be proved by computing its surface-events rejection power. The calculation is performed on a small SSB prototype that was operated in Como and is pictured in Fig. 3.7(b), together with the scatter-plot obtained from the parallel read-out of its shields. After fitting with a straight line the points corresponding to events inside the main absorber and registering the corresponding slope β, a parameter associated to each event can be defined as

$$SEI \equiv \frac{\Delta V[\text{shield}]}{\beta \cdot \Delta V[\text{main absorber}]} - 1 \begin{cases} = 0 & \text{for events in the main absorber} \\ > 0 & \text{for events in one of the shields} \end{cases} \tag{3.1}$$

SEI stands for *Surface Event Index*; in Eq. (3.1), the pair (ΔV[main absorber], ΔV[shield]) identifies a point in the scatter-plot corresponding to an event recorded by the detector. Of course, the equality of *SEI* to zero in case of energy depositions in the main absorber, given by construction, is valid within experimental error. As the SSB prototype used for the calculation has two shields, the expected distribution of SEI will feature one peak centered on 0 and two peaks centered on values higher than 0 collecting depositions in the shield; in addition to them, a small population collecting events where energy is released simultaneously in the main absorber and in the shield is expected to lie outside the three peaks: they correspond to the discussed energy depositions due to surface contaminations of the detector's active elements. The evaluation of the surface events rejection power obtained with SSBs is given by the separation between the peak of the main absorber and those of the shields. The whole procedure applied to the considered SSB prototype is reported with a full treatment in [97], and only the conclusions will be reported here. The *SEI* distribution obtained is reported in the left side of Fig. 3.8 in function of the pulse amplitude read by the thermistor on the main absorber, calibrated in energy: the plot shows the three expected bands of events (at *SEI* equal to 0, 4 and 8), which are projected in the SEI distribution in the right side of Fig. 3.8 after selecting the energy window from 2 to 4 MeV that contains the $Q^{0\nu}_{\beta\beta}(^{130}\text{Te})$. Due to simultaneous energy depositions in the main absorber and in the shields, the peak of main events features a tail at high *SEI* values. The estimation of the rejection power is obtained by Gaussian fitting the peaks. The distribution of main events, including the tail of mixed energy depositions, stops at SEI$\sim$2.5, about 13 σ away from the centroid of the nearest shield peak (whose Gaussian fit is centered on 4.208 and has σ=0.127). The final result, considering both shields, is that the ROI shows no contamination of external αs and that the rejection power is essentially 100%.

The previous analysis shows that a full recognition of events is possible with technique introduced by SSBs. These detectors have also the advantage of using materials already present in the original setup (TeO_2, epoxy for thermal connections, Ge sensors with Au wires) so that the original radio-purity is preserved. Nonetheless, their introduction implies strong complications in the detector's assembly, and reliable procedures to connect the slabs and secure SSBs in the Cu holder without damaging the shields

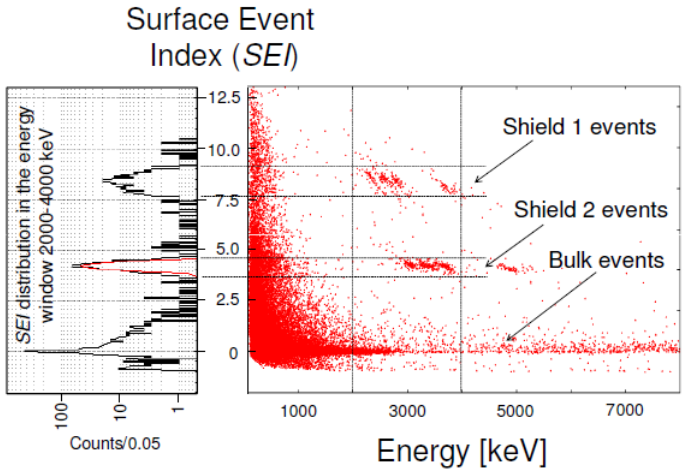

Figure 3.8: On the right, plot of the SEI as a function of the energy deposited in the main absorber for the SSB $2\times2\times0.5$ cm^3 prototype described in the text. On the left, projection of the SEI distribution for events in the region from 2000 to 4000 keV. A full treatment of the determination of the SSB's rejection power is reported in [97], which is also source for this plot.

have not been established yet up to this date. Other techniques are possible to confront the background contribution in the ROI generated by surface contaminations on the materials surrounding the bolometers. For example, the detection of out-of-equilibrium phonons can lead to recognizing the origin of events, although incomplete thermalization leads to degradation in energy resolution [99]; another solution is to couple the light signal of a scintillator to the phonon signal of a normal bolometer: in this way, a double independent read-out (heat and scintillation) will allow the required suppression of the background thanks to the different quenching factor between αs and γs [100],[101]. A review of these topics can be found in [102].

Given all these premises, the choice of the CUORE collaboration in respect to the problem of background reduction is to pursue the path of a severe surface treatment of the detector's passive elements, which will be described in the next section.

3.4 Inert detector elements and surface contaminations: passive approach

While the first strategy to confront the problem of surface contaminations relies on providing the macro-bolometers of spatial resolution, the second approach consists in the thorough cleaning of the inert materials surrounding them: in a few words, it means removing large part of the contaminants from the experimental setup instead of recognizing and rejecting them by off-line analysis. As anticipated in Sec. 3.2, cleaning efforts are applied mainly to copper, which is largely used in the detector's holding structure designed by the CUORE collaboration and is particularly affected by contaminations introduced in the stage of mechanical processing.

3.4.1 Surface treatment of copper elements

In the course of the overall R&D activity performed by the CUORE collaboration to the current date, three cleaning strategies for the surface treatment of Cu elements have

been designed: they will be described in the following subsections, while an experimental comparison of their impact on the final background level will be proposed in Sec. 3.4.2. The cryogenic run devoted to the choice of the most suitable Cu treatment for use in the imminent CUORE-0 is the closing test of the whole R&D program developed by the CUORE collaboration.

A successful treatment of Cu surfaces aims at the removal of an appropriately thick outer layer of the material, avoiding its exposure to recontamination. In the design of the cleaning approach, it should be considered that the mechanism of energy degradation underwent by α-particles could depend not only on their initial depth, but also on the roughness of the Cu surface: the interpretation is supported by a comparison between independent measurements performed on surface radio-purity and dedicated Monte Carlo simulations, which make contaminants appear as if they are site at higher depths than those foreseen if the canonic mechanisms of surface implantation of nuclides hold (recoil following a radioactive decay, diffusion, mechanical processing). If the decaying nuclide is nested in a pit on a rough surface, it is easier for the emitted α to deposit, in the course of its trajectory, part of its energy in the irregularities of the Cu element. The result foreseen by simulations is that the α-peak observed in the spectrum extends towards lower energies, as if the parent contaminant were located at higher depths into a perfectly flat surface. Cleaning processes should therefore aim at the control of material roughness, too, although no specific measurements have been performed on this topic up to now.

3.4.1.1 The classic RAD-Polyethylene protocol

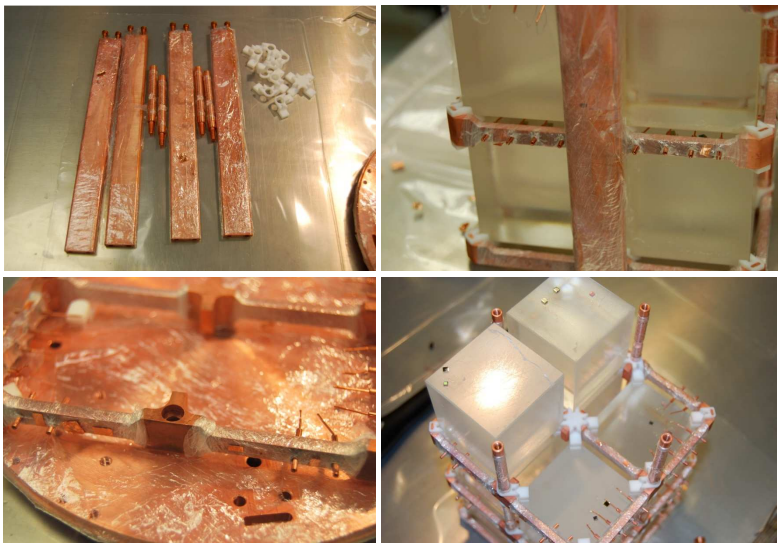

Figure 3.9: The RAD-Polyethylene treatment for Cu surface processing: coverage of the holding structure with polyethylene layers.

The first type of surface treatment described in this section has been developed at LNGS in the years previous to this thesis, in the course of the RAD campaign of measurements described in Sec. 3.1.2. The protocol proposed here was validated by the two cryogenic runs RAD3 and RAD4. The following procedure is chemically mild and does not alter appreciably the mechanical properties of the holding structure, at the expense of introducing an elaborate manual step that slows down the assembly schedule.

- **Mild chemical treatment.** The first step of the RAD-Polyethylene protocol requires that all Cu elements are washed in a solution of ultra-pure H_2O and alkaline soap (Micro 90®) at 5%, in a 10-minutes ultrasonic bath heated up at 50 °C: this removes oil remnants from mechanical processing. Then all components are immersed twice, for 30 and 15 minutes respectively, in an acidizing solution with 4% citric acid, ultra-pure water and ∼2% H_2O_2. The treatment results in the removal of a 10 to 20 μm material layer.
- **Polyethylene coverage.** After chemical pre-processing is finished, Cu elements are moved to the assembly clean-room in the underground facility and wrapped with a special radio-clean polyethylene layer designed to stop the departing α-particles. Polyethylene is selected because plastic materials feature lower level of contamination from external nuclides than metals; moreover, since the thickness of one layer is of order ∼10 μm, the bulk contamination coincides with the surface contamination: this allows HP-Ge radio-purity measurements to guide the choice of the covering material. A commercial polyethylene wrapping foil was eventually selected. All the Cu elements that face the detector are manually wrapped in seven layers of polyethylene, reaching a total shielding thickness of ∼84 μm able to stop any heavy ionizing particles generated by natural radioactivity.

3.4.1.2 The new LNGS protocol

Figure 3.10: The LNGS protocol for Cu surface processing: setup for the electro-polishing of Cu columns, bars (top), frames and shielding (bottom).

The second type of cleaning protocol was designed at LNGS and consists in combining an acidization step, much like the one requested by the Polyethylene protocol, to electro-erosion. It gives rise to an overall aggressive chemical treatment that could impact the mechanical characteristics of the assembled detector holder: needless to say, this is requested because no polyethylene shielding is inserted. Details on the procedures and estimations for the quantities of removed material are reported in [103].

- **Preliminary chemical treatment.** Cu elements are washed in a solution of ultra-pure H_2O and alkaline soap at 5%, in a 15-minutes ultrasonic bath heated up at 45 °C. Oil and powder remnants, as well as contaminants with weak bounding to the surface, are removed this way.

- **Electro-polishing.** Electro-polishing proved to be a particularly successful procedure for cleaning copper surfaces when the contaminants are polonium isotopes [104]. Due to the chemical affinity between Cu and Po, in fact, chemical etching is not effective: a Po ion removed after immersion in the acidizing solution would very probably bound again to the Cu lattice; the imposition of an electric field reduces the probability of recontamination because it can endow the ion with sufficient energy to make it drift far from the Cu surface. Cu elements, working as anods, are immersed in an acid solution composed by 85% orthophosphoric acid, 5% buthanol and 10% ultra-pure H_2O; they are faced to custom shaped cathods, so that an approximately uniform electric field is generated in the neighbourhood of the surface of the sample under treatment by imposing a potential difference of $\sim$2 V. After 90 minutes, the elements are removed from the solution and rinsed in ultra-pure water. Measurements performed at LNGS show that the total amount of removed surface ranges from $\sim$10 to 20 μm. Moreover, flatness is obtained automatically, for given potential difference between anode and cathode, due to the larger electric field acting on the rough elements on the surfaces.
- **Chemical etching.** The third step of the LNGS protocol is not aimed at removing contaminants, as etching is not effective in eliminating Po isotopes [104], but at the cleaning of acid remnants left by the electro-polishing procedure. ICP-MS measurements (see Sec. 4.3 for a few details on the technique) show that the concentration of U and Th is lower in nitric acid than in the orthophosphoric acid used for the electro-polishing step: therefore, the choice was made to immerse the polished Cu parts in a solution of 10% ultra-pure nitric acid and 90% ultra-pure H_2O, for 15 minutes at 65 °C temperature. From $\sim$20 to 60 μm of material are removed during this step.
- **Passivation.** Eventually, the surface of the treated Cu elements must be made inert to oxidative processes that could lead to unexpected effects in regard to radioactive contamination. The solution used is constituted by equal volumes of ultra-pure H_2O and H_2O_2, mixed with an equal mass of citric acid and kept at 65 °C temperature. The total immersion time is 5 minutes, although it is split in subsequent steps of a few seconds to avoid that the exothermic reaction that decomposes hydrogen peroxide, catalyzed by the presence of metallic ions, diverges resulting in violent boiling. The passivation process can remove a relevant portion of Cu, even more than 100 μm, depending on the duration of the immersions.

3.4.1.3 The Legnaro protocol

The last cleaning protocol was developed at the Legnaro National Laboratory in Padova, Italy. Comparing to the procedures in Sec. 3.4.1.1 and 3.4.1.2, the Legnaro method is fully automated. The advantage brought by dealing with automated procedures has already been mentioned in Sec. 2.3.2.3 and will be clarified extensively in the context of Chapter 6 (Sec. 6.4 and 6.4.4): however, the main motivations are summed up by the reduction of both the variability introduced by human-performed operations and the time needed to assemble a $\sim$1000-bolometers next-generation experiment. The Legnaro procedure is also known by the acronym TECM, which derives from its four steps: Tumbling, Electro-polishing, Chemical etching and Magnetron plasma cleaning. While the first three steps make the Legnaro procedure a mere evolution of the Polyethylene and LNGS protocols, plasma cleaning makes the real difference: the method has been tested for the first time ever on bolometric components in the run presented in Sec. 3.4.2. Between each step, the Cu elements under treatment are rinsed in ultrasonic bath to remove mechanical processing remnants. The Legnaro protocol is extremely aggressive, if compared to the other two, and brings appreciable modifications in the mechanical characteristics of the Cu holder.

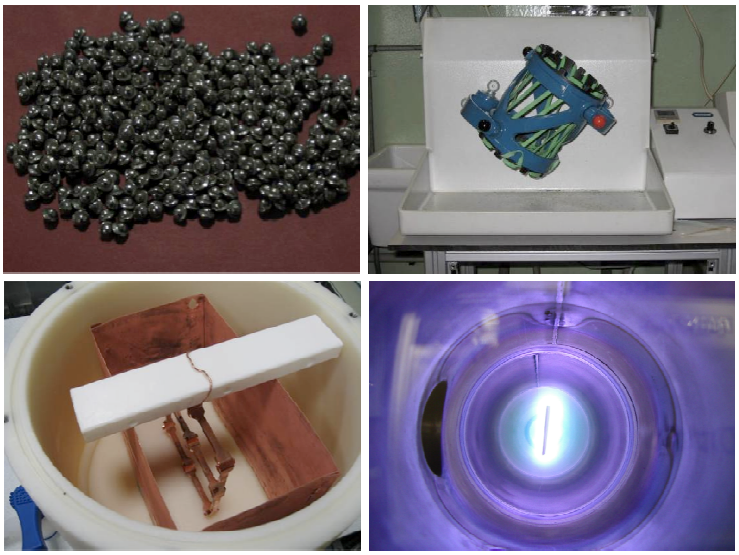

Figure 3.11: The Legnaro protocol for Cu surface processing. Top: the steel elements for tumbling (left) and the tumbling machine (left); bottom: the setup for frame electro-polishing (left) and the Ar plasma inside the vacuum chamber of magnetron plasma cleaning.

- **Tumbling.** Cu elements are inserted in the barrel of a continuously rotating machine, together with an abrasive media constituted by KCl crystals and small steel cones: the mixture erodes portions of Cu and removes its surface roughness. Layers with approximate thickness of order of fractions of μm are removed; the goal of this step is to smooth out copper, so that the effective surface of each element is reduced.
- **Electro-polishing.** As in the LNGS protocol, each Cu element serves as anod while facing a custom designed cathod. They are both immersed in an acid solution, this time constituted by 60% phosphoric acid and 40% buthanol. Electropolishing is the dominant step in the Legnaro technique, in terms of quantity of material removed ($\sim$100 μm), while the LNGS procedure is dominated by acidization and passivation.
- **Chemical etching.** Residuals of the preceding step are eliminated by immersion in a solution of sulphuric acid at 72 °C, and $\sim$10 μm are eroded.
- **Magnetron plasma etching.** As already mentioned, this step of the Legnaro protocol introduces the main difference in respect to the Polyethylene and LNGS procedures, as it allows to perform material cleaning under vacuum. Cu elements are inserted in a chamber at $\sim 3 \times 10^{-8}$ mbar where a ionized argon plasma at $\sim 5 \times 10^{-3}$ mbar is generated and accelerated to form discharges of approximately 0.1 A: atoms at the surface and residing impurities are removed by Ar ions impacting on Cu, which transfer their kinetic energy to them. The whole step lasts 60 minutes. As already mentioned in the introduction to the Legnaro protocol, magnetron plasma cleaning has been applied for the first time to the surface treatment of bolometric elements in the preparation of the cryogenic run that will be described in the next section. It should be noted that imperfections, mainly dark stains, have been observed on some Cu elements after the magnetron step: they are assumed to be caused by oxidation subsequent to plasma cleaning, and their relevance can be determined only by a cryogenic background test. Due to the excessive complications introduced by their size and number, magnetron cleaning is not suitable for the surface treatment of small Cu detector elements like the

pins for signal read-out, which are therefore subjected to the Polyethylene protocol (they will not be present in CUORE-0 and CUORE, anyway); no loss is expected in principle because of their limited contribution to the total background level.

The reduction of the background contribution in the ROI due to surface contaminations can be verified only by means of cryogenic tests in an R&D setup where conditions close to those of the final experiment are met. In order to compare the outcome of the three cleaning protocols and to adopt one of them in the assembly of the imminent CUORE-0 experiment, a dedicated low-temperature measurement was performed at LNGS. The test, which is the conclusive run in the global R&D activity for CUORE-0 and CUORE, will be presented in the next section.

3.4.2 The Three Towers Test

The last cryogenic run in the timeline of the CUORE-focused R&D activity is a background reduction test on the most delicate aspect of the future experiment's design: the choice of the surface treatment protocol for the cleaning of passive Cu detector elements, which are assumed to be source for the main contribution to the unwanted count rate in the 0ν-DBD region of ^{130}Te. Only measurements on bolometric arrays give the information necessary to extrapolate the background level in the ROI expected for the final experiment, and no other radio-purity measurements can be used to discriminate among cleaning methods with enough sensitivity for the application under discussion; moreover, besides background estimation, measurements on TeO_2 macro-bolometers at low temperatures allow to check the results of the detector in terms of response and energy resolution, evaluating thus the possible impact of the cleaning protocol on the detector's performance. However, cryogenic tests are affected by a fundamental flaw, which can nonetheless be overcome by a simple expedient: the estimation of very low background levels in the ^{130}Te $Q_{\beta\beta}$ region requires, in fact, an extremely long measuring time range. Let's take as an example a usual R&D bolometric run for radio-purity evaluation. The standard detector tower used in tests of this kind is constituted by three floors holding four bolometers each, which means that twelve crystals are measured: the total TeO_2 mass is $\sim$10 kg. In this case, a background of 10^{-2} c/(keV$\times$kg$\times$y) in the $Q_{\beta\beta}$ region, whose width is taken to be 100 keV, is measured with an accuracy of 10% in approximately 10 years. Needless to say, this would make any R&D test incompatible with the experiment's schedule. However, since the continuous background is the same above the 2615 keV ^{208}Tl line, the estimation can be extended to the wider region from 3 to 4 MeV. As a consequence, the data taking of typical R&D background-oriented runs can be limited to a few months: the observation of a large reduction of the background level in the region above $\sim$3 MeV would then imply a decrease also in the ^{130}Te $Q_{\beta\beta}$ range.

Given the aim of comparing the three Cu surface treatment protocols described in Sec. 3.4.1, the dedicated cryogenic test was designed to involve three experimental setups as much similar to each other as possible: this requires handling in comparable radio-pure environments, assembly with the same mechanical characteristics and operation in equal cryogenic conditions. If the requirements are met, possible differences evidenced by data analysis among the three setups in terms of bolometric performance and/or radioactive background would be traced back to the peculiar surface treatment protocol used. For this reason, the choice was taken to construct three twelve bolometers-towers each subjected to a distinct cleaning procedure: the cryogenic run is therefore called *Three Towers Test* (TTT). The towers, connected sequentially one to the other, collected data from September 2009 through January 2010 in the Hall A cryogenic facility that had previously hosted the Cuoricino detector. A graphic representation and pictures of the final detector are reported in Fig. 3.12.

Each tower is designed so that its crystals are exposed only to copper elements cleaned by the corresponding procedure, and in a configuration such that they are not reached by α-particles coming from the other towers. Cu disks cover the upper and lower sides of each tower, providing shielding as well as mechanical and thermal connection to the other ones and to the cryostat; lateral coverage is established by means of cylindrical shields, once again in Cu. The Cu elements, treated by the Polyethylene, LNGS or Legnaro protocols, were stored underground in nitrogen atmosphere until the beginning of assembly, to avoid oxidation or recontamination by ^{222}Rn and its daughters. The mounting was performed for the same reasons inside a radon-box (where radon activity is estimated as $\sim$1 Bq/m^3), using gloves and instruments selected by radio-purity measurements and periodically cleaned with ethanol and ultra-pure water; the total exposure to air of each tower, required by operations impossible to be performed in radon-box environment, is estimated as two days. Both gluing and wire connection for signal read-out were performed as in the assembly of Cuoricino (see Sec. 2.1.5 and Sec. 6.3). The whole assembly process of the TTT was a huge effort of the CUORE collaboration: the total eight months of full time activity required the complete disassembling of the Cuoricino tower together with the reprocessing of its crystals [1], and the construction of 36 bolometers, almost all equipped with two thermistors each.

A series of flaws affected the TTT. First, the loss of a large number of electric connections during the cooling down forced to repair the broken channels by opening the already finished detector; then, the strong earthquake that struck the town of L'Aquila on April 6, 2009 and caused the closing of the underground laboratory for several days forced to warm up the towers. After the detector was cooled down again, in spite of the repairing, 10 out of 36 crystals had no operational thermistors, and other 10 among the remaining 26 bolometers had no working heater. A map of the working bolometers in each tower is reported for convenience in Fig. 3.13.

A solution to the loss of heaters was found in the introduction of an external ^{40}K source and in the adoption of its 1461 keV γ-line as reference for the stabilization. Its use in this context brings the advantage that events generated by the interaction of γ-photons completely absorbed are monochromatic and are not affected by the instabilities that modify the behaviour of heaters (i.e., bias or temperature variations); on the other hand, the exact timing of the events to be used for stabilization is unknown, in the case of a radioactive source, due to the Poisson's distribution: the activity of the source must be selected carefully to reduce the probability of pile-up events inside the absorbers. ^{40}K is useful in this case because only two coincident γs releasing all their energy inside the same crystal can fall in the region of background evaluation, which is above 2.7 MeV. Monte Carlo simulations allowed to select the source, by making a trade-off between the intensity necessary to gain an event rate comparable with the pulser's and the request to keep the rate of ^{40}K events outside the photo-peak below an acceptable value ($\sim$ 10 mHz/ch).

The TTT was also the first run to be performed exclusively with the CUORE software for both data acquisition and analysis. The new DAQ developed for CUORE, named APOLLO [105], expands the ADC range to (-10.5 V)-(+10.5 V), about the double than in Cuoricino, and the acquisition window from the 512 samples of Cuoricino to 626 samples; the sampling rate is 125 Hz for both. Moreover, data were treated by means of the Thermal Response filter to stabilize and linearize the response [106]. A thorough, combined analysis of the TTT and Cuoricino data to update the limit on $T^{0\nu}_{1/2}(^{130}\text{Te})$ is

[1] see Chapter 4 for details on the surface treatment of TeO_2 absorbers, which can be neglected in this context

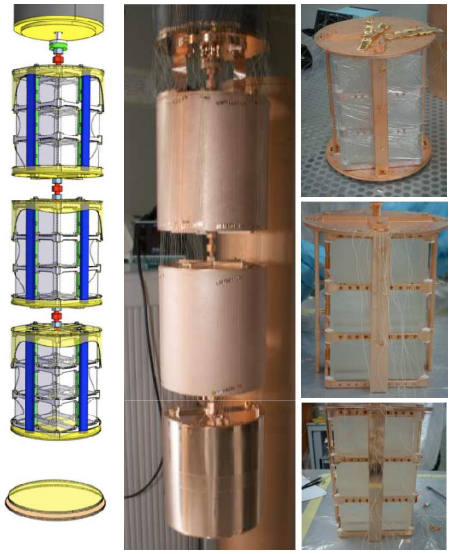

Figure 3.12: The detector of the Three Towers Test: graphic representation of the setup (left), the towers suspended from the dilution refrigerator (middle), individual pictures of the Polyethylene, LNGS and Legnaro towers (right, from top to bottom).

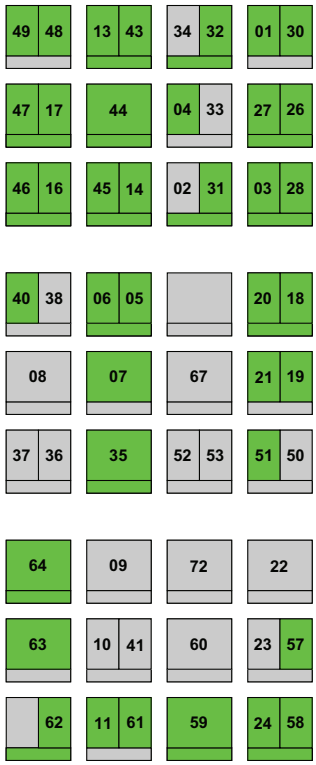

Figure 3.13: Scheme of the working bolometers in the Three Towers Test. The towers are Polyethylene (top), LNGS (middle), Legnaro (bottom). Crystals labeled with two channel numbers have two thermistors, and the horizontal band at the bottom represents the heater. Green indicates working; gray indicates not working. Heaters on crystals without a working thermistor are shaded gray because it is impossible to understand whether they are working or not. The Polyethylene tower has 12 crystals with at least one working thermistor and 9 with both a working thermistor and a working heater; the numbers are 7 and 3 for the LNGS tower, 7 and 4 for the Legnaro tower.

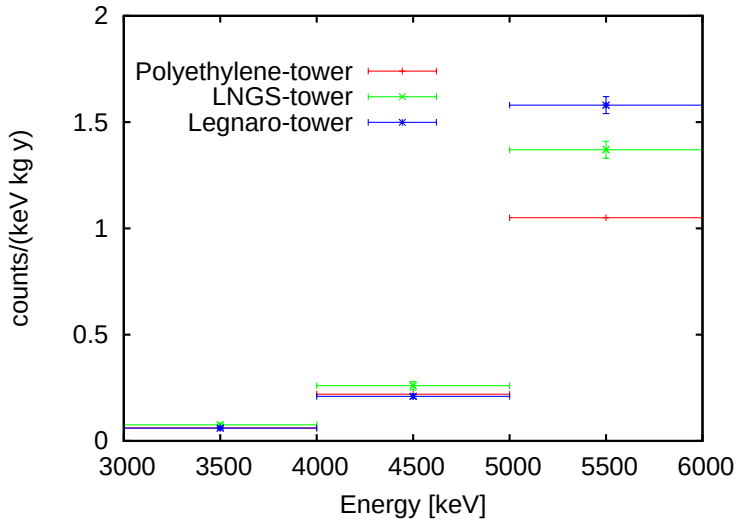

Figure 3.14: Counting rates in the α region seen by each of the three towers in the TTT. The values obtained in the 3-4 MeV interval of interest are compatible within 2σ. The counts were computed on a total statistics of 816.16 days·detector for the Polyethylene-tower, 477.69 days·detector for the LNGS-tower and 483.44 days·detector for the Legnaro-tower.

found in [107]. A treatment of the noise in the three arrays, which evidences a larger contribution for the Legnaro protocol, is given in [103].

The final live-time acquired, greatly reduced by the loss of channels, is of 816.16 days·detector for the Polyethylene-tower, 477.69 days·detector for the LNGS-tower and 483.44 days·detector for the Legnaro-tower. The counting rates obtained by the three towers in the α-region are reported in Fig. 3.14: the results indicate that the rates seen by the three towers in the 3-4 MeV region are compatible within 2σ. An analysis of coincident events shows a contamination on the surface of crystals in both ^{238}U and ^{210}Pb, which is justified by the fact that the crystals were not produced and processed by means of the new protocol fixed for CUORE (see Chapter 4); moreover, a population spread at $\sim$2800 keV has been observed among in the analysis of coincident events: the counts do not belong to an α-line, but the low statistics prevents from identifying the source responsible for them. Finally, the lowest background count rates, after performing the analysis of coincidences, were obtained by the Polyethylene-tower. Preliminary indications [108] show that the value in the 3-4 MeV range is

$$0.048 \pm 0.007(\text{stat}) \pm 0.005(\text{syst})\ \text{c/(keV} \cdot \text{kg} \cdot \text{y)} \tag{3.2}$$

The value was computed only with half of the statistics, due to the high pile-up and spurious coincidences occurred in the first part of measurements because of the ^{40}K source.

This background value should be considered when extrapolating the results expected for CUORE-0. To obtain a realistic value, one should add the contribution (3.2) to the *irreducible* background value foreseen. The irreducible background of CUORE-0, which will be cooled down in the same cryostat as Cuoricino, is given by the 30% of the Cuoricino background due to the external Th contamination in the cryostat: the most recent estimation of it (June 2010) given by the Analysis group of the collaboration is

$$0.048 \pm 0.002(\text{stat}) \pm 0.005(\text{syst})\ \text{c/(keV} \cdot \text{kg} \cdot \text{y)} \tag{3.3}$$

The counting rates mentioned should be added together to give the final upper limit of 0.12 c/(keV $\cdot$ kg $\cdot$ y) at 2σ for the CUORE-0 realistic foreseen background. The compatibility of the three towers within errors implies two possibilities: the cleaning methods proposed are not sufficient for the control of surface contaminations; on the other hand, another contribution to the counting rate in the ROI, which is distinct from the problem introduced by surface radioactivity, cannot be excluded in principle. Background levels being comparable, the final choice for CUORE-0 is the adoption of the surface treatment protocol that, among the three proposed, has the potential to provide more reproducibility: the surface treatment of the detector's Cu elements in CUORE-0 will be therefore the Legnaro protocol, whose automated steps provide a better fit to the previous request.

Chapter 4

A close look at the crystal absorbers

Chapter 3 presented the fight against the radioactive background in the region of the energy spectrum enclosing the $Q^{0\nu}_{\beta\beta}$ of ^{130}Te; it dealt with the contribution coming from U and Th surface contaminations on the passive elements of the detector, whose relevance is strongly hinted at by the experience gathered with Cuoricino and R&D activities. In the introductive part of the previous chapter, the presence of surface contaminations in the TeO_2 crystals was mentioned briefly, omitting details and stating that their contribution to the 0ν-DBD background in Cuoricino is $\sim(10\pm5)\%$. This chapter will deal with both the bulk and the surface radio-purity of TeO_2 crystals, but also with other aspects connected to it which influence bolometric performance. Remembering that the energy absorber is the core of the detector, the issue of which crucial aspects need optimization will be developed; the experimental tests performed in this context will then be reported; eventually, the conclusions drawn from them that influence directly any CUORE-0 applications will be discussed.

4.1 Crystal absorbers: what to work on

The reasons behind the choice of the isotope ^{130}Te for 0ν-DBD search and of TeO_2 as absorber material have already been explained diffusely in Chapter 2. A summary of the properties featured by the larger TeO_2 absorbers used in Cuoricino is reported in Tab. 4.1.

Once these two crucial points are fixed, the work has just began, as crystal absorbers introduce various degrees of freedom in the detector's picture. Many of their characteristics, in fact, have a direct influence on both bolometric performance as well as the possibility for the experiment to reach a certain sensitivity. This is due to absorbers being the core of the detectors when using the bolometric technique: particle energy depositions inside the crystal are measured through its temperature rise, which means that, in experiments for 0ν-DBD search like CUORE, TeO_2 absorbers are both the source of the decay and the bulk of the bolometer. Therefore, speaking of an optimization process on TeO_2 crystals implies, in the framework of the CUORE-0 R&D, treating its impact on different aspects of the experiment. This a distinguishing point between the crystal absorbers and the other issues around which the presented optimization work revolves: as the previous chapter detailed, enhancing the cleaning of copper holders affects the final background level (Chapter 3); on the other hand, the next chapters will explain that the introduction of NTD thermistors with new geometry

Property	Value
Geometry	5×5×5 cm^3 cube
Mass	790 g
Density	6.04 g/cm^3
Melting point	733° C
Debye temperature	232 K
Linear thermal expansivities [T ∼2 K]	$\alpha_{\parallel}$=6×10^{-9} K^{-1} $\alpha_{\perp}$=-4×10^{-9} K^{-1}
Optical properties	Birefringent, optically active, highly transparent in the 350 nm-5μm range

Table 4.1: List of geometric, mechanical, optical and thermodynamic properties for the larger TeO_2 crystals used in the Cuoricino experiment [80], [109], [110].

must not lead to degradation in pulse height (Chapter 5), and that the standardization of sensor-to-absorber coupling can reduce observed variations in pulse shape among different detectors (Chapter 6). As far as TeO_2 crystals are concerned, their range of action on the experiment's outcome is wider. Their most sensitive characteristics will be commented on in the following list.

- *Heat capacity* makes paratellurite crystals particularly useful as absorbers in the field of bolometric detection. TeO_2 is a dielectric and diamagnetic material and its heat capacity is calculated using the Debye law ($C \sim T^3/T_D^3$), as mentioned in Sec. 2.1.1. Thanks to the relatively high value of its Debye temperature, which has been estimated in the cryogenic experimental range with a dedicated measurement [80], the heat capacity C_{abs} of a 5×5×5 cm^3 TeO_2 absorber is suitable for bolometric detection at low temperatures: its order of magnitude is ∼10^{-9} J/K at 10 mK. This allows large temperature variations following particle energy depositions, as well as good energy resolutions. Other factors, needless to say, can interfere with these two aspects of bolometric performance: the specific properties of NTD Ge thermistors can, for example, affect the pulse height of the acquired signals; and noise sources are the real limiting factors that deviate energy resolution from its theoretical value. Nonetheless, uniformity of heat capacity among the crystal absorbers which constitute the whole detector is the zero point for any optimization work. The search for acceptable homogeneity of C_{abs} among the ∼1000 bolometers that will constitute the CUORE set follows two paths. First of all, it is an issue of crystal growth in terms of both crystalline structure and material purity: the growth process of TeO_2 must be reliable and replicable enough to limit anomalies in the crystalline structure, which could lead to deviations of C_{abs} from the Debye law; the presence of contaminants should as well be avoided for a similar reason, because of possible non-dielectric contributions that interfere with the $C_{abs} \sim T^3$ behaviour and raise heat capacity. Also, homogeneity of heat capacities in the same batch of absorbers is a matter of tolerance on dimensions, due to the linear growth of C_{abs} with volume.

- *Crystal geometry* must be defined with very strict specifications. This regards the three aspects of dimensions, surface quality and crystallographic orientation. The fact that homogeneity of heat capacity among batches of TeO_2 crystals is affected by tolerance on dimensions has just been pointed out. Moreover, low tolerances

are demanded for assembly reasons. For example, the gluing line for thermistor-to-absorber coupling presented in Chapter 6 introduces automated glue dispensing and positioning of both crystals and sensors by means of a three-axis cartesian system and an antropomorphic robot: due to the small contact surface of sensors (2.77×2.84 mm^2 for Ge thermistors, 2.33×2.40 mm^2 for Si heaters), to their borderline positioning originated by electric connection requirements (4.5 mm from the center of each sensor to the side of the crystal) and to the precise geometry of the glue distribution (a matrix of dots with $\sim$0.8 mm diameter), it is mandatory that absorber geometry is replicated with high precision. The procedure demands restrains on the flatness of faces, as well. In addition to gluing issues, other requests on crystal geometry are introduced by a specific optimization work that goes beyond the discussion of this thesis, and that has been conducted on the mechanical support structure of the detector. Its aim was to gain higher control on microphonic noise: the redesign of copper frames and PTFE stand-offs requires the crystal's linear dimensions to be known with a precision within 1‰. In the same context, standards have been fixed on the crystallographic orientation of the absorbers inside the copper holders, due to the necessity of taking into account differential thermal contractions at cryogenic temperatures; conctractions change along different crystallographic axes [109] and, in particular, the thermal expansion coefficient of TeO_2 on a plane orthogonal to the [001] axis matches very closely that of Cu [111]: attention must be paid to how the assembled crystals are oriented if minimization of mechanical strains of thermal origin is looked for in the cooling process. The exposed requests are satisfied if the following characteristics are met by crystals after the production and processing phases: the linear dimensions of TeO_2 absorbers, which are cubes with 50 mm edges and 0.5 mm chamfers, must be defined with 0.05 mm precision; the average flatness of faces must be $<$0.01 mm; square faces must be oriented parallel to the crystallographic planes ([001], [110], [1-10]) within $\pm1^\circ$ [112].

- *Absorber radio-purity* has already been stressed as one of the major factors in determining the sensitivity of a bolometric experiment for 0ν-DBD search: the extent to which it limits the range of exploration of neutrino mass hierarchies has been evaluated in Sec. 2.3.1. It is critical for the detector to be free of any contaminant that can mimic or simulate the 0ν-DBD signal by producing an energy deposition near the 2.5 MeV $Q_{\beta\beta}$ value of ^{130}Te. The contamination may come from long-lived, naturally occurring isotopes, such as ^{238}U, ^{232}Th, ^{40}K and their daughters, and from cosmogenic activation of the detector materials after their production. In the case of TeO_2 crystals, it is a problem of both bulk and surface radioactivity. Among the possible dangers, the presence of ^{210}Pb and ^{210}Po contaminations, which are seen evidently in the Cuoricino spectrum, has already been discussed briefly in Sec. 3.1.1; another recurring bulk contamination is due to the long living isotope ^{190}Pt, which decays α with energy 3.3 MeV and comes from the growth process of crystals, as will be seen in Sec. 4.2. To minimize the influence of long-lived nuclei, great care must be devoted to the selection of not just the materials, but also the accessories used to prepare the detector; to limit the occurrence of cosmogenic activation, sea level transport and underground storage must be used whenever possible. A detailed monitoring of all materials, tools and facilities used for raw oxide synthesis and crystal growth is necessary. Moreover, possible surface contamination must be controlled with great care by a strict selection of consumables and equipment used for chemical processing, mechanical processing and packaging of grown crystals: the mechanisms connected to degraded α-particles due to surface contamination of the absorbers have already been described in Sec. 3.2. The analysis of Cuoricino together with the imposition of the range 10^{-2}-10^{-3} c/(keV·kg·y) as desired background goal for CUORE, help

Material	Category	Contamination limits
Metallic Te	Raw material	^{238}U$<2\times10^{-10}$ g/g ^{232}Th$<2\times10^{-10}$ g/g ^{210}Pb$<10^{-4}$ Bq/kg ^{40}K$<10^{-3}$ Bq/kg ^{60}Co$<10^{-5}$ Bq/kg
Materials for TeO_2 powder synthesis (water, acids)	Reagents	^{238}U$<2\times10^{-12}$ g/g ^{232}Th$<2\times10^{-12}$ g/g
Water	Consumable	^{238}U$<2\times10^{-12}$ g/g ^{232}Th$<2\times10^{-12}$ g/g
TeO_2 powder before crystal growth	Intermediate product	^{238}U$<2\times10^{-10}$ g/g ^{232}Th$<2\times10^{-10}$ g/g ^{210}Pb$<10^{-4}$ Bq/kg ^{40}K$<10^{-3}$ Bq/kg ^{60}Co$<4\times10^{-5}$ Bq/kg Pt$<10^{-7}$ g/g Bi$<10^{-8}$ g/g
Ready for assembly TeO_2 crystal	Final product	^{238}U$<3\times10^{-13}$ g/g ^{232}Th$<3\times10^{-13}$ g/g ^{210}Pb$<10^{-5}$ Bq/kg ^{60}Co$<10^{-6}$ Bq/kg
Crystal polishing (SiO_2 powder and textile pads)	Consumables	^{238}U$<4\times10^{-12}$ g/g ^{232}Th$<4\times10^{-12}$ g/g
Gloves, plastic bags, cleaning tissues, ...	Accessories	^{238}U$<4\times10^{-12}$ g/g ^{232}Th$<4\times10^{-12}$ g/g

Table 4.2: Limits on the concentration of radioactive contaminants for the materials involved in the stages of TeO_2 crystal production and processing [112].

to fix a limit on the concentrations of radioactive isotopes in the materials used for crystal production, processing and handling: the defined values are reported in Tab. 4.2 [112]. The experimental methodologies for radiopurity validation will be briefly dealt with in Sec. 4.3.

- Finally, *isotopic abundance* must be quoted for completeness, although no study on the subject of enrichment is included in the CUORE-0 aimed R&D. It should not be excluded in principle, however, because it could mark a possible path for future developments. Isotopic enrichment is not always technically possible and is an expensive procedure; moreover, Sec. 2.1.1 pointed out that ^{130}Te is naturally highly abundant. Nonetheless, Sec. 2.3 remarked the contribute of isotopic enrichment to the growth in sensitivity of a bolometric experiment for 0ν-DBD search. The

potentialities of CUORE would be expanded by integrating isotopically enriched absorbers. Even though no specific work has been done on this topic, a way to keep the door to enrichment open is to find different, competitive producers of TeO_2 crystals that could be able to pursue this path. For this reason, TeO_2 crystals coming from another company were investigated besides those of the provider for both Cuoricino and the R&D tests. Experimental observations on this subject will be reported in Sec. 4.4.

4.2 Production and processing of TeO_2 crystals

The TeO_2 crystals used in the Cuoricino experiment and in the R&D tests were produced by the Chinese company Shanghai Institute of Ceramics Chinese Academy of Sciences (SICCAS), which will also be the source for the CUORE-0 and CUORE absorbers. A neat difference will be traced between the protocol for the production of Cuoricino TeO_2 crystals and the one to obtain CUORE-0 and CUORE crystals: from now on, they will be called respectively *Cuoricino protocol* and *R&D protocol*. Before initiating a direct comparison between the two methods, an introduction on their general aspects will be given.

The production process is divided into two major phases, crystal synthesis and crystal polishing, which are then divided into several sub-processes. Bulk contamination is a risk in the crystal synthesis phase, while surface contamination is the main concern during crystal processing. The Cuoricino protocol and the R&D protocol have in common the main aspects of synthesis and polishing, although several fine tunings are introduced in the second procedure to obtain a final product in accordance with the requests exposed in the previous section.

Crystals are grown by the Bridgman method. The basic process consists in obtaining TeO_2 powders by mixing pure metallic Te in a solution of chloridric and nitric acid: the reaction precipitates the TeO_2 compound, which is separated from the solution by evaporation. The obtained powder and a TeO_2 crystal seed are put in a platinum crucible at $\sim$800° C, which is in turn placed in a Bridgman furnace. Crucibles are raised to a given height to melt the top of the seed, after which the system is kept still at fixed temperature to gain a stable solid-liquid interface; the growth process is driven by the slow lowering of the crucible (less than 1 mm/h) and by the raising of furnace temperature ($\sim$3°C/h). At the end of the growth process, furnaces are cooled down slowly to avoid cracks in the crystalline structure due to thermal stress.

Crystals are grown two times. As a matter of fact, the replication of the growth process is the key to obtaining high purity crystals for 0ν-DBD application, getting rid especially of the platinum content due to the inclusion of crucible fragments. That is, two successive growths are performed with two associated iterations of TeO_2 powder synthesis: the high purity TeO_2 powder used for the second growth is prepared by dissolving in chloridric acid pieces of selected crystalline regions obtained in the first growth. The selection of ingots is stricter in the R&D protocol (approximately $\sim$1/3 of the total mass) to reduce more effectively the impurity content. The end of the second growth process terminates the crystal synthesis phase.

In the second phase of TeO_2 crystal production, the raw crystal ingots undergo a rough mechanical processing (cutting, orienting and shaping) followed by the final surface treatment and vacuum packaging. Shape, dimensions and crystallographic orientation of faces are brought very close to their nominal values during the preliminary mechanical processing. After the growth, crystals are cut in cubes and X-ray oriented with a precision better than 1°: memory of the orientation is kept throughout the whole

subsequent clean room activity and final packaging.

Another difference between the Cuoricino and R&D protocols is the site for surface processing. The Cuoricino protocol requires that crystals are grown in China, while surface treatment is performed at LNGS: the procedure designed in Gran Sasso was successfully optimized and verified during several RAD tests, which have already been described in Sec. 3.1.2. On the other hand, the R&D protocol requires that both crystal synthesis and polishing are performed in China, by integrating in the SICCAS procedure the surface treatment optimized at LNGS. The aim is to gather all the production steps in a single place, reducing any further manipulation that could introduce surface contaminations; the ready-to-use final products are sealed and shipped from China, are stored underground and are unpacked only at the beginning of the assembly phase.

Independently from the processing site, both protocols require that, after orientation measurements are completed, crystals undergo dimension refining in a clean room: there, strict operational constraints are fixed to avoid any radio-contamination risk. Etching and face polishing are performed to reach with the required tolerances the right dimensions and planarity; at the same time, the first surface cleaning is performed. The number of atomic layers removed by the two steps of surface treatment was evaluated as $\sim 10^5$ for both etching and polishing, while an estimation for the targeted number of atomic layers to be removed is $\sim 10^4$ [112]: this allows to get rid of all impurity atoms that may have adsorbed on the crystal's face and further diffused in its bulk. Surface polishing is demanded not just for cleaning requests, but because it brings crystal dimensions as close as possible to the nominal values and it improves surface quality by removing possible extended defects induced by chemical etching.

This short summary accounts for the main production steps of TeO_2 crystal absorbers; the main deviations of the R&D protocol from the Cuoricino one have been mentioned: Tab. 4.3 lists the exact differences in the two procedures. However, other steps which are included in the R&D protocol have been omitted. For example, no details were given on how the strict requirements on radio-isotopes concentrations are met and verified. In fact, radio-pureness at the levels demanded by Tab. 4.2 is the main constraint, and at the same time the more difficult to meet. This is a specific problem of 0ν-DBD search: while the optical and mechanical characteristics of the TeO_2 crystals currently produced at industrial scale for acoustic-optical applications are good enough for CUORE, radio-purity within the desired limits is normally unavailable; nonetheless, this is the real distinguishing factor that defines crystal quality from the point of view of the 0ν-DBD hunter.

In the next section, details will be provided on the methods used to certificate the radio-purity of crystals, as well as of the materials involved in their production steps. More specifically, two cryogenic tests designed to validate the R&D protocol for crystal synthesis and surface treatment as the final choice for CUORE-0 and CUORE will be presented.

4.3 Testing the radio-purity of TeO_2 absorbers

The necessity for the various stages of the production process to undergo validation checks emerged in the previous section. In the same section, a neat difference in processing difficulty has also been mentioned between making crystals with required geometry standards and within radio-purity limits. The current industrial technologies for crystal production allow, in fact, to reach easily precisions like 1‰ on linear dimensions, 10 μm on surface flatness and 1° on crystallographic orientation; but the restrains on

Step	Cuoricino protocol	R&D protocol
Powder production	80°C dry-up (Raw Dried powder), 680°C calcination in Pt crucible (Raw Calcinated powder)	*Option A-* 80°C dry-up (RD), 680°C calcination in Pt crucible (RC) *Option B-* 600°C calcination without dry-up *Option C-* 240°C dry-up in PTFE (RD), 680°C calcination in Pt crucible (RC)
Crystal growth	First growth in Pt crucible with standard Bridgman technique; ingot selection, grinding, washing, drying; new calcination and second growth.	First growth in Pt crucible with standard Bridgman technique; stricter ingot selection (∼1/3), grinding, washing, drying; new calcination and second growth.
Surface treatment	*Basic (SICCAS)-* no radio-purity restrains: polishing with Al_2O_3 powder *Advanced (LNGS)-* strict radio-purity restrains: etching with ultra-pure HNO_3 4-molar: polishing with lapping pads and SiO_2 powder	At SICCAS, with strict radio-purity restrains. Ultra-sonic cleaning; polishing with highly radio-pure Al_2O_3 powder; etching with ultra-pure HNO_3 4-molar; polishing with SiO_2 powder and lapping pads.

Table 4.3: Comparison between the Cuoricino protocol and the R&D protocol for crystal growth and surface processing. In the framework of the R&D protocol study, three alternative options A, B and C for powder production have been tested.

the permitted concentrations of radioactive isotopes are specific to the limited 0ν-DBD application.

As already stated, radio-purity validation focused on the absorber should include controls on all materials involved with TeO_2 crystal production, at any stage. The list includes raw materials, reagents, intermediary products, consumables and equipment. Some steps are particularly relevant: the validation of crystal seeds, for example, which are used for many growth cycles. Four measurement techniques are used by CUORE collaborators for radio-purity certification.

Inductively Coupled Plasma Mass Spectrometry - An ICP-MS combines a high-temperature Inductively Coupled Plasma source with a Mass Spectrometer. The sample is typically introduced in the ICP plasma as an aerosol, either by aspirating a liquid or dissolved solid sample into a nebulizer or by converting directly solid samples to the aerosol form using a laser: after introduction, its elements are converted first into gaseous atoms and then ionized towards the end of the plasma. Ions are collimated into a beam by a system of electrostatic lenses and focused into the entrance of the mass spectrometer, where they are separated by their mass-to-charge ratio. The most commonly used type of mass spectrometer is the quadrupole mass filter. ICP-MS measurements were performed at LNGS on all raw materials and intermediary products; results were systematically cross-checked following the same measurement protocol on twin samples at the Shanghai Institute of Applied Physics (SINAP), in China, and at the Lawrence Berkeley National Laboratory (LBNL), in the USA. Each laboratory applied the same protocols for the preparation of samples; protocols are developed differently according to the nature of the sample in order to maximize sensitivity. High sensitivities ranging from the order of 10^{-12} to 10^{-9} g/g, depending on the measured contaminant, were obtained for the investigated radio-nuclides listed in Tab. 4.2; the only exception was the low 10^{-6} g/g sensitivity reached for ^{40}K, which was improved by means of the second certification technique.

Gamma spectroscopy with HPGe detectors - This technique allows to evaluate the concentration of contaminants in a given sample by direct measurement of the energy of γ-ray photons emitted by radio-nuclides as a consequence of their α or β-decays. HPGe measurements related to the production process of TeO_2 crystals took place at LNGS, were the sensitivity of measurements is enhanced by the reduced cosmic ray background due to the underground location. Sensitivities of the order of 10^{-10} were achieved on the U and Th chains in $\sim$2 kg samples, which are deemed sufficient for the certification of raw materials and consumables in the synthesis of TeO_2 crystals: although lower limits could be obtained by increasing measurement times, the choice was made to stick to response times of a few weeks in order to give prompt answers without delaying the schedule of crystal production.

Alpha spectroscopy with Surface Barrier Detectors (SBD) - The previous techniques, in the context of the CUORE R&D, are devoted to the radio-purity certification of raw materials, reagents, consumables and intermediate products that could be sources of bulk radioactivity in the final TeO_2 crystals. The very low level counting in the α-decay energy range reached by the SBDs used allows, instead, to check the possible introduction of surface contaminations in the final steps of crystal production: that is, cutting, etching, polishing and packaging. One should pay attention to surface contaminations from the ^{238}U and ^{232}Th chains, of whose presence α-decays are clear signatures. Measurements with SBDs were conducted at the Milano-Bicocca University environmental radioactivity laboratory.

Components were selected by first certifying their surface radio-purity and then by monitoring it continuously to guarantee stability in time.

Cryogenic tests - The validation of the final outcome, that is the measurement of ready-to-use crystals, can be performed only by means of cryogenic tests in an R&D setup where conditions close to those of the final experiment are met. Bolometers are assembled with the TeO_2 crystals under certification, and are mounted in R&D holders in a clean environment. Cryogenic tests are performed at LNGS and are aimed at checking both the radioactive contamination level of the final detector as well as the compatibility of bolometric performances with the values expected for CUORE-0 and CUORE. Particular attention is paid to the cleanliness of the assembly phase, so that no sources of further surface contaminations are introduced. Concentrating on the presence of internal and surface contaminations in the crystals means measuring α-peaks, which are signatures of possible ^{232}Th and ^{238}U radio-contaminants: a monochromatic α-peak is a sign of bulk contamination, whereas it is always accompanied by a degraded continuum in the characteristic marker of surface contaminations; other typical signs of a surface contamination that data analysis must evidence are an asymmetry in the α-peak and the presence of events with multiplicity two on facing crystals. This latter gives an estimation of the surface-to-bulk events in the peak. All these aspects have already been treated in Chapter 3, and are now only recalled. It should be reminded that, since the continuous background is the same above the 2615 keV ^{208}Tl line, the estimation of the counting rates in the ^{130}Te $Q_{\beta\beta}$ range can be extended to the wider region from 3 to 4 MeV, compensating thus for the long measurement times required when the background in the ROI ($\sim$100 keV wide) is to be evaluated at a good confidence level with a standard R&D detector tower of twelve bolometers. More details on this problem have been provided at the beginning of Sec. 3.4.2.

Two cryogenic tests were performed before finalizing the choice of the Chinese company SICCAS as producer of the TeO_2 crystals for CUORE-0 and CUORE. The runs were denominated *Chinese Crystal Tests* (CCTs) and their aim was to validate the R&D protocol as ultimate. Only one run was planned originally, but anomalies in the experimental results forced to review some aspects of crystal surface processing and re-validate the protocol with another dedicated test. Details on the performed tests are illustrated hereafter, in Sec. 4.3.1 and 4.3.2, proving the importance of final cryogenic certification for the radio-purity of bolometric elements.

Detectors of both tests are twelve-crystals tower arrays constituted by three floors with four bolometers each. The mounting is performed in a clean-room environment by using radio-purity certified tools and consumables. The tower model used is the design elaborated by the Crystal Assembly Working Group for the optimization of the sensitivity to noise [82]; the radio-purity of the copper holder at the levels obtained with the RAD detectors (Chapter 3) is guaranteed by the coverage with polyethylene layers of frames produced with the Electrical Discharge Machining (EDM) technique.

4.3.1 The first Chinese Crystals Test

The first Chinese Crystal Test (CCT1 from now on) was performed in Summer 2007 at LNGS. The detector was assembled and measured in the R&D facilities, the clean room in Hall A and the cryogenic apparatus in Hall C. The R&D protocol for crystal production, described in Sec. 4.2, is investigated by this experimental run. In order to draw reliable conclusions, the CCT1 was designed to be a comparative test between two sets of crystal absorbers.

1. Six TeO_2 crystals whose production and surface treatment follow the R&D protocol proposed as standard process for CUORE-0 and CUORE (see Sec. 4.2); the first set is divided in three subsets, named A, B and C according to the procedure followed for powder production, reported in Tab. 4.3.

2. Six TeO_2 crystals obtained with the Cuoricino protocol and already measured in previous background-oriented RAD tests at LNGS; the background level obtained by the RAD tests constitutes a benchmark that will be used for comparative purpose later on, in this same section.

The conditions necessary for protocol validation are two: both the bolometric performance and the background level of the newly produced crystals, in terms of bulk and surface contaminations, must be comparable with or better than the results obtained by the six reference crystals. Detector assembly was performed in radio-clean conditions and paying close attention to avoiding any possible sources of surface contamination. The absorbers of the first set are equipped with two Ge thermistors of the #31 series for redundancy, while absorbers belonging to the second set have one sensor each, as in the RAD tests. As explained at the begininning of this section, the bolometers were inserted in a three-floors tower system; crystals belonging to different sets are mounted in alternate positions inside the frames, so that effects due to hypothetical surface contaminations in one group can be disentangled. Fig. 4.1 shows a collection of pictures of the test. Apart from channel loss of four bolometers with absorbers of the second type, a few anomalies in the bolometric behaviour exhibited by the first set of crystals have been evident since the very beginning of data-taking.

The first part of the comparison between the two sets of crystals and old reference data regards bolometric performance in terms of pulse height, shape and energy resolution. The behaviour featured by the bolometers of the Cuoricino experiment is used, in this case, as a benchmark. Tab. 4.4 reports the values of the performance parameters obtained by the two sets of crystals (keeping in mind that four out of six bolometers of the second set cannot be used for the evaluation).

- Pulse height values in μV/MeV obtained by crystals produced with the R&D protocol are strikingly lower than expected; the behaviour is anomalous, considering also that the array is operated at a low base temperature (T_b=10.0$\pm$0.7 mK) comparable with the Cuoricino running conditions. An estimation of the average value of pulse heights for Cuoricino 5$\times$5$\times$5 cm^3 detectors is 167$\pm$99 μV/MeV (calculated from a three days calibration measurement in Run 2). Instead, in CCT1 it is 41$\pm$28 μV/MeV for crystals in the first set, while 204 μV/MeV and 564 μV/MeV are the values obtained by RAD-style crystals in the second set: these two values are definitely higher than those reached by the R&D crystals, keeping in mind the low statistics of the second set (66% of detectors lost). The assembly process, including thermistor gluing and mounting, is the same for all CCT1 bolometers and cannot be accounted for the worse results of the first set.

- FWHM energy resolutions obtained by absorbers in the first set are also worse than those obtained by the survived absorbers in the second set. The average ΔE of the large detectors in the Cuoricino experiment, computed from the same calibration measurement used for the aforementioned average pulse height, is 7.8$\pm$2.4 keV at the ^{208}Tl 2615 keV line; ΔE values for the CCT1 detectors in the second set, reported in Tab. 4.4, are compatible with this estimation. A peculiar anomaly regarding the pulse shape-energy resolution relationship is evidenced by data analysis. As in Cuoricino, the average pulses of each detector were fit by a double exponential in decay time and single exponential in rise time, with the second τ_d constant longer than the first one; signals read by thermistor 1 on crystal

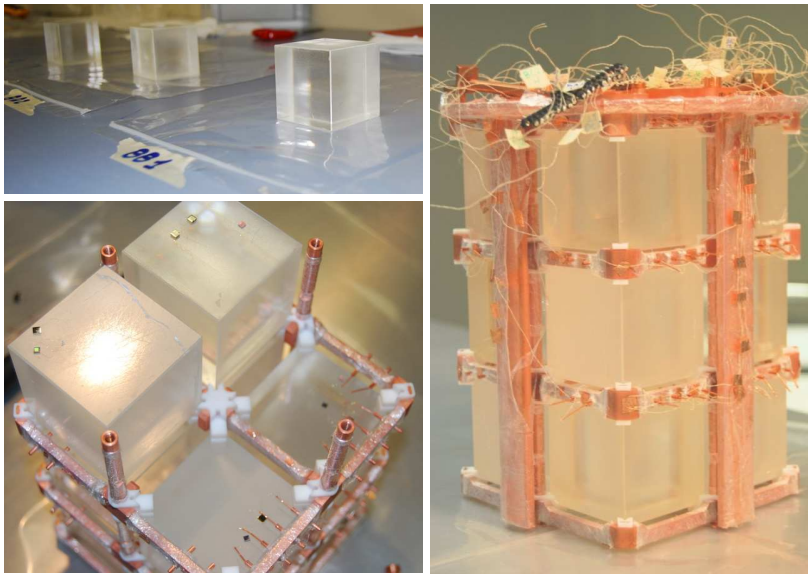

Figure 4.1: Collection of pictures of the first Chinese Crystals Test: from upper left, counterclockwise, the crystals produced with the R&D protocol, an intermediate stage of mounting, the final tower of bolometers.

Crystal	Set	Origin	Thermistor	R_b [MΩ]	T_b [mK]	A [μV/MeV]	ΔE [keV]
BC1	1	R&D protocol	1	246	10.9	13	14
BC1	1	R&D protocol	2	1410	9.2	93	17
BB2	1	R&D protocol	2	286	10.7	10	18
BB2	1	R&D protocol	1	563	10.0	25	40
BA1	1	R&D protocol	2	607	10.0	35	23
BA1	1	R&D protocol	1	615	10.0	46	21
BA2	1	R&D protocol	1	1600	9.1	99	26
BA2	1	R&D protocol	2	404	10.4	30	49
BB1	1	R&D protocol	2	535	10.1	42	39
BB1	1	R&D protocol	1	851	9.6	49	35
BC2	1	R&D protocol	1	258	10.9	31	32
BC2	1	R&D protocol	2	200	11.2	19	58
B64	2	ex RAD	Single	843	9.7	204	8
B68	2	ex RAD	Single	2538	8.7	564	7

Table 4.4: Bolometric performances of the CCT1 detectors. No measurements are given for four detectors in the second set, due to electric disconnection of thermistors or heaters in the cool-down phase. Energy resolutions are calculated at 2615 keV. Temperatures are computed by taking as VRH parameters for all the thermistors the values R_0=0.92 Ω and T_0=4.11 K, according to the assumptions made in Sec. 2.1.6.

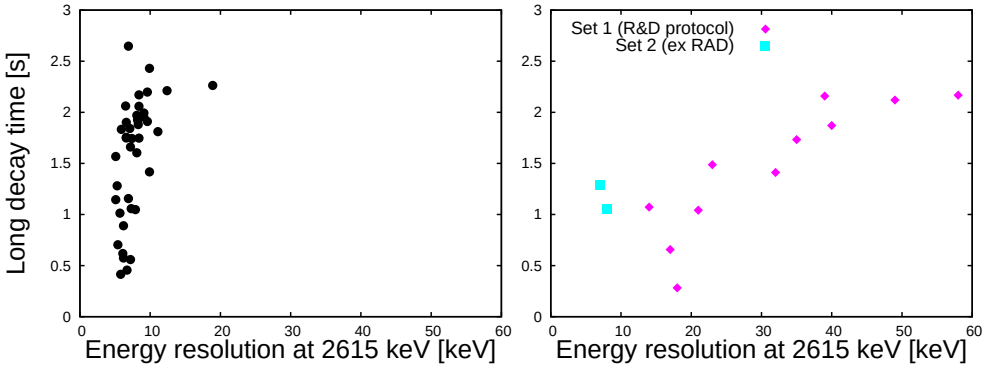

Figure 4.2: Behaviour of long τ_d in function of FWHM ΔE for detectors (a) in the Cuoricino experiment and (b) in CCT1. Values for the Cuoricino experiment are taken from a three days ^{232}Th calibration in Run 2: one Cuoricino detector with long τ_d=8.5 s and ΔE=7.1 keV is not plotted, for a clearer comparison with CCT1 data in the same decay time-energy resolution window. CCT1 bolometers in graph (b) are distinguished according to the set they belong to.

BA2 are not fit by this model, suggesting that more decay constants are at play: an anomalous thermistor behaviour seems to originate this deviation, though, as thermistor 2 on BA2 is coherent with the two-τ_d dependence. In a rough estimation, the average value for the ratio of the two decay constants featured by the first set of crystals is 7$\pm$4%, which is compatible with values seen in the Cuoricino experiment; however, data analysis suggests a correlation between longer decay constants and higher energy resolutions that has not been observed in Cuoricino. This is reported in Fig. 4.2.

The second part of the comparison between the two sets of crystals regards background analysis. In this case, results from two RAD tests combined (RAD 3 and 4, see Sec. 3.1.2) are used as reference data set. Fig. 4.3 shows the superimposition of three sum energy spectra in the range from 2.7 to 8 MeV, cut out of all the events with multiplicity higher than one: the spectra of the reference RAD tests combined, the spectra of crystals produced with the R&D protocol and the spectra of crystals obtained with the Cuoricino protocol. Note that the analysis of CCT1 is affected by low statistics, $\sim$330 hours for each bolometer, since data-taking was stopped soon as a consequence of the low bolometric performances.

- First, there is an excess of counts on the right side of the 2615 keV peak that apparently is not correlated, however, to radio-contamination issues: both first set and second set crystals share a high value of the integral in the 2.7-3.2 MeV range (0.30$\pm$0.06 c/(keV·kg·y) for first type crystals, 0.30$\pm$0.10 c/(keV·kg·y) for second type crystals). Although the question is still unanswered, there are hints about the exceeding counts being linked to a variation of calibration in time.

- Reliable considerations regarding the 3.2-3.4 MeV energy range are prevented by the low statistics. This is the range of the ^{190}Pt α-emitter, which produces a 3.25 MeV line with half-life $T_{1/2}$=6.5$\times$10^{11} years. The platinum contamination detected in the absorbers of the Cuoricino experiment was introduced by the growth crucibles. As for the first set in CCT1, no appreciable improvement is observed in this area of the spectrum; in addition to that, no conclusions can be drawn about differences in ^{190}Pt content among crystals grown from the different powder productions A, B and C.

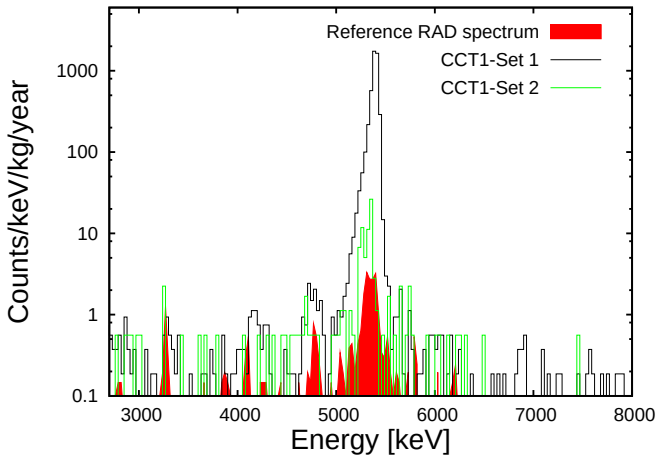

Figure 4.3: Sum energy spectra with single events in the 2.7 to 8 MeV range of the two sets of crystals in CCT1; a previous RAD reference spectrum (eight crystals for a total measurement time of 1893 hours) is reported as a background reference. Binning is 30 keV.

- Moving on to the 4-5 MeV energy range, the rate is higher than the reference RAD data sets, although compatible with Cuoricino results: the structure of peaks in this part of the spectrum, although not clear, seems correlated to a ^{238}U contamination; nonetheless, the poor statistics on multiplicity 2 events prevents from discriminating between bulk or surface origin.
- Finally, higher ^{210}Po peaks, compared to RAD results, are present in the 5-6 MeV energy range of CCT1 crystals's spectra: this is expected because the RAD bolometers used as reference data have absorbers dating back to the Cuoricino batch, while the two sets of CCT1 crystals were grown more recently (^{210}Po has $\sim$138 days half-life).

The previous lists can be summed up by saying that no appreciable improvements in the background are seen as a consequence of the application of the designed R&D protocol to crystal processing; moreover, the gathered statistics is not sufficient for a quality check among the three powder productions A, B and C; the most dangerous behaviour exhibited by newly produced crystals in the first set regards pulse height and energy resolution: the average values observed are unacceptable, in view of the CUORE goal. Two reasons were identified as possible origins of the featured behaviour. The first hypothesis regards the introduction, during the growth process, of oxygen vacancies in the structure of crystals belonging to the first set: a change in heat capacity, leading to lower pulse heights, would then be explained. On the other hand, the second hypothesis relies on an inadequate surface processing: the lapping pad used by SICCAS in the polishing stage was different than the one used in the RAD LNGS treatment, and a consequence would be the insufficient removal of the acid/H_2O layer left on the surfaces by the etching bath; in this case, worse performances would derive from a change in the conditions of crystal surfaces. Therefore, the first interpretation is a bulk problem, while the second one is a surface problem. Both interpretations are supported by experimental results and by the observation of crystals produced with the R&D protocol, which are yellowish in colour, whereas crystals processed with the Cuoricino protocol are white. The yellowish colour could be originated either by different crystal structure, either by surface residuals of the Chinese lapping pad.

Immediate action was taken to verify the credibility of the two hypothesis. To check the first interpretation, four new crystals were ordered from SICCAS requiring to use the

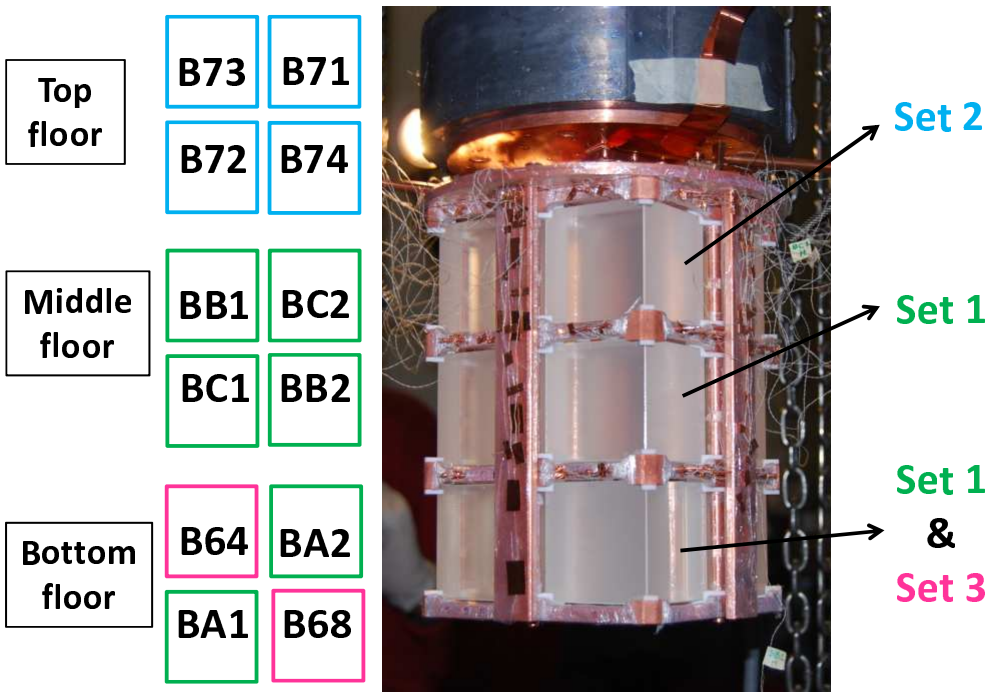

Figure 4.4: Scheme and pictures of the detector in the second Chinese Crystals Test: the detector is attached at the cold finger of the dilution refrigerator, waiting for read-out wires to be connected.

exact Cuoricino protocol; to check the second interpretation, the six crystals produced with the R&D protocol were reprocessed with the standard RAD surface treatment at LNGS. All crystals were then used, along with a few reference samples, in an urgent dedicated test.

4.3.2 The second Chinese Crystals Test

The Second Chinese Crystal Test (CCT2) was assembled and measured in Winter 2007, as an immediate action to gain better understanding of the CCT1 results. As anticipated in the final part of the previous section, three sets of crystals were used as bolometric energy absorbers.

1. Six TeO_2 crystals tested in CCT1, produced at SICCAS with the R&D protocol but reprocessed at LNGS with the standard RAD surface treatment.
2. Four new TeO_2 crystals produced at SICCAS entirely with the Cuoricino protocol.
3. The two TeO_2 crystals used in previous RAD tests and measured in CCT1.

Crystals in the first set are provided with two Ge thermistors of the #31 series each; crystals in the third set are provided with one sensor of the same kind; as for crystals in the second set, they will be considered as equipped with just one Ge thermistor even though a pair is attached to each of them: the reason for such omission is that one sensor in each pair has geometry and doping that differ from usual Cuoricino thermistors, with consequent deviations from the standard behaviour. The topic of thermistors with innovative contact geometry will be discussed in Chapter 5, and results of CCT2 in this matter will be presented in Sec. 5.4.3. The bolometers were assembled at LNGS in a

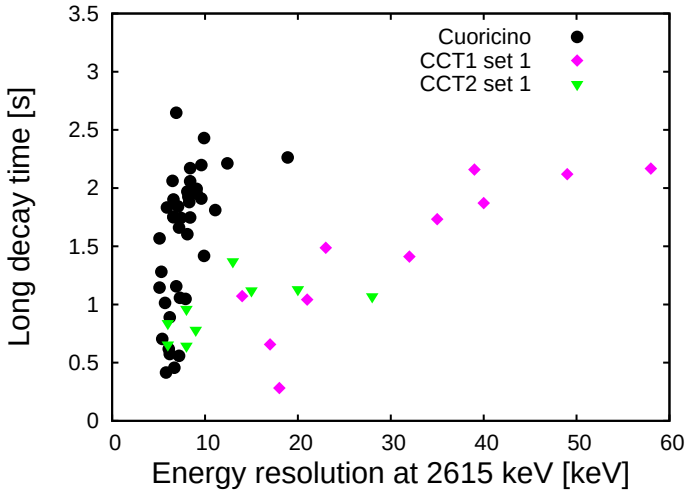

Figure 4.5: Behaviour of long τ_d in function of FWHM ΔE for three sets of detectors: set 1 in CCT1 (crystals produced with the R&D protocol); set 1 in CCT2 (the same R&D crystals after surface reprocessing); detectors in the Cuoricino experiment. Values for the Cuoricino experiment are taken from a three days ^{232}Th calibration in Run 2 and one Cuoricino detector with long τ_d=8.5 s, ΔE=7.1 keV is omitted for convenience.

clean environment with radio-purity restrains and were mounted in the same holder used for CCT1 (copper frames covered by polyethylene layers). The twelve-crystals tower was cooled down in the Hall C cryogenic facility; a few contacts were lost, but thanks to double thermistoring all the bolometers were measured. Fig. 4.4 reports a scheme and pictures of the detector. As done in Sec. 4.3.1, bolometers will be compared in terms first of pulse height and energy resolution performances, then of radioactive background in the energy region of interest.

Once again, the set of reference for bolometric performances is constituted by the results of Cuoricino bolometers. Tab 4.5 reports the values of the performance parameters obtained by the three sets of crystals. The average base temperature, computed on all bolometers, is T_b=12.5$\pm$1.3 mK, which is slightly higher than the 10.0$\pm$0.7 mK of CCT1.

- Average pulse heights of all sets are compatible with Cuoricino results. The average heights are 98$\pm$53 μV/MeV for the first set, 97$\pm$69 μV/MeV for the second set and 207$\pm$155 μV/MeV for the third set (167$\pm$99 μV/MeV is the reference value obtained from Cuoricino analysis already mentioned in Sec. 4.3.1).
- Energy resolutions of all sets are compatible with Cuoricino results. The set of reprocessed crystals shows reduced energy resolutions in respect to the CCT1 results. Average pulses can once again be fit with a double exponential in decay time, with τ_{d2} longer than τ_{d1}: long decay times are plot in function of energy resolutions in Fig. 4.5. The comparison with the CCT1 results obtained by the same crystals before surface reprocessing indicates that no hints at the dependency of τ_d on ΔE are now present.

As for background results, the statistics collected ($\sim$1044 hours for crystal, approximately three times the live time of CCT1) helps drawing conclusions on ^{210}Po contaminations and on the energy range between 4 and 5 MeV, where peak structures due to ^{238}U and ^{232}Th contaminations should appear. Fig. 4.6 shows the superimposition of three sum energy spectra: the one of crystals grown with the R&D procedure and

Set	Crystal	Thermistor	R_b [MΩ]	T_b [mK]	A [μV/MeV]	ΔE [keV]
Set 1	BA1	1	25	14.0	46	20
(R&D	BA1	2	29	13.8	69	15
protocol	BA2	2	138	11.6	193	9
reprocessed)	BB1	2	112	11.9	85	6
	BB2	1	56	12.8	152	8
	BC1	1	97	12.0	93	28
	BC1	2	15	14.9	21	13
	BC2	1	76	12.4	94	8
	BC2	2	57	12.8	131	6
Set 2	B71	Single	34	13.4	57	7
(New with	B72	Single	308	10.7	200	–
Cuoricino	B73	Single	37	13.3	67	7
protocol)	B74	Single	58	12.6	64	–
Set 3	B64	Single	186	11.2	97	7
(Ex RAD)	B68	Single	418	10.3	316	7

Table 4.5: Bolometric performances of the CCT2 detectors. Note that, in the compute of temperatures, the values R_0 and T_0 of series #34 (1.20 Ω and 3.95 K) were used for the thermistors on crystals B71, B73 and B74, instead of the values considered in this thesis for series #31 (0.92 Ω and 4.11 K): more details and an explanation will be given in sections 5.2.2 and 5.4.3. FWHM ΔE are given at the 2615 keV ^{208}Tl peak, except for bolometers B72 and B74, whose data acquisition was suppressed due to a huge polonium rate.

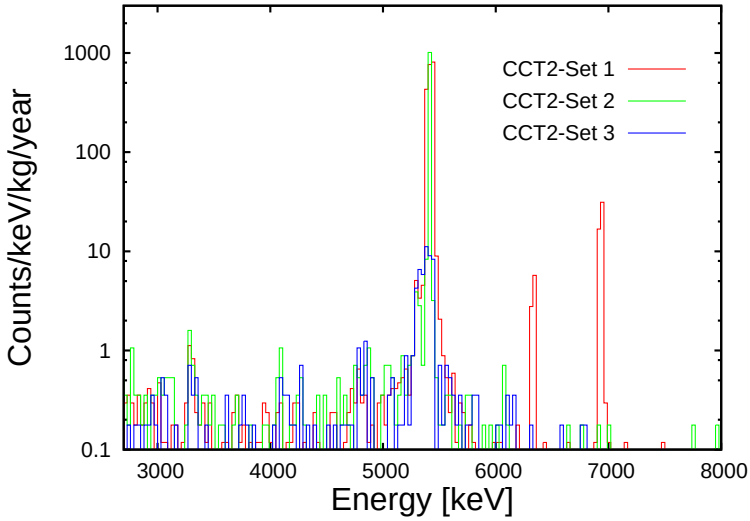

Figure 4.6: Sum energy spectra with single events in the 2.7 to 8 MeV range of the three sets of crystals in CCT2: set 1 collects the six R&D crystals reprocessed; set 2, the two crystals of new production with low polonium; set 3, the two crystals of the ex-RAD reference dataset. Binning is 30 keV.

mechanically reprocessed at LNGS (set 1), the one of crystals grown and treated with the Cuoricino protocol (set 2) and the reference data set of two RAD tests combined (RAD 3 and 4). For more clarity, two graphs comparing the counts normalized for keV, kg and year in the energy ranges of interest are reported: all three sets of crystals in CCT2 are shown in Fig. 4.7; in Fig. 4.8, CCT1 data from the crystals produced with the R&D protocol is overlaid on their results in CCT2 obtained after surface reprocessing.

- An excess of counts is still measured in the 2.7-3.2 MeV energy region, which confirms CCT1 data. The changes in detector composition from CCT1 to CCT2 (four crystals substituted, six crystals reprocessed, new location of bolometers in the holder, and so on) suggest that the excess counts have nothing to do with the crystals: they are unaffected by crystal treatment and are observed also in the spectra of the old, RAD style bolometers B64 and B68. Appearently, bolometers B71 and B73 of set 2 count more than the other ones in this region, even though the observation cannot be confirmed due to a large spread in counting rates. No answer can be given about the origin of such excess: the statistics is too low for this; moreover, problems in the detectors, such as the spread in the position of heater peaks among the bolometers (Chapter 6 will deal with the issue) further complicate the analysis.

- The analysis of the 3.2-3.4 MeV range shows that the bulk contamination in ^{190}Pt is compatible with the average contamination measured in the Cuoricino experiment for both crystals processed with the R&D protocol and crystals processed with the Cuoricino protocol. Slight differences in such contamination are possible but are not easy to be measured due to the continuum which underlies the peak.

- Looking at the 4-5 MeV energy range, the ^{238}U and ^{232}Th peak region, the RAD-style surface reprocessing performed on crystals grown with the R&D protocol results in a lower counting rate. Bulk contaminations in TeO_2 crystals of both set 1 and set 2 are not observed. Considering the low statistics, limits on such contaminations are computed which are compatible, given the current sensitivity, with the Cuoricino ones.

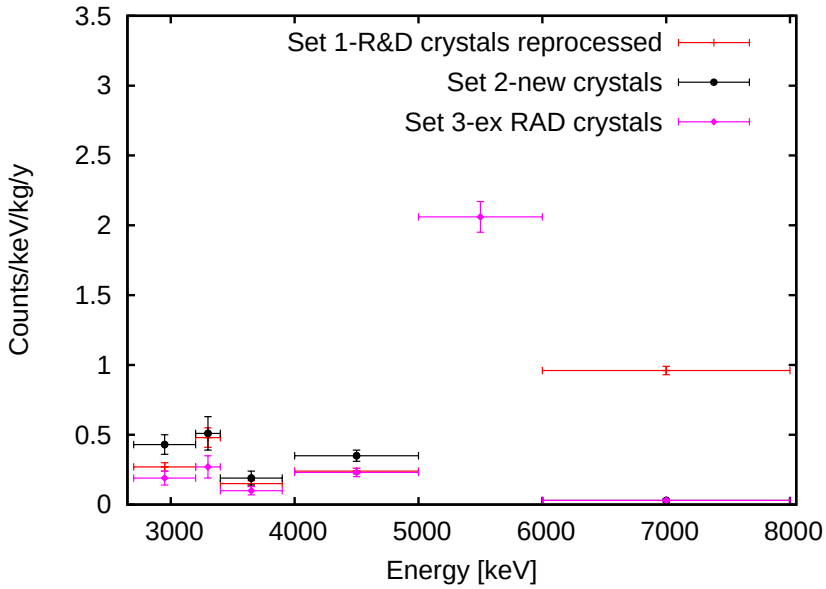

Figure 4.7: Comparison of the counts seen in the energy ranges of interest by the three sets of crystals in CCT2. The horizontal bar in each marker indicates the integration area for the counts, while the vertical bar is the error. Counts of sets 1 and 2 in the 5-6 MeV energy window are outside the y-range: they are 76.80±0.37 c/(keV·kg·y) for the first set and 39.70±0.46 c/(keV·kg·y) for the second set. Note that bolometers B72 and B74 are omitted and excluded from set 2 because of their large polonium contamination (see text).

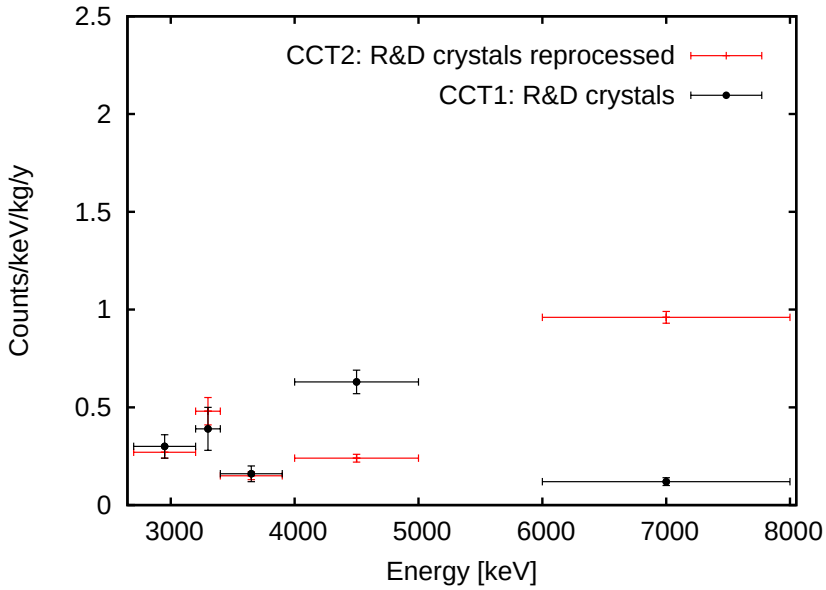

Figure 4.8: Comparison of the counts seen in the energy ranges of interest by crystals produced with the R&D protocol in CCT1 and in CCT2, after surface reprocessing. The horizontal bar in each marker indicates the integration area for the counts, while the vertical bar is the error. Counts in the 5-6 MeV energy window are outside the y-range: they are 142.00±0.89 c/(keV·kg·y) in CCT1 and 76.80±0.37 c/(keV·kg·y) in CCT2.

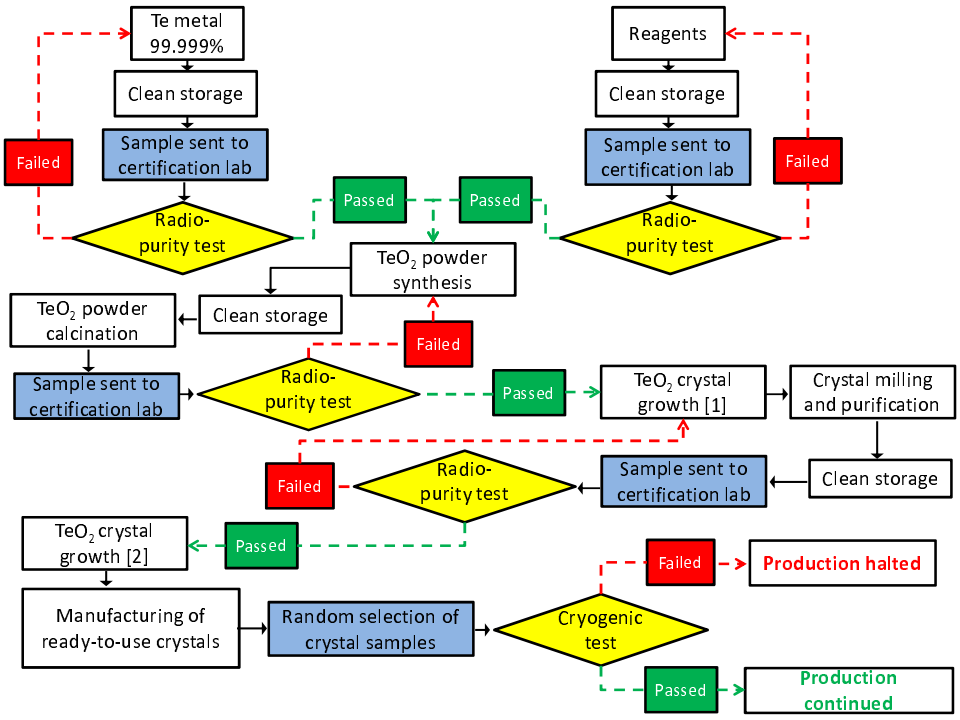

Figure 4.9: Scheme of the final validation protocol for the growth and treatment of TeO_2 crystals. For a detailed review, see [112].

- Two crystals of the second set (B72 and B74) show a very high polonium rate corresponding to the monochromatic peak at 5.4 MeV: the rates are ∼1000 and 2000 c/h respectively; for comparison, the other two crystals of the same set have rates of 3.4 c/h (B71) and 3.6 c/h (B73). Data analysis shows, for one of these crystals, a rate of polonium pulses that decreases in time quite in good accordance with the half life of ^{210}Po. There is no evidence for ^{210}Bi presence, which seems to confirm that the contamination should be ascribed to ^{210}Po and not to ^{210}Pb. The study of coincidences between B72, B74 and the crystals facing them indicates a bulk origin.
- The excess of counts seen by the R&D reprocessed crystals of the first set in the 6-8 energy range should not worry, as it is due to residual heater pulses which have not been flagged in the analysis.

Although some points in the analysis of the background are yet to be cleared, as for example the high counting rates in the 2.7-3.2 MeV range, the presented data supports the R&D protocol as a reliable way to grow and process TeO_2 crystals in view of CUORE-0 and of the final CUORE experiment. Moreover, the comparison between CCT1 and CCT2 stresses the importance of a well-defined and replicable procedure for mechanical surface processing, not just for background reasons but also because of an observed influence of surface quality on average pulse heights, shapes and energy resolutions.

4.3.3 The ultimate production protocol

The results presented in sections 4.3.1 and 4.3.2 played a fundamental role in defining the detailed dedicated protocol for the radio-purity related quality control of the crystal

production process, from metallic tellurium synthesis to the final processing of ready-to-use TeO_2 crystals. The ultimate choice for the CUORE-0 and CUORE applications is the R&D protocol presented in Tab. 4.3. The runs CCT1 and CCT2 did not evidence differences in radio-purity or performance among crystals grown from powders produced with the A, B or C method: therefore, the powder synthesis process already used for Cuoricino crystals is applied to new productions. The entire process of crystal growth and treatment is subjected to a complex validation protocol, which includes radio-purity certification procedures in each production phase and immediate actions to be taken in case of failure. Whenever problems arise, crystal production is halted until a solution is found. Fig. 4.9 shows a scheme of the validation protocol for the growth and treatment of TeO_2 crystals. Moreover, a bolometric validation run is foreseen for every batch of products sent by SICCAS to LNGS: four crystals are chosen randomly from each batch, certified in a cryogenic test and discarded as final CUORE-0 and CUORE absorbers. The production of the required one-thousand crystals started in 2008, and up to this date (Summer 2010) four validation runs have already been completed.

4.4 An investigation on crystal producers

Up to this point, Chapter 4 has dealt with the characteristics of TeO_2 crystals produced by the chinese company SICCAS, which has been selected as ultimate source for absorbers in CUORE-0 and CUORE. However, the end of Sec. 4.1 hinted at the advantage of investigating alternative crystal producers despite the selection already made. The possibility of a choice among different reliable crystal sources would impact on future developments of the CUORE experiment. In a time range of five years from now and in a picture where 0ν-DBD is still searched for with the application of the bolometric technique developed by CUORE collaborators, two aspects connected to the characteristics of energy absorbers could enhance dramatically the sensitivity of the experiment: isotopic enrichment, which would increase the abundance of ^{130}Te without enlarging the global detector mass; and the doping of TeO_2 in order to stimulate a scintillation light emission, which is an appealing path for future developments of 0ν-DBD search. Good crystal providers who offer energy absorbers conform to CUORE requirements on geometry and radio-purity could not easily have the capability to pursue isotopic enrichment or paratellurite doping. A way to keep the door open to these foreseeable future paths is to find producers with the previous technological abilities; the necessary requirement is that the base product demanded, the TeO_2 crystal described until now, has geometric and radioactive properties comparable with or better than those of the selected SICCAS absorbers.

The alternative producer investigated is the US company Chrystal Technology Incorporated (CTI). Crystals are grown with the Czochralski system instead of the Bridgman, applied by SICCAS, and this could decrease the observed ^{190}Pt content due to the absence of platinum crucibles [113], [114]; the synthesized TeO_2 powder for growth comes from another company, the General Western Inorganic (GWI).

The first investigation on the radio-purity of CTI crystals was performed at LNGS by means of a cryogenic test in 2006. Four TeO_2 crystals were cooled down in a twelve-bolometers array including other eight SICCAS products. Results were discouraging because of the detection of a huge ^{210}Po bulk contamination in the three readable absorbers survived to cool-down; also, a ^{232}Th contamination slightly higher than the reference RAD value was found. The comparison of counting rates is reported in Tab. 4.6: although numbers are only indicative due to the high pile-up rate, which prevents from precise quantifications, the ratio of CTI-to-SICCAS counting rates at the 5.4 MeV peak is easily estimated as ranging from the order of magnitude of $\sim 10^2$ to $\sim 10^3$. Moreover,

Contamination	Counting rates [c/h]			
	CTI 1	CTI 2	CTI 3	RAD reference
^{210}Po	500	90	80	0.4
^{232}Th	$(40\pm10)\times10^{-4}$			$(19\pm5)\times10^{-4}$

Table 4.6: Contaminations of the CTI crystals. The 5.4 MeV energy and ^{232}Th bulk contaminations are compared to the RAD mean values.

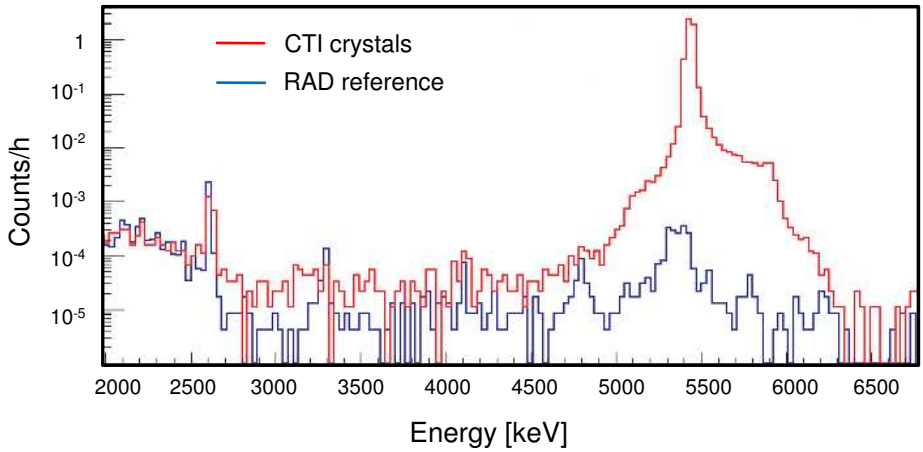

Figure 4.10: Comparison between the radioactive background spectra obtained with CTI crystals and the one measured with SICCAS crystals in the reference RAD 3 and 4 tests combined.

Fig 4.10 overlays the sum energy spectra of the three CTI crystals on the reference spectra of the two RAD tests combined, used in Sec. 4.3: again, the distortion in shape of the ^{210}Po peak at 5.4 MeV can be attributed to the presence of pile-up induced by the high counting rates.

The high polonium contamination observed led to further questions on its source. Two hypothesis are compatible with the results: the contamination enters the system during the growth process; or, it is already present in the TeO_2 powder itself. In the first case, the crystal growth procedure should undergo a thorough radio-purity validation process; in the second case, a quality check on the synthesis of TeO_2 powder, or even a change in the powder supplier are advisable. Another notable point is the gap in polonium counting rates between the crystal CTI 1 and the other two. No explanation has been given yet because there are no available details on differences in their growths; the only known information is that CTI 1 was produced first in the set. A dedicated cryogenic test was designed with the purpose of disentangling the origin of the ^{210}Po contamination. Its description and a short summary of its analysis will be presented in the next section.

4.4.1 Sources of TeO_2 crystals: a dedicated test

The test to trace the origin of contaminations in CTI TeO_2 crystals grown from GWI powders was performed in Summer 2008 at the Cryogenics Laboratory in Como. The experimental run was realized in close cooperation with the CUORE collaboration group based at the Lawrence Livermore National Laboratory (LLNL). Due to the aboveground

location of the testing facility and the consequent high counting rate induced by cosmic rays, no Cuoricino-size $5\times5\times5$ cm^3 crystals could be tested; the size of the crystal samples had to be reduced and the $1\times1\times1$ cm^3 volume was chosen. This led to two consequences: apposite crystal samples on small scale were prepared and processed with the same mechanical surface treatment fixed by the CUORE-0 R&D work; and a dedicated copper holder had to be designed, due to the different thermal parameters of the small-size absorbers in respect to the large ones.

Twelve small crystal samples with the aforementioned dimensions were assembled in bolometers, cooled down and measured; the samples are divided in three four-crystals groups according to their composition and growth.

Group 1 [SS]- Grown at SICCAS from TeO_2 powder synthesized by SICCAS itself: the SS samples are the small-size equivalent of the future CUORE-0 and CUORE energy absorbers.

Group 2 [CS]- Grown at CTI from TeO_2 powder synthesized by SICCAS: this batch is designed to test the introduction of ^{210}Po contaminants during the growth process.

Group 3 [CG]- Grown at CTI from TeO_2 powder synthesized by GWI: the CG samples are the small-size equivalent of the crystals tested at LNGS in 2006; the measurement of this batch, only if combined with data obtained from the other two sets, would give information on a possible contamination in the powder, that is at the roots of the crystal production process.

The twelve crystals were all etched and polished at LNGS, following the surface treatment protocol defined and already presented in Sec. 4.2; all the other steps of the experimental run, from holder testing to detector assembly, from cryogenic measurements to data-taking, were performed in Como. As for the experimental setup, an apposite Cu holding structure was designed in Como. The holder was designed as a small tower with two horizontal copper plates large enough to host a 2×3 matrix of samples each; crystals are glued directly by epoxy on small Cu stand-offs integrated on the plates and with 3 mm^2 top surface area. The use of glue was deemed an acceptable way to couple the absorbers to the holder; as a matter of fact, due to the small size of the samples, the PTFE coupling used in the Cuoricino and CUORE R&D cases is difficult to apply. A thermal model of the bolometers used in this thesis work has been described in Sec. 1.4: in the model, the factor that determines the thermal conductance of the PTFE holders is their contact area with the TeO_2 crystal, which is $\sim$150 mm^2 in Cuoricino; by scaling the contact factor in accordance with the reduced total surface of the samples, and considering both the difference in material (glue vs. PTFE) and the higher base temperature reached by the Como cryostat in respect to the Cuoricino one [81], the crystal-to-holder connection was realized with a single epoxy dot of $\sim$0.8 mm diameter and 50 μm height. A cryogenic test preliminary to the official cool-down was performed at 4 K to verify the mechanical integrity of glue couplings between TeO_2 and Cu and to decide the crystallographic orientation of the crystals, due to the change in thermal contractions depending on the axis [109]: the final choice was to couple the crystals by contact on the hard faces. The assembly was performed in a class 10000 clean room, following the handling protocol defined during the R&D of CUORE to avoid the introduction of further surface contaminations in the setup; as in the RAD tests, the copper surfaces facing TeO_2 were wrapped with more layers of polyethylene foil. Each bolometer was equipped with a Ge thermistor with both dimensions ($3\times1\times0.6$ mm^3) and doping different from the standard #31 series Cuoricino sensors: the values R_0=6.24 Ω, T_0=3.11 K were used for temperature computation in this case. A collection of pictures

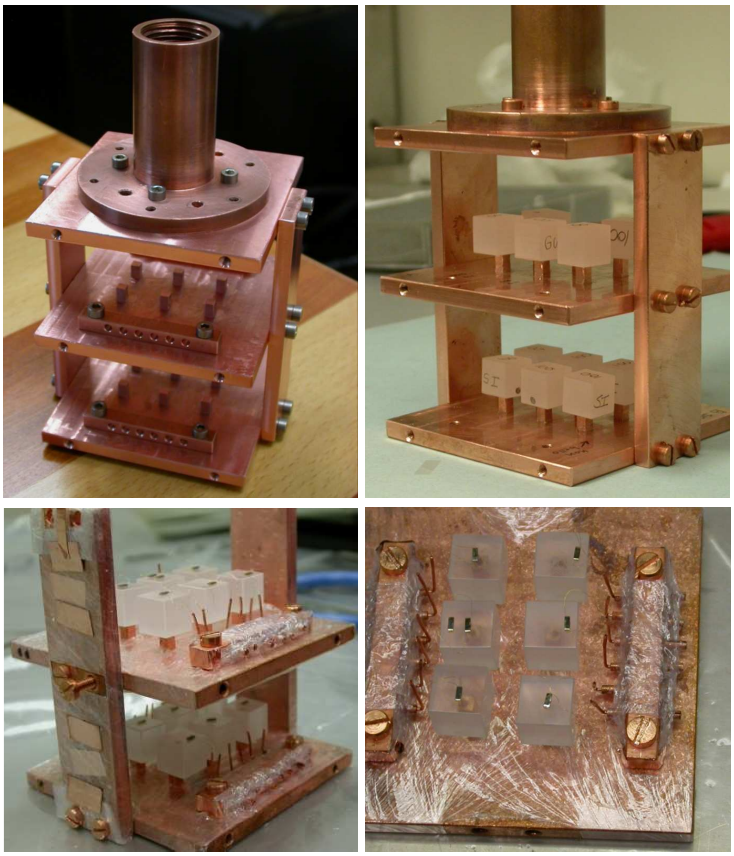

Figure 4.11: Pictures of the detector used in the test on small-size CTI crystals to trace the origin of ^{210}Po contaminations. From upper left, counterclockwise: the Cu holder before detector assembly, with the screw for connection to the dilution refrigerator's cold finger; the setup for the 4 K preliminary test; the small samples glued on the copper stand-offs; the detector before outer shielding coverage.

of the assembled detector is presented in Fig. 4.11.

The detector was cooled down in the L-He free dilution refrigerator in Como and brought to a base temperature whose mean value, calculated on the whole set of bolometers, is T_b=18.7$\pm$0.8 mK; data concerning the bolometric performances of the samples is listed in Tab. 4.7. Due to the limited number of available electronic and DAQ channels, the overall measurement was divided in the two subsets Run 1 and Run 2, with six bolometers acquired in the course of each. A scheme of the position of the crystals in the two-floors detector is shown in Fig. 4.12, together with information on their acquisition run. The total hours of measurement collected are, given the different duration of the two runs, 1820 h for the SS samples, 1932 h for the CS samples and 2047 h for the CG samples: the test is up to now (Summer 2010) the longest cryogenic run ever mantained in the L-He free refrigerator at the Cryogenics Laboratory in Como.

The behaviour of these bolometers in terms of pulse height A and shape can be considered quite homogeneous, although slight differences arise in A, τ_d and τ_r which can be ascribed to a lack of reproducibility in the thermal coupling realized by TeO_2 gluing on copper. The mean values for A are 48$\pm$8 μV/MeV for the SS group, 47$\pm$15 μV/MeV for the CS group and 39$\pm$11 μV/MeV for the CG group; on the other hand, the variation in pulse shape parameters can be observed in a direct comparison of average

Bolometer	R_b [MΩ]	T_b [mK]	V_{bol} [mV]	R_w [kΩ]	A [μV/MeV]
SS1	3.2	18.0	8.9	712	42
SS2	2.2	19.1	6.4	513	56
SS3	2.7	18.5	7.2	583	40
SS4	1.9	19.5	5.8	469	53
CS1	2.5	18.7	7.4	598	37
CS2	1.6	20.1	4.9	390	43
CS3	4.7	17.0	12.8	1029	38
CS4	2.5	18.7	7.0	559	68
CG2	2.8	18.4	7.7	617	43
CG3	2.9	18.3	7.8	630	45
CG4	2.6	18.6	7.3	582	23
CG5	2.2	19.0	6.2	499	45

Table 4.7: Bolometric performances of the bolometers in the test on small-size CTI crystals. Values are reported for the base resistance R_b, the base temperature T_b, the work point V_{bol} (which is the voltage at the terminals of the thermistor), the resistance in the work point R_w, the height of pulses A in μV/MeV.

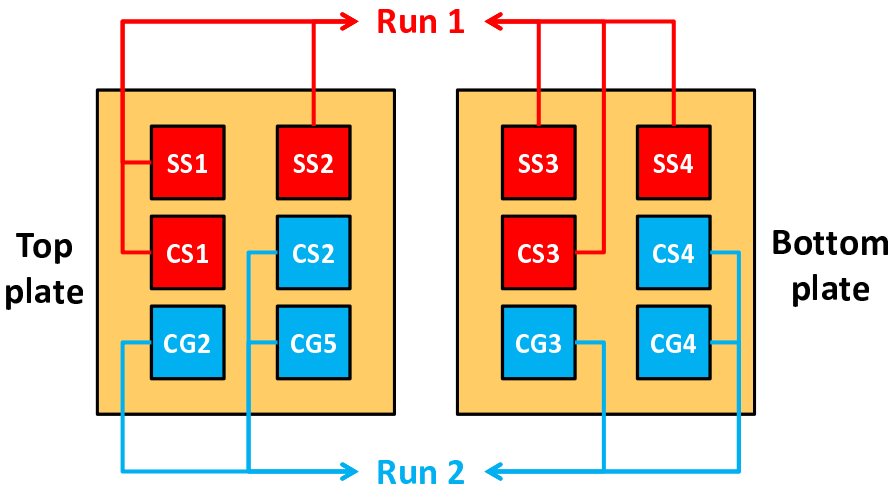

Figure 4.12: Crystal position and acquisition subset scheme for the test on small-size CTI crystals.

pulses among bolometers belonging to the same measurement subset: this is plotted in Fig. 4.13. In the same figure, the values of τ_r(10%-90%) and τ_d(90%-30%) are listed for each pulse; the values must be considered only as indicative because they are affected by low energy noise and change slightly with increasing energy (see Fig. 4.14 for an example of this behaviour).

Data analysis is complicated by DAQ and electronic problems that interfere especially with the cure of pile-up, which has been treated only partially in the process to obtain the results presented here: a refinement of the analysis with deeper pile-up processing, a delicate and complex step, is foreseen in the next future; as a consequence, the limits and values given later in this section are not finalized and should be considered indicative. In addition to that, measurements are affected by temperature variations in the dilution refrigerator that cannot be corrected by the data stabilization method used in the Cuoricino experiment and in the R&D runs at LNGS: in fact, the small-size bolometers are not equipped with Si heaters. However, this is a solvable inconvenient. Despite the lack of a dedicated system in the setup, stabilization is performed anyway by means of the ^{40}K 1460 keV γ-line. As an example, Fig. 4.15 shows the time variation of the ^{40}K line in the SS1 crystal during a 3-days data taking both before and after the measurement is stabilized. After stabilization, the identification of natural radioactivity lines allows to calibrate the energy spectra of single detectors: Fig. 4.16 reports, as an example, both the calibrated spectra of detector SS1 and a zoom in its γ-β region at low energy, where the main γ-lines are marked; in the high energy range, the bump due to cosmic muons is seen at about 8 MeV.

Finally, a single sum spectrum was obtained for each group by combining processed data from the energy spectra of the single crystals. Sum spectra up to 6 MeV for the SS, CS and CG crystals are shown in Fig. 4.17. Before investigating the ^{210}Po peak region at 5.4 MeV, which corresponds to the aim of the test, the energy resolutions obtained by the three groups are calculated at low energies. The 1460 keV line of ^{40}K and the 2615 keV line of ^{208}Tl are used as reference peaks: the measured values are reported in Tab. 4.8. The last step is the analysis of the region of interest for the goal of this test, which is the 5-6 MeV range. Fig 4.18 shows a detail of the investigated energy region for each group of small samples. The ^{210}Po α-peak was searched for, in the quoted area, by fitting each spectrum with a gaussian function over a linear background. The best fit of the CG crystals spectrum has a 5.42 MeV peak with an energy resolution of 50 keV. The large FWHM ΔE measured for the CG group is somehow expected: in fact, each crystal has been energy calibrated separately and only in the low energy region, which does not take into account deviations from linearity at energies above $\sim$3 MeV; therefore, the combination of the single calibrations can easily result in wide high energy peaks at the end of the spectra summing process. The area under the identified 5.42 MeV peak in the CG spectrum encloses 161$\pm$52 counts, which corresponds to

Sample group	**Energy resolution [keV]**	
	at ^{40}K	at ^{208}Tl
SS	10	14
CS	10	15
CG	12	16

Table 4.8: Energy resolutions FWHM measured for the sample groups SS, CS and CG at the ^{40}K and ^{208}Tl lines.

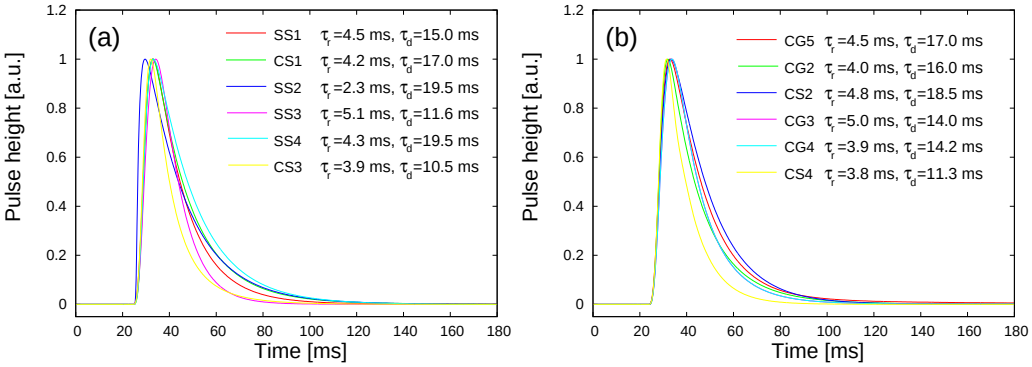

Figure 4.13: Average pulses of the detectors in the Como run on CTI crystals, renormalized and grouped according to their acquisition subset: (a) average pulses for the bolometers measured in Run 1; (b) average pulses for the bolometers measured in Run 2. Approximate values of τ_r and τ_d for each crystal are listed.

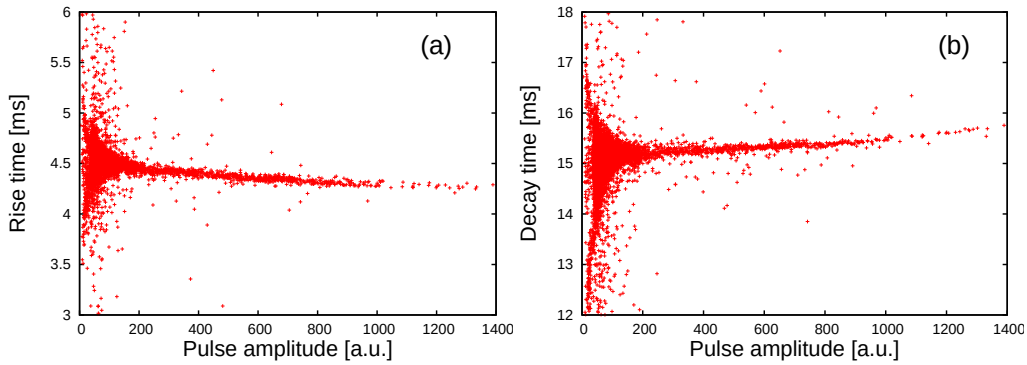

Figure 4.14: Pulse rise time and decay time plots in function of pulse amplitude for the SS1 bolometer in the Como CTI run. For both parameters, note the spread at low energy due to noise and the slight variation with increasing energy.

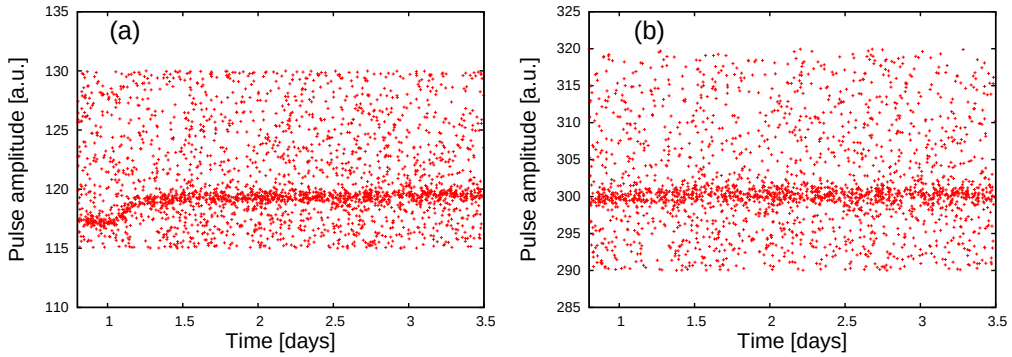

Figure 4.15: The ^{40}K line as a function of time, (a) before and (b) after the stabilization.

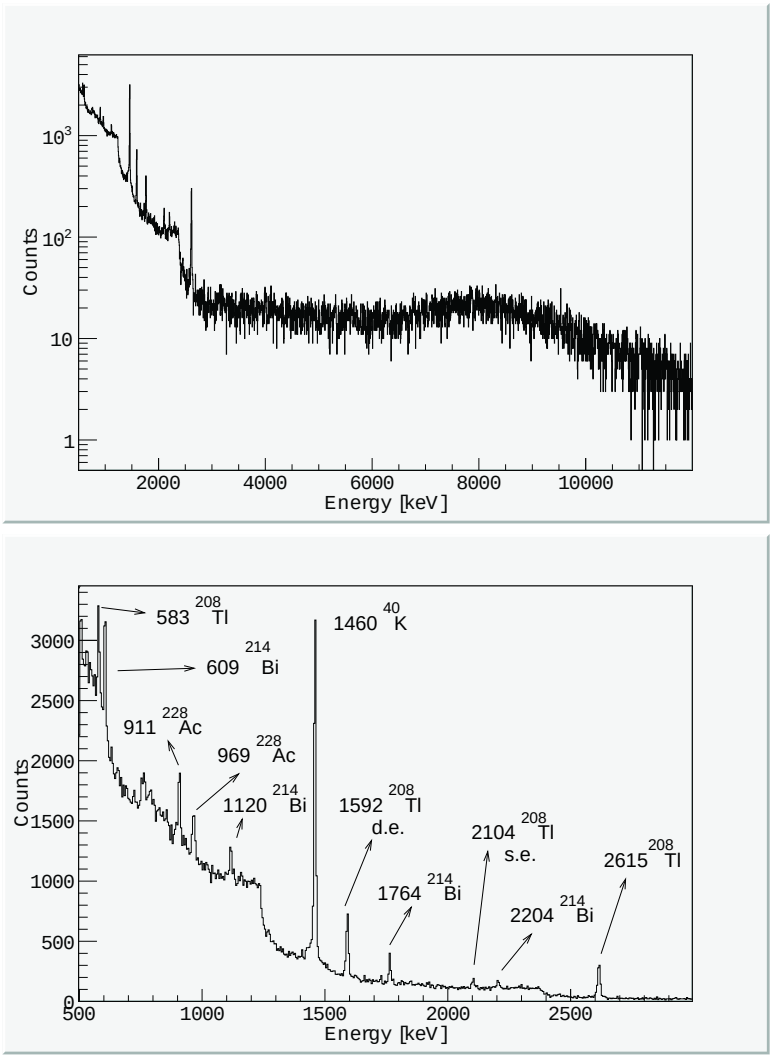

Figure 4.16: Energy spectrum of the SS1 crystal: (a) view up to 10 MeV; (b) zoom on the γ-β region and identification of the major γ-peaks.

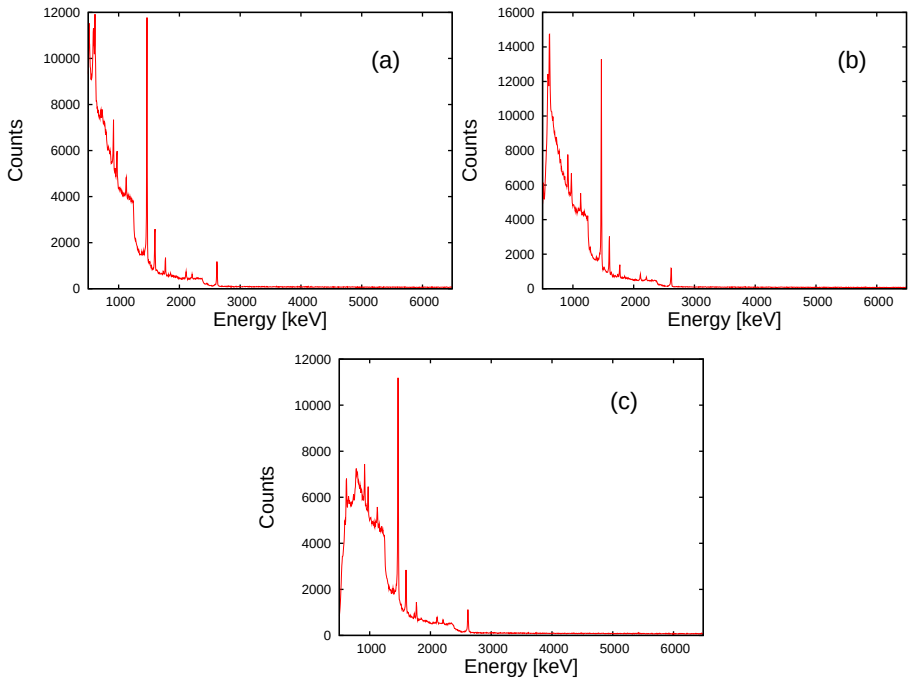

Figure 4.17: Sum energy spectra of the three groups of small samples: (a) SS, (b) CS and (c) CG.

$(7.0\pm2.0)\times10^2$ counts/(year·crystal). The count rate is given in respect to small crystals. The same method is applied to both the SS and CS datasets, but in this case no evidence is found and only limits at 90% confidence level are provided: $<3.6\times10^2$ c/(y·crystal) for SS samples and $<6.1\times10^2$ c/(y·crystal) for CS samples. However, it should be stressed that the result is not clear in the case of SC crystals, due to a possible but doubtful identification of a peak: a refinement of the analysis, with particular attention to pile-up treatment, could solve the ambiguity.

The obtained estimation of the ^{210}Po contamination in CG crystals should be compared with the values seen in the CTI-produced large crystals measured at LNGS in 2006. Needless to say, the comparison is not trivial also because of the different background produced by cosmic rays in the two measurements; it is useful, however, as a sign of compatibility among the values obtained. As already mentioned at the beginning of Sec. 4.4, three crystals grown at CTI from GWI TeO_2 powders showed high counting rates originated by a polonium contamination, and the values listed in Tab. 4.6 can be adapted to the case under study. First, they are normalized to the 1 cm^3 volume of the small samples; then, the 420 days elapsed from the production of the small crystals to the start of the measurement in Como must be taken into account: they correspond to three half-lives of ^{210}Po ($\tau_{1/2}$=138 days), whereas the large CTI crystals were measured at LNGS shortly after their growth. All results, expressed in terms of counts/(year·crystal), are listed in Tab. 4.9.

In the picture proposed, the contamination level seen in the CG small samples, grown at CTI from TeO_2 powders produced by GWI, is compatible with the lowest contamination level observed in the larger crystals measured at LNGS, which have the same origin. Appearantly, no peaks abscribable to a ^{210}Po contamination detectable in the Como setup are present in the SS samples (grown at SICCAS from SICCAS powders) and in the CS samples (grown at CTI from SICCAS powders). However, as al-

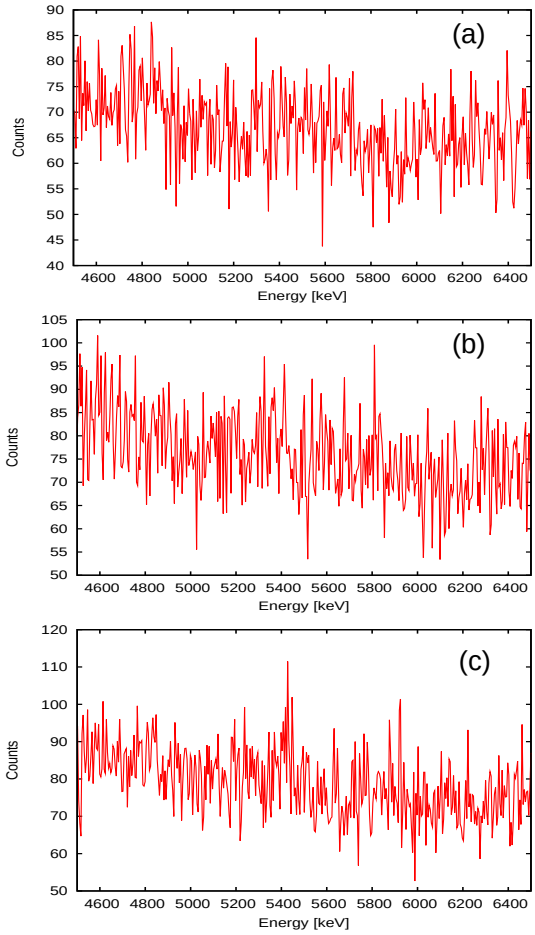

Figure 4.18: Zoom in the 5-6 MeV region of the sum energy spectra of (a) SS, (b) CS and (c) CG.

Data fit or limit for small samples (90%) [c/(y·crystal)]		
SS	*CS*	*CG*
$<3.6\times10^{2}$	$<6.1\times10^{2}$	$(7.0\pm2.0)\times10^{2}$
Old CTI crystals at LNGS	**Assumed contamination [c/h]**	**Expected events [c/(y·crystal)]**
CTI1	500	4.4×10^{3}
CTI2	90	7.9×10^{2}
CTI3	80	7.0×10^{2}

Table 4.9: Data fit and limits on the ^{210}Po contamination in the small samples of the Como test on CTI crystals: they correspond to the measurement times of 1820 hours for the SS group, 1932 hours for the CS group and 2047 hours for the CG group. Values are compared with the results of the 2006 LNGS run: the assumed contaminations of $5\times5\times$ crystals is normalized to the volume of small samples and to the time elapsed before their measurement, so that polonium decay is taken into account.

ready mentioned, a deeper pile-up analysis could be performed on the presented data: this would lead to a refinement of the results proposed and to an ultimate comprehension of the contamination origin. Should the absence of a peak in the CS samples be confirmed, it would indicate the GWI TeO_2 as source of the ^{210}Po detected; on the other hand, its identification would attribute the responsability to the growth process. The function of the SS samples, instead, is to work as a control group.

4.5 Final remarks

The first two tests presented in this chapter lead to the ultimate definition of the protocol for the production and surface treatment of the TeO_2 crystals for CUORE-0 and CUORE. Data comparison between them gave insight into the problem of the mechanical processing of crystal surfaces and helped correcting a flaw that corrupted bolometric performance. As a consequence of the CCT1 and CCT2 tests, the production of CUORE crystals started; batches of future absorbers are now being delivered and randomly sampled at LNGS. The bulk and surface contamination levels obtained are compatible with the requirements of the CUORE baseline. On the other hand, tests on TeO_2 crystals produced by the CTI company evidenced, as opposed to SICCAS crystals, high counting rates due to large ^{210}Po contamination levels. The test at the Cryogenics Laboratory in Como aimed at understanding if the origin of the contamination can be traced back to the growth process or to the initial TeO_2 powders; however, a deeper analysis with more attention to pile-up treatment is required to finalize the results. Should the source of the contamination be identified and the problem removed, CTI would make a viable choice for a possible future R&D on the paratellurite absorbers, involving isotopic enrichment or crystal doping, with the aim of raising the sensitivity to 0ν-DBD of the technique designed by the CUORE collaboration.

Chapter 5

Innovative contact geometry for germanium thermistors

The ingredients which contribute in delineating a sensitive bolometric experiment for 0ν-$\beta\beta$ investigation can be distinguished in those which create an effective environment for the search (such as, for instance, a suitable nuclide and a clean background) and those which shape up a well-performant detector. While this overview, up to now, has been dealing mainly with the first category of requirements in the form of radio-purity issues, Chapters 5 and 6 will focus the discussion on two elements with direct influence on bolometric performance: the temperature sensor for signal read-out and its coupling to the crystal absorber.

The main character of the following paragraphs will be the NTD-Ge thermistor. Its doping properties and size had already been optimized in the R&D previous to the Cuoricino experiment, and had been kept unaltered from that moment on: the high statistics collected in both Cuoricino and the following R&D tests proved the specific properties of the selected thermistor type to be suitable for operation with TeO_2 macro-bolometers. During the preliminary studies for CUORE-0, however, new assembly requirements emerged which triggered strongly a revision process of one aspect of thermistor design: the position of its electric contacts.

The reasons for this request and the importance of its fulfillment will be explained hereafter; the different prototypes proposed and tested will then be presented, along with the experimental results which motivate the choice of the ultimate thermistor model for CUORE-0.

5.1 A matter of assembly

The optimization of contact geometry for NTD-Ge thermistors can be summed up in a sentence as a very practical and simple necessity that generates a bunch of technological complexities. Before entering the details of the requirement, a few words should be spent on the temperature sensors used in Cuoricino, pictured in Fig. 5.1. The thermal and electric behavior of NTD-Ge thermistors, as well as the production steps they undergo, have already been described in general terms in Chapter 1 and, in the specific case of their application to Cuoricino, in Chapter 2. They are rectangular solids with volume $3\times3\times1$ mm^3 cut from germanium wafers doped by the neutron transmutation technique [75]. In order to form excellent Ohmic contacts, boron ion implantation is fol-

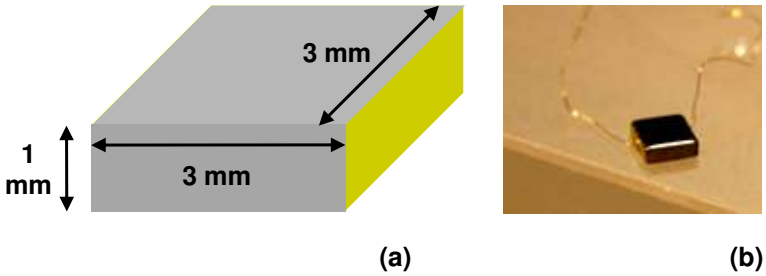

Figure 5.1: Standard thermistor used in the Cuoricino experiment: scheme (a) and picture (b).

lowed by annealing and the deposition of both a thin (200 Å) Pd adhesion layer and a thicker (1000-2000 Å) Au contact layer. The resulting gold pads lie, after cutting, on the two lateral 3×1 mm^2 sides. Electric contact is provided by gold wires with 50 μm wide diameter, which are connected to the gold pads by means of ultrasonic ball-bonding [115]: the cause behind the revision of contact geometry is actually due to assembly issues introduced by thermistor bonding.

Ball-bonding is a technique widely used in the microelectronic industry to perform the connection of metal wires [116]. The process is allowed by the appropriate definition of a set of parameters, mainly force, power, time, temperature and ultrasonic energy, which are different according to the properties of the metallic interface. During Au/Au ball-bonding, the wire is fed through a ceramic capillary set on the mobile part of a bonding machine; a gold ball with diameter ranging from 1.5 to 2.5 times the wire diameter is first formed by melting the end of the wire through electronic flame-off: its consistency, controlled by the flame-off and the tail length (the portion of wire elongating out of the capillary), is critical for successful bonding. The so-called free-air ball is brought into contact with the bond pad. Adequate amounts of pressure, heat, and ultrasonic forces are then applied to the ball for a specific amount of time, forming the initial

Bonding parameter	**Value**
Au wire diameter	50 μm
Ball size	10
Bonds per wire	2
Lift before torch	300 μm
Ultrasonic power (both bonds)	200
Ultrasonic time (both bonds)	45
Loop height	50 mm
Wire tail	100
Calibration force	130 g

Table 5.1: Typical paramenters used for Au/Au ball bonding on the NTD-Ge thermistors under study. The West-Bond Inc. model 7700E has been used for CUORE-0 R&D and will be used to assemble the ultimate detector. Two bonds are made for each wire: a ball-bond on the gold pad of the sensor and a wedge-bond, which will be connected directly to a copper pad for signal read-out in the assembly of CUORE-0. US power, US time and calibration force parameters will be lowered, respectively, to 150, 30 and 85 g for CUORE-0.

metallurgic weld between the ball and the bond pad; the ball bond itself is deformed into its final shape. The connection is favored by the inter-diffusion of atoms in the interface. In some cases, the interface is heated up to promote inter-diffusion, but this is not required for Au/Au bonding. The ceramic tip is then lifted up to form a gradual arc or "loop" profile, and lowered down to realize the second bond, which closes the cycle along with wire cutting. Even resistant ball-bondings must be handled with caution to avoid disconnection: the most probable disruptive events are ball lifting, which consists in gold ball detachment from the pad, and breakage in the wire section immediately above the ball bond, which has been made weaker by the melting of the wire during free-air ball formation. The device used for Au/Au ball-bonding on NTD-Ge thermistors of the Cuoricino kind is the West-Bond Inc. model 7700E [117]. Tab. 5.1 reports the set of parameters used throughout the work presented here. It should be mentioned, however, that a few among the parameters mentioned in the table were modified for their future use in CUORE-0; because of the fracture of pads on some thermistors after a low temperature thermal cycle, the US power, US time and calibration force parameters were deemed too high and lowered, respectively, to 150, 30 and 85 g.

Once the correct machine parameters are set, the necessary boundary conditions for successful Au/Au ball-bonding are [118]:

- uniform deposition of the pads, planar, adherent to the underlying Ge surface and with negligible imperfections: the presence of voids may result in ball lift;

- accurate cleaning of the pads, so that no particulate or organic contaminants lay on them: this is automatically fulfilled by the cleaning procedure of bolometric elements required for radio-purity reasons. Contamination can generally cause early bond failure. The presence of certain atoms or molecules favors oxidation at the interface and consequently enhances the probability of ball lift. Typically, impure metal oxides or organics at the bond interface act as barriers to a clean contact, thus inhibiting extensive metallic bonding;

- perpendicular position of the ceramic bonding capillary with respect to pad surface: when they are not orthogonal with good approximation, the final result may be poor power deposition leading to weak metallurgic weld.

The chronological order of thermistor bonding is set *prior* to absorber coupling in the Cuoricino assembly procedure. Chapter 6 will speak diffusely about the realization of such coupling, which consists in gluing the thermistor on the crystal's surface, and Sec. 6.3 will present the Cuoricino gluing method. A few details should be anticipated, though, in order to introduce the necessity for the optimization of contact geometry.

The gluing of wired thermistors required by the Cuoricino assembly protocol comes from the practical difficulty in bonding them after the connection to the absorber is fixed: due to the lateral position of pads, in fact, there is little room for a perpendicular descent of the bonding ceramic tip on the Au surface; for the capillary to deposit power on the pad in the correct position, the crystal has to be tilted of a different angle from one thermistor to the other, due to a small tolerance on the rotation of sensor surface in the X-Y plane introduced by gluing. The whole process becomes highly operator dependant. In spite of the "bonding prior to gluing" expedient, problems could still arise from subsequent steps, as thermistor handling during the coupling process often leads to wire breakage or ball lifting. Therefore, the Cuoricino protocol implies a non-negligible probability of damaging the electric connection of thermistors: it becomes slow, unpractical, difficult to automate and consequently unsuitable for integration in a serial assembly line. In view of the CUORE experiment, which will require the mounting of $\sim$1000 bolometers,

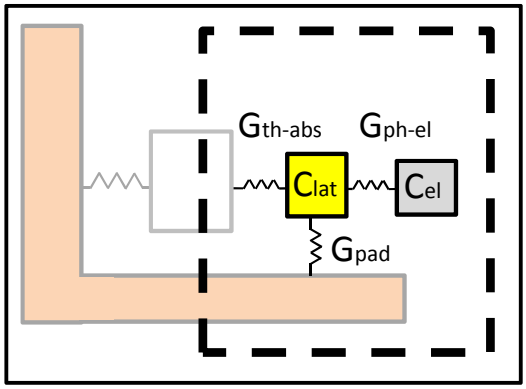

Figure 5.2: Thermal model of the temperature sensor. The parameters that define the thermistor's thermal behaviour are listed in the picture: the heat capacities C_{el} and C_{lat} of both electrons and lattice; the sensor-to-absorber coupling G_{th-abs}; the conductance between the electronic and the phononic systems G_{ph-el}; the thermal link to the heat bath G_{pad} provided by gold wires and depending on the area of contact pads.

a reproducible as well as error-proof strategy is required.

The most intuitive way to overcome such assembly impasse is switching from *lateral bonding* to *frontal bonding*. This requires to move or alternatively extend the position of gold pads on the upper surface of the NTD-Ge thermistor. The new geometry would then allow a straightforward wire ball-bonding *after* thermistor-to-absorber gluing. As intuitive as it may seem, the expedient implies the design of an appropriate pad configuration, with a revision of both size and manufacturing steps, by keeping thermistor performances unaltered or comparable with the Cuoricino standard.

5.2 Tampering with contact geometry: dos and don'ts

The final aim of the optimization work reported in this chapter is to obtain a viable strategy for thermistor frontal bonding without degrading the average performance exhibited by detectors in the Cuoricino experiment. Both energy resolution and detector response should remain, for temperature sensors with revised contact geometry, comparable to the average values seen in Cuoricino: values around 7 keV for ΔE and 100 μV/MeV for detector response are deemed acceptable (go back to Chapter 2 for details). This restrain translates in a series of minimal requirements to be satisfied when designing new types of NTD-Ge thermistors.

5.2.1 General approach to thermistor design

The following requests on sensor geometry, although presented in separate categories, are not stand-alone but feature a certain degree of interplay: successful thermistor design is not unique; on the contrary, it stems from a combination of trade-offs that can be mixed in different measures and take into account production necessities, as well. Reference values for the parameters that describe the standard Cuoricino thermistor are listed in Tab. 5.2.

Cuoricino "standard" thermistor properties	
Volume	9 mm^3
Pad area	3 mm^2
C_{el}	$9.90\times10^{-9}\cdot T$ J/K
C_{lat}	$2.70\times10^{-8}\cdot T^3$ J/K
G_{th-abs}	$2.34\times10^{-3}\cdot T^3$ W/K
G_{ph-el}	$7.02\times10^{-1}\cdot T^{4.37}$ W/K
G_{pad}	$4.80\times10^{-5}\cdot T^{2.4}$ W/K
R_0	0.92 Ω
T_0	4.11 K

Table 5.2: List of geometric, thermal and electric properties of the Cuoricino standard thermistor [81],[119]. As already mentioned in Chapter 2, the values of R_0 and T_0 reported here are the result of a characterization performed at the Cryogenics Laboratory in Como [79].

5.2.1.1 Thermal properties

New typologies of thermistors should be designed to retain the basic thermal properties of the Cuoricino standard. When considering the thermal behavior of NTD-Ge sensors, the HEM predicts that it is constituted by two systems with different thermal capacities communicating through a thermal link (see Fig. 5.2). This modelling has already been presented in Sec. 1.4 along with the main dependencies of the aforementioned thermal parameters: C_{el} and C_{lat}, the capacities of the electron and the lattice systems, and G_{ph-el}, the conductance linking them, all grow linearly with thermistor volume. This translates in the straightforward assumption that new thermistor volume should be kept comparable to the Cuoricino standard, unless issues concerning Ge wafer processing interfere. Needless to say, the previous consideration does not imply restrains on the single X, Y and Z dimensions but only on their product. However, it should be noted that a change in contact geometry could affect G_{ph-el} also for reasons not connected to a variation in linear dimensions, as will be mentioned in the following point.

5.2.1.2 Electric properties

The request to preserve the electric properties featured by the Cuoricino standard is structured in two points.

- *Electric field effects* internal to the sensor during polarization may be relevant, in a qualitative picture, if the position of pads is moved from the sides. While the electric field in Cuoricino thermistors can be thought as uniform with parallel field lines, the case is different when pads are frontal. The intuitive picture is that field lines crowd the region of thermistor bulk next to the upper surface: as a consequence of this view, one could assume the existence of an effective thickness for conduction and of a "dead volume", which does not play any role electrically although it contributes to the thermistor's thermal parameters mentioned above. The presence of a non-uniform electric field inside a thermistor with frontal contacts is reflected directly in the resistance value measured following polarization at a given temperature T. Let's assume a resistivity $\rho(T)$ of the material fixed by the doping process:

in the “side pads” design of Cuoricino sensors, then,

$$R(T) = \rho(T) \cdot \frac{l}{S}, \tag{5.1}$$

where l is the inter-pad distance and S the cross section normal to the direction of current, that is the area of each pad. The formula can not be considered valid when frontal pads are introduced in the thermistor's design. A proportionality factor K between R and ρ must be introduced, with dimensions [mm^{-1}]: it depends on the peculiar geometry of sensors and can be determined by a study of the internal electric field and potential; in the case of Cuoricino standard thermistors, of course, it coincides with the l-to-S ratio. Once the K factor is found by computing the internal electric field for a given geometry, the thermistor's dimensions along each axis can be tuned to make its resistance comparable with the Cuoricino reference values, taking also into consideration the doping of the starting Ge material. A further consideration must be added to the one made about resistance. The non-uniformity of the internal electric field may also affect the behaviour of electron-phonon coupling in thermistors with frontal pads: because of inhomogeneities in the current density, in contrast with the side-pads design, the assumption is that a temperature gradient is established and that power deposition is not uniform; however, the determination of the G_{ph-el} factor's behaviour is far from being trivial and will not be discussed in this chapter. In the evaluation of the electron-phonon coupling, only the dependence on the thermistor's volume will be considered and electric field effects will be neglected. The conclusions, reported in Sec. 5.7, will demonstrate that the previous assumption is acceptable. The influence of contact geometry on the electric field internal to thermistors will be explored in detail in Sec. 5.2.2.

- *Doping levels* define how resistivity depends on temperature through the ρ_0 and T_0 parameters in the $\rho(T)$ function, valid for the VRH conduction regime (see Sec. 1.3.3). Therefore, the net impurity concentration (N_n=N_{mag}-N_{min}) and the compensation degree (D=N_{min}/N_{mag}) must be kept as much similar as possible to the values of the original Cuoricino wafers, which translates in comparable neutron energy and dose in the NTD protocol for the same starting intrinsic Ge material.

5.2.1.3 Pad size

A variation in the dimension of gold pads has a direct effect on the thermal conductance G_{pad} between the lattice system and the heat bath, which depends linearly on their area. A trade-off must be found with the requests exposed previously.

5.2.1.4 Thermistor “footprint”

This term defines the surface where glue is deposited for absorber connection. While its geometry may look as a side problem, Chapter 6 will detail the importance of the thermistor-to-absorber coupling. The thermistor's base surface must be wide enough to house the nine epoxy dots which optimize the G_{th-abs} conductance value: considering a 0.8-0.9 mm diameter for each spot, this is achieved by an area of the order 3×3 mm^2.

Combining all the listed requirements at their best value can be made only on paper. As a matter of fact, trade-offs among them are necessary and many different thermistor designs are possible. Due to the number of factors to be balanced, only experimental testing can point out qualities and flaws of the designed sensors. Practically, when switching from lateral to frontal bonding thermistors one must deal with issues that fall into three categories.

- Technological issues, which concern the production process: the quality of electric contacts, obtained by ion implantation and gold coating of the Ge wafer, must be kept acceptable for ball-bonding in spite of any modifications introduced by the manufacturing of upper pads; moreover, the production process must be devised to give the same yield rate of sensors, so that over sophisticated thermistor designs requiring long manufacturing times should be rejected.
- Structural issues, mainly due to possible electric field effects introduced by the different position of contacts on frontal bonding thermistors.
- Geometry issues. As mentioned before, the ideal thermistor volume is fixed by the size of the Cuoricino standard sensor. There could be reasons, however, to change V at the price of modifying the desired thermal behaviour of the sensor: for example, manufacturing necessities (which are linked to the aforementioned technological problems) or the attempt to compensate for possible effects of non-uniform internal electric fields (linked to the category of structural problems).

Four thermistor models with frontal contacts were designed which combine in different proportions the previous guidelines. An introductive sketch of the characteristics featured by the four frontal-bonding sensors is presented in Fig. 5.3, using the Cuoricino basic thermistor as a reference; the properties of the single models will be detailed independently in dedicated paragraphs of this chapter. The models were introduced following what could be called a "trial-and-error" strategy, as each design is meant to compensate structural flaws or low performance evidenced by experimental tests on the preceding model. Due to this feature, experimental results on frontal contact NTD thermistors will be introduced in a chronological order, presenting both individual and comparative low temperature tests. Before reviewing experimental data from each design, however, attention will paid to the issue of how switching from side to frontal contacts influences the thermistors' internal electric field.

5.2.2 Geometry effects on the internal electric field

Among the minimal requirements for successful thermistor design presented in Sec. 5.2.1, the necessity for comparable electric properties between the frontal contact and Cuoricino models was evidenced. The different dependence of their resistance on geometry was also mentioned, specifying that the l/S value for the $R(T)/\rho(T)$ ratio is valid only for the lateral-pads device, while it is an upper limit when contacts are on top. A correct choice of the final thermistor model requires that a deeper understanding is gained on how the internal electric fields deviate from the standard Cuoricino case. For this reason, dedicated simulations were performed using the commercial software COMSOL Multiphysics® v.3.4 [120], which is a modelling package designed to simulate physical processes described with partial differential equations, based on the finite elements method.

Two kinds of sensors were modeled, both with size $3\times3\times1$ mm^3: a standard thermistor with lateral pads and a thermistor for frontal bonding, whose pads are two 0.2×3 mm^2 stripes positioned at opposite sides of the upper surface. The Poisson's equation $\sigma\nabla^2 V=0$ is written for the interior points of the domain; at the boundaries, the conditions $\mathbf{n}\cdot\mathbf{J}=0$ for electric insulation are imposed where no electric contact is provided, while a fixed current is inserted in the pads. The thermistors are assumed to have the same resistivity, corresponding to the value assumed by the #31 series at 10 mK. The results of simulations on 2D and 3D modelings of the designs are reported here.

Figures 5.4 and 5.5 show the computed current density lines and equipotential surfaces by representing sections of both simulated thermistor models in the XZ plane.

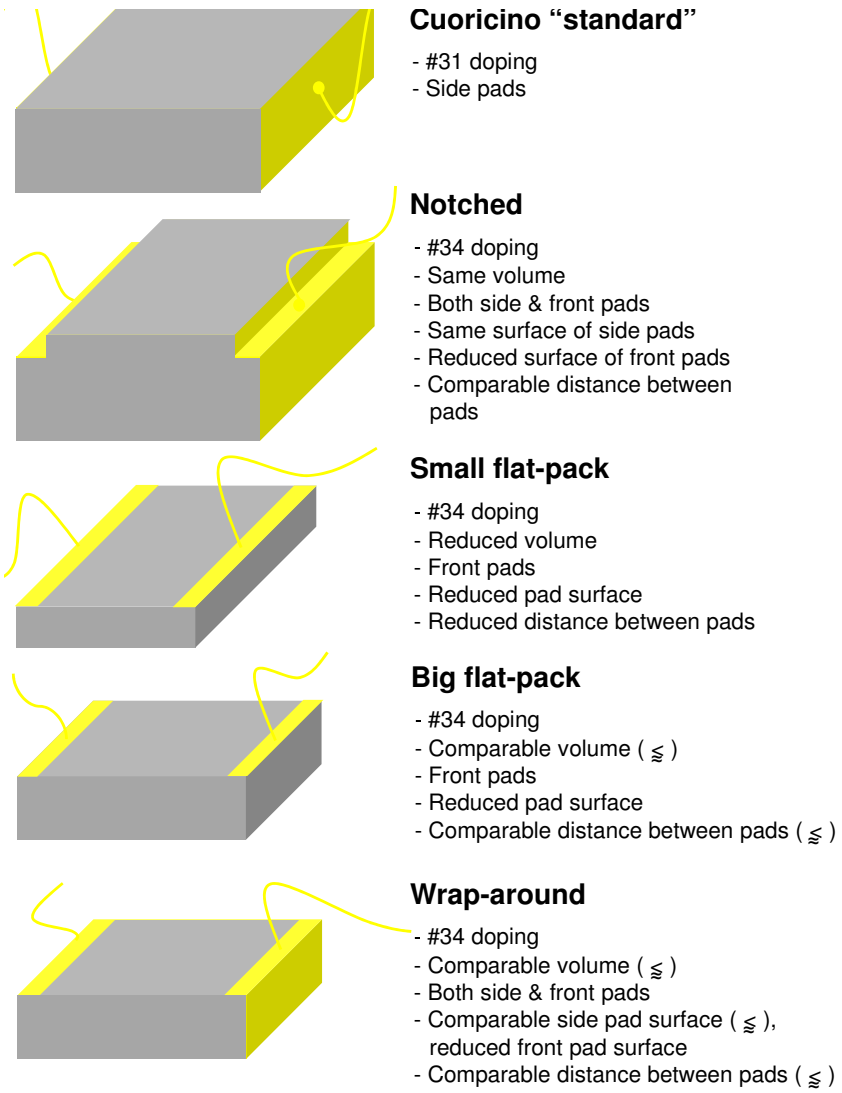

Figure 5.3: Aspects and characteristics of the four thermistor models with frontal electric contacts, using the Cuoricino standard sensor as a reference. The main features are presented in the picture; quantitative details will be provided later in dedicated sections of this chapter.

From these calculations, the geometric K factor of proportionality between the resistance R and the resistivity ρ is obtained: the value for the simulated device with upper contacts is K_{front}=1.5 mm^{-1}, which must be compared to $K_{side}=l/S$=1 mm^{-1} for the equivalent side-pads sensor; the l/S ratio (l inter-pad distance, S pad surface) is equal to 5 mm^{-1} for the thermistor with frontal contacts, which is obviously an overestimation of the R-to-ρ ratio. The variation of K is linear with the length of the thermistor for both models, and quite obviously also with the width. An interesting result is obtained when the dependence of K on the thermistor's height is computed: in particular, the study of this behaviour allows to understand the role of the so-called "dead volume", the region of the thermistor that does not contribute to electric conductance, foreseen in Sec. 5.2.1 as a non-negligible effect for sensor geometries with top contacts. It turns out that, for heights comparable to those of the devices under study in this thesis, simulations do not predict the presence of a dead volume: figures 5.6 and 5.7 show that the relevance of this effect is manifested when thermistor height gets larger than $\sim$1.5 mm.

The modelings and simulations performed suggest that electric field effects should not be particularly relevant when contacts for signal read-out are moved from the sides to the top of the thermistor. However, the previous examples give qualitative indications, and only experimental testing can prove the final performance of each design; moreover, the simulations do not account for the unpredictable effects of non-uniform electric fields on the electron-phonon conductance G_{ph-el}.

Before introducing the issue of experimental performance comparison, one last remark should be made on the electric properties of the designs that will be presented. The new thermistor models are fabricated from Ge wafers whose doping is slightly different from the #31 Cuoricino thermistors: the difference is due to a variation in neutron dosing which corresponds to a doping series called #34. Of course, the T_0, ρ_0 and R_0 parameters of the VRH law with Coulomb gap are needed for a complete description of the Ge sensors. The pair (R_0, T_0) must be determined by low temperature characterization of the thermistors, and ρ_0 can be calculated from R_0 by means of the geometry-dependent factor K. The problem of characterization has already been pointed out in Chapter 2: it is an operation critically depending on the correctness of the temperature scale adopted. The values of R_0 and T_0 used for all the doping series involved in this thesis result from a single characterization performed at the Cryogenics Laboratory in Como, where particular care was given to determining the proper temperature scale [79]. The T_0 and R_0 values for the standard Cuoricino thermistors has already been quoted in Sec. 2.1.6 and Tab. 5.2: the corresponding ρ_0^{31} is 0.92 Ω·mm. On the other hand, a thermistor sample of the same material as the frontal contact devices studied in this chapter (series #34, wafer C) was characterized in the Como run and was used as a reference: in this case, T_0=3.95 K and R_0=1.27 Ω. In order to obtain ρ_0, the geometric K factor was determined to be 1.06 mm^{-1} by simulating as before the geometry of the characterized thermistor, which lead to the final result ρ_0^{34}=1.20 Ω·mm [1]. The $\rho(T)$ laws for Cuoricino standard and frontal design thermistors are reported for comparison in Fig. 5.8.

5.2.3 Remarks on comparative testing

As far as comparative testing is concerned, a few preliminary observations on its reliability should be stressed. The first point regards performance comparisons spanning

[1] Note that the used values are compatible with a previous characterization of 34C samples at the Kamerlingh Onnes Laboratory (Leiden): T_0=3.92 K and R_0=1.53 Ω. The samples tested in Leiden were of the *small flat-pack* design type, which will be presented later in this chapter. Anticipating their K factor as 1.45, the resulting ρ_0=1.06 Ω·mm is compatible with the assumed 1.20 Ω·mm value. The difference could be attributed to a small error in the measurement of dimensions.

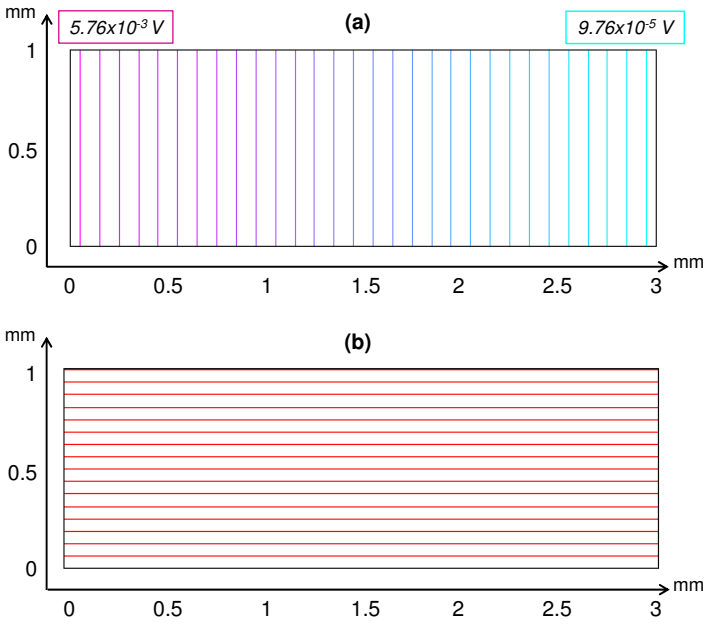

Figure 5.4: DC conductivity 2D-simulations of a standard thermistor with lateral pads, assuming #31 doping and $3\times3\times1$ mm^3 dimensions. (a) Equipotential surfaces; the numbers on top left and top right indicate the maximum and minimum voltage measured when a current of order $\sim$10 pA is injected. (b) Current density lines.

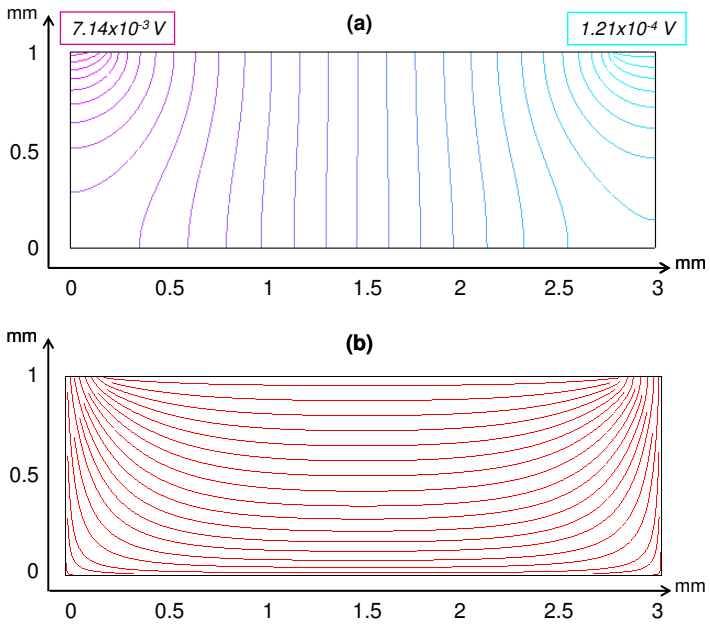

Figure 5.5: DC conductivity 2D-simulations of a thermistor with frontal pads, assuming #31 doping, $3\times3\times1$ mm^3 dimensions and two stripes with 0.2×3 mm^2 area as pads. (a) Equipotential surfaces; the numbers on top left and top right indicate the maximum and minimum voltage obtained when a current of order $\sim$10 pA is injected. (b) Current density lines.

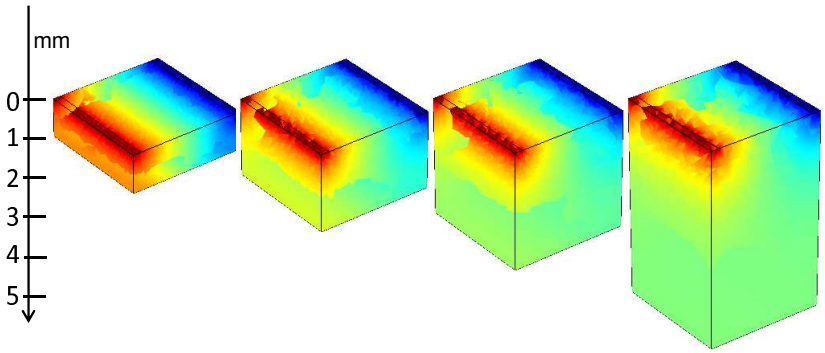

Figure 5.6: DC conductivity 3D-simulations with false-colour representation of the potential inside thermistor samples with frontal pads and varying heights. The four thermistors have heights of 1, 2, 3 and 5 mm. It is easy to see the appearance of a dead volume at constant potential that does not contribute to electric conduction.

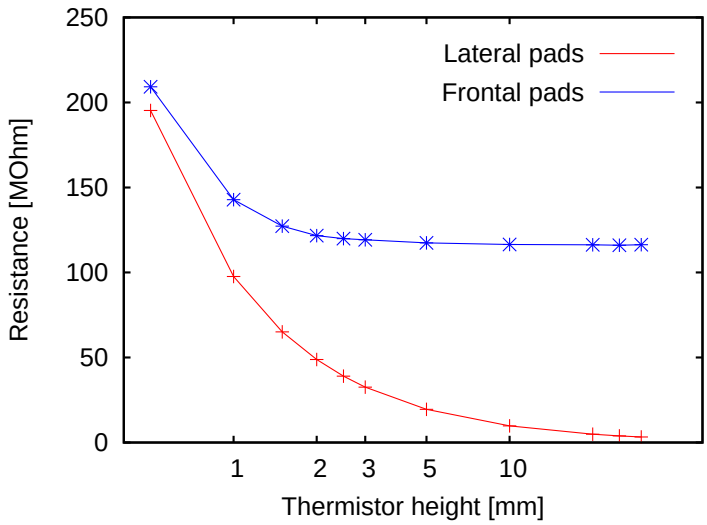

Figure 5.7: Resistance vs. height behaviour obtained by simulations of thermistor models with lateral and frontal pads. The values of resistances were obtained from #31 resistivities at 10 mK. It is easy to see that, approximately from 1.5 mm on, increasing the height of the thermistor with frontal contacts does not change its DC behaviour: the effect is summarized by defining a dead volume, which is negligible for electric conduction but still contributes in determining the thermal characteristics of the sensor.

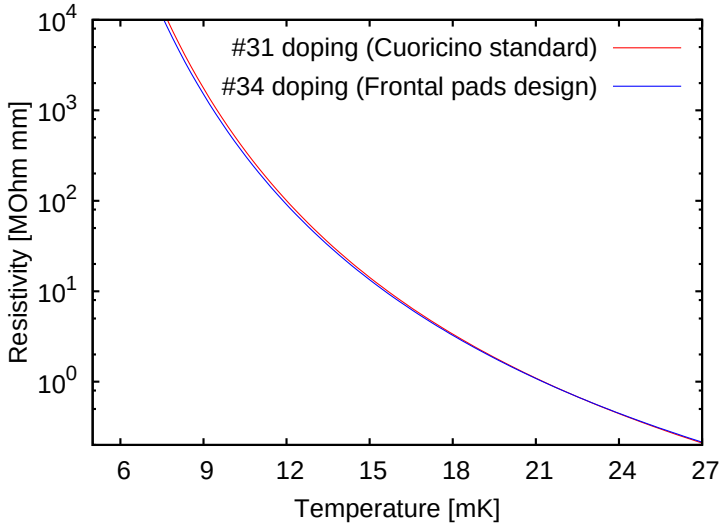

Figure 5.8: Behaviour of resistivity in function of temperature, according to the $\rho(T)=\rho_0 \exp[\sqrt{T_0/T}]$ law (see Sec. 1.3.3), for Cuoricino standard and frontal design thermistors in the experimental range of interest: the behaviours are very similar. The Cuoricino standard thermistors, produced from #31 Ge wafers, have ρ_0=0.92 Ω·mm and T_0=4.11 K; the frontal design thermistors are cut from #34 Ge wafers and are characterized by ρ_0=1.20 Ω·mm, T_0=3.95 K. The parameters VRH reported here were obtained during the same characterization run, using the same temperature scale and scaling R_0 according to the geometry of the tested sample.

on different runs, which do not lead to straightforward conclusions due to changes in experimental conditions: a loss in the sensitivity of the detector, for instance, can be originated by a rise in the holder's temperature due to spurious noise, which is often unstable and different from run to run being strictly connected to the quality of the cryogenic set-up. In addition to that, performance comparisons on different bolometers can generally be misleading: as an example, a "loose" absorber-to-heat bath coupling may result in a stronger sensitivity of the bolometer to vibrational noise, leading to low performance. The consequence is that the most significant comparative tests on thermistor performance consist in considering sensors connected to the same crystal absorber. However, there are experimental restrains. The total time required by each run is notable when carrying out a campaign of measurements, and the concurrent number of thermistors that can be tested in the available cryogenic set-up is small. A trade-off is therefore necessary between making comparison tests on single bolometers and the experimental limits that restrain the statistics obtainable from a dedicated work.

There is a way to overcome this difficulty, allowing acceptable performance comparisons between thermistors on separate bolometers. When comparing two or more detectors with different thermal parameters, the intuitive method is to confront pulse amplitudes corresponding to the same energy release in the absorbers: but higher pulses do not necessarily imply higher signal-to-noise ratio, and because of this a less direct approach must be applied. As already explained in Chapter 1, a *R-P* load curve is collected for each thermistor at a given bath temperature T_b by measuring its resistance at different power values supplied to the electron system; data can then be arranged to produce a corresponding *I-V* curve. The following step, which is possible whenever a Si heater is connected to the bolometer, is to find at fixed T_b the optimum operation point by releasing constant power and determining the voltage bias that yields the highest pulse. If a set of optimum points is collected at different base temperatures, a new curve can be drawn: the plot of detector responses A (in μV/MeV) versus thermistor resistance.

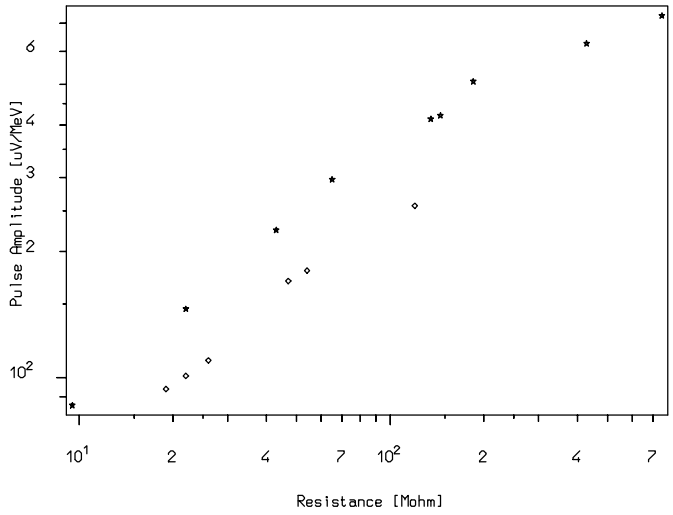

Figure 5.9: Example of the comparison between different detectors using their *A-R* curves.

This *A-R* curve is, with reasonable approximation, a straight line in a bi-logarithmic scale.

Some considerations can be made to support *A-R* curves as instruments to compare the performances of different detectors. The fact that a thermistor with higher resistance gives higher pulses does not imply better performances: in fact, higher resistance means higher sensitivity to spurious noise (microphonic, cross-talks and slow heat pulses, which excite the low frequency region of the noise spectrum at 1-5 Hz). On the other hand, when detectors work at lower T_b higher pulses are reached, but once again at cost of worse spurious noise because of the higher resistance. The previous considerations are in agreement with the experimental observation that a detector generally has a uniform behavior, in terms of S/N ratio, along its *A-R* curve: there is no great difference in working at 8 or 12 mK, for example, as what one gains in pulse amplitude is lost in spurious noise and viceversa; as a general rule, one tries to avoid working at the extremes of the curve, which mean respectively extremely high noise and very low pulse amplitudes.

Basing on the preceding arguments, the behaviour of a detector is well characterized by its *A-R* curve, which is denominated *curve of merit*. A reliable way to choose among a set of detector performances is to compare bi-logarithmic curves of merit. The bolometer whose *A-R* curve lies above the other ones, as pictured in Fig. 5.9, features the winning performance in the set: the best detector, when working at its optimum point and at fixed heat bath temperature, gives higher pulses at equal thermistor resistance. This implies that a meaningful comparison of detector responses for different bolometers should be done at the same resistance: for this reason, the *Detector Figure of Merit* (DFM) is introduced. The DFM is defined as the μV/MeV signal height at a fixed work resistance, for example 100 MΩ. A thorough choice would also require that other parameters are evaluated along with the DFM: a few possible ones are the voltage across the thermistor V_{bol}, the work temperature T_w, the pulse rise time τ_r (10% - 90%) and the pulse decay time τ_d (90% - 30%). Nonetheless, general considerations about the thermistors and bolometers used limit the relevance of such parameters as choice factors: for example, the next sections will point out that deductions based on T_w are misleading, as they can be triggered by errors in the characterization of thermistors; and, as far as τ_r and τ_d are concerned, Chapter 6 will show that the thermistor-to-absorber coupling influences the value of pulse shape parameters to the point of making inconclusive their

use in the evaluation of sensor quality.

A final remark should be made about those detectors whose *A*-*R* curves cannot be collected, for example when the experimental setup allows neither stabilization at different temperatures, nor controlled power depositions by heater usage because of cross-talk issues or device disconnection. When this happens, only one *A*-*R* point is known. In spite of this restrain, the whole curve can still be extrapolated. For example, the analysis of data from Cuoricino and its R&D tests shows that, in a log-log scale, the slopes of the best-fits for the existing detailed *A*-*R* curves are reasonably approximated by the value 0.65. Normally, if the bias value is the only reason for the change in pulse amplitude at different working points, *A* would scale as $\sqrt{R}$: but other effects depending on specific characteristics of the setup make the slope depart from its 0.5 value. Sec. 5.4 will provide more details on this topic: generally, the results of simulations preliminary to cryogenic tests help fixing reasonable coefficient values to extrapolate curves of merit. Experimental data presented later on will show that the real slopes lie in the assumed range.

All the considerations exposed constitute the background for performance comparisons among the thermistors tested during the optimization work. Evaluations will be based on static behaviour, mostly the value of base resistances and the shape of *I*-*V* and *R*-*P* curves, and on dynamic behaviour, by the extrapolation of both curves of merit and DFMs; energy resolutions will be given only in the direct comparison of frontal bonding to Cuoricino standard thermistors, and only for optimized experimental setups.

Two categories of experimental investigations were carried out on this subject.

- Tests on small bolometric prototypes. Thermistors are glued on TeO_2 absorbers with $2\times2\times0.5$ cm^3 reduced size; compared to CUORE large mass crystals, this corresponds to $\sim$1/60 of the volume. Tests of this kind are performed at the aboveground Cryogenics Laboratory in Como, using the LHe free dilution refrigerator. Detectors are designed so that two or three different models of thermistors are connected to each crystal, allowing for direct comparison. Due to the different dimensions and experimental space available, the shapes of copper and PTFE holders are radically different from those of the typical CUORE-0 R&D structures: less reproducibility is obtained among distinct bolometers in the same run and single energy resolutions are not optimized. As a consequence, no absolute conclusions regarding the performance of frontal bonding sensors can be extracted from this category of experimental runs. The only significant information is the behaviour relative to other reference sensors. Nevertheless, the preliminary data obtained is useful to unveil evident anomalies, decide the direction of further investigations and, generally, to get an introductive picture of the new devices.

- Tests on large mass bolometers. Thermistors are glued on TeO_2 absorbers with $5\times5\times5$ cm^3 volume, whose assembly makes use of the improved Cuoricino copper and PTFE holders designed for the CUORE-0 R&D. Bolometers are cooled down in the cryostats at the underground Gran Sasso National Laboratory. A variable number of thermistors, ranging from one to three, is connected to each crystal; thermistors on the same absorbers can be of just one or two different models. The statistics extracted from these experimental tests can be compared directly to the Cuoricino results, which are used as a reference.

Tab. 5.3 offers an overview on the experimental tests performed both in Como and at LNGS. The following paragraphs will focus on the characteristics and performances obtained by the four models of sensors with frontal pad design. All devices are fabricated at the Lawrence Berkeley National Laboratory.

	Detector size	Type of frontal-bonding thermistors tested	Number of bolometers	Number of frontal-bonding thermistors	Comparative test?	Notes
TEST 1	Small prototypes	Small flat-packs	4	4	Yes	
TEST 2	CUORE size	Small flat-packs	4	4	Yes	Part of the second Crystal Chinese Test
TEST 3	Small prototypes	Small flat-packs Large flat-packs	4	4 small flat-packs 4 large flat-packs	Yes	
TEST 4	CUORE size	Large flat-packs	2	2	No	Part of Test 7 (separate analysis)
TEST 5	CUORE size	Large flat-packs	2	2	Yes	Part of the Three Towers Test
TEST 6	CUORE size	Wrap-arounds	1	3	No	
TEST 7	CUORE size	Wrap-arounds	6	6	Yes	

Table 5.3: Summary of the tests performed on thermistors with frontal electric contacts.

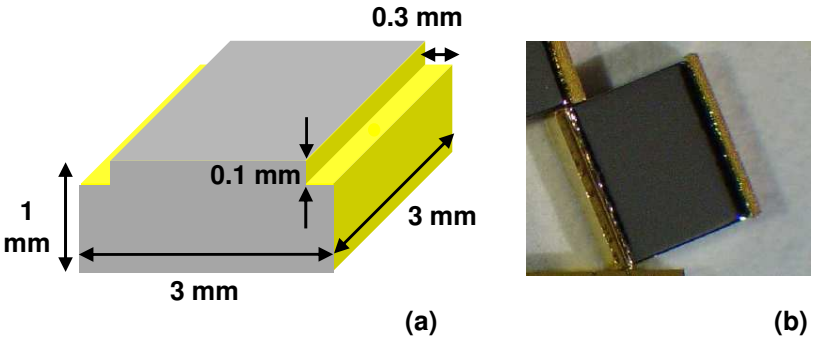

Figure 5.10: The first sensor model with frontal electric contacts: the notched thermistor.

5.3 Notched thermistors

The most intuitive idea to realize frontally bondable sensors consists in performing two additional gold depositions for pads on the upper surface of Cuoricino thermistors: in principle, such solution would lead to NTD sensors whose design criteria, according to the list presented in Sec. 5.2.1, are very near those of the classic model with lateral pads. The project was eventually abandoned because of unaffordable fabrication issues, namely the time consuming requirement to process each thermistor singularly instead of the whole Ge wafer.

The first concrete attempt was the design of the so-called *notched* thermistor model. Its name is due to a production feature that can be explained by pointing out the difference with the manufacturing of the standard Cuoricino model.

Cuoricino thermistors are cut from a 3 mm-thick Ge wafer after electrical contacts are made on its opposite large sides by ion implantation and gold coating along the whole surface; a 1 mm$\times$3 mm grid of cuts is performed through the wafer and the obtained raw sensors are cleaned and etched. The production of notched thermistors requires one additional step: before ion implantation and gold evaporation are performed, shallow grooves are made on both the large sides of the wafer with a wider saw blade, using the same 1 mm final cut grid, and etched. In this way, gold for electric contacts is deposited not just on the surface but inside the grooves as well, so that processed thermistors have two narrow 0.3$\times$3$\times$0.1 mm^3 "notches" on the top. The notched areas work, therefore, as frontal pads. Such sensors would be almost identical, as far as thermal parameters are concerned, to Cuoricino standard thermistors, provided that their geometry is the one represented in Fig. 5.10.

One batch of notched thermistors was produced for experimental testing. However, all the sensors in the batch failed the preliminary step of assembly due to a failure in electric contacts: ultrasonic ball bonding perforated and removed the gold layer deposited in exactly half of the notches. An explanation was found in the fact that surfaces produced by the grooving method and gold coated do not meet in a replicable way the strict quality requirements necessary for successful ultrasonic ball bonding. Work on the notched design was abandoned as a consequence. The following alternative strategy for the manufacturing of frontal contacts was found in the *flat-pack* series.

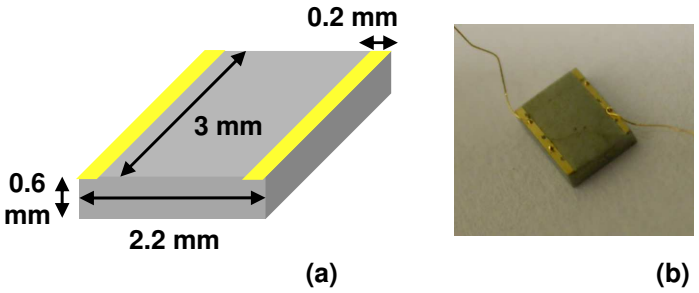

Figure 5.11: The second sensor model for the frontal bonding of wires: the flat-pack thermistor with small geometry.

5.4 Flat-pack thermistors with small geometry

The design work on flat-pack thermistors was mainly concentrated on solving the manufacturing problems encountered with the notched model: a reliable and quick production method for the deposition of frontal gold pads was elaborated. The "flat-pack" designation is given because they are compact devices with contacts departing from one surface, somehow recalling a kind of flat integrated circuit. For reasons that will be explained at the end of this section, two flat-pack models following the same design concept but with different geometry were produced: the subsequent paragraphs will detail performances obtained with the earlier prototype, called *small flat-pack* thermistor.

5.4.1 The how-to of flat-pack thermistors

The main difference with the notched model, leaving aside for the moment any considerations about dimensions, is that these thermistors do not have lateral pads. The production process developed for the flat-pack design is comparable to the manufacturing of the Cuoricino standard in both fastness and reliability. As opposed to the Cuoricino procedure, electric contacts are deposited on just one side of the starting bare Ge wafer and are provided by lithography-made gold stripes; thermistors are cut and etched after the surface with gold depositions is covered with wax for protection. The resulting sensors have therefore two thin gold stripes on the top, where read-out wires are ball-bonded, and no pads on the sides: the aspect of the final thermistors is sketched in Fig. 5.11.

Once the production process is fixed, some preliminary considerations regarding the geometry of small flat-pack thermistors are necessary before investigating their behaviour. The guidelines presented in Sec. 5.2 are still valid: the flat-pack model is designed mainly to keep the work resistance R_w, the volume V and the footprint for absorber coupling as much close to the Cuoricino standards as possible. The flat-pack prototype introduced in this section features, however, a few remarkable differences.

1. The thermistor pictured in Fig. 5.11 has a reduced height, compared to the 1 mm of the Cuoricino standard sensor, and is, as a matter of fact, cut out of a thinner Ge wafer. This at first appears to row against the principle of keeping volumes comparable. The DC conductivity simulations shown in Sec. 5.2.2 suggest that, in the range of the typical dimensions of the thermistors used here, dead volume is not a problem and that, therefore, no advantage is gained in reducing height. However, no assumption can be made in principle regarding the behaviour of the electron-phonon conductance when only frontal contacts are present. As a consequence, the choice was made to be conservative in this regard: the reduced

height is required to keep the internal electric field as much similar as possible to the standard Cuoricino sensor, avoiding appreciable consequences on G_{ph-el}. The height 0.6 mm instead of the canonic 1 mm was deemed reasonable.

2. The consequence of using a Ge layer with smaller height, if contact distance is kept at 3 mm, is an increase in R_w; the reduced length of 2.2 mm was selected.

3. Although thermistor width could be increased to compensate for the reduced volume due to smaller height and length, it is kept at the 3 mm value so that the shape of the footprint for glue deposition is not changed drastically. Flat-pack thermistors can host 6 glue spots instead of the usual 9 dots that connect Cuoricino sensors to TeO_2 absorbers.

The current density lines and equipotential surface for the small flat-pack model, obtained from DC conductance simulations, are reported in Fig. 5.12; the R/ρ=K_{sf} factor for this geometry is predicted to be 1.45 mm^{-1}. Small flat-pack devices are designed to limit as much as possible deviations in the behaviour of the internal electric field from that of Cuoricino standard thermistors. Similar devices had already been tested in the past for other applications [121]: results showed that the electric field inhomogeneities introduced by this design did not appear to cause any problems in typical applications, for example in regard of the electron-phonon coupling. However, those thermistors had reduced geometry ($300\times200\times50$ μm^3) and positive conclusions cannot be extended to the current case.

Tab. 5.4 sums up the geometric, thermal and electric parameters of flat-pack thermistors with small geometry. Due to the doping difference already introduced in Sec. 5.2.2, their $R(T)$ behaviour deviates from that of Cuoricino $3\times3\times1$ mm^3 sensors: this is pictured in Fig. 5.13.

It should be noted that the link of the thermistor's phononic system to the heat-bath, according to the bolometric three-nodes model adjusted to the typical values of Cuoricino-style macro-bolometers, has always been reputed to be dominated by the pads for electric contact: the reduction of surface implied by the small flat-pack design, however, could lead the conductance of gold wires for electric read-out to become relevant. In the following analysis this aspect will be neglected, but it should be considered in case of any anomalous behaviours of the thermistor.

Before thermistors were tested on real bolometers at cryogenic temperatures, another kind of preliminary simulation work was conducted: apart from the DC conductance modelling already shown, thermal simulations based on the composite model of Sec. 1.4 were realized; in this case, dedicated software in C language under the Linux-i386 operating system was used to determine the behaviour of bolometers in the case of varying sets of thermal parameters. Both the static and the dynamic response of detectors equipped with different thermistor models can be evaluated according to the following procedure. First, a $5\times5\times5$ cm^3 TeO_2 absorber mounted in a typical R&D setup and connected to a Cuoricino standard thermistor is simulated at the working temperature of 10 mK: the results are used as a reference for subsequent comparisons. The parameters of the thermal model used in the simulations have already been listed extensively in Sec. 2.1.6. In the following simulation, the same bolometer at the same operating temperature is equipped with a frontal bonding thermistor. The static outcome is represented by the two curves *I-V* and *R-P*; *R-P* curves are presented with the ratio of *R* over the base resistance as dependent variable in order to highlight the relative behaviour of the thermistors. Then, dynamic simulations are performed to obtain *A-R* curves by executing this routine: the optimum point of each bolometer is calculated at three working temperatures (10, 12.5 and 15 mK) by simulating a 1 MeV particle energy deposition in the crystal absorber; the optimum bias value and pulse amplitude are

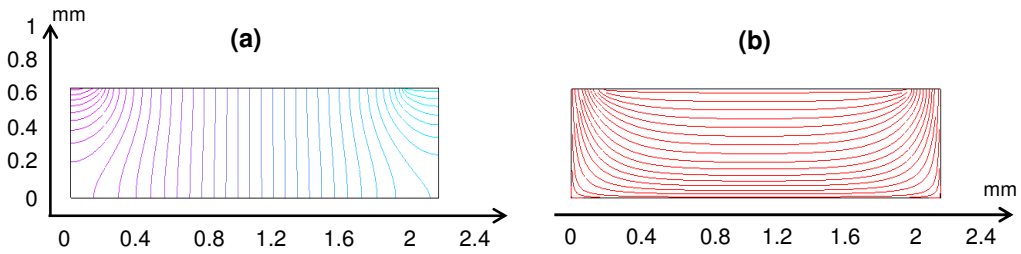

Figure 5.12: DC conductivity 2D-simulations for the small flat-pack device. (a) Equipotential surfaces. (b) Current density lines.

Small flat-pack thermistor properties		**Small flat-pack to Cuoricino**
Volume	3.96 mm^3	4/9
Pad area	0.60 mm^2	1/5
C_{el}	$4.36\times10^{-9} \cdot T$ J/K	4/9
C_{lat}	$1.19\times10^{-8} \cdot T^3$ J/K	4/9
G_{th-abs}	$1.56\times10^{-3} \cdot T^3$ W/K	2/3
G_{ph-el}	$3.09\times10^{-1} \cdot T^{4.37}$ W/K	4/9
G_{pad}	$9.60\times10^{-6} \cdot T^{2.4}$ W/K	1/5
$R/\rho = K_{sf}$	1.45 mm^{-1}	
R_0	1.74 Ω	
T_0	3.95 K	

Table 5.4: List of geometric, thermal and electric properties for small flat-pack thermistors. The last column reports, for each property, the approximate ratio of the small flat-pack thermistor value to the Cuoricino thermistor value. The K_{sf} factor was computed from DC conductivity simulations, as shown in Sec. 5.2.2.

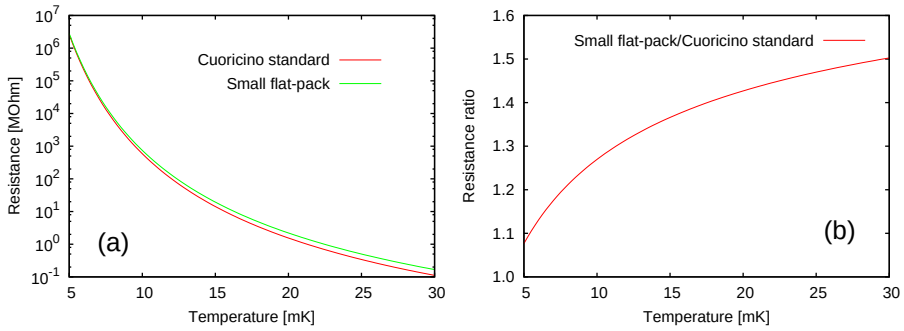

Figure 5.13: Due to the different size and Ge doping, the $R(T)$ behaviour of small flat-pack thermistors is different from that of Cuoricino standard thermistors. (a) $R(T)$ behaviour comparison between the small flat-pack and Cuoricino standard thermistors in the experimental temperature range of interest. (b) Expected resistance ratio of small flat-pack to Cuoricino standard in the same T range.

registered; the work resistance corresponding to the optimum bias value is extracted from static simulations at each T_w; eventually, the three R_w are plotted along with their corresponding detector responses; best-fits allow to define the corresponding curve of merit and to extract the theoretical DFM at 100 MΩ.

Static results for small flat-pack thermistors are reported in the graphs of Fig. 5.14, and the *A*-*R* curve is shown in Fig. 5.15. All results are plotted together with the reference curves of the Cuoricino standard thermistor for easier comparison. The static behaviour of small flat-packs is quite different from that of Cuoricino sensors, due to both different thermal parameters and geometry-determined resistance. However, the *A*-*R* curve is acceptable. The DFMs at R_w=100 MΩ, obtained from the simulation of a CUORE-size bolometer mounted in a typical R&D setup, are $\sim$95 μV/MeV for the Cuoricino sensor and about 90 μV/MeV for the small flat-pack.

As for the bi-logarithmic slope in the *A*-*R* plane, simulations give the 0.60 value for the Cuoricino thermistor, while they compute 0.65 for the small flat-pack one. The change in value can be ascribed mainly to small flat-packs being more resistive. However, this value can only be used as indication, because it may change a lot experimentally due to its dependence on many characteristics of the setup. The value also changes when a small $2\times2\times0.5$ cm^3 bolometer, mounted in the typical Como setup with different absorber-to-heat bath coupling, is considered: in this case, simulations suggest that an acceptable value for the *A*-*R* slope in a log-log scale is 0.5. It will be thus used to extrapolate curves of merit in the case of small prototypes tested at just one work temperature.

Simulations give preliminary hints at the feasibility and are merely introductory. For a proper comparison of the two types of thermistors one has to consider not just the listed thermal characteristics but also the difference in the electric fields due to the distinct paths followed by electrons in the two devices. For this reason, only experimental tests can give relevant information on the performance of the new type of thermistors. Two runs were conducted on a batch of small flat-pack sensors: one with reduced size prototypes in Como and one on large mass detectors in Gran Sasso.

5.4.2 Test 1: introducing small flat-packs

For the introductive experimental run at the Cryogenics Laboratory in Como, which took place in June 2007, four small size prototype detectors were assembled (see the final remarks of Sec. 5.2.3). One small flat-pack and one Cuoricino-type thermistor are glued on each of the four TeO_2 $2\times2\times0.5$ cm^3 crystals; an auxiliary thermistor for base temperature T_b evaluation and additional bolometric tests (#H34b, R_0=6.24 Ω and T_0=3.11 K) is glued along with the aforementioned pair of sensors. The connection of read-out wires by ball-bonding was performed after gluing, and the assembly of the four detectors proved that the force applied in the bonding operation does not damage the quality of thermistor-to-absorber coupling. A uranium radioactive liquid source with α peaks at 4.2 MeV and 4.7 MeV lays on the surface of three out of four detectors. A scheme of the four detectors is pictured in Fig. 5.16.

The four bolometers were cooled down in the LHe-free dilution refrigerator; two channels corresponding to the additional thermistors for bolometric control were lost in the thermal cycle. Tab. 5.5 reports the base temperatures along with the base resistances for the remaining readable thermistors in the run, whose T_b range from $\sim$16 to 24 mK. Although base temperatures will be reported whenever possible in the tests presented in this chapter, any considerations about T_b differences between different thermistor mod-

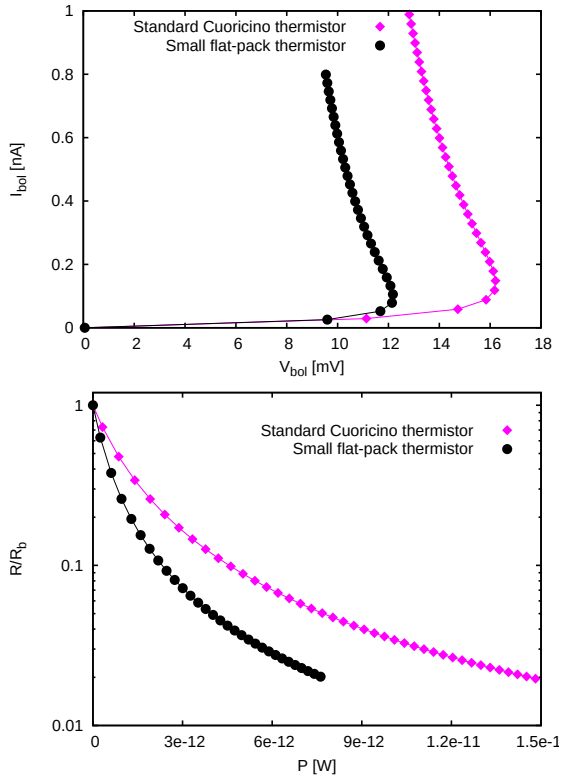

Figure 5.14: Static simulations at 10 mK comparing the behaviour of two CUORE-size bolometers equipped one with a Cuoricino standard sensor and one with a small flat-pack. The *I-V* (left) and the R/R_b-*P* (right) curves are plotted together for direct comparison.

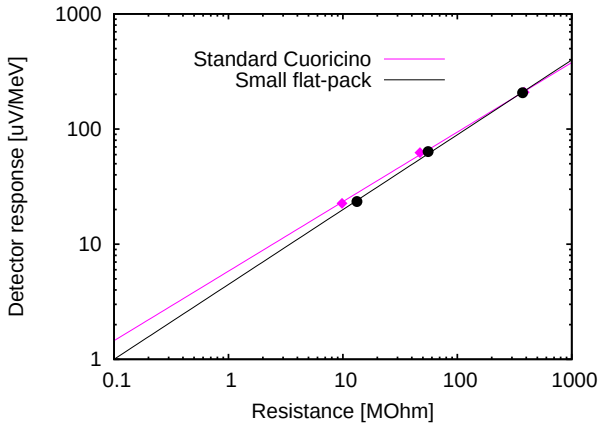

Figure 5.15: Simulated curves of merit of two CUORE-size bolometers equipped one with a Cuoricino standard sensor and one with a small flat-pack.

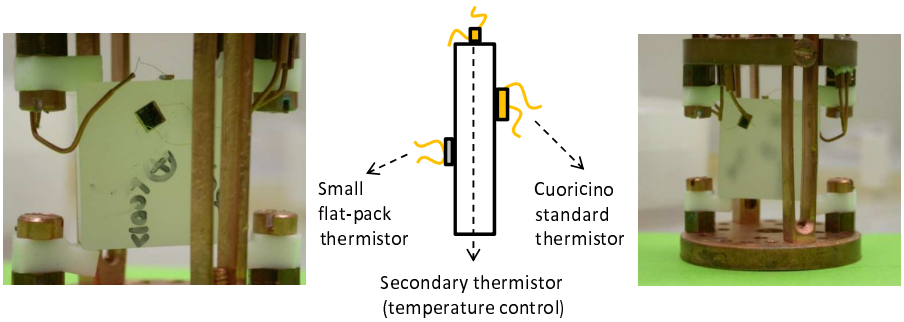

Figure 5.16: Detector scheme and pictures for the first Como run on small flat-pack thermistors. The total number of assembled bolometers is four; each is a small prototype with $2\times2\times0.5$ cm^3 crystal absorbers.

els is misleading. Careful attention should be paid to comparing temperatures among sensors with distinct geometry, because the observed effect could be due to the different characterization of the two kinds and not on a systematic effect depending on the properties of frontal bonding thermistors: the real comparison should be made between resistances. The values of T_0 and R_0 used throughout this thesis were obtained from the same characterization and by using the same temperature scale, but even small errors on the estimation of the characterized samples' geometries could lead to wrong assumptions. If we evaluate the ratio of small flat-pack to Cuoricino base resistances for each detector, we find out that it does not reflect the relationship between base temperatures, as seen in the columns R_b(SF)/R_b(C) and T_b(SF)/T_b(C) of Tab. 5.5. However, a general consideration can be extracted from the same data by comparison with Fig. 5.13(b): the ratio of base resistances is somehow compatible with what expected in the considered temperature range (from 10 to 20 mK).

Other effects are clearer. The static behaviour of small flat-pack sensors, which is fully described by the *I-V* and *R-P* curves reported in Fig. 5.17 and Fig. 5.18, shows some degradation comparing to the static features of Cuoricino thermistors. Various mechanisms could account for the worse static performance. The electronic and phononic systems are more decoupled because of the thinner volume; and the coupling to the absorber is also lower, namely of a factor 1/3. While the importance of thermistor-to-absorber coupling will be extensively treated in Chapter 6, both contributes should be

Detector	R_b **[MΩ]**		$\frac{R_b(\mathbf{SF})}{R_b(\mathbf{C})}$	T_b **[mK]**		$\frac{T_b(\mathbf{SF})}{T_b(\mathbf{C})}$
	SF	C		SF	C	
A1	0.96	1.50	0.64	22.6	20.1	1.13
B1	0.66	0.41	1.61	23.9	24.3	0.99
C1	10.63	9.49	1.12	16.2	15.8	1.03
D1	1.66	0.77	2.16	20.8	22.1	0.94

Table 5.5: Resistance and temperature values for the thermistors in Test 1. Base resistances and base temperatures are reported for both Cuoricino-type (C) and small flat-pack (SF) sensors, along with the ratios between pairs on the same detector.

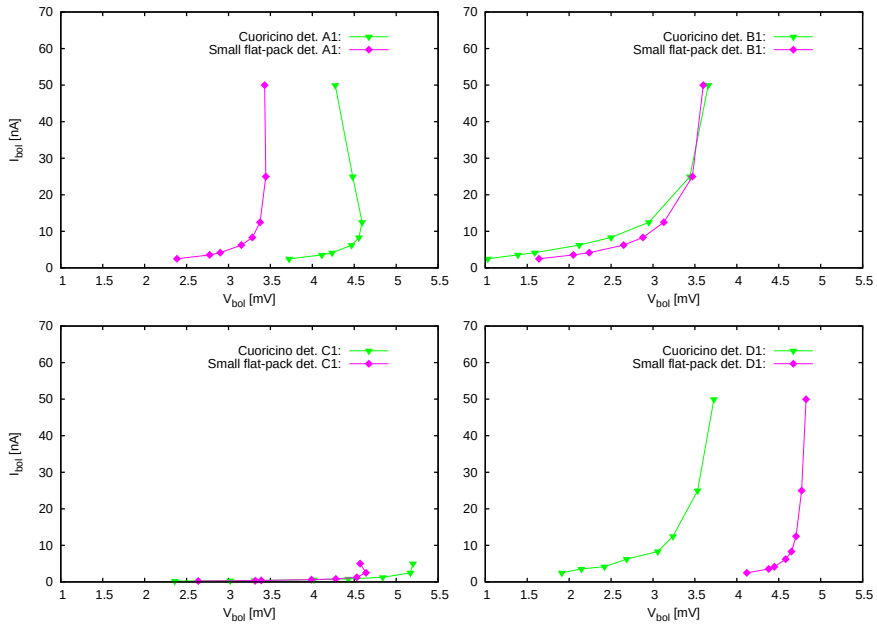

Figure 5.17: *I-V* curves for the four detectors in Test 1. V_{bol} is the voltage at the terminals of the thermistor and I_{bol} is the current across it.

taken into account, as the shape of static curves suggests that higher decouplings in different stages of the thermal network are at play, although more statistics is necessary to support the consideration.

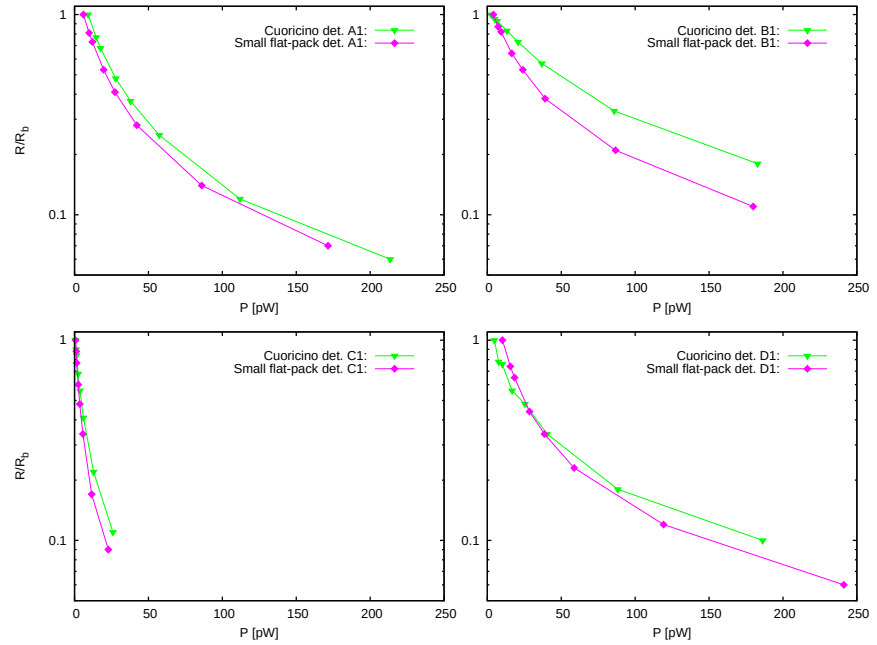

Figure 5.18: *R-P* curves for the four detectors in Test 1: the dependant variable is the ratio of R to the base resistance R_b.

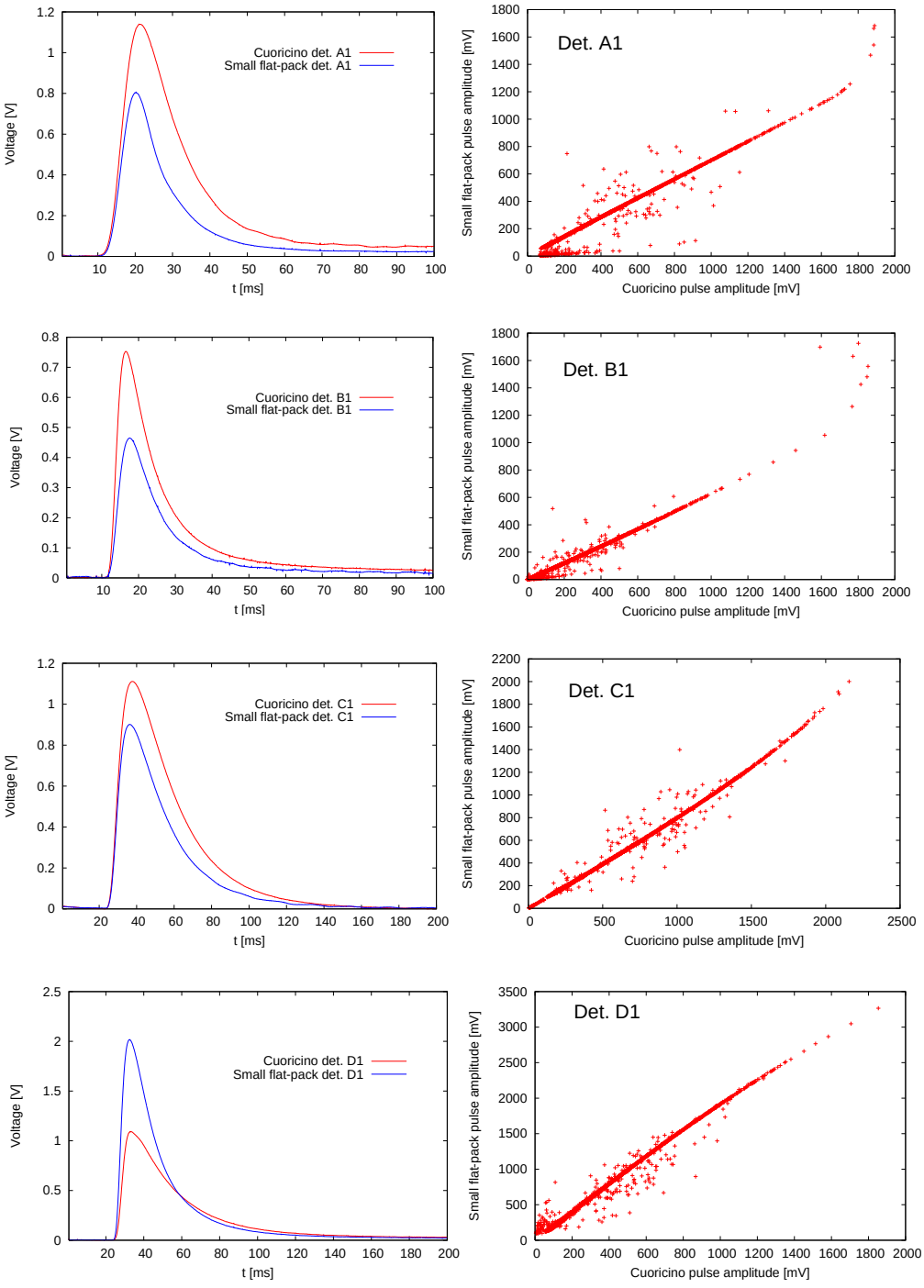

Figure 5.19: For each detector in Test 1, examples of pairs of coincident pulses read by the small flat-pack sensor and the Cuoricino one are reported; each pair is accompanied by the pulse amplitude scatter plot for the relative detector.

Detector	**A1**		**B1**		**C1**		**D1**	
Thermistor	*SF*	*C*	*SF*	*C*	*SF*	*C*	*SF*	*C*
V_w [mV]	3.2	4.5	3.5	3.4	4.3	4.4	4.8	3.7
R_w [MΩ]	0.51	0.72	0.14	0.14	5.15	5.33	0.19	0.08
A [μV/MeV]	52	72	13	22	181	239	143	72

Table 5.6: Test 1: work resistances at the chosen working points V_w and pulse heights in μV/MeV are reported for each thermistor on the four detectors. V_w is the voltage at the terminals of the thermistor.

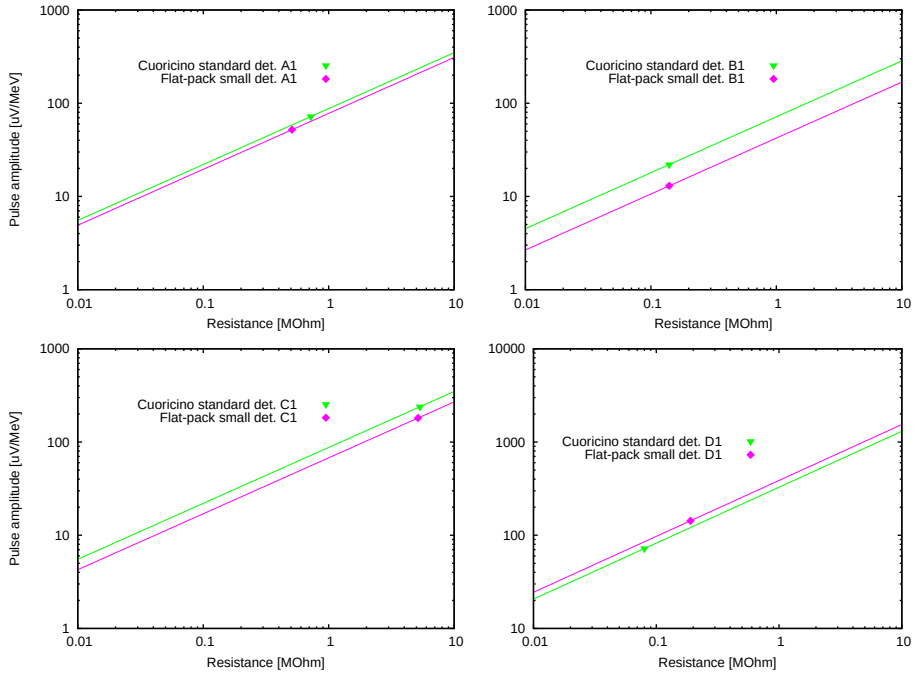

Figure 5.20: Curves of merit for all the thermistors in Test 1: pairs of sensors on the same detector are plotted together for performance comparison; experimental data points (R_w, A) are highlighted. Basing on the motivations exposed in Sec. 5.2.3 and at the beginning of Sec. 5.4, the graphs are obtained by extrapolating from the experimental points a line with 0.5 slope in log-log scale.

DFM [μV/MeV] (@ R_w=1 MΩ)			
Detector	Small flat-pack	Cuoricino standard	SF/C ratio
A1	73	85	0.9
B1	35	59	0.6
C1	80	104	0.8
D1	328	255	1.3

Table 5.7: Test 1: detector Factors of Merit normalized at R_w=1 MΩ. Data is extracted from the corresponding curves of merit. Amplitude ratios are evaluated in the last column.

Dynamic measurements were conducted after the completion of static characterization. Pair of coincident pulses from all four detectors are shown in Fig. 5.19 along with scatter plots of pulse amplitudes. Spectra calibration for the bolometers allowed, then, to gather the requested evaluation of dynamic performance, whose μV/MeV results are listed in Tab. 5.6. The first observation regards the large spread in values from one detector to the other, due to low assembly reproducibility; the effect can also be enhanced by the low statistics available. On the other hand, ratios of detector responses have a narrower distribution, hinting at a coherent behaviour of thermistor pairs belonging to the same bolometer. According to Sec. 5.2.3, the real comparison in performances between thermistors in the same pair is done when work resistances are equal. Curves of merit are extracted by imposing the quoted 0.5 coefficient in log-log scale for small-size prototypes (Fig. 5.20) and DFMs are calculated by normalization at the 1 MΩ value (Tab. 5.7). The comparison at equal R_w leads to the average ratio of small flat-pack to Cuoricino responses of 0.9$\pm$0.3.

The ratios are reasonably next to 1 but the result is far from being conclusive. The described experimental test is flawed by low reproducibility in detector assembly and insufficient statistics: a second run was therefore performed at the R&D facility at LNGS.

5.4.3 Test 2: small flat-packs and large mass detectors

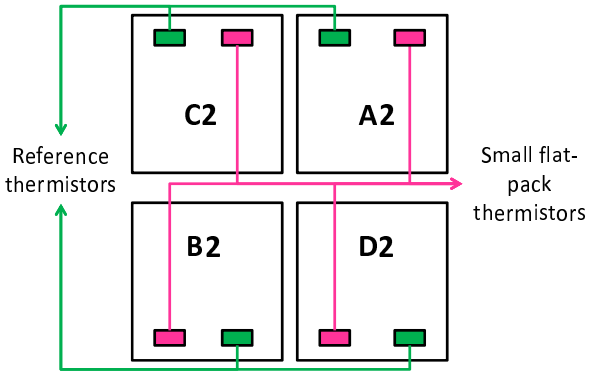

Figure 5.21: Detector scheme for Test 2. The four-crystals plane reported in the picture is part of the three-floors tower of the CCT2 run (see Sec. 4.3.2).

The experimental run on flat-pack thermistors with small geometry at LNGS is not a dedicated test. Four sensors were cooled down in the second Chinese Crystals Test, described in Chapter 4 (Sec. 4.3.2). The run was seen as an opportunity to grab more statistics on the thermistor type under testing by inserting samples in a reliable assembly structure: the attempt is to reduce performance reproducibility issues among separate detectors, which affect results from the Como test described in the previous subsection. As a matter of fact the two possible reasons for the spread in the performance of devices, namely different crystal-to-heat bath couplings among detectors due to copper holders and a possible intrinsic lack in reproducibility of small flat-pack thermistors, cannot be disentangled in the analysis of Test 1. As all the technical details on the run have already been provided, only final results on the small flat-pack thermistors will be shown.

The four detectors of the CCT2 run are sketched in Fig. 5.21. The bolometers equipped with small flat-packs are assembled in the same tower plane. Each sensor with frontal pads is paired with a reference sensor, which is a Cuoricino standard #31

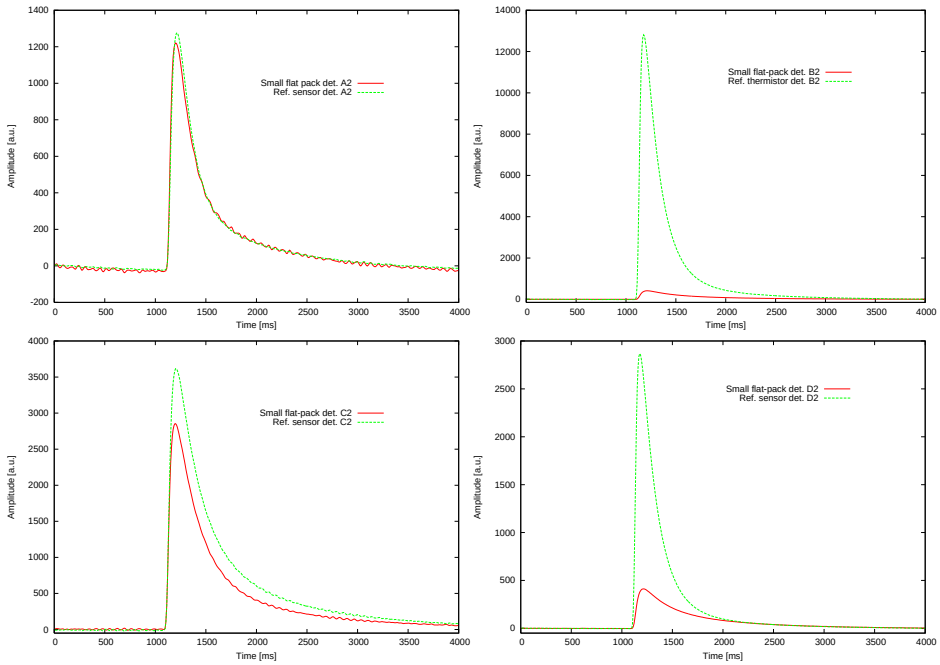

Figure 5.22: Examples of coincident pulses for the small flat-packs and reference thermistors in Test 2 (see Sec. 4.3.2).

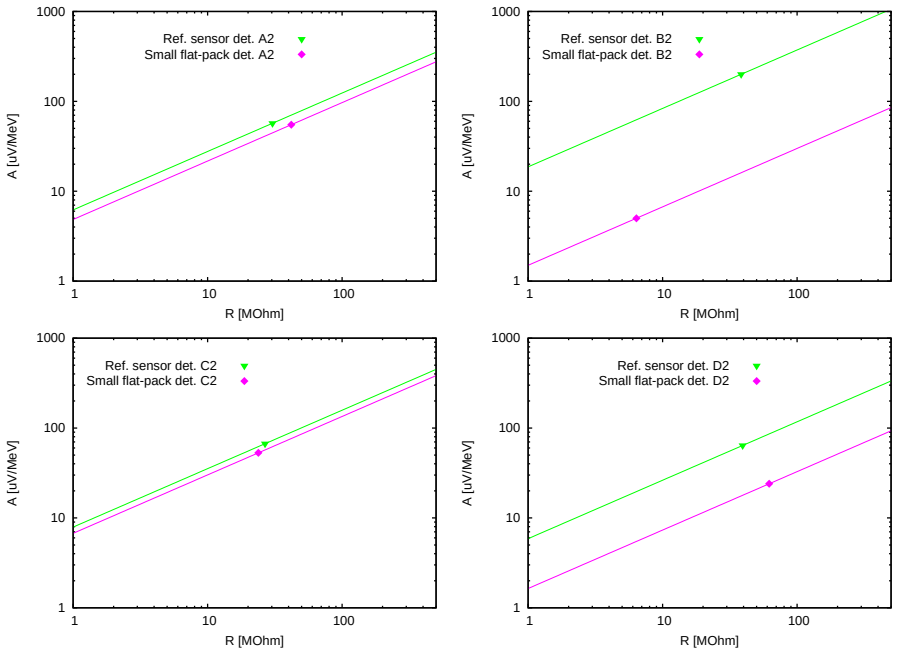

Figure 5.23: Curves of merit for all the thermistors in Test 2. Experimental data points (R_w, A) are highlighted and the corresponding curves of merit extrapolated by imposing a line with slope 0.65 in log-log scale (basing on the motivations exposed in Sec. 5.2.3 and at the beginning of Sec. 5.4).

device only on one out of four detectors (C2); the other three reference sensors are the notched thermistors described in Sec. 5.3: they are bonded laterally, so that no deviations from the usual behaviour of side bonding thermistors is expected, aside from the effects due to the different Ge doping (#34 series instead of #31).

The relationship between work resistances and responses for all the detectors is reported in Tab. 5.8. Pairs of coincident pulses corresponding to the same particle energy deposition in the same absorber are reported in Fig. 5.22 as an example of thermistor behaviour in the work points. Curves of merit in Fig. 5.23 are extrapolated from experimental data points using, in log-log scale, a 0.65 slope: as already explained, such value is justified by simulations and previous R&D results on CUORE-size bolometers. The same extrapolation allows to define DFMs at 100 MΩ, which are listed in Tab. 5.9 along with energy resolutions for detectors A2 and C2 evaluated at the 2615 keV peak. No ΔE is provided for detectors B2 and D2 due to a high ^{210}Po contamination and a consequent high pile-up rate that affects data analysis.

Some observations can be made in comparison with the results of Test 1. While work resistances in the Como run have very different values from one detector to the other, the four bolometers in Test 2 have similar R_w behaviour, exception made for the very low work resistance of the small flat-pack thermistor on B2. This said, the DFM ratios still feature a non negligible spread, although the usual remarks about the low statistics should be kept in mind. In an intuitive picture, bolometers in the LNGS batch behave more similarly to each other than bolometers in the Como run, while DFM ratios are quite different: a possible explanation is that performance similarity among detectors has been increased by the use of a typical R&D setup, while a lack of reproducibility intrinsic to small flat-pack thermistors remains.

As a consequence, the results on flat-pack thermistors with small geometry obtained by both the Como and LNGS tests are not sufficient to endorse the substitution of Cuoricino standard devices. The performances exhibited by frontal bonding sensors hint at a design flaw concerning mainly specific thermal parameters: data suggest that the electron-phonon conductance G_{ph-el} as well as the thermistor-to-absorber coupling G_{th-abs} are too low in the case of small flat-pack sensors. Because the main dependency of the aforementioned parameters is on thermistor volume and footprint area, the intuitive solution is to increase the linear dimensions of the model. As a final remark, it should be pointed out that any considerations on increasing the flat-pack thermistor volume to improve the amplitude of pulses are not conclusive: a change in the volume brings a change in shape and a subsequent modification of the internal electric fields with possible side effects, so that only experimental testing can say the final word.

Detector	**A2**		**B2**		**C2**		**D2**	
Crystal	B71		B72		B73		B74	
Thermistor	*SF*	*Ref*	*SF*	*Ref*	*SF*	*Ref*	*SF*	*Ref*
R_w [MΩ]	41.90	30.37	6.39	38.37	23.85	26.74	62.03	39.38
A [μV/MeV]	55	57	5	200	53	67	24	64

Table 5.8: Work resistances and pulse amplitudes in μV/MeV are reported for each thermistor on the four detectors of Test 2. The names of the 5$\times$5$\times$5 cm^3 crystal absorbers are reported in the second row.

	DFM [μV/MeV] (@ R_w=100 MΩ)			ΔE [keV]	
Detector	SF	Ref	SF/Ref ratio	SF	Ref
A2	97	124	0.8	16	6.7
B2	30	373	0.1	–	–
C2	135	158	0.9	10	7.4
D2	33	117	0.3	–	–

Table 5.9: Detector Factors of Merit normalized at R_w=100 MΩ, amplitude ratios between pairs of sensors and FWHM energy resolutions for the bolometers in Test 2. DFMs are extracted from the corresponding curves of merit. No energy resolutions are given for detectors B2 and D2 because of the motivations explained in the text.

5.5 Flat-pack thermistors with large geometry

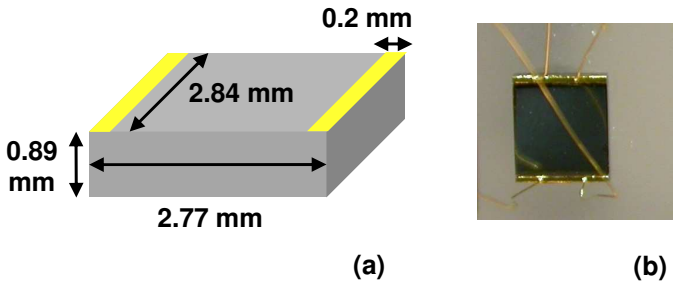

Figure 5.24: The flat-pack thermistor with large geometry.

The response to the poor performances shown by the small flat-pack model is an enhanced device obtained by the same production process but with larger linear dimensions: because it consists on a redesign, the sensor takes the name of *large flat-pack* thermistor. The device is sketched in Fig. 5.24; its parameters are listed in Tab. 5.10. It is evident from the table that the enhanced volume makes the thermal parameters under discussion in the previous section closer to the Cuoricino thermistor values. The deviation in the $R(T)$ behaviour from the Cuoricino standard thermistor due to different size and Ge doping is pictured in Fig. 5.25.

Again, as for small flat-pack thermistors, two kinds of simulations have been performed on large flat-packs: one on DC conductivity, reported in Fig. 5.26, and a thermal one on the static and dynamic behaviour of a bolometer equipped with such thermistor. Static results for large flat-pack thermistors are reported in the graphs of Fig. 5.27, and the *A*-*R* curve is shown in Fig. 5.28. All results are plotted together with the reference curves of the Cuoricino standard thermistor for easier comparison. The *I*-*V* and R/R_b-*P* curves of the large flat-pack are very near those of Cuoricino sensors, probably due to a successful combination of slightly different Ge doping, resistance modified by the geometry and thermal parameters; comparing to small flat-packs, also the *A*-*R* graph looks very promising. The good starting point offered by large flat-pack sensors is confirmed also by the simulated value of the DFM at R_w=100 MΩ: it is $\sim$100 μV/MeV, which should be compared to the 95 computed for the Cuoricino sensor: in principle, large flat-packs have the characteristics to provide even better performances than standard thermistors with lateral pads. The value of the bi-logarithmic slope in the *A*-*R* plane obtained from the simulations is 0.64 (quite similar to the estimation of 0.65 for small flat-packs).

Large flat-pack thermistor properties		Large flat-pack to Cuoricino
Volume	7.00 mm^3	7/9
Pad area	0.57 mm^2	1/5
C_{el}	$7.70\times10^{-9} \cdot T$ J/K	7/9
C_{lat}	$2.10\times10^{-8} \cdot T^3$ J/K	7/9
G_{th-abs}	$2.34\times10^{-3} \cdot T^3$ W/K	1
G_{ph-el}	$5.46\times10^{-1} \cdot T^{4.37}$ W/K	7/9
G_{pad}	$9.10\times10^{-6} \cdot T^{2.4}$ W/K	1/5
$R/\rho = K_{lf}$	1.53 mm^{-1}	
R_0	1.84 Ω	
T_0	3.95 K	

Table 5.10: List of geometric, thermal and electric properties for large flat-pack thermistors. The last column reports, for each property, the approximate ratio of the large flat-pack thermistor value to the Cuoricino thermistor value. The K_{lf} factor was computed from DC conductivity simulations, as shown in Sec. 5.2.2.

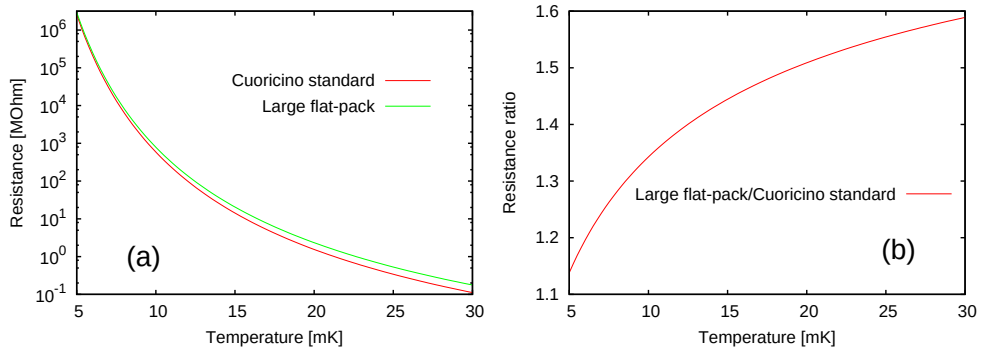

Figure 5.25: (a) $R(T)$ behaviour comparison between the small flat-pack, large flat-pack and Cuoricino standard thermistors in the experimental temperature range of interest. (b) Expected resistance ratio of large flat-pack to Cuoricino standard in the same T range.

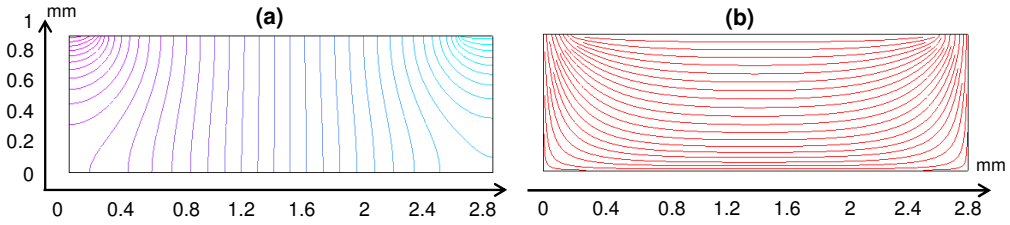

Figure 5.26: DC conductivity 2D-simulations for the large flat-pack device. (a) Equipotential surfaces. (b) Current density lines.

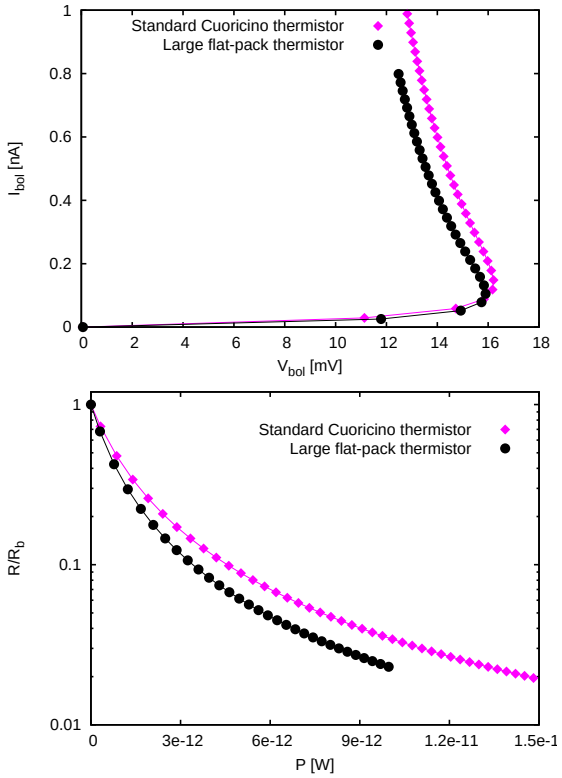

Figure 5.27: Static simulations comparing the behaviour of two CUORE-size bolometers equipped one with a Cuoricino standard sensor and one with a large flat-pack. The *I-V* (left) and the R/R_b-*P* (right) curves are plotted together for direct comparison.

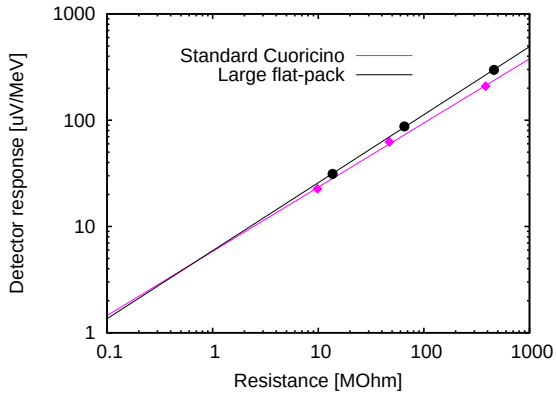

Figure 5.28: Simulated curves of merit of two CUORE-size bolometers equipped one with a Cuoricino standard sensor and one with a large flat-pack.

5.5.1 Test 3: elimination round in Como

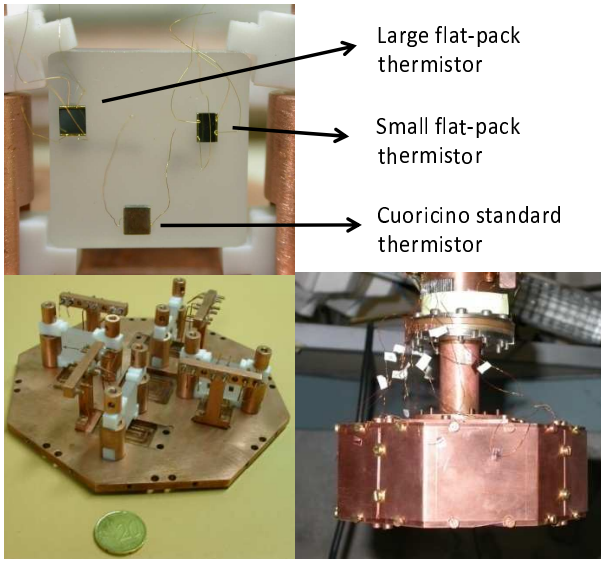

Figure 5.29: Detector pictures for Test 3, the second Como run on flat-pack devices. From upper left, counterclockwise: one of the $2\times2\times0.5$ cm^3 crystal absorbers with the three types of thermistors; the copper holder designed specifically for this run; the final detector attached to the cold finger of the dilution refrigerator.

The first test on flat-pack sensors with large geometry was performed in Como in March 2008, once again with small mass prototypes. The concept of the run slightly differs from the one presented in Sec. 5.4.2, as comparisons are made in triplets of thermistors and not in pairs: in fact, aside from a large flat-pack and a Cuoricino style sensor, a small flat-pack device as well is mounted on each detector for direct comparison. The presence of three thermistors on the same small-size crystal can lead to some degradation of performance, as the heat capacities of the $2\times2\times0.5$ cm^3 absorber and of the sensors become comparable at 10 mK (the C_{abs} value for a CUORE-size crystal is one order of magnitude higher): however, the run's aim of a relative comparison among thermistors connected to the same bolometer makes the consideration negligible.

The four detectors assembled have the following characteristics: as already stated, each $2\times2\times0.5$ cm^3 TeO_2 absorber features one small flat-pack thermistor, one large flat-pack thermistor and one of the Cuoricino type; while large flat-pack thermistors are connected to crystals through the same G_{th-abs} as Cuoricino thermistors, the coupling of small flat-pack sensors is 1/3 of this value. A uranium radioactive source with α peaks at 4.2 MeV and 4.7 MeV lays on the surface of each detector. Another difference with the Como run presented in Sec. 5.4.2 is the use of a detector holder specifically designed to increase performance reproducibility. Pictures of the setup are shown in Fig. 5.29.

The experimental run was signed by two events which limit the analysis of results: data from the Cuoricino thermistor on one detector was lost, allowing comparison on the sole large flat-pack/small flat-pack pair; moreover, in the middle of data taking the LHe-free dilution refrigerator was affected by a super-leak which corrupted the stability of the cryogenic system and shortened the duration of the test.

Detector	R_b [MΩ]			T_b [mK]		
	C	SF	LF	C	SF	LF
A3	0.03	0.35	0.30	38.1	26.5	27.4
B3	1.75	1.26	1.04	19.7	21.7	22.5
C3	0.30	1.08	0.43	25.5	22.2	25.8
D3	–	0.34	0.53	–	26.6	25.0

Table 5.11: Base resistances and temperatures for the Cuoricino standard (C), small flat-pack (SF) and large flat-pack (LF) thermistors on the four detectors in Test 3. No values are given for the Cuoricino-type sensor on bolometer D3 due to channel disconnection.

Detector	Thermistor	V_w [mV]	R_w [MΩ]	A [μV/MeV]
A3	C	1.3	0.05	–
	LF	2.3	0.09	–
	SF	2.2	0.18	–
B3	C	4.1	0.50	37
	LF	3.4	0.40	29
	SF	2.9	0.34	22
C3	C	2.1	0.17	15
	LF	2.5	0.20	15
	SF	2.9	0.47	11
D3	C	–	–	–
	LF	2.5	0.10	14
	SF	2.5	0.30	11

Table 5.12: Work resistances at the chosen working points V_w and pulse amplitudes in μV/MeV for the thermistors on the four detectors in Test 3. As explained in the text, no amplitude values are given for detector A3 and for the Cuoricino thermistor on detector D3.

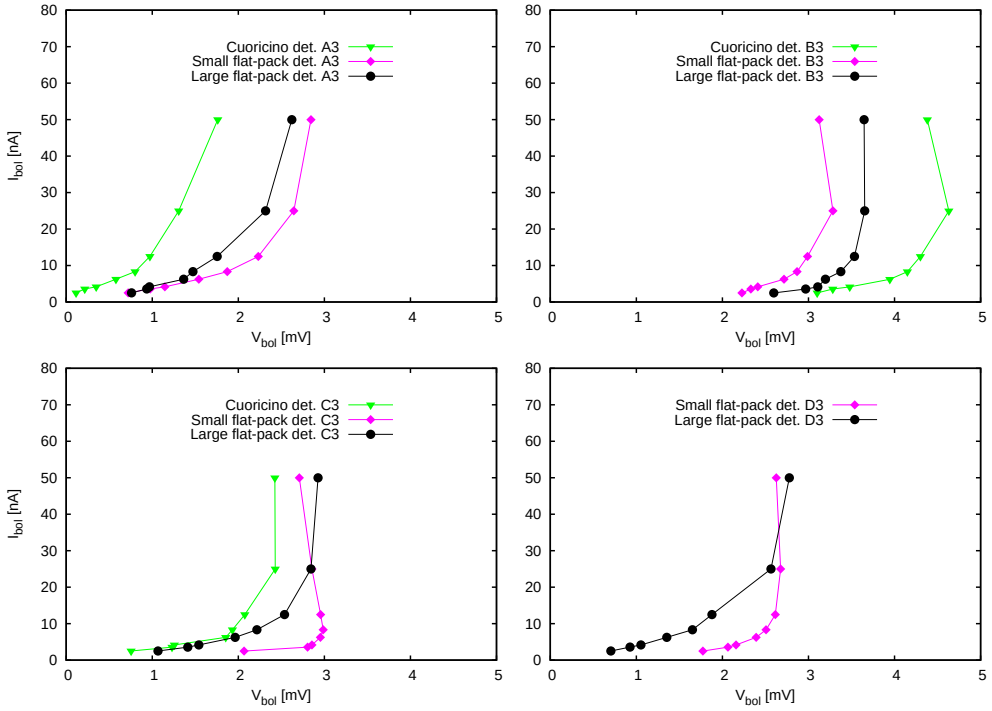

Figure 5.30: *I-V* curves for the thermistors in Test 3.

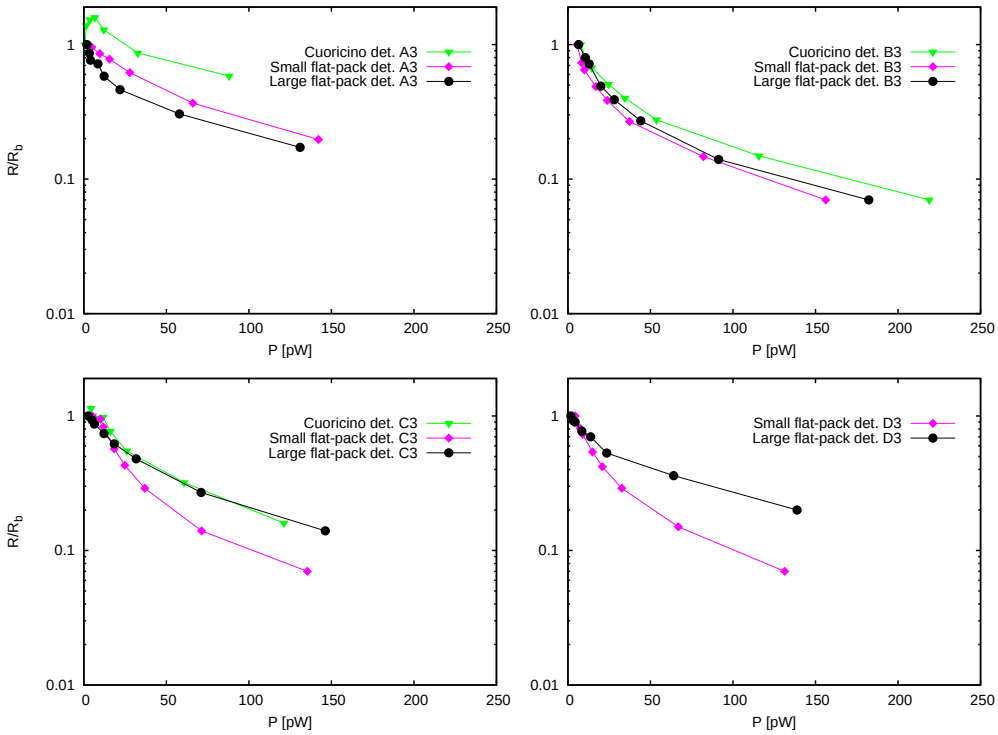

Figure 5.31: *R-P* curves for the detectors in Test 3: the dependant variable is the ratio of R to the base resistance R_b.

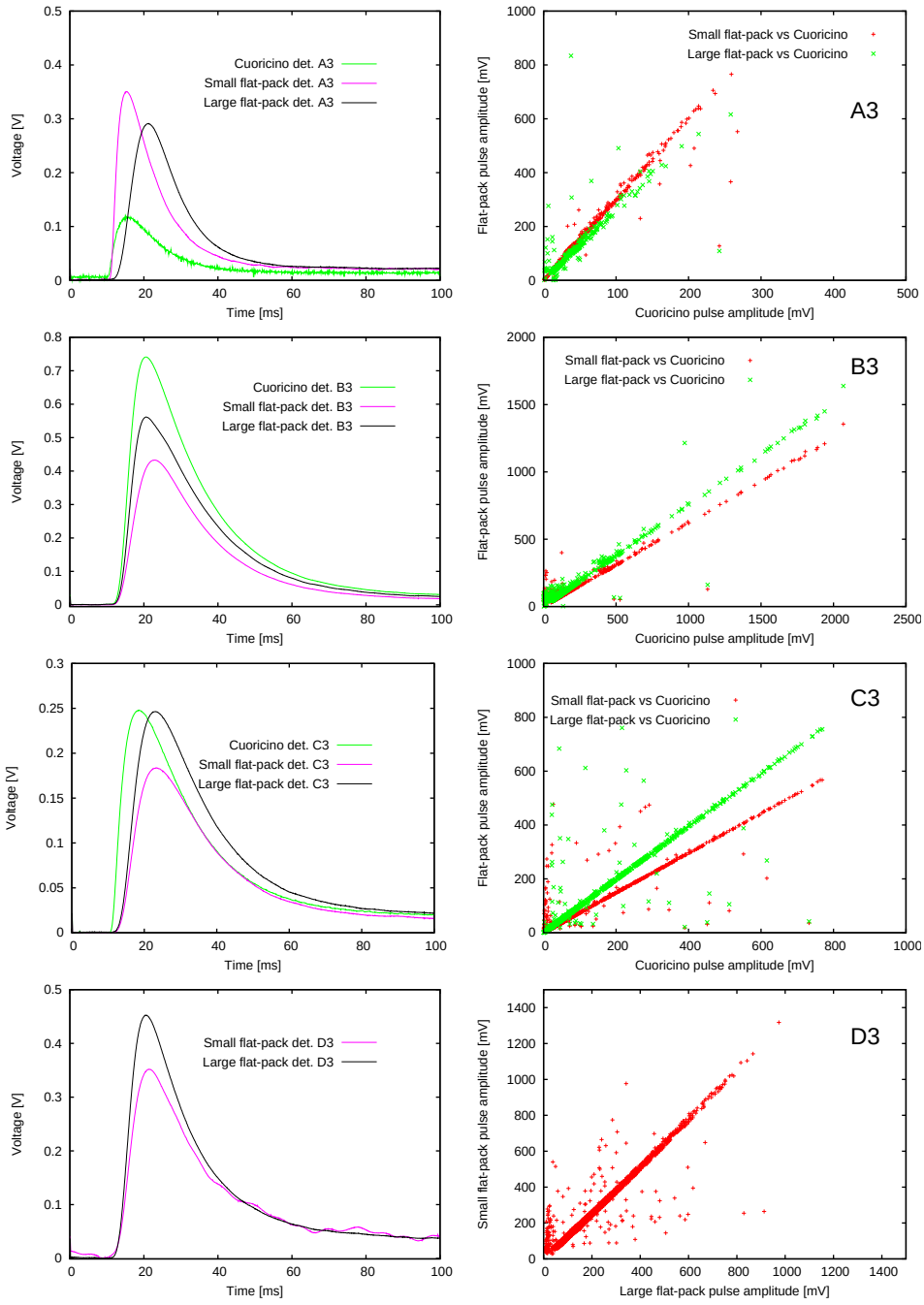

Figure 5.32: Examples of coincident pulses and amplitude scatter plots for the thermistors connected to the same detector in Test 3. Due to the lost channel of the Cuoricino-type thermistor on bolometer D3, the two flat-pack sensors are compared directly in the corresponding scatter plot.

Tab. 5.11 reports the base resistances and temperatures for the 11 remaining readable thermistors in the run; their T_b range from $\sim$20 to 38 mK, although, as already pointed out, the real comparison should be made between resistance values. A striking observation is that the base resistance of the Cuoricino thermistor on A3 is one order of magnitude lower than the R_b of the other two sensors. The static behaviour is then described by the *I-V* and *R-P* curves reported in Fig. 5.30 and Fig. 5.31. In two out of four detectors, large flat-pack thermistors exhibit static behaviour closer to the Cuoricino model than small flat-pack devices, as predicted by simulations on the thermal model; no considerations can be drawn from detector D3 because the Cuoricino reference sensor is missing. On the other hand, data from the first bolometer contradicts the initial observation: the small flat-pack sensor has a better static performance than the other two, considering also that the *R-P* curve of the Cuoricino thermistor shows anomalous features (mainly an initial growth of work resistance with electric power).

As for the dynamic characterization, pair of coincident pulses from all four detectors are shown in Fig. 5.32 along with amplitude scatter plots. The μV/MeV figures are obtained from energy calibration of the spectra acquired from the bolometers. Calibration is not available for the A3 detector due to the lack of understanding of its spectra: large peak structures are present that cannot be brought back to known radioactivity. One possible explanation is an alteration in the bolometer's response due to a loose thermal connection between the crystal and the heat bath. The interpretation is supported by the analysis of baseline fluctuations in time for the three thermistors connected to A3: they feature abrupt variations, which at times even push the signals out of the dynamic voltage range of data acquisition. Detector A3 is therefore affected by a cryogenic instability, whose most probable cause is a loosening of the crystal's coupling to the copper holder. As a consequence, the results exposed previously to compare the static and dynamic behaviour among thermistors on this bolometer should be regarded cautiously in respect to the other three detectors.

The μV/MeV results are listed in Tab. 5.12. Once again, curves of merit are extracted by imposing the quoted 0.5 coefficient for small prototypes (Fig. 5.33) and DFMs are calculated by normalization at the 1 MΩ value (Tab. 5.13). The comparison at equal R_w gives the average ratio of detector responses equal to 0.9 for large flat-pack to Cuoricino thermistors, 0.6$\pm$0.2 for small flat-pack to Cuoricino thermistors and 1.8$\pm$0.5 for large flat-pack to small flat-pack thermistors.

General observations are that the performance of large flat-pack devices seems reasonably close to that of Cuoricino-type devices, and that it outruns the dynamic behaviour of small flat-pack devices. If the superiority of large to small flat-pack thermistors is confirmed, it would mean that one parameter in the thermal model of Fig. 5.2 can be excluded as a source of performance degradation: in fact, G_{pad} is the same for both flat-pack models and for this reason cannot originate the better dynamic results of devices with large geometry. Nonetheless, the test cannot be considered conclusive due to the low statistics collected, which is furthermore thinned by the lost channel and the cryogenically unstable behaviour of one bolometer.

5.5.2 Test 4: large flat-packs at LNGS, first round

Another occasion to evaluate the performance of flat-pack devices with large geometry came in summer 2008, when a R&D run aimed at general purpose thermistor testing was assembled and cooled down at LNGS. Four types of thermistors were investigated on bolometers with large mass absorbers: two large flat-packs, four of the Cuoricino

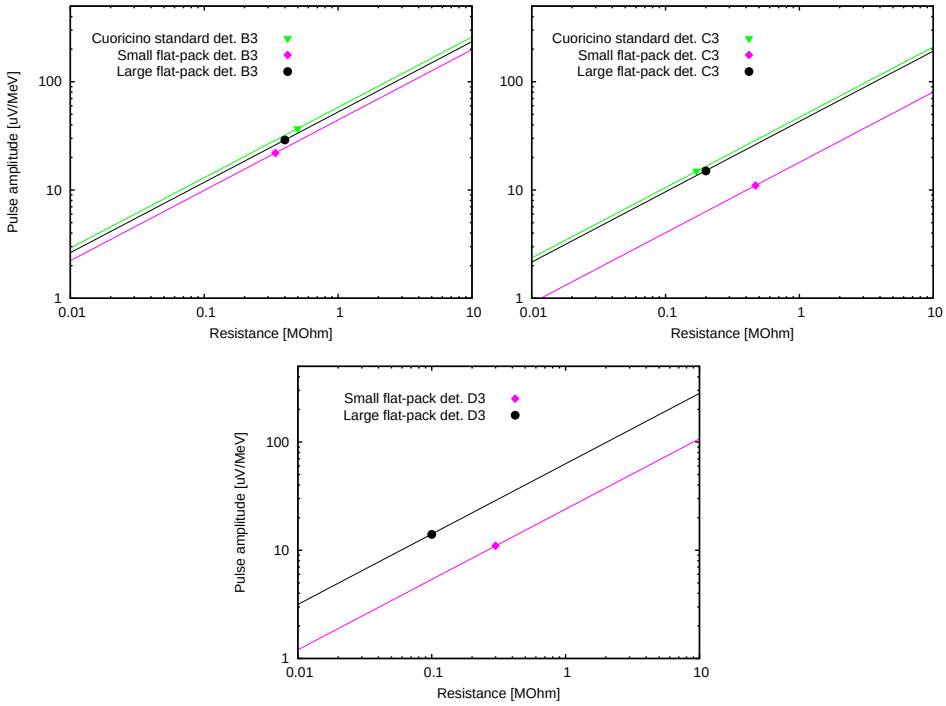

Figure 5.33: Curves of merit for the thermistors in Test 3: triplets or pairs of sensors on the same detector are plotted together for performance comparison; experimental data points (R_w, A) are highlighted. All graphs are obtained by imposing a line with 0.5 slope in a bi-logarithmic scale.

Detector	Thermistor	DFM [μV/MeV] @ 1 MΩ	DFM ratios	
B3	C	52	**LF/C**	0.9
	LF	46	**SF/C**	0.7
	SF	38	**LF/SF**	1.2
C3	C	36	**LF/C**	0.9
	LF	34	**SF/C**	0.4
	SF	16	**LF/SF**	2.1
D3	LF	44	**LF/SF**	2.2
	SF	20		

Table 5.13: Test 3: detector Factors of Merit normalized at R_w=1 MΩ. Data is extracted from the corresponding curves of merit. Amplitude ratios are evaluated in the last column.

kind, two lateral pads sensors belonging to the doping series #40 (different from both #31 and #34), and six devices with frontal bonding that have not been introduced yet and will be described in Sec. 5.6. The analysis presented in this section will focus on results of the sole large flat-packs; as for the other six frontal bonding thermistors, their performances will be reported in Sec. 5.6.2 after a preliminary discussion on their production and characteristics.

The two large flat-pack thermistors, as seen from the detector scheme in Fig. 5.34, are glued separately on two 5×5×5 cm^3 TeO_2 crystals. Each bolometer hosts one of

Temperature	Detector	R_b [MΩ]	T_b [mK]
T1	A4	109.5	12.3
	B4	181.0	11.7
T2	A4	216.4	11.4
	B4	331.4	10.9
T3	A4	1383.0	9.5
	B4	1796.0	9.2

Table 5.14: Base resistances and base temperatures of the two large flat-packs tested in Test 4 (the summer 2008 run at LNGS). The R_b and T_b values are measured at three different stabilization temperatures of the cryogenic system.

Temperature	Detector	R_w [MΩ]	A [μV/MeV]
T1	A4	21.74	78
	B4	38.66	184
T2	A4	83.20	195
	B4	117.70	387
T3	A4	474.00	412
	B4	527.00	687

Table 5.15: Work resistances and pulse amplitudes in μV/MeV of the two large flat-packs operated in Test 4. Values are given for the whole set of stabilization temperatures.

DFM [μV/MeV] (@ R_w=100 MΩ)	
Detector	Large flat-pack
A4	189
B4	316

Table 5.16: Detector Factors of Merit normalized at R_w=100 MΩ for Test 4: data is extrapolated from the corresponding curves of merit.

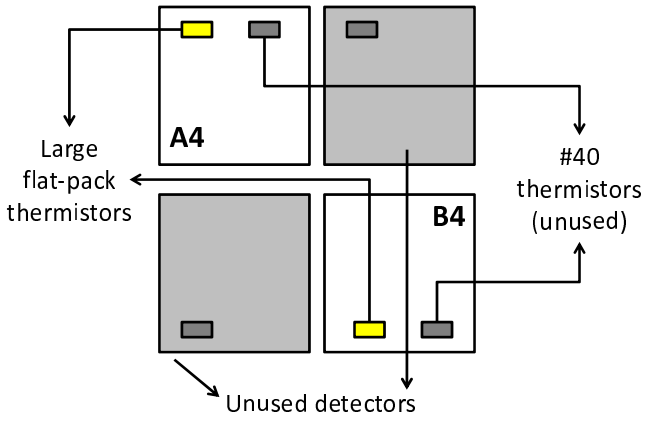

Figure 5.34: Detector scheme for the first LNGS run on large flat-pack devices. The two $5\times5\times5$ cm^3 bolometers marked "unused" in the picture feature another model of frontal bonding thermistors: they will be analyzed in Sec. 5.6.2, where more pictures of the whole detector will also be provided.

them in pair with a #40 thermistor: however, #40 devices cannot be used as reference sensors because, although for another purpose, they are under investigation as well; as a consequence no considerations regarding them will be provided, and data analysis will not feature direct comparisons of large flat-packs with other models of sensors. Useful indications can still be extracted from data analysis and will be integrated in Sec. 5.7 with results from other tests on large mass bolometers.

Static and dynamic measurements were performed at the three base temperatures $T_3 < T_2 < T_1$ at which the cryogenic system was stabilized. Base resistances and temperatures in the three cases are reported in Tab. 5.14. Temperature calculation from the base resistances of the two flat-packs leads to the average values T_1=12.0$\pm$0.2 mK, T_2=11.2$\pm$0.4 mK and T_3=9.3$\pm$0.2 mK. *I-V* and *R-P* static curves are reported in Fig. 5.35 as an example only for the lowest temperature, T_3. Both thermistors reach the inversion point in the *I-V* curves at all stabilization temperatures.

Due to heater channel loss for both detectors, the optimum point search could not be performed by the usual method of plotting pulse amplitude variation to bias voltage following power depositions by the pulser. A ^{40}K source inserted in the cryostat external shielding was used for this purpose. First, the inspection range is constrained by analyzing the shape of load curves, which helps identifying the extension of the optimal working zone; then, 20 minute data-acquisitions are performed at different bias voltage. The optimum point is evaluated by observing the change in position of the ^{40}K peak at 1460 keV. Due to both the length of the procedure and the discrete partition of the full reference voltage, bias voltage was set at rather wide steps in the neighbourhood of the optimum point. The maximum amplitude determined is, for this reason, only a reasonable approximation of the larger true maximum amplitude. This underestimation is more sizeable at the lowest operation temperature T_3 because the bias voltage steps were coarser. However, it is reasonable to estimate that maximum amplitude was determined within 10% - 20% of its real value.

Finally, longer data-acquisitions were performed on the two large flat-pack thermistors operated at the optimum point. Energy spectra were acquired and calibrated to

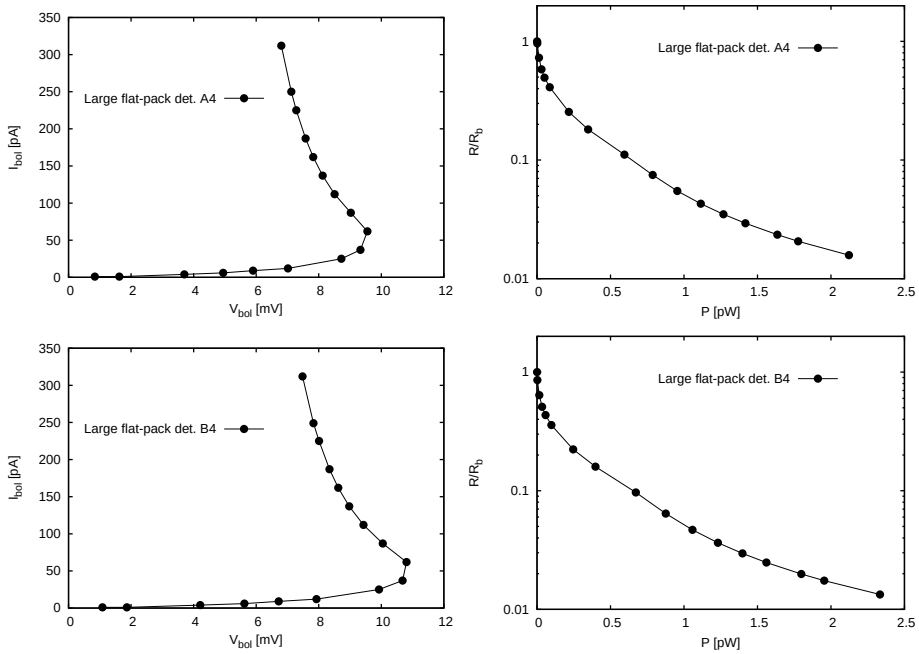

Figure 5.35: *I-V* curves (left) and R/R_b-*P* curves (right) for the two large flat-packs in Test 4. The static curves reported are relative to the stabilization temperature T_3, evaluated as 9.3±0.2 mK.

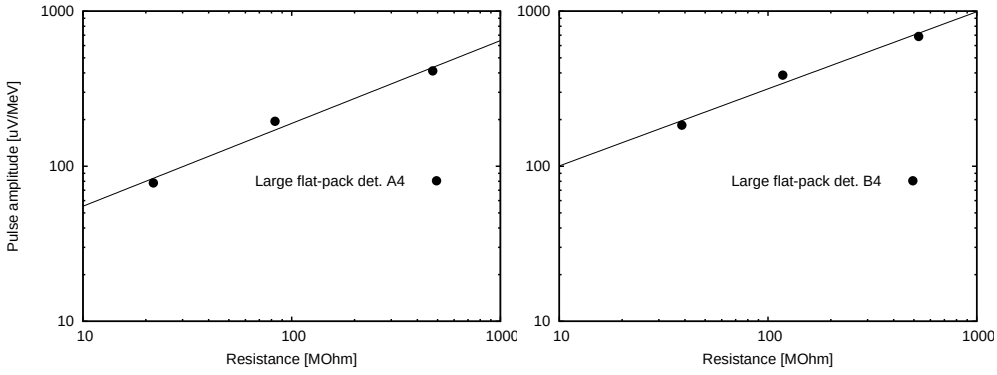

Figure 5.36: Curves of merit for the two large flat-packs in Test 4. Experimental data points (R_w, A) are highlighted and best-fit functions for each data set are plotted. The best-fits, with R_w in MΩ, are $A = 16.15 \cdot R_w^{0.53}$ for detector A4 and $A = 32.00 \cdot R_w^{0.50}$ for detector B4.

obtain detector responses in μV/MeV. Different sources were used: ^{40}K for T_1, ^{232}Th for T_2 and T_3. Results are reported in Tab. 5.15. The stabilization at three base temperatures performed in this run allows to build experimental curves of merit, which are reported in Fig. 5.36, as well as to extrapolate DFMs at 100 MΩ by best-fitting each data set. Data presented in Tab. 5.16 can be considered outstanding. Performances featured in this run by the two large flat-pack devices are very promising even though the statistics is too narrow to draw any conclusions. Test results, however, point strongly towards further investigation on flat-pack thermistors with large geometry.

5.5.3 Test 5: large flat-packs at LNGS, second round

Detector	Crystal	A [μV/MeV]	
		LF	Ref
A5	B15	93	–
B5	B25	22	86

Table 5.17: Responses of the two remaining detectors with large flat-pack thermistors in the Three Towers run (here called Test 5).

The second test on large flat-pack thermistors at LNGS was inserted in a R&D run that has already been introduced in Chapter 3: the Three Towers Test. Eight flat-pack thermistors were glued on detectors belonging to the tower cleaned with the Gran Sasso procedure. The run was discussed by omitting to mention the presence of sensors with frontal bonding. Only final performance results will be provided in this section. Data analysis is affected by the loss of a great number of read-out channels, as already mentioned in Sec. 3.4.2: only two out of the eight channels connected to large flat-pack thermistors survived the cool-down of the towers. Coherently with the denomination used in this chapter, the two bolometers hosting the remaining flat-pack samples will be called A5 and B5. Each detector is equipped with a large flat-pack and a reference sensor, which is a #40 thermistor on A5 and a Cuoricino standard #31 thermistor on B5. Data referred to the #40 thermistor on A5 will be omitted for the reasons already explained in Sec. 5.5.2. Tab 5.17 is a summary of the μV/MeV responses featured by the thermistors on A5 and B5. The exact value of work resistances is not reported, although they are in the range of 100 MΩ. The unfortunate course of the test, which resulted in the 75% of frontal bonding thermistors lost, makes the statistics of this test inadequate to drawing any conclusions on thermistor performance. The limited results of this run will be therefore incorporated with those of the other tests and discussed in general terms in the conclusive section (Sec. 5.7).

5.6 Wrap-around thermistors

Before the experimental testing of large flat-packs was concluded, another model of thermistors had already been designed and put in production. The reason behind the proposal of a new model of sensor with frontal contacts lies in the attempt to create a thermistor with more reliable and replicable performances by exploiting the knowledge obtained from flat-pack devices. The proposed *wrap-around* thermistors are designed to merge in one device all the desired thermal properties highlighted by experimental tests with the electric properties of the Cuoricino thermistor, avoiding any possible

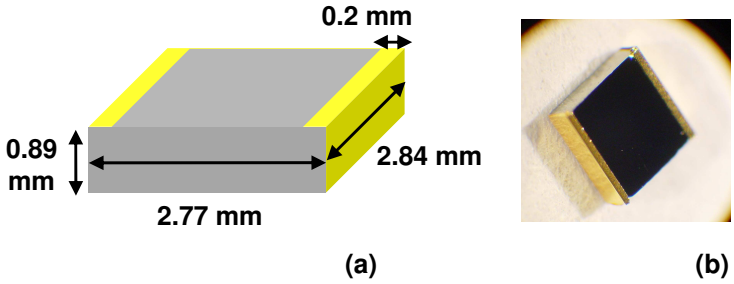

Figure 5.37: Scheme and picture of the wrap-around thermistor.

modification of the G_{ph-el} conductance driven by non-uniformity of the electric field. Basically, wrap-around devices can be seen as large flat-pack thermistors where frontal contacts coexist with lateral Cuoricino pads. The denomination "wrap-around" comes from the fact that the Ge bulk literally looks wrapped in the gold layer for electric contacts. Fig. 5.37 and Tab. 5.18 show that these sensors share volume and most thermal parameters with the large flat-packs. At the same time, the presence of lateral pads makes their resistive behaviour closer to that of Cuoricino thermistors: DC conductivity simulations (see Fig. 5.38) allowed to compute the geometry-dependent K factor of proportionality between R and ρ, which is K_{wa}=1.06 mm$-$1 and is very similar to the parameter l/S=1 mm^{-1} that holds for Cuoricino standard sensors; the two $R(T)$ laws, which take also into account the doping difference in the starting Ge materials, are plotted for convenience in Fig. 5.39). In addition to that, larger pads imply higher G_{pad} as well, but experimental tests have evidenced that this factor apparently does not influence dynamic performances.

The reason why this almost obvious solution was not proposed at first, before flat-pack design and study took place, has already been mentioned in Sec. 5.3: the idea of a Cuoricino model with upper surface pads constituted the first attempt to approach the problem of frontal bonding, and was discarded due to the unacceptable length of the production process implied. The easy manufacturing of flat-packs pushed efforts in their direction, but in the end they do not guarantee enough reproducibility of performance; the knowledge gathered with the preceding models eventually helped in defining the production process for wrap-around thermistors. Nonetheless, the higher similarity to the Cuoricino sensors used as reference is still at expense of a manufacturing procedure slower and more delicate than the one underwent by both flat-pack models. In fact, gold coating must take place in separate steps due to the position of pads on both the thermistor's upper surface and sides.

Once again, with the same routines followed in the case of the two flat-packs model, the simulated performance of a 5$\times$5$\times$5 cm^3 bolometer equipped with a wrap-around thermistor was compared to the simulated performance of another detector with same absorber size connected to a Cuoricino standard device. Static results are reported in the graphs of Fig. 5.40; the A-R curves are shown in Fig. 5.41. The simulated I-V and R/R_b-P plots for the wrap-around thermistor are in the neighbourhood of those simulated for the Cuoricino sensor, and the same holds for the A-R graphs. However, simulated results are less promising than those obtained for large flat-pack thermistors in Sec. 5.5. For example, the simulated DFM at R_w=100 MΩ for the wrap-around is $\sim$80 μV/MeV, which should be compared to the 95 μV/MeV value of the Cuoricino sensor: this is not discouraging because the two values are very near; also, simulations based on the composite thermal model have only a qualitative meaning and must not be considered reliable for quantitative predictions. Only experimental testing can reveal

Wrap-around thermistor properties		Wrap-around to Cuoricino
Volume	7.00 mm^3	7/9
Pad area	3.1 mm^2	1
C_{el}	$7.70\times10^{-9}\cdot T$ J/K	7/9
C_{lat}	$2.10\times10^{-8}\cdot T^3$ J/K	7/9
G_{th-abs}	$2.34\times10^{-3}\cdot T^3$ W/K	1
G_{ph-el}	$5.46\times10^{-1}\cdot T^{4.37}$ W/K	7/9
G_{pad}	$4.96\times10^{-5}\cdot T^{2.4}$ W/K	1
$R/\rho = K_{wa}$	1.06 mm^{-1}	
R_0	1.27 Ω	
T_0	3.95 K	

Table 5.18: List of geometric, thermal and electric properties for wrap-around thermistors. The last column reports, for each thermal property, the approximate ratio of the wrap-around thermistor value to the Cuoricino thermistor value.

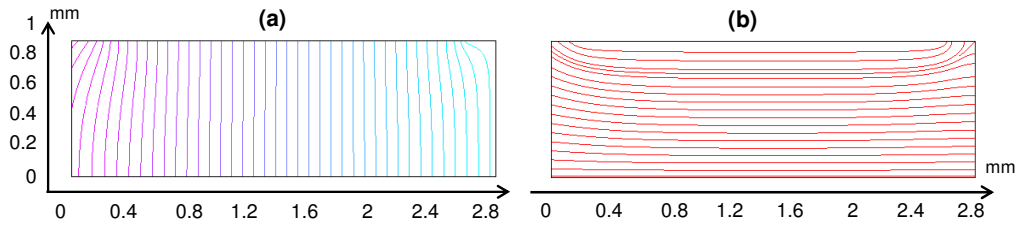

Figure 5.38: DC conductivity simulations: the wrap-around device. (a) Equipotential surfaces. (b) Current density lines.

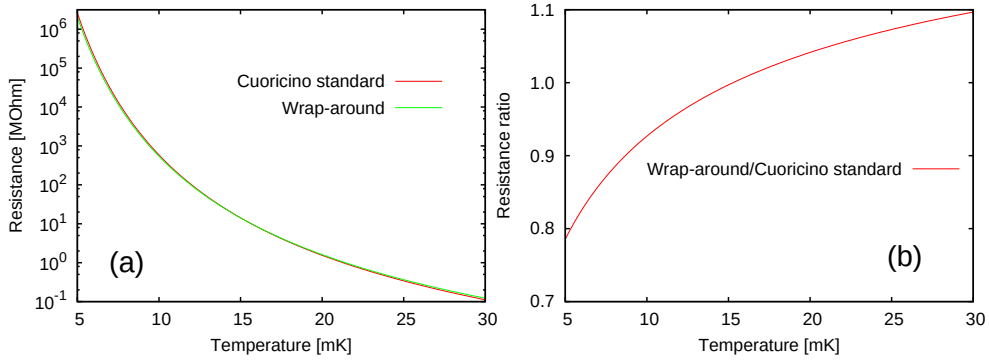

Figure 5.39: (a) $R(T)$ behaviour comparison between the wrap-around, small flat-pack, large flat-pack and Cuoricino standard thermistors in the experimental temperature range of interest. (b) Expected resistance ratio of wrap-around to Cuoricino standard in the same T range.

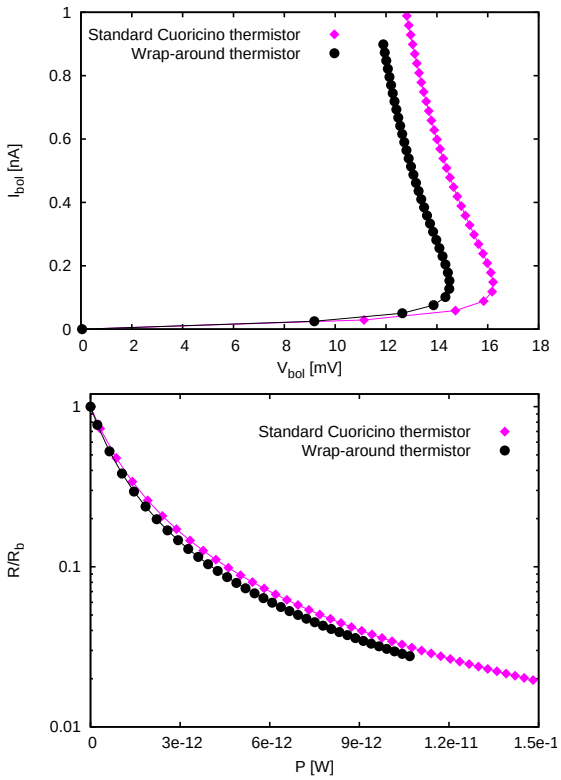

Figure 5.40: Simulated static behaviour of two CUORE-size bolometers equipped one with a Cuoricino standard sensor and one with a wrap-around device. The *I-V* (left) and the R/R_b-*P* (right) curves are plotted together for direct comparison.

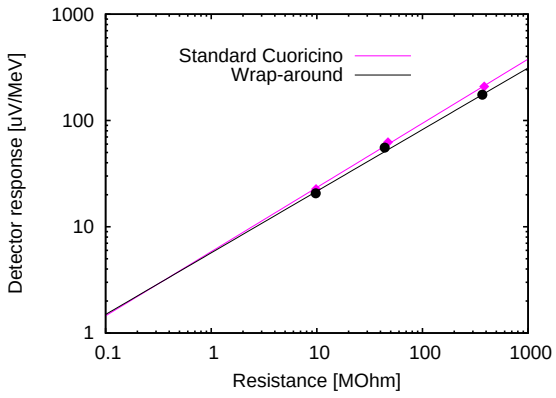

Figure 5.41: Simulated curves of merit of two CUORE-size bolometers equipped one with a Cuoricino standard sensor and one with a wrap-around device.

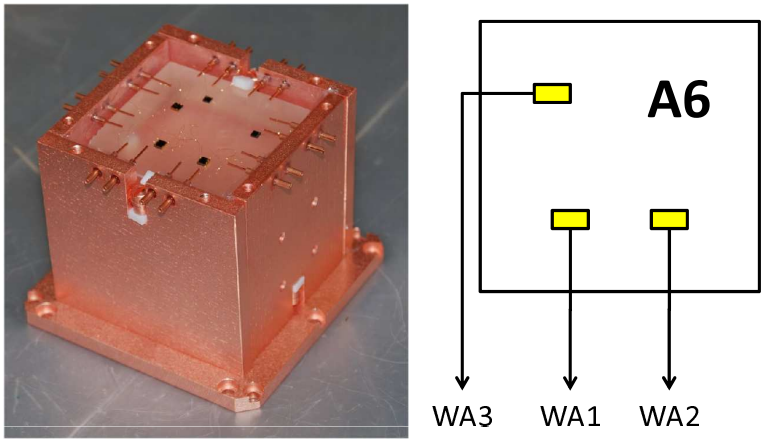

Figure 5.42: Detector scheme and picture for the first LNGS run on wrap-around devices. The $5\times5\times5$ cm^3 bolometer is enclosed in a copper holder different from the usual CUORE-0 R&D setup. Two Si heaters, seen in the picture but not reported in the scheme, are also connected to the crystal absorber.

the potentialities of the thermistor designs. To complete the preliminary picture, the two theoretical curves of merit have slightly different slopes, with a smoother dependence for the wrap-around (0.58 instead of the 0.65 found for the Cuoricino sensor).

Unlike the previous models, wrap-around thermistors have not been tested above-ground on small-size bolometric prototypes but only at the R&D facility in Hall C at LNGS.

5.6.1 Test 6: meet the wrap-arounds

The run presented hereafter can be considered an introductory test on wrap-around thermistors because it was not designed as a dedicated study on this model of sensors: due to the concurrent measurement of a $5\times5\times5$ cm^3 ^{222}Rn exposed TeO_2 crystal, in April 2008 the chance was taken to get preliminary information about their behaviour. Therefore, three wrap-around thermistors were connected to the crystal under investigation with no Cuoricino sensors as a reference. Fig. 5.42 shows pictures of the bolometer inside the copper holder, which is remarkably different from the usual CUORE-0 R&D structure and includes a total of four PTFE holders instead of the usual eight. The crystal is equipped with two Si heaters as well. The single detector measured in this experimental run will be called A6 from now on, consistently with the other tests presented in this chapter.

Static measurements are presented at three different stabilization temperatures of the cryogenic system, $T_1 < T_2 < T_3$. Average values for them are calculated from data in Tab. 5.19: T_1=12.2$\pm$0.8 mK, T_2=12.6$\pm$0.9 mK and T_3=13.2$\pm$1.0 mK. *I-V* and *R-P* curves are reported in Fig. 5.43 as an example only for the lowest temperature, T_1. The abrupt steps appearing in the voltage variation at the terminals of sensor W1 are due to an unrecovered sudden change in the offset of the preamplifier; other static features of the three thermistors are compatible with Cuoricino-like observed behavior, in both shape and position of the inversion point.

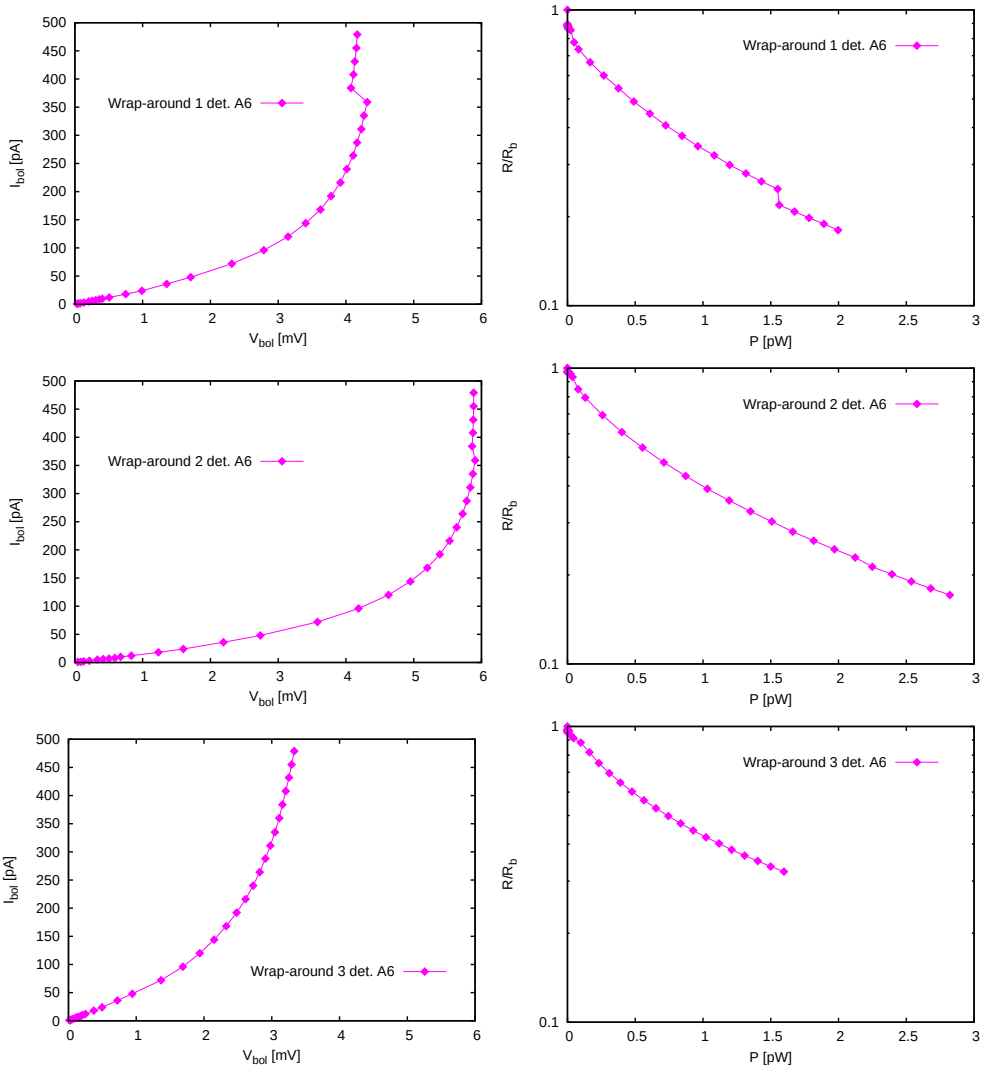

Figure 5.43: *I-V* curves (left) and R/R_b-*P* curves (right) for the two flat-packs in Test 6. The static curves reported are relative to the stabilization temperature T_1, the lowest of the set, evaluated as 12.2±0.8 mK.

Temperature	Thermistor	R_b [MΩ]	T_b [mK]
T1	A6-WA1	93.31	12.0
	A6-WA2	150.89	11.4
	A6-WA3	44.82	13.1
T2	A6-WA1	66.36	12.5
	A6-WA2	113.09	11.8
	A6-WA3	34.06	13.5
T3	A6-WA1	48.41	13.0
	A6-WA2	71.75	12.4
	A6-WA3	21.50	14.3

Table 5.19: Base resistances and base temperatures of the three wrap-arounds operated in Test 6. The R_b and T_b values are measured at three different stabilization temperatures of the cryogenic system.

Preliminary to dynamic measurements, the optimum point was evaluated at all stabilization temperatures for the three thermistors. The presence of heaters allowed the use of the canonic method for optimum point determination: a signal with fixed amplitude is sent through one heater from the pulser; bias voltage is changed and the consequent pulse amplitude read by the wrap around thermistor is registered. The particle-like energy corresponding to such excitation is determined in a subsequent step, through calibration of energy spectra: detector responses in μV/MeV are therefore measurable. They are presented, along with optimum points and work resistances, in Tab. 5.20. Values of V_{bol}, R_w and A at temperatures T_1 and T_2 look almost indistinguishable, so that the two regimes can be considered degenerate: this appears to contradict the difference in static behaviour observed previously. The reason is a temperature drift which substantially equaled T_1 and T_2 after load curves were recorded. From now on, $T_1 \sim T_2$ and the two regimes will be considered degenerate as far as the A-R relationship is considered.

The data points A-R_w reported in Tab. 5.20 are collected in single curves of merit (Fig. 5.44), whose best-fits allow DFM extrapolation at 100 MΩ (Tab. 5.21).

Although a direct comparison with the statistics obtained from Cuoricino will be presented in Sec. 5.7, a few remarks regarding the values obtained can be made. One thermistor gives pulses abnormally low with respect to Cuoricino; performances by the other two thermistors seem to be compatible with Cuoricino pulse height results, even if slightly lower. Since the wrap-around thermistors are geometrically identical and reproducible in terms of $R(T)$ curves, there is a high chance that the bad behaviour of one of the sensors is due to a bad thermistor-to-absorber coupling.

A necessary note regarding the performances seen in this test is that three thermistors are connected to the same crystal, instead of the single sensor on Cuoricino bolometers and the pair on CUORE-0 R&D runs. In line of principle, this should not lead to any degradations in performance because the thermistor's heat capacity is lower than the crystal's one by one order of magnitude at 10 mK, even though the assumption was made of an increase at low temperature coming from a magnetic component associated to boron implantation [122].

Temperature	Thermistor	V_{bol} [mV]	R_w [MΩ]	A [μV/MeV]
T1	A6-WA1	3.76	52.28	25
	A6-WA2	5.31	73.89	84
	A6-WA3	3.02	25.24	41
T2	A6-WA1	3.45	47.97	26
	A6-WA2	4.99	69.39	87
	A6-WA3	2.79	23.33	43
T3	A6-WA1	3.15	26.27	15
	A6-WA2	4.19	43.66	55
	A6-WA3	2.48	12.94	25

Table 5.20: Optimum points, work resistances and detector responses in μV/MeV of the wrap-around thermistors measured in Test 6. Values are given for the whole set of stabilization temperatures.

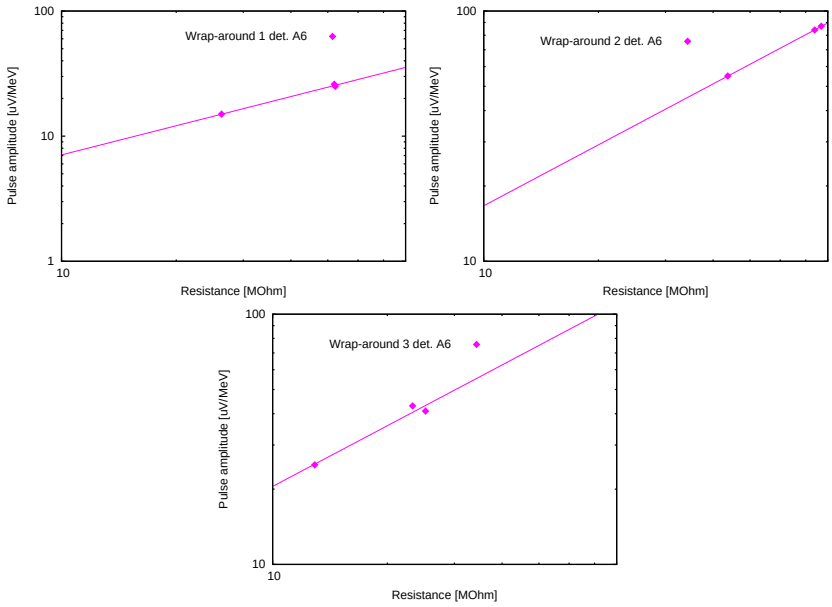

Figure 5.44: Detector curves of merit in the first LNGS run on wrap-around thermistors. Experimental data points (R_w, A) are highlighted and best-fit functions for each data set are plotted. The best-fits, with R_w in MΩ, are $A = 1.19 \cdot R_w^{0.77}$ for thermistor W1, $A = 2.58 \cdot R_w^{0.81}$ for thermistor WA2 and $A = 3.20 \cdot R_w^{0.81}$.

Thermistor	DFM [μV/MeV] (@ R_w=100 MΩ)
A6-WA1	42
A6-WA2	107
A6-WA3	131

Table 5.21: Test 6: detector Factors of Merit normalized at R_w=100 MΩ for the thermistors on detector A6. Data is extrapolated from the corresponding curves of merit.

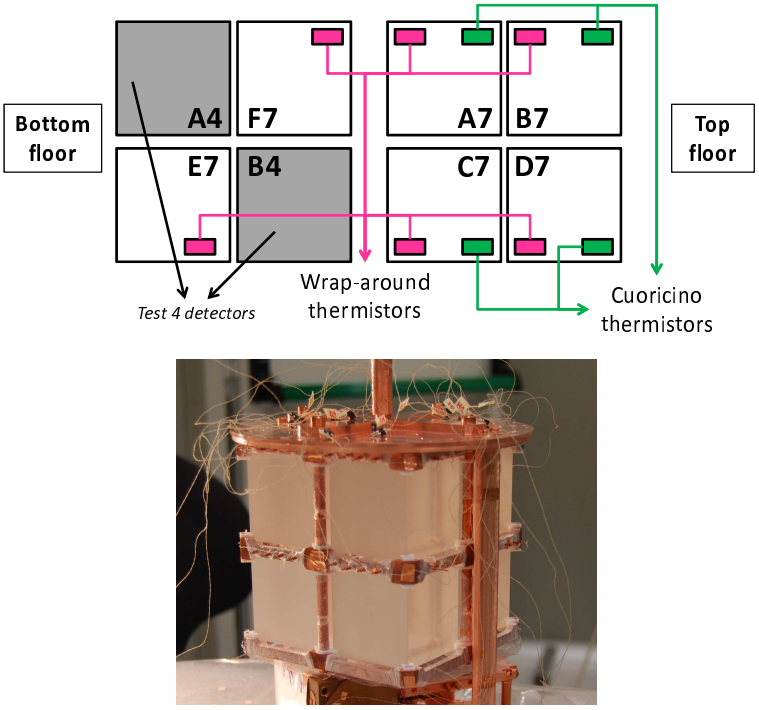

Figure 5.45: Detector scheme and picture for the second LNGS run on wrap-around devices, called Test 7. Analysis of detectors A4 and B4 has already been presented in Sec. 5.5.2.

Given the previous considerations on both gluing and the number of thermistors, only a test featuring direct comparison with a sensor model used as reference can give an ultimate answer regarding the usability of wrap-around thermistors in CUORE-0.

5.6.2 Test 7: final run at LNGS

The last experimental run on thermistors with frontal pads was performed in the summer 2008 at LNGS and was specifically aimed at wrap-around sensors testing. The run has already been introduced in Sec. 5.5.2, although results have been provided for just the large flat-pack devices, placed on two out of eight total bolometers. This section will detail the performance of the wrap-around thermistors cooled down in the run.

The total eight $5\times5\times5$ cm^3 bolometers in the test are equipped with different types of thermistors: wrap-arounds, large flat-packs, standard Cuoricino and samples of the #40 doping series. Four crystal absorbers host a wrap-around and a Cuoricino standard thermistor; two are connected to one wrap-around thermistor each; and two have a pair of large flat-pack and #40 thermistors each. Fig. 5.45 reports the scheme of the detector, along with pictures. Results from the two bolometers with large flat-packs have already been presented; moreover, as mentioned in Sec. 5.5.2, #40 thermistors are beyond the aim of this discussion: only six bolometers will be analyzed hereafter, four of which allow comparative testing of wrap-around to Cuoricino thermistors, and two of which give results on wrap-arounds alone.

Both static and dynamic measurements were taken at three stabilization temperatures of the cryogenic system. Tab. 5.22 sums up base resistances and temperatures read by the thermistors under study. The average temperatures are T_1=12.9±0.8, T_2=12.0±0.9 and T_3=9.7±0.7: they are all 1 mK systematically higher than the mean values obtained by reading out flat-pack thermistors (see Tab. 5.14). The static behaviour featured by wrap-arounds is compatible with that of the Cuoricino reference sensors: this is reported in the *I-V* and R/R_b-*P* static curves shown in Fig. 5.46 and 5.47. Only plots relative to the lowest stabilization temperature, T_3, are shown as an example.

Optimum point search was conducted in two separate ways for "paired" and "single" wrap-around thermistors. Detectors from A7 to D7 had, in fact, a heater connection, which was not available for bolometers E7 and F7. Both ways have been already described in the previous sections. As long as A7, B7, C7 and D7 are concerned, the optimum point search was performed by plotting pulse amplitude variation to bias voltage following power depositions by the pulser; in the case of E7 and F7, the shift of the ^{40}K peak in energy spectra was evaluated by performing brief data-acquisitions at different bias voltage. Working point resistances and pulse amplitudes are listed in Tab. 5.23. Once again, direct comparison is still not conclusive at this point, due to different values of working resistances among thermistors. Experimental (R_w, A) points are plotted in a bi-logarithmic scale in Fig. 5.48, and best-fits are extracted. The function for curve of merit fitting is, as in the previous runs, A=a·R^b. The mean value of b, which is the slope in log-log scale, is estimated as 0.63±0.09 by averaging on all ten thermistors: the value is compatible with the coefficients used in other sections of this chapter to extract curves of merit when just one experimental data point is available; it is also coherent with the b value obtained by the fitting of curves of merit for detectors in the Cuoricino tower.

The final step is DFM extrapolation at 100 MΩ from the shown fitting of *A-R* curves. Results are listed in Tab. 5.24, comprehensive of amplitude ratios when available. Moreover, energy resolutions are reported: they are calculated at the 2615 keV peak at the lowest temperature T_3. The average percentage resolution FWHM at this temperature is $\Delta E/E$=0.53±0.27% for wrap-around thermistors and $\Delta E/E$=0.41±0.16% for the Cuoricino standard ones: the two values are compatible. As for pulse amplitudes, three out of four paired wrap-around thermistors perform better than the corresponding Cuoricino reference sensors; both single wrap-around thermistors show performances compatible with results from the Cuoricino statistics. The next section will clarify this sentence through a comparison of all the results gathered from data presented in this chapter; it will also justify the ultimate decision of wrap-around sensors as the thermistor model to be used in CUORE-0.

5.7 Drawing conclusions: the choice for CUORE-0

The two categories of runs performed, the ones with small-size prototypes and those with CUORE-like bolometers, contributed in different ways to the study of thermistor performance. Experimental tests in Como using small detectors (tests 1 and 3) are useful to get introductive information about the behaviour of frontal bonding thermistors; results obtained from them are not conclusive, and no absolute evaluation can be drawn because of the degradation in performance originated by the connection of sensor triplets to the same small-size absorber. Relative evaluations among different models are still possible, although the low statistics gathered must be considered. The tests were performed on flat-pack devices with both small and large geometry, which were compared to samples of Cuoricino thermistors used as a reference. Fig. 5.49 sums up the results

		Wrap-around		Cuoricino	
Temperature	**Detector**	R_b **[MΩ]**	T_b **[mK]**	R_b **[MΩ]**	T_b **[mK]**
T_1	A7	60.78	11.2	152.21	9.5
	B7	53.18	11.4	45.57	10.9
	C7	22.78	12.5	37.97	11.1
	D7	56.22	11.3	31.89	11.4
	E7	97.32	10.7	–	–
	F7	57.74	11.3	–	–
T_2	A7	124.75	10.4	323.70	8.8
	B7	107.98	10.6	91.22	10.1
	C7	39.49	11.8	60.78	10.5
	D7	107.98	10.6	34.93	11.2
	E7	185.81	10.0	–	–
	F7	115.60	10.5	–	–
T_3	A7	1094.60	8.4	2333.20	7.3
	B7	951.67	7.8	757.94	8.1
	C7	289.46	9.6	501.75	8.4
	D7	862.94	8.6	271.39	9.0
	E7	1437.27	8.2	–	–
	F7	944.26	8.5	–	–

Table 5.22: Base resistances and base temperatures for the thermistors under study in Test 7, given at the three stabilization temperatures of the cryogenic system.

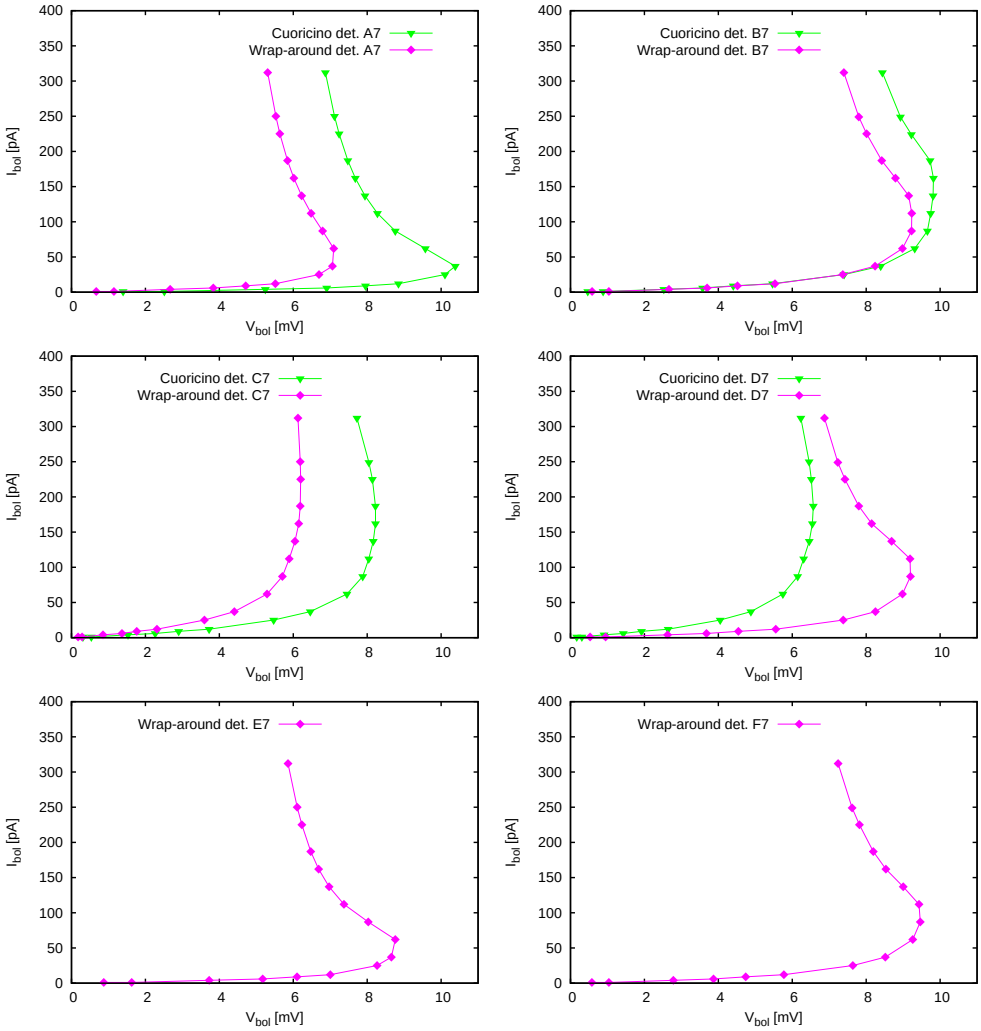

Figure 5.46: *I-V* curves for the thermistors in Test 7, plotted together when belonging to the same bolometer. The static curves reported are relative to the stabilization temperature T_3, the lowest of the set, evaluated as 9.7$\pm$0.7 mK.

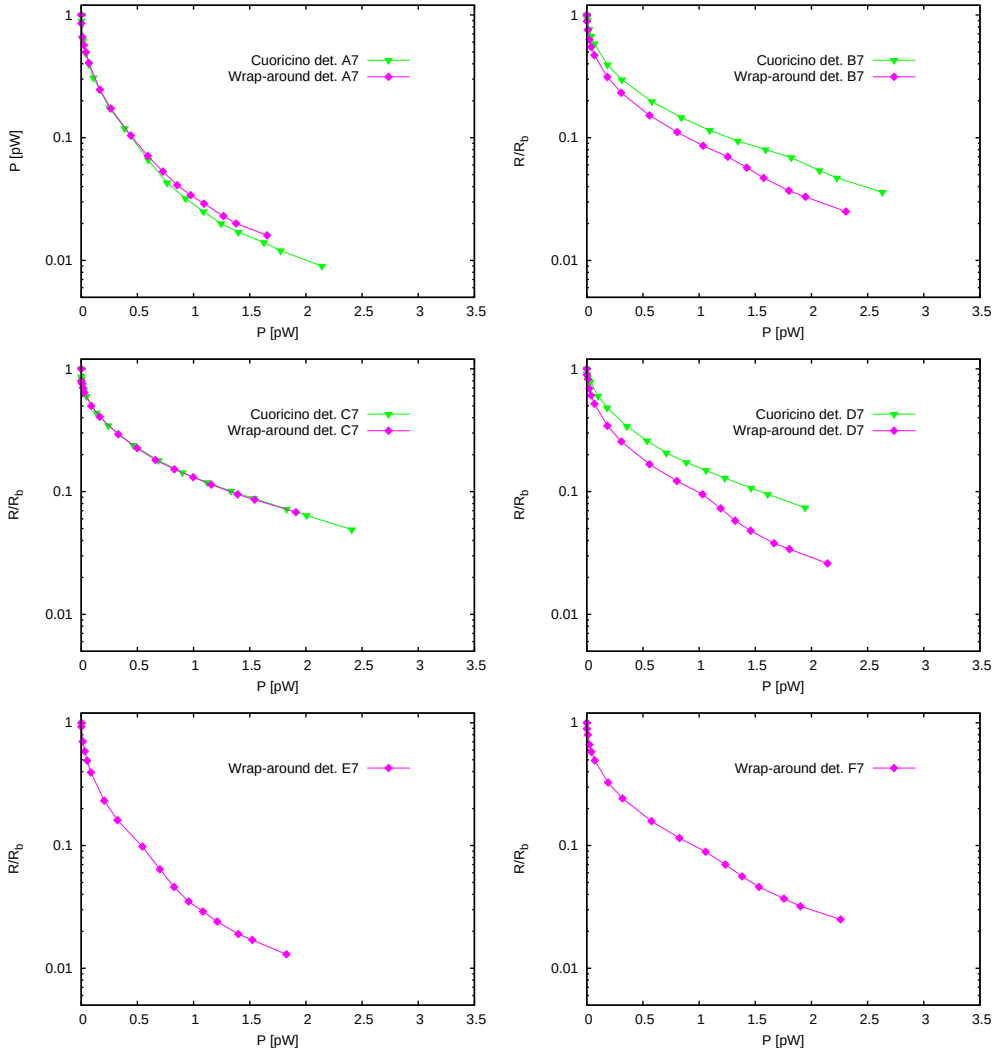

Figure 5.47: R/R_b-P curves for the wrap-around and Cuoricino thermistors in Test 7. Pairs of thermistors connected to the same absorber are plotted together. Only graphs relative to the lowest stabilization temperature, T_3, are reported.

		Wrap-around		Cuoricino	
	Detector	R_w **[MΩ]**	A **[μV/MeV]**	R_w **[MΩ]**	A **[μV/MeV]**
T_1	A7	32.90	42	71.09	98
	B7	16.61	59	10.05	50
	C7	8.10	34	20.37	43
	D7	29.46	74	9.37	26
	E7	15.86	31	–	–
	F7	15.39	56	–	–
T_2	A7	78.00	74	178.90	166
	B7	42.80	121	44.70	90
	C7	18.10	58	37.00	87
	D7	46.90	120	19.20	50
	E7	103.70	120	–	–
	F7	64.20	131	–	–
T_3	A7	360.00	213	782.00	435
	B7	246.00	271	333.00	248
	C7	93.60	194	190.00	274
	D7	335.00	338	132.00	152
	E7	612.00	275	–	–
	F7	292.00	334	–	–

Table 5.23: Work resistances and responses for the detectors in Test 7. Values are relative to all the three stabilization temperatures of the cryogenic system. No Cuoricino standard thermistors are attached to detectors E7 and F7.

Detector	**DFM @ 100 MΩ [μV/MeV]**		**WA/C**	**ΔE [keV]**	
	WA	C		WA	C
A7	89	119	0.7	6	17
B7	171	139	1.2	26	6
C7	202	169	1.2	9	11
D7	167	130	1.3	13	10
E7	100	–	–	–	–
F7	173	–	–	–	–

Table 5.24: DFMs and energy resolutions for the thermistors in Test 7. DFMs are extracted from the corresponding curves of merit by normalizing at the value R_w=100 MΩ; the FWHM ΔE is evaluated at the 2615 keV peak for the lowest temperature T_3.

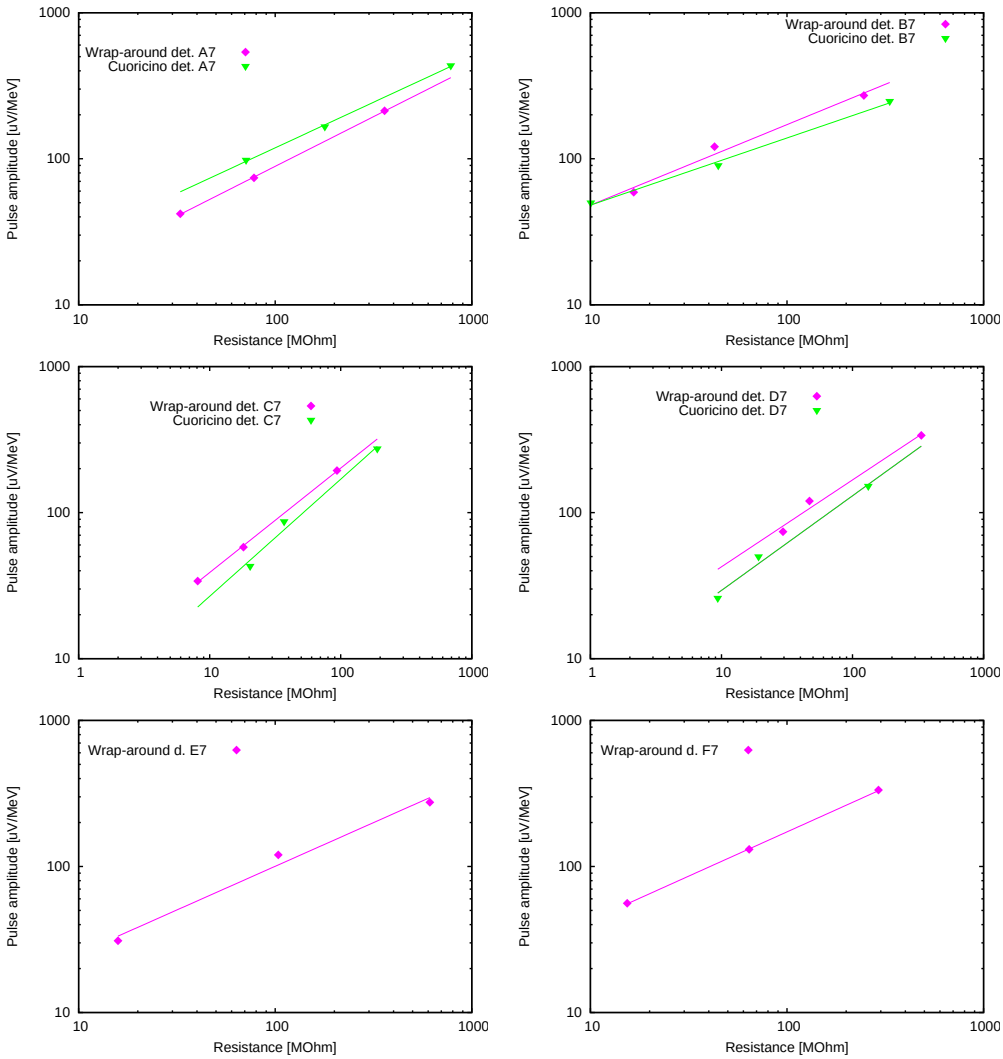

Figure 5.48: Curves of merit for the detectors in Test 7, comprehensive of experimental data points (R_w,A) and best-fitting lines. The average slope of the best-fits is 0.63, which is compatible with the considerations made in the text.

collected in terms of two distributions: DFMs normalized at 1 MΩ and DFM ratios between pairs of different thermistor models (reference data has already been reported in Tab. 5.7 and 5.13). Tests on small size prototypes hint at large flat-packs having better performances than small flat-packs, even though still slightly inferior to those of Cuoricino standard thermistors. Wrap-around devices have not been tested in Como.

Tests on CUORE-like bolometers (Test 2 and tests from 4 to 7) give results that can be compared directly with the statistics obtained from the Cuoricino experiment. Some of them also allow direct comparison between different thermistor models (Test 2, 5 and 7): these tests give, thanks to the optimized setups, an estimation of energy resolutions as well, which is significant only in comparative terms between sensors connected to the same bolometer.

The comparison of performances in terms of detector responses is reported in the graphs in Fig. 5.50. In the comparison, the set of reference is constituted by two subsets: the distribution of DFMs of the thermistors in the Cuoricino experiment, whose normalization at R_w=100 MΩ is extracted from Ref. [48], and the DFMs of the reference sensors used in the tests at LNGS presented in this chapter.

The first observation about tests on large mass bolometers is that a rough look at their analysis is sufficient to rule out some of the contributes theorized in Sec. 5.2.1 as sources of the difference in performance among thermistor models. For example, the influence of effects due to non-uniform electric fields, which couldn't be neglected in principle, is very limited: this goes in the direction of the DC conductivity simulations reported in Sec. 5.2.2, according to which the K factors of proportionality between resistance and resistivity do not differ much, in the case of a frontal bonding model with height $\sim$1 mm, from the value of lateral-pads device; moreover, the presence of a dead volume that does not contribute to electric conductivity is reasonably ruled out, according to simulations, for the thermistor designs presented in this thesis. When it comes to experimental data, the following consideration can be made. Small flat-packs are designed specifically to get internal electric fields as similar as possible to the Cuoricino case; should deviations from the Cuoricino configuration of electric fields be source of performance worsening, any effects would be enhanced in large flat-pack devices because of their geometry. This does not happen. The better behaviour of large flat-packs, when compared to small flat-packs, suggests strongly that these presupposed effects are negligible in respect to the importance of thermal parameters. Large flat-packs "win" because their thermal properties are nearer to the reference values of Cuoricino standard thermistors. Moreover, the thermistor-to-heat bath coupling G_{pad}, which depends on the size of pad surface, can be ruled out as well because it remains constant in both flat-pack models.

The previous considerations redesign the general picture of thermistor performance: it can now be seen as the result of a delicate interplay among the electron-phonon conductance G_{ph-el}, the doping characteristics and the thermistor-to-absorber coupling G_{th-abs}. While the first two can be tuned by adjusting the size of the device, the last one makes an independent problem. The importance of a correct connection between the sensor and the crystal absorber is also stressed by the spread in performances evidenced in all seven tests. The question on which role the quality of thermistor-to-absorber coupling plays in this recurring aspect has not been avoided but only postponed: the next chapter will focus on the answer, showing how the goal of performing reproducible sensor connections is mandatory.

Wrap-arounds are the devices that show more similarity with the behaviour, both

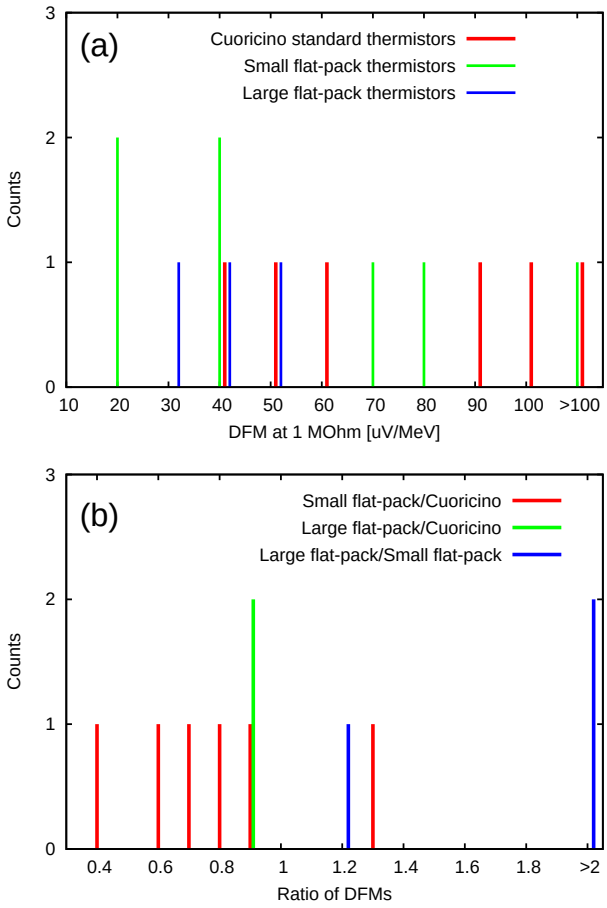

Figure 5.49: Distribution of the results obtained from Como tests on small bolometers: DFMs normalized at 1 MΩ (a) and DFM ratios between pairs of different thermistor models (b).

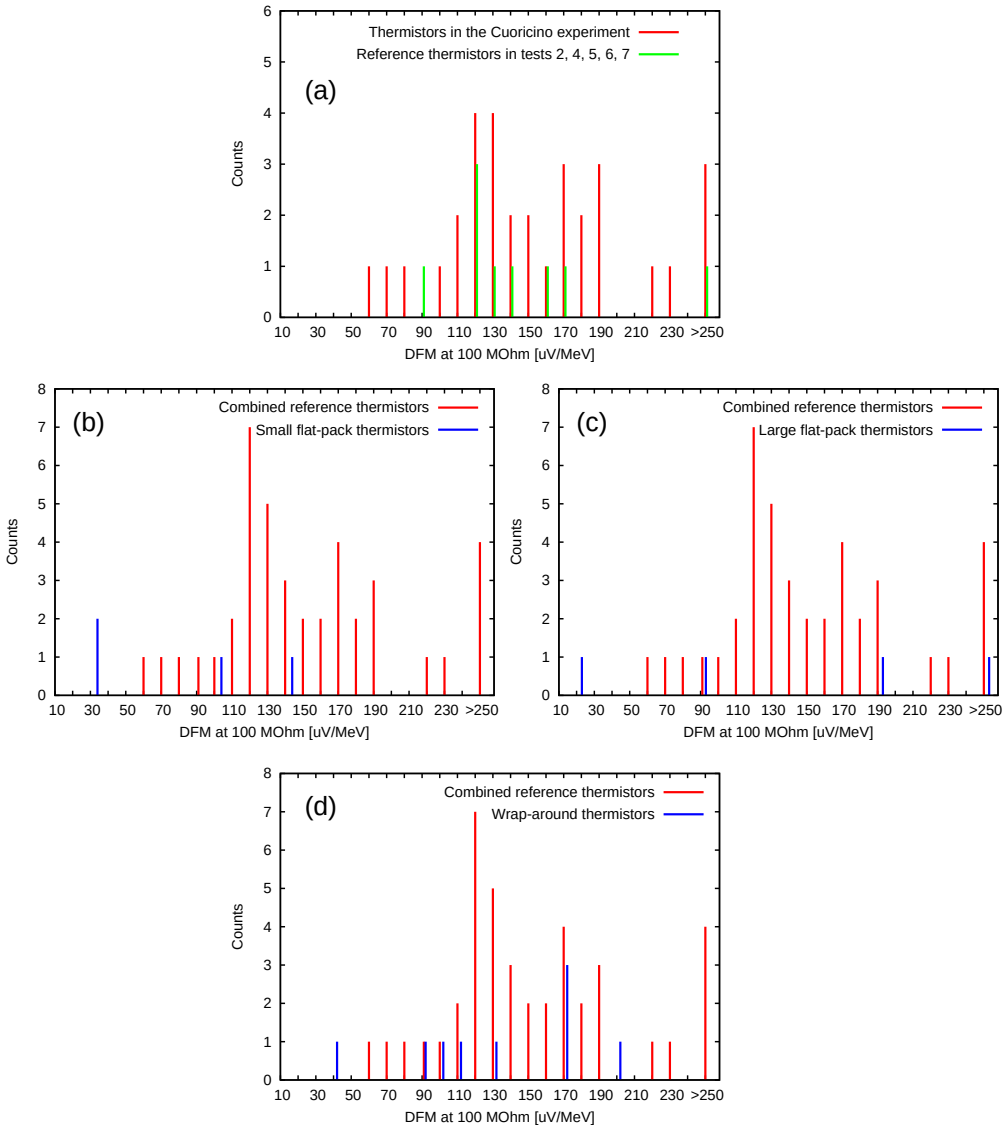

Figure 5.50: Distribution of the DFMs normalized at 100 MΩ for different thermistor models obtained from LNGS tests on CUORE-size bolometers. (a) DFMs of the thermistors used in the Cuoricino experiment and of the reference sensors used in the LNGS tests presented in this chapter: the two distributions are combined in the following three graphs. (b) Comparison of DFMs between the reference thermistors and the tested small flat-packs. (c) Comparison of DFMs between the reference thermistors and the tested large flat-packs. (d) Comparison of DFMs between the reference thermistors and the tested wrap-arounds.

static and dynamic, of Cuoricino sensors. This is also predicted by preliminary simulations. Wrap-around thermistors are a winning trade-off among the required properties; they satisfy the main goal of this R&D work: their size and the coexistence of lateral with frontal pads result in electric properties highly similar with those of the thermistors used in the Cuoricino experiment. The only price to pay is a slower, although reliable and replicable, production process.

The ultimate choice for CUORE-0 is based on a conservative approach. Large flat-pack thermistors, although promising, do not show performances replicable enough in the experimental tests performed, also because of the low statistics collected. Wrap-around devices gave more reliable results; moreover, the striking similarity of their internal electric field to the one that would manifest in a lateral-pads device limits any possible unexpected effects on the electron-phonon coupling. Therefore, the choice is to equip the bolometers of the CUORE-0 experiment with wrap-around devices. This will allow frontal bonding in the assembly phase, without loss in the final performance.

Chapter 6

The sensor to absorber coupling

"I am rubber,
you are glue"
– Guybrush Threepwood [123]

A last sensitive point needs to be dealt with for a thorough overview on CUORE-0 oriented single-module innovations: the connection of sensors to tellurium dioxide crystal absorbers. The coupling, both thermal and mechanical, plays a relevant role in defining the quality of detector performance, as will be detailed later on; once again, the combination of Cuoricino to R&D tests data gives the statistics to endorse such assessment. The optimization work performed regards many aspects in the procedure for the realization of the coupling: it develops from the starting point of a totally manual method and ends up in the design of a semi-automatic line for absorber connection to both germanium thermistor and silicon heater. The assembly line will be not just the choice for the assembly of CUORE-0, but it will also provide a ready-to-go system for the larger CUORE experiment. Although the final system involves heater connection as well, explicit mention of it will be omitted in this review and focus will be given to the sole thermistor-to-crystal coupling: the technical considerations and solutions developed in the case of the NTD thermistor will be easily extended to the heater itself. No loss of generality is expected, as the following paragraphs will show that, when it comes to absorber coupling, the most sensitive point is the Ge sensor; of course, given the heater's function described in Sec. 2.1.4, an improvement in reproducibility of heater-to-absorber connections among different bolometers is also required: pulses with amplitudes as much similar as possible to each other should in fact be obtained following a given power deposition (voltage is supplied to heaters in parallel electric configuration). However, this requirement is a subset of those that will be listed for the Ge thermistor; hence, any direct reference to heaters will be omitted.

6.1 A soft point in the bolometric model

Before illustrating in detail the aforementioned optimization work, a brief introduction is necessary on the scientific reasons which motivate it and make it a fundamental step in the development of detectors for CUORE-0. The question to answer is to which extent the characteristics of the connection between TeO_2 crystals and NTD Ge thermistors influence the overall bolometric performance. When performance is evaluated, there

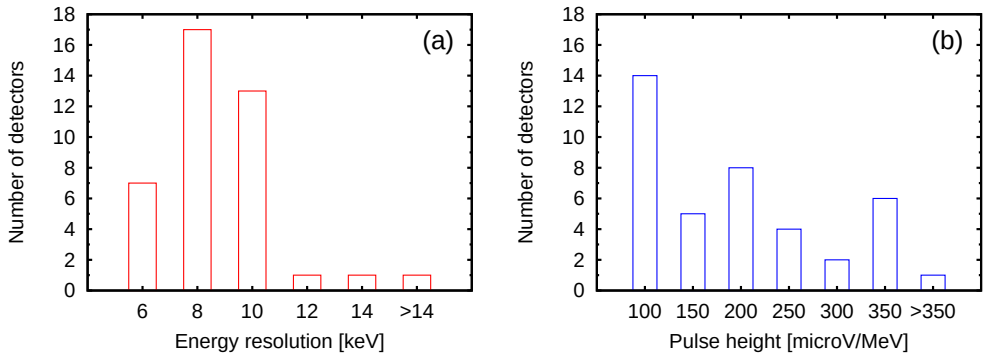

Figure 6.1: Examples of distributions of detector performance parameters for the 5×5×5 cm^3 bolometers in the Cuoricino tower; the data in the histograms is taken from a 3 days ^{232}Th calibration which took place during Run II on the 40 surviving big detectors. (a) FWHM resolutions at 2615 keV. (b) Pulse heights in μV/MeV.

are two possible aspects of concern: energy resolution and pulse shape.

As already seen in Chapter 2, the energy resolution of bolometers in the Cuoricino experiment has a definite spread. This is reminded by Fig. 6.1(a). One could argue about the possibility for heterogeneous quality of thermistor-to-absorber couplings among different bolometers to originate such distribution. As for the issue of pulse shape, a specific discussion will be made to deduce a definite link between variable characteristics of thermistor-to-absorber couplings and non-uniform detector responses, so that reproducibility of couplings may be seen as a mandatory aim to improve experimental results. First of all, the variation in pulse shapes obtained by different detectors is a fact observed in both Cuoricino and the following R&D runs. As evidence of this experimental circumstance, Fig. 6.1(b) reports the distribution of amplitudes in μV/MeV for the Cuoricino tower and Fig. 6.2 shows a selection of pulses from a sample of Cuoricino detectors: neat differences in heights, rise times, decay times can be noticed in the pulses reported, and variations in other shape parameters from one signal to the other are evidenced by data analysis. Two main reasons justify concern on the spread in pulse shapes when comparing different bolometers in the same run. The first point regards the overall comprehension of detector's behaviour: the unexpected shape variations hint at a shallow understanding of some aspects in the thermal model, which have to be clarified because of the obvious consideration about non-predictable elements in the responses meaning that full control on the detector has not been reached yet. The second point involves data analysis (for details, refer to Appendix C and to the brief summary given in Sec. 1.5 on the extraction of 0ν-DBD information from Cuoricino). In view of CUORE, the growth in detector number up to the order of 1000 makes it advisable to automate certain steps in the analysis process: for instance, discrimination of those groups of signals that cannot be due in principle to $\beta\beta$-0ν events, such as thermistor pulses or non-flagged heater pulses; or, again, recognition and discard of pile-up signals. These classes of events can be distinguished by specific rejection parameters, which are linked to the shape of signals and change accordingly to the aforementioned variations. In order to develop software tools so that part of the data analysis process is handled by automatic procedures, the unpredictability introduced by the overall spread in pulse shape parameters in the same run has to be reduced: the more similarly bolometers respond, the faster and more reliable is data analysis.

In light of the previous considerations and enlarging the view from the behaviour of a lone bolometer to arrays constituted by multiple detectors, achieving global uniformity

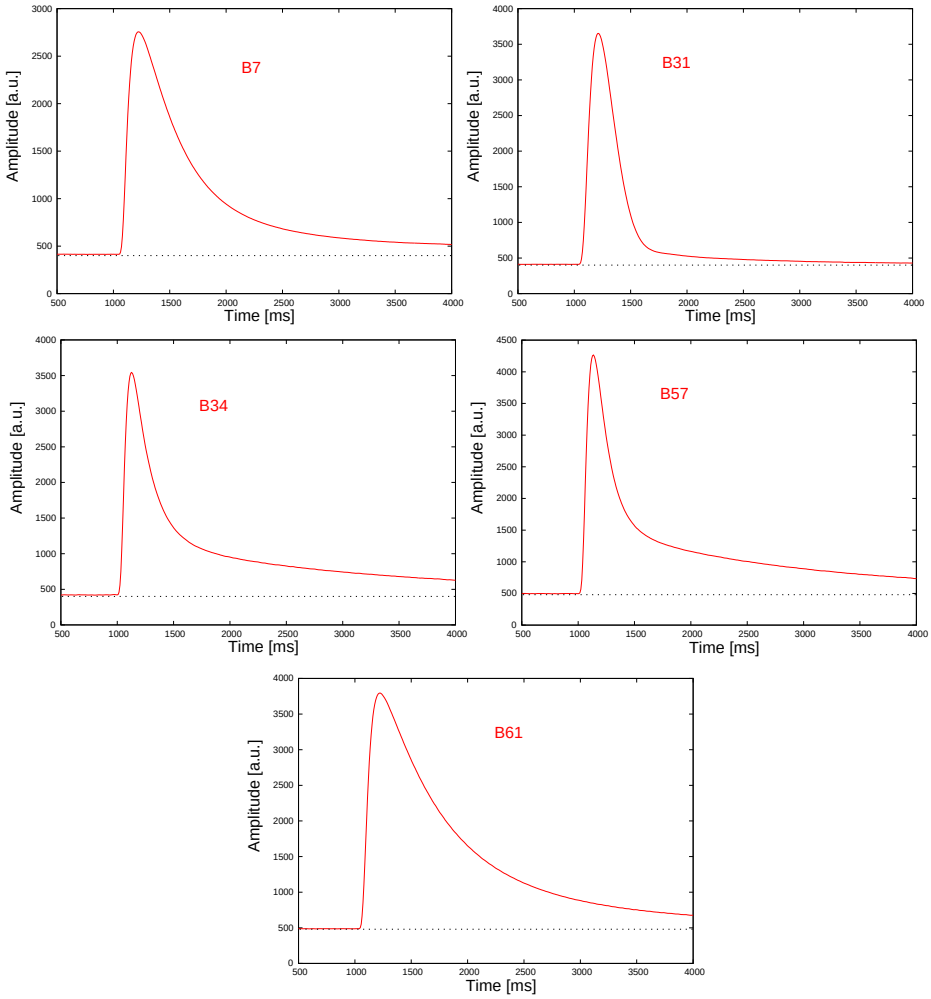

Figure 6.2: Examples of pulses from selected bolometers in the Cuoricino tower (B7, B31, B34, B57 and B61) featuring variations in shape parameters.

of performance should be definitely seen as a plus.

The bolometric model in Fig. 6.3, already examined briefly in Chapter 2, is used as a reference to discuss what components are candidate to be responsible for pulse shape variations and to which extent; for the values of the capacities and conductances listed here, refer to Sec. 1.4.

1. *Phonon-electron conductance.* Thermistors in the Cuoricino experiment were obtained from the same wafer and were exposed to the same irradiation: variations in the HEM conductance from one detector to the other are therefore expected not because of doping differences but only from tolerance on dimension, as G_{ph-el} grows linearly with thermistor volume. Such contribution is negligible: the precision is estimated as ± 75 μm in all directions, which corresponds to a variation of order lower than 0.1‰ in conductance value for Cuoricino $3\times3\times1$ mm^3 thermistors.

2. *Conductance of read-out wires.* This is a Kapitza conductance whose value, at fixed temperature, depends linearly on the contact surface in the Au/Ge interface. The previous consideration applies: the only variation is introduced by tolerance

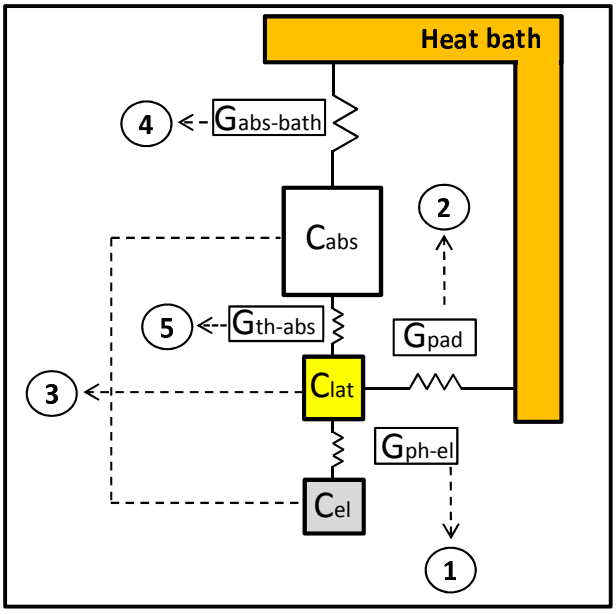

Figure 6.3: Bolometric model of reference for the discussion on pulse shape variations. The parameters taken into account as possible sources of the variations are enumerated with the same notation in the figure and in the list in Sec. 6.1.

on the dimension of pads for electric contact, and again the contribution is negligible (1% on G_{pad} for Cuoricino thermistors with 3×1 mm^2 pads).

3. *Heat capacities.* While the capacity terms of the thermistor, C_{lat} and C_{el}, can be neglected because of the previous considerations (1‰ variation on volume at worst), a few more words should be spent for the C_{abs} term. Chapter 4 reported the optimization conducted on the production of TeO_2 crystals, which aimed specifically at uniforming the purity, the reliability and the geometry of the batches of absorbers for future use in CUORE-0 and CUORE. According to the results of the work done, the spread in the heat capacity values of crystals is negligible (one part in a billion) and no consequent appreciable contributions to the origin of pulse shape variations in different detectors are expected.

4. *Absorber-to-heat bath coupling.* In the frame of the R&D activity focused on background reduction and summarized in Chapter 3, an investigation was made regarding exotic contributions to the counting rate in the 0ν-DBD region of the energy spectrum: the study aimed at verifying the possibility for PTFE crystal holders to release heat in the absorbers as a consequence of thermal relaxation processes, mimicking particle interactions. This idea has already been mentioned in Sec. 3.1.2, and is beyond the goal of this thesis. However, this work, which was performed during the RAD5 and RAD6 measurements, offers insight on why the $G_{abs-bath}$ term should not be considered a candidate for the origin of pulse shape variations from one detector to the other. The results of the attempted substitution of PTFE holders prove the point under discussion. Eight detectors, which had already been tested and constituted a performance benchmark, were reassembled in the frame of their last test keeping the setup identical apart from PTFE holders, replaced by copper clamps: all the other elements (NTD thermistors, read-out wires, crystals, thermistor-to-absorber couplings) and working conditions (base temperature, electronics) remained comparable. The data obtained suggests that the difference between pulse shapes, from the mounting with PTFE holders to the

one with Cu clamps, is negligible [84].

5. *Thermistor-to-absorber coupling.* The last candidate among the parameters of the thermal model used here is the connection between the Ge sensor and its crystal. As a general remark, there is an obvious influence of this conductance on pulse shape: the fraction of heat which reaches the thermistor following energy deposition in the absorber depends on the value of G_{th-abs}, and this is reflected on pulse height and rise time; the simulation work developed during Cuoricino R&D shows that when sensor-to-absorber coupling gets larger, the detector optimum pulse amplitude initially increases and eventually reaches saturation due to electron-phonon HEM decoupling becoming the limiting factor [48]. Besides this immediate consideration, evidence of the link between G_{th-abs} and pulse shape can be extracted by the analysis of bolometers with a pair of equal thermistors connected to the absorber: in this case, the only distinguishing factor in the pair is thermistor-to-absorber coupling, because the crystal is the same and all the other parameters in the model are equal or have negligible variations according to the considerations exposed previously. As an example, two pair of pulses coming from the CCT2 detector (see Chapter 4, Sec. 4.3.2) are reported in Fig. 6.4. The detectors considered are BA1 and BC2, both with two equal thermistors connected to the absorber; each pair of pulses is generated by the same particle deposition in the corresponding absorber, and each pulse is seen by a different thermistor: pulses read by thermistors on the same crystal show differences in shape. As a last remark, another feature hints at the importance of thermistor-to-absorber coupling in the definition of detector performance. In order to explain it, calibrated energy spectra of the thermistors on crystal BC2 are reported in Fig. 6.5: while the notable peaks due to particle energy depositions have a good superimposition in the two spectra, an energy shift of the heater peak of $\sim$20 keV is observed from one spectrum to the other. A possible explanation is that the mechanism of signal development differs slightly for heater and particle depositions. This is due to the contribution of those athermal phonons that hit the sensor-absorber interface and are transmitted to the thermistor, where their energy is thermalized quickly through interaction with the conduction electrons (details on the conversion of particle energy to thermal phonons have already been given in Chapter 1). In other words, heater depositions generate signals that constitute a stand-alone class and have a different athermal component than usual particle depositions in the bulk. The probability that an athermal phonon is absorbed by the sensor is p=$\alpha(\sigma/S)$, where S is the surface of the crystal, σ is the surface offered by the thermistor-to-absorber coupling and α is the transmission coefficient of the high energy phonons: however, α does not take into account an effect that could explain the observed energy shift between heater peaks, which is thermistor-to-absorber coupling acting as a selection filter for phonon energy. This would change the ratio of athermal to thermal contribution in the heater pulse, in function of variations in the thermistor-to-absorber coupling. For completeness, other possible motivations should be mentioned: a position effect, for example, due to one thermistor (TR) being nearer to the heater as compared to the other one. The previous considerations on the link between G_{th-abs} and the shift in heater lines should be therefore considered a hypothesis.

6. *Treatment of crystal surfaces.* This item is not integrated in the thermal model used here: however, a brief treatment of its possible contributions to the subject under discussion is required for completeness. The main reference for this topic is Chapter 4, and more specifically Sec. 4.3. Experimental facts reported in the mentioned section hint at the treatment of crystal surfaces as determinant for the quality of bolometric performance. Four crystals of the CCT1 run, which had given

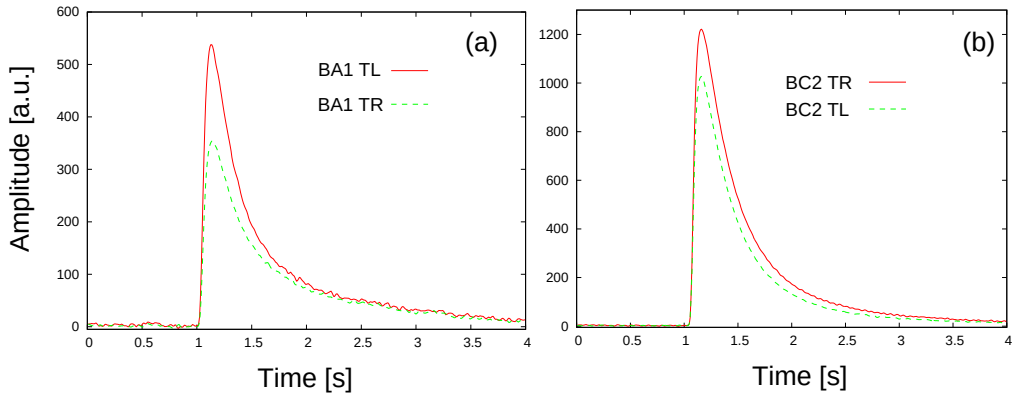

Figure 6.4: Each pair of pulses is due to a particle deposition seen by two thermistors coupled to the same crystal in the CCT2 run. The thermistors are all of the 31, Cuoricino-like, series. (a) Pulses read by the pair of thermistors on crystal BA1: pulse height is 69 μV/MeV, τ_r is 49 ms and τ_d is 414 ms for TL, while pulse height is 46 μV/MeV, τ_r is 52 ms and τ_d is 541 ms for TR. (b) Pulses read by the pair of thermistors on crystal BC2: pulse height is 94 μV/MeV, τ_r is 45 ms and τ_d is 398 ms for TL, while pulse height is 131 μV/MeV, τ_r is 44 ms and τ_d is 416 ms for TR.

modest results in terms of pulse amplitudes, rise and decay times, gave acceptable results in the CCT2 run after their surfaces were reprocessed: the reason of their anomalous lower-than-average behaviour in the CCT1 run was attributed to a layer of acid and H_2O left on each crystal from the etching process; performances were brought back to normality after its removal. The underlying mechanism of the observed behaviour has still to be cleared. Nonetheless, the same protocol of surface treatment is now applied equally to all crystals; it also cannot account for pulse shape variations seen in signals read by two equal thermistors connected to the same absorber (as detailed in the previous item of this list).

The last reason that supports a thorough optimization work on the technical aspects of G_{th-abs} realization concerns the self-evident aspect of assembly timing. The production of sensor-to-absorber connections for the Cuoricino detector, which, as already stated, was a 62-crystals array, took approximately two months; the same assembly step took about three months for the last CUORE-0 R&D test, the Three Towers run described in Sec. 3.4.2, which was constituted by 36 detectors with two thermistors each and was built with the Cuoricino procedure as well. A quick extrapolation suggests that the realization of sensor-to-absorber couplings for the whole CUORE will take about two years and a half, if carried out with the same rate. This is evidently, and euphemistically, impractical, not to mention the time required by all the other phases in the assembly chain. The winning solution to cut on time is to revise the coupling procedure from its foundations. The Cuoricino procedure is totally manual and operator dependant, as will be shown in Sec. 6.3, and there is plenty of room for time saving innovations.

Summing up, the optimization of the sensor-to-absorber coupling preliminary to CUORE-0 is focused on reproducibility. Following the principles fixed by the Cuoricino R&D on the physical characteristics of the conductance, this is mainly a technological problem: all the steps in the realization of the coupling have to be reviewed and standardized, getting rid of those actions which are intrinsically not reproducible. As simple as it may seem, the task hides a good collection of tricky points. This is due to various restrains which will be listed right after and constituted the starting point for the work done.

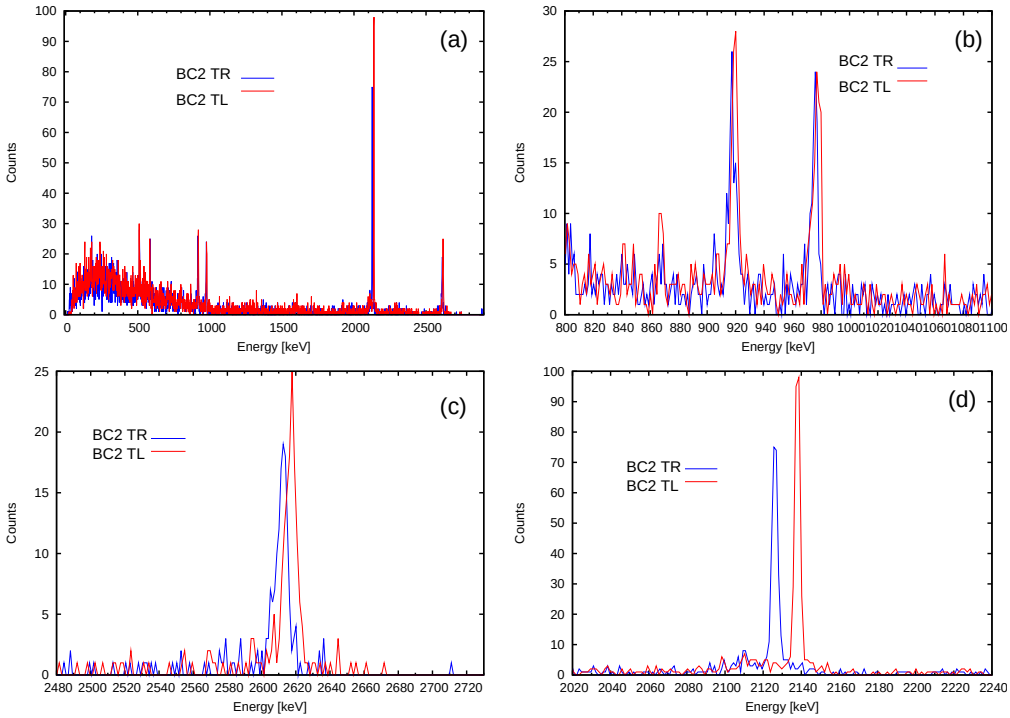

Figure 6.5: Superimposed energy spectra for the two thermistors of detector BC2 in the CCT2 run. (a) View of the two spectra up to 2.9 MeV; the highest peak is the heater line. (b) Zoom on the superimposition of the ^{228}Ac 911 keV and 969 keV peaks. (c) Zoom on the superimposition of the ^{208}Tl 2615 keV peaks; FWHM ΔE evaluated at this energy is 8 keV for the TR sensor and 6 keV for TL. (d) View of the heater lines. As opposed to the good correspondence shown by the other peaks, the two heater peaks are separated by a $\sim 2\sigma$ gap.

6.2 Coupling sensors to crystals: restrains to the process

The necessary starting conditions for optimization of the coupling between sensors and absorbers were fixed by the Cuoricino R&D and assembly. Such restrains include the material used to connect the two elements and the geometry of its distribution, as well as some characteristics of the environment hosting the assembly: they are mainly temperature, humidity and the strict exclusion of contaminants which could possibly rise the radioactive background for the assembled bolometer.

6.2.1 The "Araldite affaire"

The interface between the two surfaces of the sensor and of its crystal is an adhesive. Realizing the coupling translates, therefore, into the gluing process of different materials (germanium or silicon to tellurium dioxide). The type of glue is unavoidably fixed: for reasons which will be cleared later in this subsection, the bi-component epoxy Araldite Rapid, produced by Huntsman Advanced Materials, is used.

This kind of epoxies come in two different components, an epoxy resin and a catalyzing agent (commonly called *hardener*), whose exothermic chemical reaction results in a thermosetting polymer. The resin is made of monomers or short-chain polymers with an epoxy group at each end; the hardener is constituted by polyamine monomers. As the

two components are mixed with fixed ratio and for a given time, the aminic and epoxy groups react and a covalent bond is set up: the resulting polymer is highly cross-linked. The features of the polymerization process, known as *curing*, endow epoxy glues with high adhesion, chemical and thermal resistance and electric insulation. The specific use in the field of bolometry implied here, additionally requires the chosen epoxy to withstand the severe conditions found at cryogenic temperatures: the adhesive properties of the fully cured glue should resist a complete down-to-10 mK thermal cycle and compensate differential thermal contractions between the glued items, which can be relevant for the Ge-TeO_2 couple, so that detachments and fractures are avoided.

As thermosetting polymers, the properties of epoxies depend on the curing environment but also on their thermal and environmental history. The temperature at which the curing process develops sets various features of epoxy adhesives. For instance, these materials are characterized by a so-called glass transition temperature T_g, that is the temperature under which the polymer goes from a rubber like state to a hard, glass like state; T_g varies according to the curing degree and the water content. Various studies in literature (i.e. [124]) show that glue vitrifies when its curing is performed at temperatures lower than the ultimate glass transition of the completely cross-linked epoxy: the epoxy will then be vitrified but under polymerized, so that the cross-linking reaction slows down drastically and a long time may occur for the adhesive to reach its final properties. One should then pay due attention to the choice of curing temperature.

Curing times may vary consistently for different bi-component epoxies. The following introduction of parameters that describe this process helps characterizing the glue used in our application.

- *Mix ratio* - The ratio of resin to hardener, in volume or weight, needed to start the polymerization reaction.
- *Pot life* - The time available for glue application before it gets unusable. The end of pot life is marked by a steep rise in both the mixture viscosity and temperature. Moving the glued items after this time limit implies breaking the forming macromolecules and preventing the correct development of curing. Pot lives range from a few minutes to hours depending on epoxy and environmental parameters.
- *Handling time* - The intermediate time threshold after which the glued system can be moved without risking that vibrations abort curing. However, more time is needed for the epoxy to reach its full qualities.
- *Curing time* - The total time necessary for the epoxy to gain its specific final gluing properties.

The aforementioned times are functions of temperature T. A general behavior of epoxies is the reduction of pot life and curing time corresponding to a growth in T; moreover, the degree of curing reached by the epoxy features a strong correlation to viscosity [125]: as an example, Fig. 6.6 shows the dependence of viscosity on curing time at three different temperatures for the Araldite 2014 glue, a kind of Araldite with longer pot life and curing time than the Araldite Rapid used in this application [126].

Such behavior forces operators to balance the conditions for glue dispensing: higher T means lower viscosity, which makes epoxy application easier, but it also implies shorter time to complete the operation. The previous consideration is useful mainly for that class of epoxies with the shortest pot lives (a few minutes).

The Araldite Rapid glue extensively tested in bolometer assembly for the Cuoricino experiment and CUORE-0 R&D runs is a short pot life epoxy; it can be cured at room

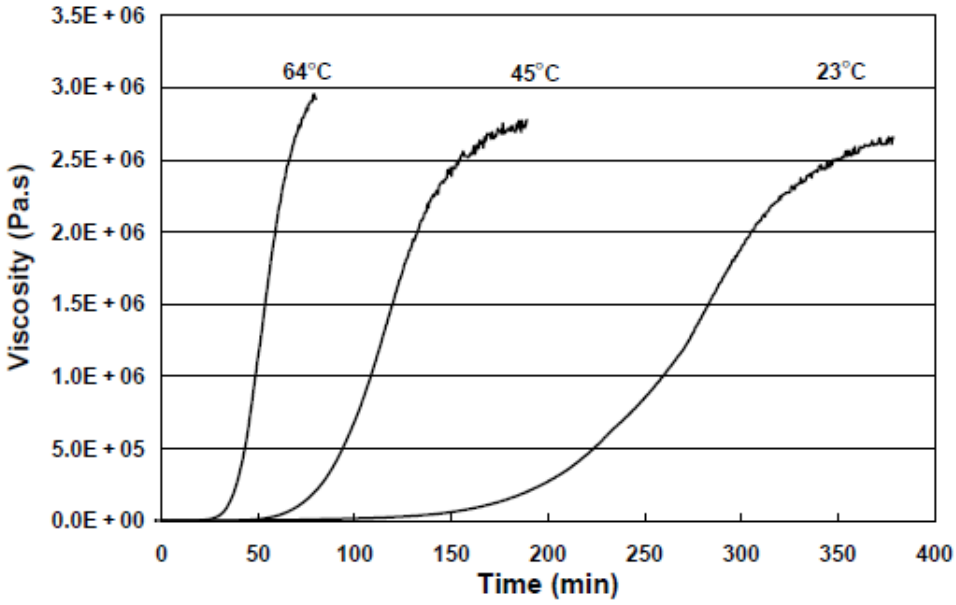

Figure 6.6: Correlation between the degree of conversion and the viscosity of the epoxy Araldite 2014, of the same family of Araldite Rapid but with longer pot life, at three curing temperatures: the graph was taken from reference [126].

temperature.

Araldite Rapid takes different names according to the country of distribution, which is Switzerland for the product used in this application; it shows variations in colour within different batches, mainly in the hardener which can vary from white to yellow, even sometimes light orange, according to the site of production and the source of the production materials. As guaranteed by the producer, these differences have no influence on the ultimate mechanical performance; however, radio-purity at the levels required by the CUORE collaboration was tested and approved only for the batches of Araldite Rapid selected by CERN laboratory in Geneve. Therefore, this is the supplier of the epoxy we are currently using and intend to use in both CUORE-0 and CUORE.

Since Araldite Rapid is distributed as a common do-it-yourself product, in order to gain detailed information on glue properties one has to refer to technical data sheets of its industrial version, which goes under the name of Araldite 2012. A selection of its chemical, mechanical and thermal properties is presented in Tab. 6.1. The reported pot life of a few minutes may be reputed very short for the requirements of this application: in particular, it makes quite complex the phase of glue distribution, whose peculiar geometry will be discussed in the following subsection. In spite of the disadvantaging brief time window available for gluing operations, Araldite Rapid has been extensively tested in terms of bolometric performance and radio-purity: both evaluations are excellent and supported by the large statistics collected [127]. The epoxy Araldite Rapid was chosen for CUORE-0 and CUORE assembly because of its reliability in these fields and its outstanding mechanical properties throughout cryogenic thermal cycles. The aforementioned qualities compensate possible complexities in the assembly.

The general rule for a bi-component epoxy, as previously mentioned, is that its properties depend strongly on the environmental conditions of curing and dispensing. The same is true, of course, for Araldite Rapid. The relevant parameters are temperature and humidity in the gluing site: consequent requests on them will be listed in subsec-

Property	Araldite 2012 (mixed)
Colour (visual)	Pale yellow
Relative density	ca 1.18
Viscosity at 25°C [Pas]	25-35
Pot life (100 g at 25°C)	5 minutes
Shelf life (2-40°C)	3 years
Mix ratio (volume)	1:1
Cure time to reach lap shear strength>1 MPa	20 min at 25°C
Cure time to reach lap shear strength>10 MPa	60 min at 25°C

Table 6.1: List of chemical, mechanical and thermal properties for the epoxy Araldite 2012, the industrial version of Araldite Rapid [128]. Please note that, although a 5 minutes pot life is quoted, the experimentally observed work life of the epoxy is shorter (approximately 3 minutes at room temperature), due to the rapid growth in viscosity which reduces its usability.

tion 6.2.3.

6.2.2 Defining the geometry of the epoxy interface

The most intuitive way to glue a sensor to the corresponding crystal is, perhaps, to deposit a homogeneous epoxy layer between the two surfaces: one can easily picture the procedure to be fast and compatible with short pot lives; even performing the operation manually inside a glove-box would not complicate it strongly. This is not the case, however. Epoxy deposition in form of a homogeneous layer, as thin as it may be, is excluded for reasons of mechanical performance at cryogenic temperature. Experimental evidence says that, throughout a low temperature thermal cycle, a thin layer of Araldite Rapid is not elastic enough to compensate differential thermal contractions in the Ge/TeO_2 and Si/TeO_2 pairs: fractures in crystal absorbers may often happen. The interface should then be designed with the aim of a higher elasticity. The epoxy distribution most successful for this application is a dot matrix. As we know from Chapter 5, which has already hosted a discussion on thermistor geometry, the area of the so-called footprint is fixed at approximately 9 mm^2 for the NTD sensor; the single-spot dimension and the total number of spots in one matrix were decided during Cuoricino R&D. Details on how the required spots were obtained previously to the optimization described here are reported in Sec. 6.3.

Glue spots deposited with the Cuoricino assembly system have diameters ranging from 0.5 mm to 0.8 mm; spot height is fixed at 50 μm by using an appropriate spacer and pressing together sensor/absorber pairs. If neighbouring epoxy dots merge together when pressed, a layer can form. 50 μm, the chosen height, is a limit value: if pressed under this value, the largest spots merge with their neighbours due to an excessive growth in their diameters. The change in dimensions that glue dots undergo when pressed can be estimated roughly by a simple geometrical model. According to the model, an unpressed epoxy dot can be approximated by a spherical cap: when

the sensor and the crystal are pushed together, the dot is pressed and an amount of epoxy corresponding to a smaller spherical cap is moved to its sides; the pressed dot becomes therefore a spherical segment. A reasonable estimation for the average height of unpressed spots is $\sim$100 μm, based on the experience made during the assembly of both Cuoricino and R&D tests; in this case, if a 800 μm large epoxy dot is reduced to a 50 μm height, according to this model the growth of its diameter is $\sim$200 μm. The value acquires meaning once the amount of epoxy dots requested in the coupling is known: a dedicated simulation work was performed in the Cuoricino R&D phase to identify the number of spots leading to the highest pulse amplitude for a given energy deposition in the absorber, and taking into account the size of thermistor footprint, the optimum was found to be nine epoxy dots [48]. Therefore, a 200 μm growth in the diameter of larger spots, corresponding to the 50 μm height reduction, is the limit value before neighbouring epoxy dots in a 3$\times$3 matrix merge together and form a layer.

The heat conductance of the average Cuoricino Araldite spots was measured in Milan and the phenomenological relation

$$\sim 2.6 \times 10^{-4} (T[\mathrm{K}])^3 \ [\mathrm{W}/(\mathrm{K} \cdot \mathrm{spot})] \,, \tag{6.1}$$

already quoted in Sec. 2.1.6, was found [81]. This is coherent with the interpretation of a thermal boundary conductance with phonon heat transmission (Kapitza conductance) [129].

Fig. 6.7 shows a typical Cuoricino nine-dots matrix deposited on an old, transparent crystal. Due to the current opacity of surface-treated crystals, the resulting matrix cannot be visually inspected easily and different methods to check its quality, such as mechanical tests, must be used.

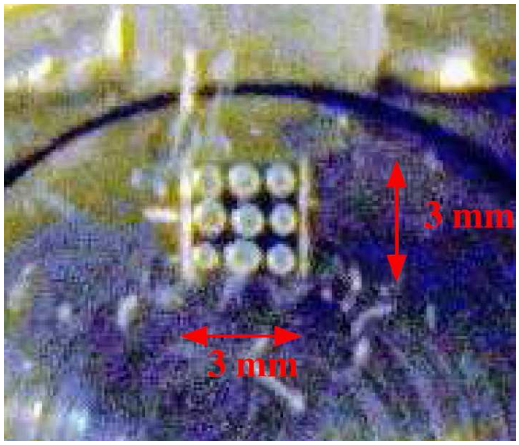

Figure 6.7: Nine-dots matrix obtained during the Cuoricino assembly, in false colours.

6.2.3 Restrains on environmental conditions

The third and last category of preliminary restrains on sensor-to-absorber coupling regards environmental conditions in the gluing site.

The importance of temperature control has already been discussed in subsection 6.2.1. A growth in temperature T leads to higher fluidity of the epoxy, but at the same

time it may reduce dramatically the time window available for gluing because of fast polymerization. As in this case short pot life combines to complex dispensing, the preferrable choice is to keep T a bit lower than room temperature (around 19°C - 20°C) in order to slow down the process; pushing temperature under this range could lead to alterations in epoxy properties, as already stated in 6.2.1. Needless to say, T should be kept constant until gluing operations, curing included, are over. As a final remark, another reason not to tamper excessively with temperature ranges in both directions is the sensitivity of TeO_2 crystals to sudden variations in T, which can result in cracks due to thermal contractions.

Humidity should also be supervised. Cured resins are quite sensitive to water, considering the highly polar and hydrogen-bonding character of epoxies: in high humidity conditions, water disrupts the inter-chain hydrogen bonding and the net effect of this physical hydrolysis is a lowering of tensile strength. Therefore, an increasing water content in the epoxy with exposure time can compromise the mechanical properties of glue. Usually, water works as a plasticizer leading to a softening of the material [130], [131]. This effect has been witnessed regularly in clean-room assembly tests at humidity levels high as 70%: the epoxy does not reach the required levels of lap shear strength even days after the end of regular cure time; it stays in a rubber-like state.

There is also another evidence of how humidity affects gluing, this time coming from a property of the crystal absorber: black signs emerge in the points where the glue dots and the TeO_2 crystal's surface are in contact, as shown in Fig. 6.8. Two mechanisms lie behind this phenomenon. First of all, the catalyzing agent of the epoxy reacts with the oxygen of the TeO_2 material: tellurium is freed and forms a black layer on the crystal's surface. Then, TeO_2 is slightly dissolved by H_2O and this enhances the effect, as in presence of high humidity levels greater amounts of TeO_2 are freed on the surface and can interact with the hardener forming the black layer.

Figure 6.8: An example of the effect of high humidity in the gluing environment: black epoxy spots.

However, humidity in the gluing site is automatically regulated when another restrain is satisfied: the assembly procedure must take place inside a glove-box where nitrogen gas is constantly flushed to avoid radon contamination. The N_2 atmosphere does not compromise epoxy polymerization. The curing of the bi-component glue used is a pure reaction between an epoxy resin and an amine hardener, therefore it does not need any oxygen or moisture like other products. The curing occurs unaltered under a nitrogen atmosphere. Glove-box assembly also helps to minimize the contact of assembled bolometers with possible sources of radioactive contamination. Operators must handle instrumentation and detector elements only inside a protected environment, where materials whose levels of radio-purity have not been guaranteed by previous certification cannot be introduced.

6.3 A brief history of gluing

Before Cuoricino assembly took place, couplings between sensors and absorbers were realized with a procedure whose results lacked of reproducibility. The sensor was positioned over an epoxy matrix deposited on crystal surface by means of a nine-pins fixed array; a 50 μm-mylar mask was interposed to obtain the desired spot height. This method presented many issues: first of all it was completely operator-dependant, implying intrinsically variable gluing quality; then the method of the fixed-pins array often led to an uneven distribution of glue among spots in the same matrix; the preparation of the procedure was quite long and incompatible with the assembly of a large number of detectors; the sensor had to be positioned by eye with great precision so that its sides rested on the border of the mylar mask, with the risk of a "tilted" gluing; last but not least, failures in sensor positioning or in spot formation resulted in frequent repetitions of the whole operation, and in the worst cases gold wires got cut during mylar mask removal.

In order to override the problems of reproducibility and timing, a dedicated gluing method was designed for use in the Cuoricino assembly. The innovation introduced by the Cuoricino method was a single manual gluing tool able to dispense epoxy, fix the height of spots and host the detector for the whole duration of curing time. The main idea behind the procedure is to deposit glue spots on the sensor and not on crystal surface, solving the previous problem of positioning. Fig. 6.9 shows a picture of the Cuoricino gluing tool.

The thermistor is placed in the indentation on the central cylinder and firmly held by vacuum. The central cylinder moves up and down on the Z-axis and can be fixed using a proper spacer, so that a gap 50 μm wide is set between the upper surface of the sensor and the external ring of the tool. Note that this approach eliminates the problem of different thickness between thermistors, which could prevent from direct glue deposition on the sensor: the precision on the dimension of Cuoricino thermistors is $\pm 75\mu$m. The nine-dots matrix is again obtained with a set of pins, the difference being the possibility to adjust the vertical position of each pin, allowing the array to touch sensor surface evenly: for this reason the array of pins is mounted inside a cap that can slide on the top of the gluing tool. The two components of Araldite in 1:1 volume ratio are mixed manually for 30 seconds; the epoxy is then put in a small basin, levelled out and the pins are dipped in it. The final phase is crystal positioning. The TeO_2 surface rests on the outer ring of the gluing tool and 50 μm-high epoxy dots are formed. Summing up, the gluing procedure can be divided in subsequent steps:

Sensor positioning. The sensor is placed in the indentation on the central cylinder, it is pushed by means of a spacer and its Z-position is fixed 50 μm under the outer ring of the tool.

Epoxy mixing. The two components are dosed by eye and mixed manually for 30 seconds.

Epoxy dispensing. A nine-pins array is dipped in the glue and pushed on the sensor's upper surface.

Crystal deposition. The absorber is placed on the cylinder and kept firm by a PTFE holder.

The last three stages must take no more than the three minutes corresponding to Araldite Rapid's pot life at 20°C; the detector rests on the PTFE holder for the whole duration of curing time. The previous listing is a useful benchmark, because the new gluing method that will be proposed in Sec. 6.4 is chronologically divided in the same

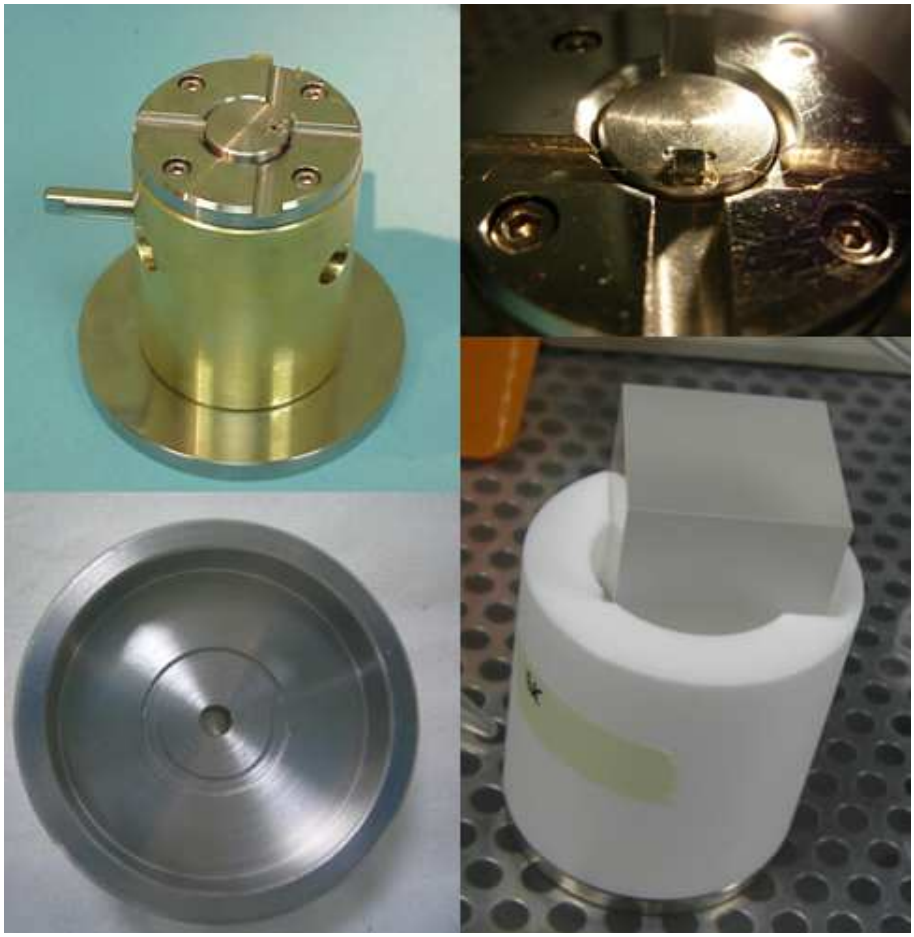

Figure 6.9: The gluing tool developed for Cuoricino assembly and used in the subsequent R&D tests. From upper left, clockwise, the main cylinder, the thermistor in the inner ring's indentation, the crystal placed by means of the PTFE holder and the lid-shaped spacer for 50 μm positioning.

steps, although their contents are radically altered in great part.

The Cuoricino procedure helped getting rid of a great number of uncertainties intrinsic to the mylar mask method. However, some of its features still prevented from gaining the desired level of reproducibility in serial gluing. Room for improvement can be found in each of the stages previously introduced.

1. Thermistors may be damaged during *sensor positioning*. The 50 μm-gap is formed by pushing a lid-shaped spacer on the upper surface of the thermistor, which can be cracked when force is not applied perpendicularly. Also, frequent usage of the gluing tool results in scratches on the inner and outer cylinders and on the lid-shaped spacer, with a consequent growth of error on the nominal 50 μm.

2. The fact that glue components are dosed by eye and mixed manually, may affect the stage of *epoxy mixing*. An unequal proportion of resin to hardener leads to a variation in glue properties: this can happen when dosing is not quantified. Moreover, manual mixing does not guarantee thorough uniformity in the final result.

3. Dirtiness and erosion of the nine-pins matrix interfere with *epoxy dispensing*. Uneven quantities of glue are picked up by the pins when they are in different cleaning conditions, leading to a spread in the diameters of spots belonging to the same matrix. This could mean epoxy dots so small that they don't touch crystal surface, as well as spots large enough to merge with the neighbouring ones.

4. Precision in *crystal deposition* is not guaranteed by manual positioning and by possible deformations of the PTFE holder.

The described procedure was used not just during Cuoricino assembly but also in CUORE-0 R&D tests. The experience gathered with this method evidenced the necessity to build an optimized gluing line, in view of the serial assembly of bolometers for the CUORE experiment.

6.4 The CUORE-0 way to gluing

The gluing line project started in 2007. The work presented here will offer an improved gluing procedure as the official choice for CUORE-0 and a prototype for CUORE. The new system for the coupling of sensors to absorbers, aimed at obtaining highly reproducible results, has been designed to be reliable and fast, even though limited by curing times. Each step of the gluing chronology has been optimized according to these lines of action:

- *Sensor positioning*: design of a non-intrusive method to fix the 50 μm-gap with an error of the order of the μm.

- *Epoxy mixing*: better dosing of the resin-to-hardener ratio and more homogeneous mixing.

- *Epoxy dispensing*: calibration of the single-spot volume to reach uniformity in the nine-dots matrix and definition of the environmental parameters to get a reasonable trade-off between epoxy viscosity and pot life duration.

- *Crystal deposition*: design of an *error-free* placement system with limited contact between the absorber and other materials.

Moreover, the general philosophy of the project is to remove as much as possible the variability introduced by manual work: operator dependant stages are, wherever allowed, automated. Automation of certain steps also gives the advantage of precise timing, which is useful considering the short time window of epoxy use. A final note regards the implications of radio-purity restrains. First of all, detector elements cannot touch materials whose radio-purity has not been proved (PTFE and specific types of steel are allowed) and, as a general rule, contact is minimized. Then, machinery use is permitted provided that clean room certification is class 1000. And finally, a failed gluing (e.g., an error in positioning or in spot formation) implies getting rid of the detector elements: no cleaning is allowed after contact with the epoxy because the use of dichloromethane and/or acetone would contaminate the sensors and alter the careful surface treatment of crystal absorbers. The gluing line is therefore designed to be *error-free* by inserting safety controls in various points of the procedure timeline.

The following subsections detail the performed optimization work.

6.4.1 Epoxy mixing

In the initial phase of the project study, two paths were considered for epoxy mixing: a *dynamic* and a *static* solution. The first idea consists in using a laboratory mixer supplied with mixing rods suitable to stir average viscosity fluids. This path was abandoned mainly because pouring epoxy from the mixing site to the dispensing container proved to be inconvenient, because this process lead easily to incorporating unwanted air in the mixture, and also because of the possibility to contaminate glue with small particles of material originated by some degree of rod erosion; moreover, a solution for two-components dosing had yet to be found. The winning choice was the so-called static mixing, which is both a very simple and effective method. A dual cylinder syringe in nylon or polypropylene with side-by-side barrels is used (Fig. 6.10(a)). The barrels, with equal capacities in order to satisfy the 1:1 proportion, are filled separately each with one epoxy component; when the syringe opening is still closed, two bleeding-valve pistons are pushed into the cartridges so that air is drained out. Barrel filling may take place in nitrogen atmosphere. As bleeding valves are sealed, a plunger is inserted and the syringe is ready for use. The mixing is then performed by connecting to the syringe opening a *static mixer*, which is a tubular housing with an internal system of plastic baffles. The diameter of the tip and the number of internal mixing elements are selected according to epoxy requirements. Provided that a small initial quantity of processed material is rejected, the resin and the hardener are automatically dosed. The resulting epoxy is thoroughly mixed through three processes: in the division process, the fluid is split in half every time it passes through an element; in the conversion process, the fluid, which glides along the inner walls of each element, moves from the central area of the housing to the walls and vice versa, being sorted in the meantime; in the inversion process, the fluid changes direction of rotation in each element and is consequently agitated. For fluids whose viscosity is similar to Araldite Rapid, the division and the conversion processes prevail. Another advantage intrinsic to this procedure is simplicity in filling containers for the following step of glue dispensing. Needless to say, static mixers are disposable due to Araldite Rapid's short pot life. A selection of static mixers with different lengths, diameters, shapes and internal mixing elements has been tested during the project study (Fig. 6.10(b)). The selected mixer has a 5.3 mm wide tubular housing which contains 24 elements, whose square shape guarantees a more effective mixing comparing to the common internal helix: Fig. 6.11 depicts its principles of operation.

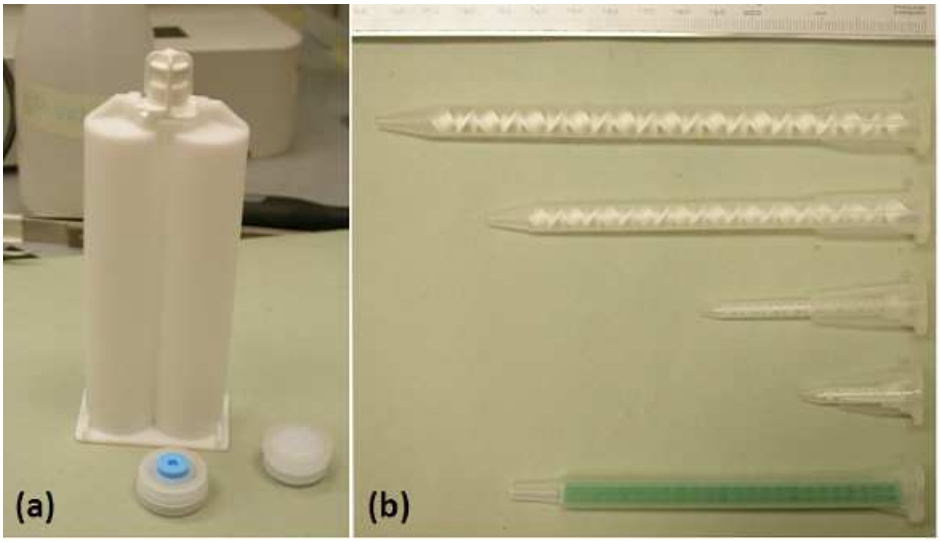

Figure 6.10: (a) 50 ml dual cylinder syringe with bleeding-valve pistons to contain resin and hardener. The cartridge is filled in N_2 atmosphere; (b) tested static mixers. The effectiveness of mixing for a given epoxy depends on the diameter of the tubular housing, as well as on the number and shape of mixing elements. From top to bottom, the inner diameter and the number of elements for each mixer are: 6.3 mm$\times$21, 5.4 mm$\times$21, 3.0 mm$\times$17, 3.0 mm$\times$7, 5.3 mm$\times$24. The top four mixers have an internal helix, while the last one is square shaped.

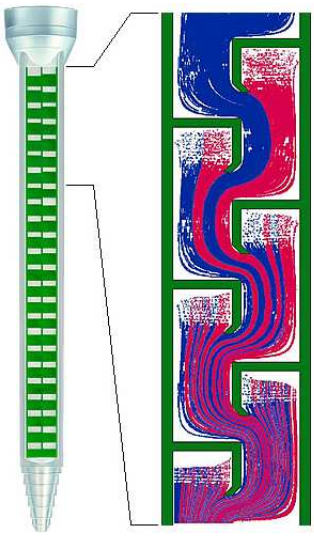

Figure 6.11: Principles of operation of the selected epoxy static mixer. The resin and the hardener are mixed mainly by the mechanisms of division and conversion. The specific geometry allows to build the mixer in a very compact and short way.

6.4.2 Epoxy dispensing

Epoxy dispensing represented an intriguing challenge in the optimization process but eventually outstanding results were reached.

The first attempt was based on an evolution of the nine-pins array procedure. Some problems were initially solved by substituting common pins with Pogo-pins. These devices have application in electronics to establish contact between printed circuit boards: single-tip Pogo-pins, the type we used, are small cylinders containing a sharp, spring-loaded tip. Pogo-pins with variously shaped tips and different lengths were tested in the preliminary study, as shown in Fig. 6.12.

The advantage of Pogo-pins as opposed to the common ones is the spring-loaded mechanism, which leads to an automatic adjustment of the array pressure on sensor surface; moreover, when force is applied, the outer cylinder of the pin pushes glue off the retracting tip, contributing thus to uniform epoxy deposition. Encouraging results were obtained, although characterized once again by problems in reproducibility among different depositions and in dot-dimension equality inside the same matrix. An important factor was found to be the accurate cleaning of pins: tips with dirty surfaces perform larger glue depositions. A series of matrices deposited with the same array of Pogo-pins is shown in Fig. 6.13.

A study of spot size was conducted during the testing of Pogo-pins. The average increase in dot diameter following height reduction down to the 50 μm requirement was evaluated (an estimation based on a simple geometrical model has already been proposed in Subsec.6.2.2). Fig. 6.14 reports an example. This study is compatible with previous estimations and leads to the conclusion that the average increase in spot diameter is $\sim$100-150 μm. Ideal spots in 9-dots matrices have an initial diameter of $\sim$0.7 mm, which turns to approximately 0.8 mm after height reduction. A superior limit for the diameter of unpressed spots should be fixed at 0.85 mm, because the probability of merging for neighbouring dots in the same matrix becomes relevant.

Because the desired level of uniformity and reproducibility was not reached (as testified by the variation of spot size and position in Fig. 6.13), Pogo-pin arrays started to be regarded as a backup solution and another dispensing strategy became appealing. The chosen path is epoxy *single-dot micro-dispensing*. The term micro-dispensing refers to the technique of producing liquid media dosages in volumes smaller than 1 μl. The common industrial application of this system is to deposit adhesives in small quantities as well as in extremely precise and repeatable patterns: as this is the same challenge of the CUORE-0 gluing line project, the introduction of micro-dispensing seemed a viable option. The idea is to deposit matrices dot by dot and in principle this approach allows spot size definition by controlling the amount of glue released singularly. A micro-dispensing system is constituted by two main elements:

- An *automatic dispenser* with an electronic controller to perform glue distribution. The dispenser has a syringe as barrel reservoir and is programmed to control the parameters for glue expulsion, which are very different according to the dispensing technique (mainly, pneumatic or air-free).

- A controlled system for syringe displacement. The best solution for our application is to use a *cartesian coordinate robot*, an industrial machine whose three principal axes of control are linear and at right angles to each other: the syringe translates across an XY plane following the pattern of the nine-dots matrix and is moved vertically along the Z-axis for glue deposition.

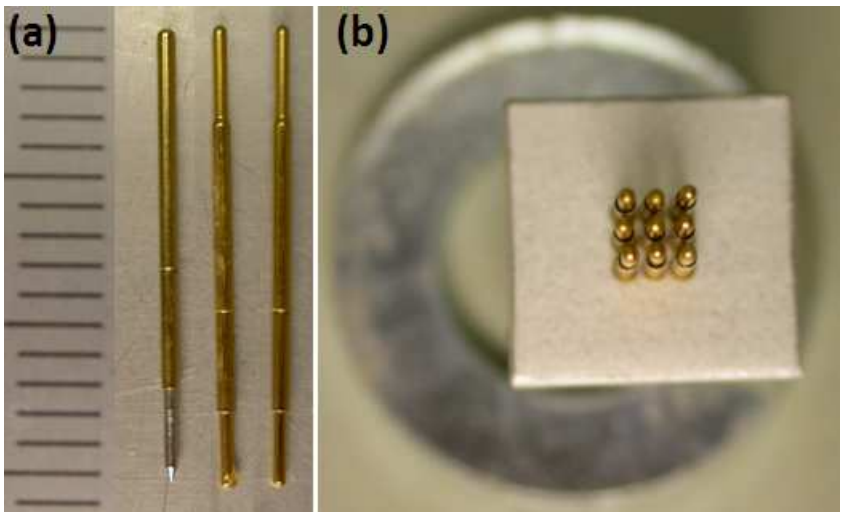

Figure 6.12: Pogo-pins for use in the nine-pins array gluing procedure. (a) Tested types of Pogo-pins; (b) Pogo-pins mounted in the fixed array.

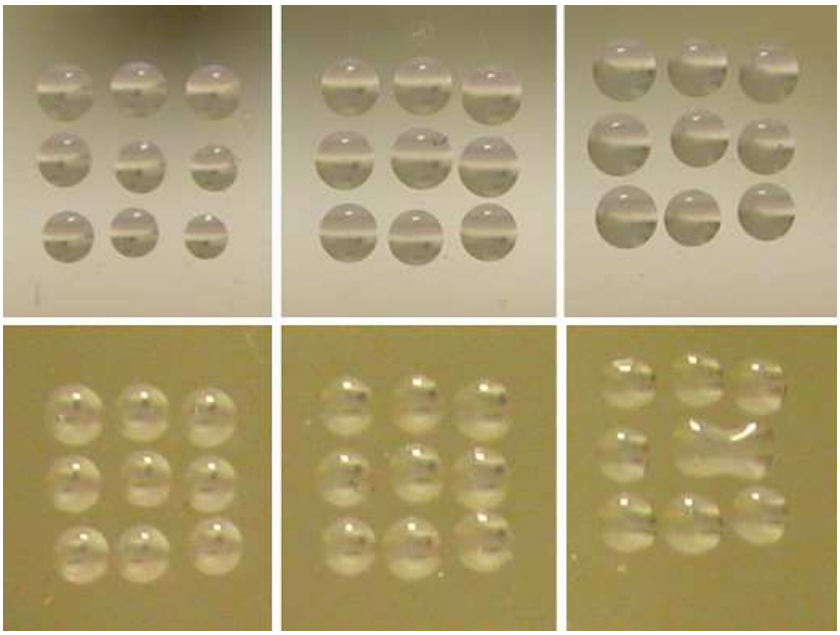

Figure 6.13: Nine-dots matrices realized with the same array of Pogo-pins. Pogo-pins were cleaned with ethanol between depositions, and a new amount of freshly mixed glue was used for each matrix. Slight variations in both position and dimension of dots can be seen from one matrix to the other. The tests were performed in the same conditions, at $\sim$21°C and few seconds after epoxy mixing.

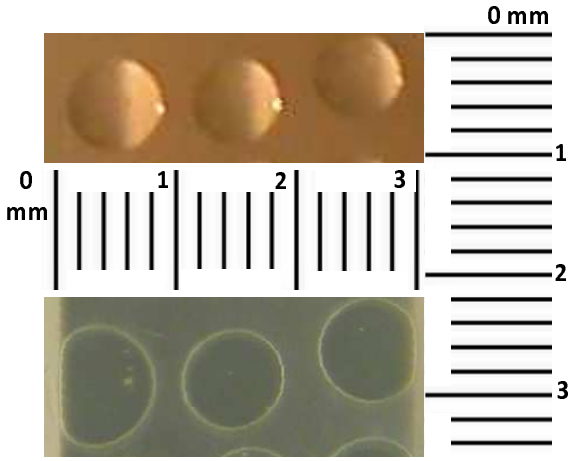

Figure 6.14: Example of diameter enlargement in a row of a nine-dots matrix due to height reduction at 50 μm. The same row of spots was photographed before and after thermistor application on a transparent crystal dummy.

However, the effectiveness of micro-dispensing depends largely on epoxy properties, and works well if the parameters controlled by the automatic dispenser can be kept constant throughout the deposition process. This is generally easier with long pot lives, when epoxy viscosity does not show appreciable variations for a reasonable time. As the viscosity of Araldite Rapid increases drastically in about three minutes, micro-dispensing can be applied provided that a set of conditions is satisfied: the whole dispensing must be performed in a time window shorter than pot life; a limited number of matrices can therefore be deposited; any non-replaceable part of the dispenser should be kept out of contact with glue to avoid rapid sticking. A remark on the first point is that pot life is slightly reduced by epoxy containment inside a syringe. In fact, a concentrated mass will cure faster than epoxy spread out over a large flat area because heat cannot be dispersed easily.

Overall, the dispensing process can be divided in four phases:

Zero-point location. The zero-point Z_0 is the Z-position of contact between the syringe needle and the upper surface of the sensor. Disposable plastic syringes are characterized by high tolerances on their dimensions which are incompatible with the total ± 10 μm required by this positioning, so that zero-point search must take place anew for every gluing. The operation is scheduled before epoxy mixing in order to save on the available time; however, it may be necessary to remove the syringe from the cartesian robot, fill it and fix it back: in this case, zero-point is lost unless mechanical connection to the robot is provided by a specific joint that allows repeatability. In our tests, the zero-point is found by verifying electric contact between the steel needle of the syringe and a thin strip of aluminium fixed on the test slab. The actual height Z_d of single-spot deposition is $Z_0+\Delta Z$, where ΔZ varies according to the dispensing technique.

Syringe filling. As mentioned in the previous item, syringe removal from the robot is usually necessary before filling. This is what happened during tests at the Cryogenics Laboratory in Como, although a system for syringe filling avoiding removal is being considered for the ultimate gluing line. The syringe is generally filled at less than one half of its volume to avoid that large epoxy mass concentration accelerates curing time. While filling, epoxy should not be dropped directly into the needle in order to avoid clogging.

Model	WR300 by AEB Robotics
Movement	520 mm along X and Y, 150 mm along Z
Repeatability	$\pm$20 μm
Minimum resolution	6 μm
Maximum load	10 kg on working surface, 5 kg on the moving arm
Axis velocity	1-600 mm/s along X,Y and Z

Table 6.2: Technical characteristics of the table-top cartesian robot used in the Como dispensing tests.

Purge. It is the process of pushing epoxy through the needle right after syringe filling: as explained later, it is complicated by the viscosity of Araldite Rapid.

Single-dot deposition. According to the dispensing technique, glue can be pushed out of the syringe with continuity or in singularities. This process is described by a set of parameters whose interplay leads to the required spot size.

Dispensing tests at the Cryogenics Laboratory in Como were performed using the table-top cartesian robot WR300, shown in Fig. 6.15, by the Italian company AEB Robotics. Its main specifics are reported in Tab. 6.2.

As for the automatic dispenser, two systems were selected for testing: an air-free model produced by Fishman Corporation and a pneumatic pressure-driven one by Loctite, part of Henkel International. Other technologies, such as Archimedes valves, which incorporate an auger, and positive displacement piston pumps, are commercially available: they are however unsuitable for Araldite Rapid use because of cleaning issues. Fig. 6.16 presents the difference in syringe configuration between the two techniques. Pneumatic dispensers are simple in design, in that they consist primarily of a piston sliding within the syringe under air pressure, which can be continuous or pulsating. The volume dispensed depends on the viscosity of the material, air pressure and amount of time the pressure is applied, and epoxy flow is controlled by the size of the dispense tip. So easiness of use is counterbalanced by the impossibility of having full initial control on the volume dispensed. On the other hand, the air-free model we used works with a linear actuator-driven mechanical lead screw. The head of the screw is inserted in a disposable piston and moves it out on command from a microprocessor control unit. With this kind of dispensing, control is achieved with the linear drive system and is not given by the size of the needle. The shot is delivered volumetrically: after system calibration at the beginning of the process, the control unit, instructed on barrel capacity, automatically calculates the distance the plunger must travel forward and backward for the correct shot size. In addition to that, drawback of the plunger may be programmed to prevent material drip. More control on the single dot is achieved in principle, at price of introducing some complications which will be discussed later on.

The aim of dispenser testing in Como was to select the model for the ultimate gluing line at LNGS. Matrix quality being comparable, fastness of the dispensing procedure was used as a choice standard. Higher easiness of processing was also preferred, as the selected dispenser is meant for use inside a glove-box. Tests have not been performed in a tightly controlled environment due to their selective purpose: the final tuning of parameters will take place in the CUORE-0 clean room at LNGS.

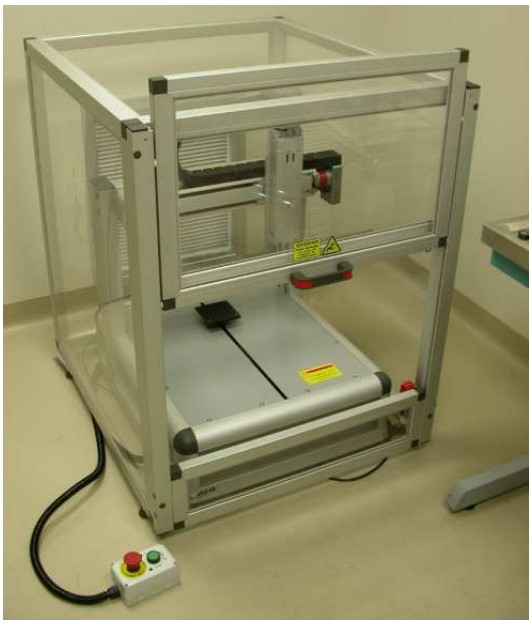

Figure 6.15: The table-top cartesian robot WR300 used in Como dispensing tests.

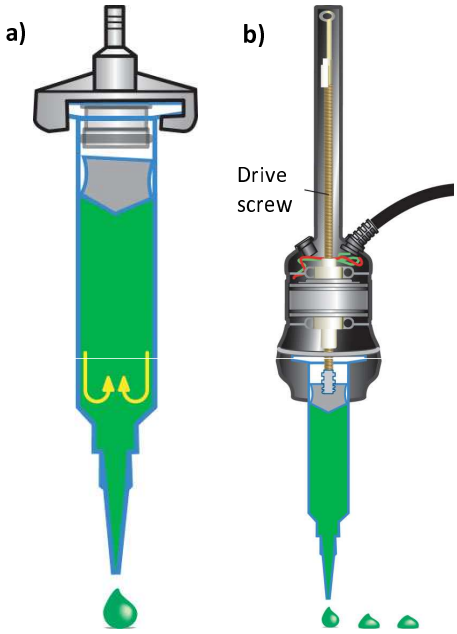

Figure 6.16: (a) Syringe configuration in the pneumatic dispensing system: the barrel is connected to a pressure supply (N_2 in our case) controlled by the dispenser; (b) Syringe configuration in the air-free model: the inner piston is mounted on the head of the drive screw, whose extension and retraction is controlled by the dispenser according to the desired drop volume.

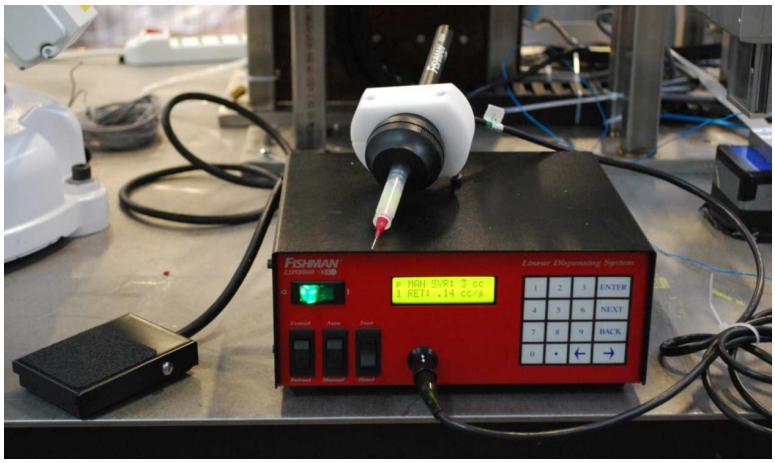

Figure 6.17: The air-free Fishman LDS9000-SDAV epoxy dispenser with its dispensing gun.

The behavior of tested instruments in the four phases of glue dispensing are presented hereafter.

6.4.2.1 The air-free epoxy dispenser

The air-free dispenser is the Fishman Corp. model LDS9000-SDAV (Fig. 6.17). This instrument achieves dot volumes as small as 2.5×10^{-4}cc at 3σ for the 3 cc syringe used in the tests. The principles of this kind of air-free dispensing have already been described in the previous paragraph. The dispenser has two operative modes: a manual mode, which gives the operator real-time control on the duration of screw extension and retraction, and an automatic mode, whose parameters are fixed to gain the desired dot size. An ad hoc mechanical joint is used for syringe connection to the robot, so that the reservoir may be filled and reinstalled keeping Z_d within a 10 μm error. Approximately 1 cc of glue is used (one third of the overall syringe volume).

The most delicate phase is purge. Epoxy is pushed through the needle by screw extension until a drop forms. If the process is too quick, however, the high viscosity fools the system into believing that syringe bottom has been reached, and extension is blocked by an automatic control: gluing is aborted and a new syringe must be used. This forces to proceed with small, subsequent screw extensions that consume about 1 minute of the available time. Some drawback follows successful purge to lower internal pressure and prevent dripping. All the previous operations are performed by manual control of the dispenser. After that, the system is ready for single-spot deposition and the dispenser is switched from manual to automatic mode. The cartesian robot takes the syringe at the coordinates (X_1, Y_1, Z_d) of the first point and stays in position while single-spot dispensing is completed. A set of parameters, regarding both the robot and the dispenser, proved particularly relevant for this type of air-free dispensing.

- ΔZ: tests with ΔZ ranging from 30 μm to 300 μm were performed: examples of matrices are the B/B' cases shown in Fig. 6.18. The optimum Z_d is found 200 μm higher than zero-point.

- *Shot size*: the volume of each shot is fixed according to the diameter requested for the deposited dot. Approximating the shape of the epoxy drop released to half of a sphere, a 700 μm diameter corresponds to a volume of the order of 10^{-4} cc. Shot size is fixed at the smallest value achieved by the dispenser: 2.3×10^{-4} cc. This

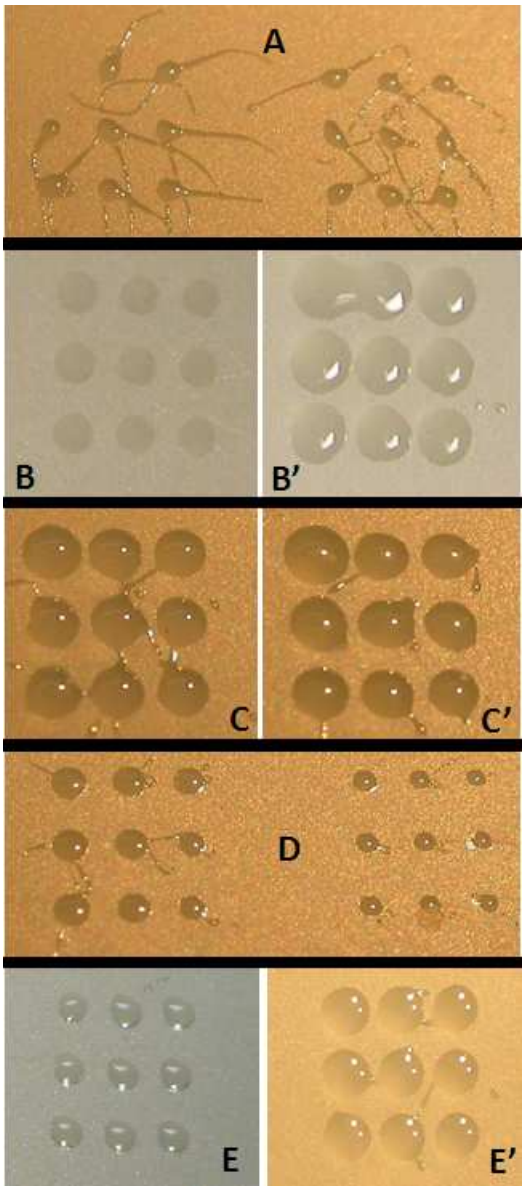

Figure 6.18: Selection of nine-dots matrices realized with the air-free dispensing technique. Pair of matrices indicated by the same capital letter illustrate each the effect of a peculiar dispensing condition or the variation due to the tuning of one parameter. Filaments and small size in the A matrices are due to insufficient after-purge drawback; matrix B was dispensed with ΔZ=30 μm, B' with ΔZ=200 μm; matrices C and C' are characterized by point-to-point rise equal respectively to 12 mm and 15 mm; the D matrices were dispensed in row at advanced pot life (2 minutes after mixing) and show reduction in spot size due to viscosity increasing steeply; matrices E and E' were dispensed by needles with different $\oslash_{in}$: 0.20 mm and 0.25 mm. For all cases, the unmentioned parameters are equal to the ordinary values listed in the text.

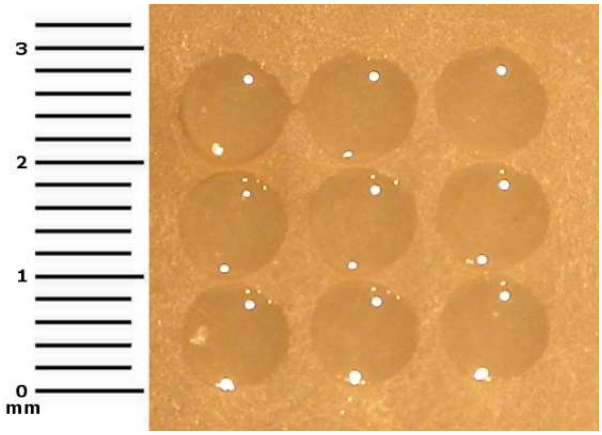

Figure 6.19: Nine-dots matrix dispensed by air-free technique with the set of parameters defined as optimal: ΔZ=200 μm, shot size=2.3$\times 10^{-4}$ cc, dispensing rate=0.135 cc/s, drawback=500 steps, single-point working time=3 s, point-to-point rise=15 mm.

does not mean that larger spots are deposited, as both needle size and viscosity contribute in shaping the glue dot.

- *Dispensing rate*: when the speed of screw extension is too high, the needle clogs due to Araldite Rapid viscosity. In order to save on working time, the dispensing rate is fixed at the limit value before clogging manifests: 0.135 cc/s.

- *Drawback*: screw retraction, known as drawback, is relevant right after purge as well as following each single-spot deposition. In the first case, drawback is used manually to control the heavy flow of epoxy caused by purge (Fig. 6.18, case A, shows what happens when not enough drawback is applied). In the second case, automatic drawback helps preventing the formation of glue filaments that compromise matrix quality. The value of automatic drawback following each single-spot deposition is fixed at its maximum: 500 steps.

- *Single-point working time*: this parameter is determined by the amount of time necessary for screw extension and drawback in single-spot deposition. With dispensing rate equal to 0.135 cc/s and drawback fixed at 500 steps, the necessary time window is 3 s.

- *Point-to-point rise*: after single-spot deposition is complete, the syringe moves to the following point in the matrix. Movement along the X and Y axes should be preceded by a vertical rise. Due to Araldite Rapid viscosity, in the detachment of the needle from the deposited dot a glue filament forms and smears on the surface if an immediate X or Y translation follows: this may result in adjacent epoxy dots merging together. An increase in point-to-point rise helps breaking the filament with no surface remnants. This parameter has small influence on air-free dispensing, as depositions are volumetrically quantified and drawback helps relieving internal pressure. Fig. 6.18 reports examples of matrices (C and C') characterized by a different point-to-point rise. The ultimate value chosen is 15 mm.

In addition to the previous list, two stainless steel needles with 12.7 mm long tips and different inner diameters (0.20 mm and 0.25 mm) were tried: the E/E' pair in Fig. 6.18 shows the difference in matrices dispensed by the two kinds. Requested spot diameter is given by the second type, the 0.25 mm needle, which is adopted also for use with the pneumatic dispenser.

Figure 6.20: The pneumatic Loctite 98666 epoxy dispenser.

When air-free dispensing is performed as described, a “calibration” dot and two subsequent nine-dots matrices are obtained with a single syringe filling. Epoxy dots satisfy size requirements. A reproducible example of matrix dispensed with the optimal set of parameters previously listed is reported in Fig. 6.19.

6.4.2.2 The pneumatic epoxy dispenser

The pneumatic dispenser is the Loctite 98666 model, pictured in Fig. 6.20. As already pointed out, the technique does not give the operator full power on the volume dispensed. However, this feature can be counterbalanced, and control on epoxy flow is obtained by tuning the parameters of the cartesian robot. Compared to air-free dispensing, the procedure is remarkably simpler. After zero-point determination, the syringe, now with 10 cc capacity, is removed and filled; approximately 2 cc of epoxy are used (one fifth of the overall volume). A disposable piston is inserted and the pneumatic tube commanded by the dispenser is attached: N_2 gas is used instead of air due to environmental requirements described in Subsec. 6.2.3. Repositioning that keeps the syringe at Z_d within a 10 μm error is guaranteed by a mechanical joint different from the one used in the Fishman case. Purge is a straightforward operation because the pneumatic dispenser has not pressure controls that stop epoxy expulsion. Pressure is opened at the beginning of the dispensing process and then supplied continuously while matrices are composed.

The following parameters proved relevant in pneumatic dispensing.

- ΔZ: the optimal Z_d is 100 μm higher than the zero-point. A selection of tests done with changing ΔZ is presented in Fig. 6.21, cases I and I’.

- *Dispensing pressure*: the maximum pressure reachable in the experimental setup at Como Laboratory is 2.8 bar. Working with higher pressures is advisable because of the resistance opposed by epoxy viscosity (Fig. 6.21, II and II’). Optimization of system performance at pressure over 3 bar will be investigated in the final LNGS setup.

Matrix number	ΔZ [μm]	Dispenser pressure [bar]	Single-point working time [s]	Z-axis speed [mm/s]
I	*500*	2.8	1	600
I'	*100*	2.8	1	600
II	100	*2.0*	1.2	600
II'	100	*2.8*	1.2	600
III	200	2.8	*3*	600
III'	200	2.8	*2*	600
IV	100	2.8	1	*600*
IV'	100	2.8	1	*200*

Table 6.3: List of dispensing parameters for the selection of epoxy matrices in Fig. 6.21. Only matrices belonging to the same pair can be compared. For all matrices, epoxy dispensing is performed with the $\oslash_{in}$=0.25 mm needle and 150 mm point-to-point rise.

- *Single-point working time*: as opposed to air-free dispensing, this time window is not fixed by other parameters but plays a relevant role. This happens because pressure is supplied continuously and not on a point-by-point basis. Other parameters being equal, higher single-point working times result in larger epoxy dots. After tests ranging from 0 to 4 s (see III and III' in Fig. 6.21), the 1 s time interval was selected.

- *Point-to-point rise*: this parameter, which has limited influence in air-free dispensing, is relevant in pneumatic dispensing because no drawback is applied. Lifting the syringe vertically in the X-Y transfer from one point of the matrix to the following limits the formation of epoxy filaments. Point-to-point rise is fixed at the maximum value obtainable by the cartesian robot: 150 mm.

- *Z-axis speed*: if a glue filament forms when the needle is lifted from the deposited spot, slow movements of the robot keeps it from smearing on the matrix. The value v_z=600 mm/s is adopted. An example is the IV/IV' pair in Fig. 6.21.

One should note that, as opposed to air-free dispensing, the previous parameters are strongly interconnected. For instance, higher single-point working time leads to larger spots but can be counterbalanced by lowering dispensing pressure; or again, high point-to-point rise helps limiting the problem of glue filaments unless v_z is too high.

A total of one "calibration" spot and two nine-dots matrices whose size satisfies requirements are deposited with one syringe filling. A reproducible example of matrix dispensed with the optimal set of parameters previously listed is reported in Fig. 6.22.

6.4.2.3 Comparison between dispensing techniques

Air-free and pneumatic dispensing gave satisfying results in terms of spot dimension. The behaviour of both dispensers is understood and the fine tuning of parameters will be performed in the ultimate gluing site, at LNGS. The two techniques have fundamental differences. Air-free allows volumetric dosage of each spot at price of handling complications originated by Araldite Rapid being a short pot life, high viscosity epoxy; on the

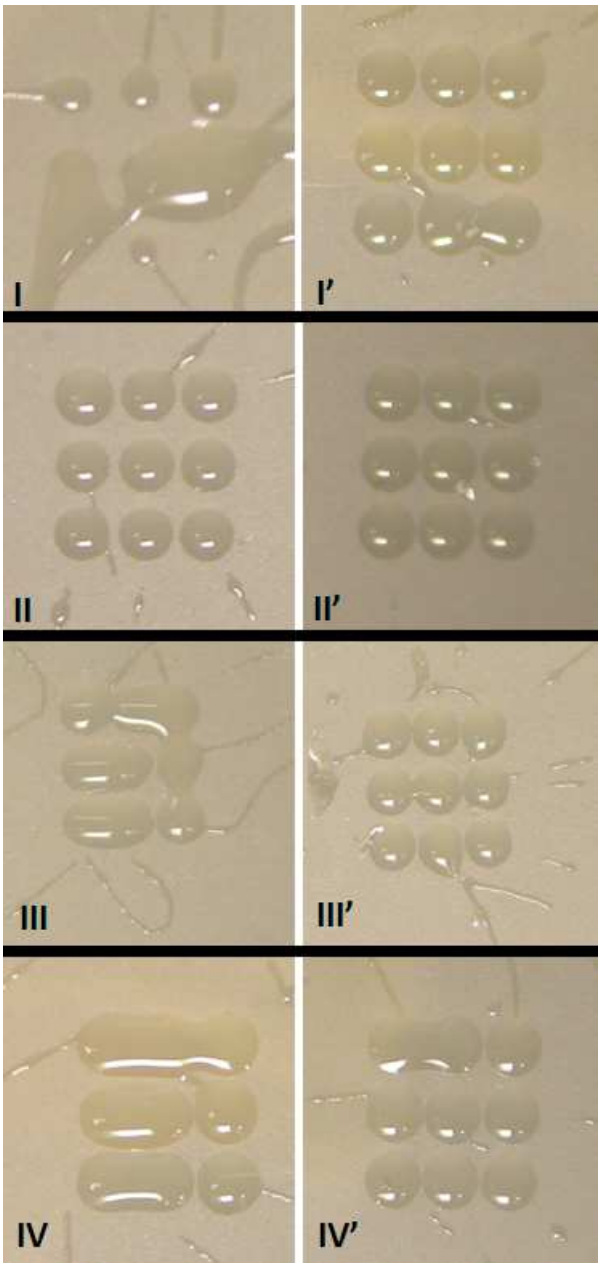

Figure 6.21: Selection of nine-dots matrices realized with the pneumatic dispensing technique. Pair of matrices indicated by the same roman number were obtained with an equal set of parameters apart from one: ΔZ for pair I, dispensing pressure for pair II (lower P corresponds to smaller spots, while filament production remains unaltered), single-point working time for pair III and Z-axis speed for pair IV. The complete set of parameters for each pair is reported in Tab. 6.3.

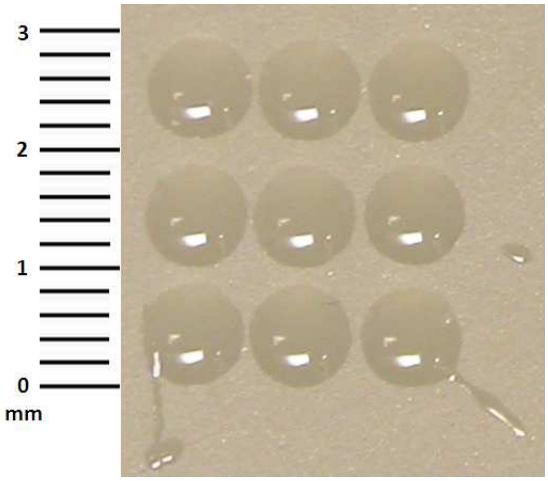

Figure 6.22: Nine-dots matrix dispensed by pneumatic technique with the set of parameters defined as optimal: ΔZ=100 μm, dispensing pressure=2.8 bar, single-point working time=1 s, point-to-point rise=150 mm, Z-axis speed=600 mm/s. Final parameter tuning will take place in the ultimate gluing site at LNGS to get rid of the epoxy filaments visible in the picture.

other hand, pneumatic dispensing allows control on spot size only by interaction of the dispenser's parameters with those of the cartesian robot. Table 6.4 reports a quantitative overview on dispensing parameters for both techniques.

The pneumatic technique has simpler application and requires shorter time windows. Results being comparable, our choice is oriented on the Loctite 98666 model.

6.4.3 Sensor positioning

As anticipated in Sec. 6.4, the optimization of sensor positioning consists in designing a non-intrusive method to fix within a 5 μm error the 50 μm-gap between sensor and crystal. The project was guided by the following principles:

1. use of a single tool to position sensors, support them during epoxy dispensing and host the glued crystal until expiration of curing time (or handling time, see Subsec.6.2.1);

2. no dependency on sensor thickness to allow epoxy deposition on the footprint of thermistors and heaters. The precision on the dimension of NTD wrap-around thermistors (see Chapter 5, Sec. 5.6) is 890$\pm$75 μm, while the variation in height of heaters at 3σ is 525$\pm$10 μm for chips from the same wafer and $\pm$15 μm for chips from different wafers. The footprint area is 2.77$\times$2.84 mm^2 for wrap-around thermistors (a nine-dots matrix fits) and 2.33$\times$2.40 mm^2 for heaters (a five-dots matrix fits);

3. for each crystal, one-shot gluing of both thermistor and heater. The sensors must be glued on the same crystal side due to assembly requirements on the bonding of signal read-out wires, although positioning standards on the XY plane had yet to be fixed by the Crystal Assembly Working group at the time of prototype design;

4. no pressure on the sensors during positioning to avoid breakage (see Sec. 6.3);

5. as radio-purity is concerned, use of safe materials to build the outer shell of the tool (stainless steel 303/304, PTFE), no oils that could undergo de-gasification

	Air-free dispenser	**Pneumatic dispenser**
Model	Fishman Corp. LDS9000-SDAV	Loctite 98666
T range	20-21° C	20-21° C
Syringe capacity	3 cc	10 cc
Volume of epoxy used	$\sim$1 cc	$\sim$2 cc
Needle $\oslash_{in}\times$L	0.25 mm$\times$12.7 mm	0.25 mm$\times$12.7 mm
Dispensing mode	Point-by-point	Continuous
ΔZ	200 μm	100 μm
Shot size	2.3×10^{-4} cc	-
Dispensing rate	0.135 cc/s	-
Drawback	500 steps	-
Dispensing pressure	-	2.8 bar
Single-point working time	3 s	1 s
Point-to-point rise	15 mm	150 mm
Z-axis speed	600 mm/s	600 mm/s
Average purge time	60 s	30 s
Average deposition time (one spot + two nine-dots matrices)	57 s	19 s

Table 6.4: Comparison between dispensing techniques: best parameters for epoxy deposition as deduced by Como tests. The temperature range reported accounts for the testing environment in Como not being tightly controlled. Items eight to ten are parameters of the cartesian robot.

or particulate production and easy dismounting for accurate cleaning whenever necessary. The use of aluminum is accepted provided that no contact with detector elements takes place;

6. limited contact of the crystal with any mechanical parts, and in any case only with the stainless steel and PTFE elements.

The idea for the tool, called *Z-positioner*, was developed in Como and a prototype was accordingly designed and built.

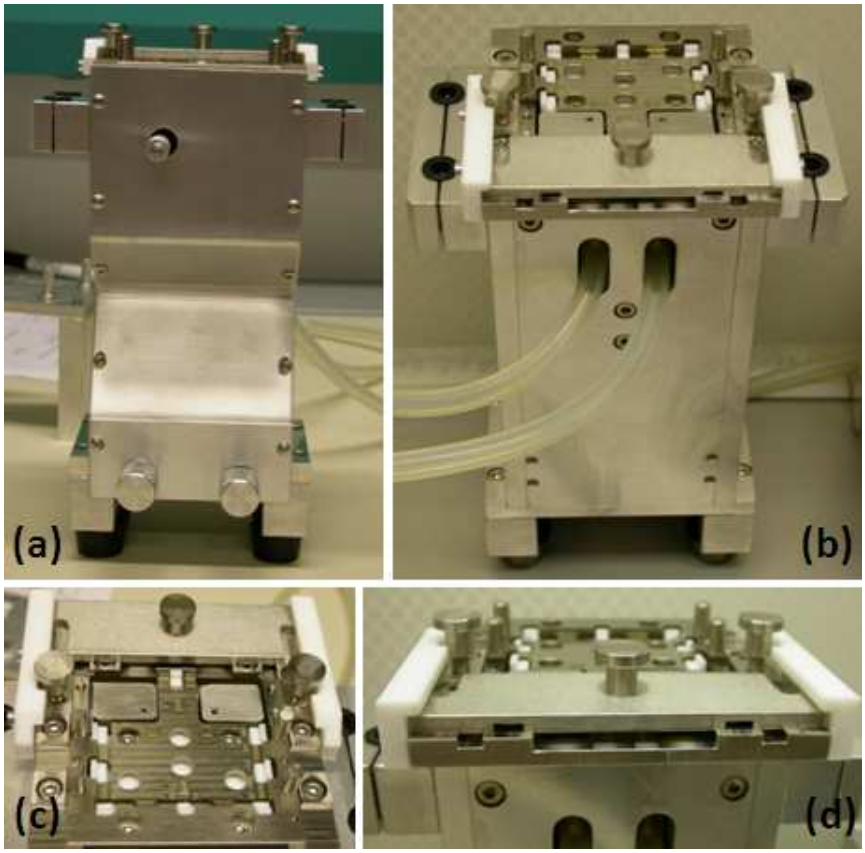

Figure 6.23: The Como prototype of Z-positioner. (a) Front view: the two handles for vertical adjustment of the chip holders and the handle for displacement of the crystal PTFE frame are visible. (b) Rear view: the vacuum tubes reach the chip holders and are connected to a small pump. (c) View of the zero plane, the chip holders, the PTFE frame and the mobile plane on the back. (d) Zoom on the mobile plane in its rest site, prior to positioning on the chip holders.

In the prototype, the 50 μm-gap is obtained by putting in mechanical contact a zero-plane with a mobile plane, which has an integrated spacer 50 μm lower than the zero-surface. Two chip holders are mounted on the heads of inner vertical ratchet-stop micrometers that move along the Z-axis. The operator regulates manually and independently the position of each micrometer. The sensors are placed in the insets on the chip holders, where they are firmly held by vacuum, and lowered under the zero-plane level. The mobile plane is moved on the zero plane and fixed by two screws. The chip holders are raised and thanks to the ratchet stop mechanism, the extension of the micrometers is blocked when the upper surface of each sensor touches the spacer: the 50 μm-gap is therefore fixed without causing any damage to the sensors, due to the limited force applied; the error on positioning depends on micrometer tolerance as well as on the quality

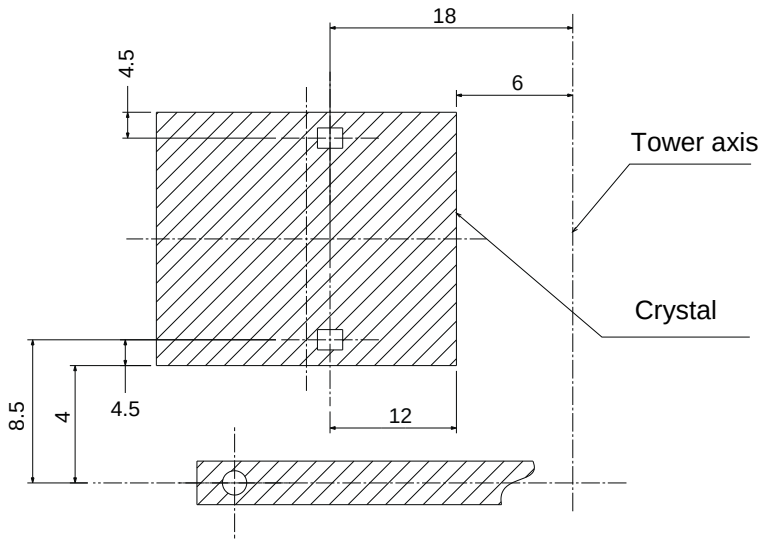

Figure 6.24: Position of sensors on the crystal surface in the standard defined by the Crystal Assembly Working group.

Figure 6.25: The revised model of Z-positioner realized at Lawrence Livermore National Laboratory.

of both the zero plane and the mobile plane, which must undergo precision grinding. The mobile plane is unscrewed and removed after the gap is set, leaving the upper surface of the sensors free for glue deposition. At the end of dispensing, the crystal is laid upon a PTFE frame, which is lowered until the TeO_2 lower surface rests on the epoxy dots and on a set of steel pedestals providing support: the position of the pedestals compensates the possibility of a slight curvature of crystal surface, mainly because of lapping. The assembled detector is left on the Z-positioner until curing time is over. The prototype, shown in Fig. 6.23, was built in 2008 and underwent several positioning tests. The idea behind the functioning of the prototype Z-positioner proved to be successful and remained basically unaltered. Some features, however, were revised to improve global tolerance and repeatability, as well as to meet the new requirements on sensor position on crystal surface (see Fig. 6.24) and those originated by the parallel development of the other stages of the gluing procedure (e.g. integration with automated elements, see Subsec. 6.4.4). The ultimate model of Z-positioner is currently being realized at Livermore National Laboratory (Fig. 6.25): preliminary tests show that the tool fixes the 50 μm-gap with a 5 μm error.

6.4.4 Introduction of automated elements

As already stated in Sec. 6.4, the introduction of automated steps comes from the necessity of a definite timing for the gluing procedure as well as of reducing the lack of reproducibility intrinsic to human intervention. Nonetheless, the realization of a totally automatic system is out of purpose in this case: there are operations in the procedure whose results are not improved in precision and may be, in specific cases, even complicated by automation. A semi-automatic approach, with automated and manual stages cohabiting, allows for a more straightforward approach.

As mentioned in Subsec. 6.4.2, syringe displacement and epoxy dispensing are both automated: while the three-axes cartesian robot is programmed to move the glue barrel along a fixed sequence of coordinates depending on the ultimate layout of the gluing line, the epoxy dispenser performs dot deposition according to a memorized set of predetermined parameters. The cartesian robot used during Como tests will not be incorporated in the ultimate gluing line at LNGS because its dimensions and portal configuration imply restrictions on the layout; a three-axes system by Jenny Science AG (Fig. 6.26, left), allowing a versatile assembly of the independent linear axes and easier integration with the other components of the layout, will be used. Compared to the robot used in Como tests, the final cartesian system has also higher technical standards: minimum repeatability ± 2 μm, resolution 1 μm, maximum velocity 2500 mm/s.

Another automation element is introduced in the placement of sensors and crystals. The gluing line will incorporate the six-axes anthropomorphic robot IRB 140 produced by ABB Robotics, which has maximum payload 5 kg, 810 mm reach and ± 30 μm position repeatability (Fig. 6.26, right). While crystals are grabbed and moved by a PTFE-coated clamp mounted on the robot's arm, sensors are picked up by a suction cap attached to one side of the clamp, with the advantage of reducing operator contact with cleaned detector elements as well as reaching positioning repeatability and precision which would manually be unobtainable. The use of the robot is compatible with a clean room environment.

A vision system constituted by a camcorder and an image acquisition software will provide check on the quality of epoxy dots.

Syringe filling automation is still under discussion. The Loctite 97042 pneumatic gun with manual trigger for double-barrel syringes is currently used. Manual trigger bypass by integration of a flow valve for automatic gas supply (N_2) is evaluated.

Process	Operational mode
System preparation	Manual
Sensor displacement	Automatic
Z-positioner adjustment	Manual
Syringe height correction	Automatic
Syringe filling	Manual
Syringe purge	Manual
Epoxy dispensing	Automatic
Image acquisition	Automatic
Crystal displacement	Automatic
Detector removal for storage	Automatic

Table 6.5: List of automatic and manual operations in the gluing sequence. Up to this date, both syringe filling and purge are manual operations; automation is currently in study.

6.4.5 A final glimpse of the gluing line

The final phase in the design of a functioning semi-automatic gluing line is system integration, when the components individually tested and approved are interfaced to communicate and interact. A PLC will serve this purpose. All instruments are mounted on an optical table and two Z-positioners are installed on the working surface.

Thanks to this design, two detectors can stay in the operational area at the same time. However, gluing runs are performed on one crystal at a time, so that epoxy deposition on different crystals is done with a separate syringe filling: the choice was made not to force working times, which are already short due to the three minutes pot life of Araldite Rapid; in line of principle, if no unexpected events take place, this guarantees epoxy dots whose quality, on the same as well as on different detectors, is safe from time variations in glue viscosity. One calibration dot, a thermistor nine-dots matrix and a heater five-dots matrix are dispensed with a single syringe filling. When the 30 minutes handling time for the first crystal expires, so that no vibrations disturb matrix polymerization anymore, the gluing of the second crystal begins. The first absorber is not removed from the Z-positioner during this procedure and is moved to a storage area only at the end of curing time. The total duration of a gluing run includes system preparation, besides curing time. According to the timetable presented, the gluing line can lead to the daily yield of twelve detectors.

For this reason, the system layout includes a repository which contains the twelve crystals and the corresponding number of sensors employed in a working day. Fig. 6.27 shows the most recent layout of the gluing line, according to the simulated movements

of both the anthropomorphic and the cartesian robots. To complete the preliminary view of system performance, a flowchart which describes operator logics combined to the gluing sequence is reported in Fig. 6.28.

6.5 Future steps

The optimization work presented, which began in 2007, led to improvements in all the gluing procedure stages.

- The use of *double-barrel syringes* combined with *static mixers* guarantees reproducible resin and hardener dosing, as well as thorough epoxy mixing.
- *Single-dot micro-dispensing*, although a tricky process when short life bi-component epoxies are used, allows full control on the gluing process: the amount of fluid released for each spot is fixed and uniformity of matrices is guaranteed.
- The *new Z-positioning system* does not damage sensors. After tests of the Como prototype, preliminary measurements on the final tool produced at LLNL show that it leads to 50 μm$\pm$5 μm positioning.
- The *use of automation* in certain steps of the gluing process (such as crystal handling or syringe displacement) eliminates the human error and quality variation intrinsic to operator-dependant procedures, besides introducing definite timing.

The gluing line is now in the assembly phase, although a limited set of operations still needs to be completed: a possible automation of the syringe-filling phase and of the purge phase is evaluated, and the final Z-positioner model from LLNL has to undergo conclusive tests. The first CUORE-0 gluing is foreseen to take place in the second half of October 2010.

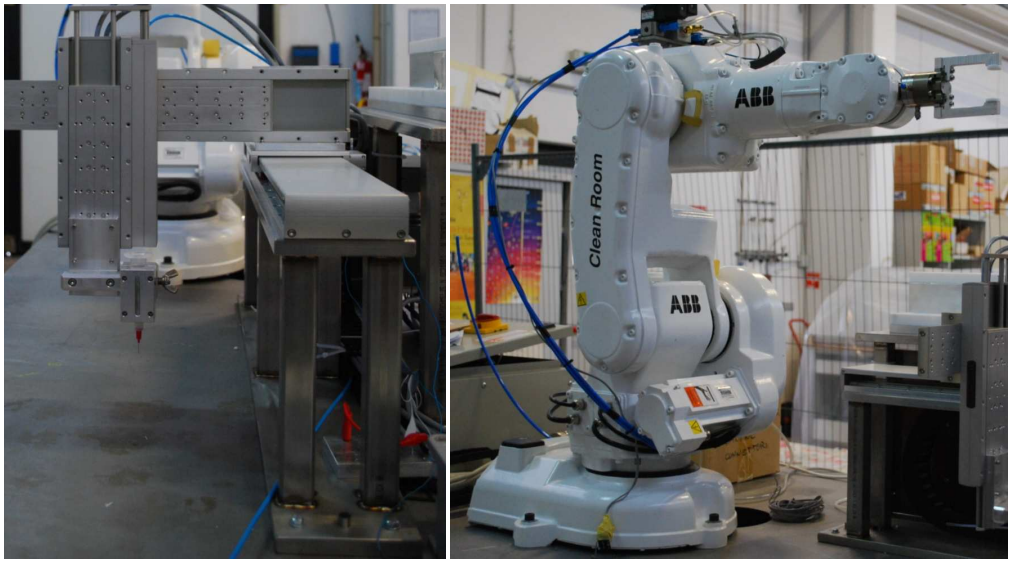

Figure 6.26: Devices for the CUORE-0 gluing line at LNGS. Left: the three-axes system by Jenny AG. Right: the anthropomorphic robot IRB 140 by ABB Robotics.

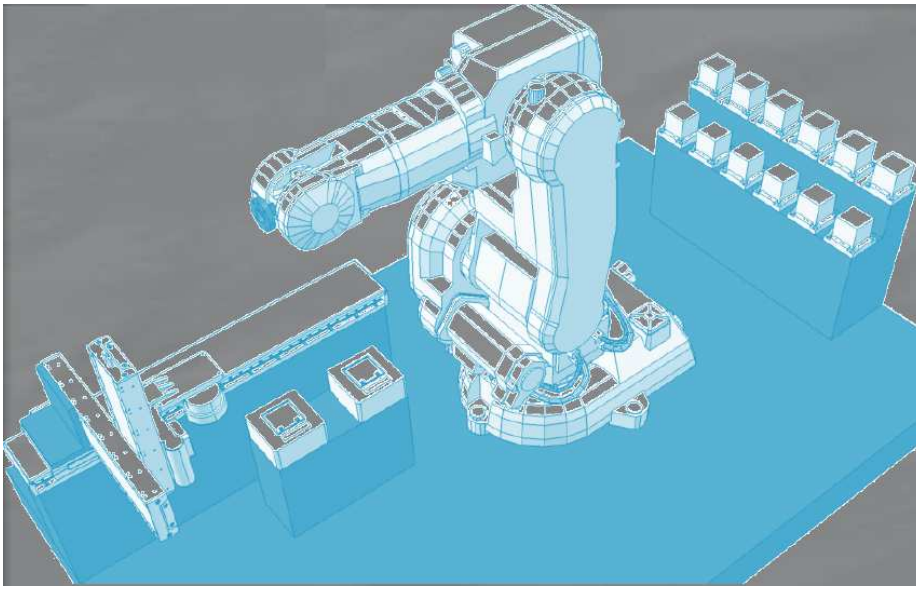

Figure 6.27: Layout of the gluing line, obtained according to movement simulations of the two robots (anthropomorphic and cartesian).

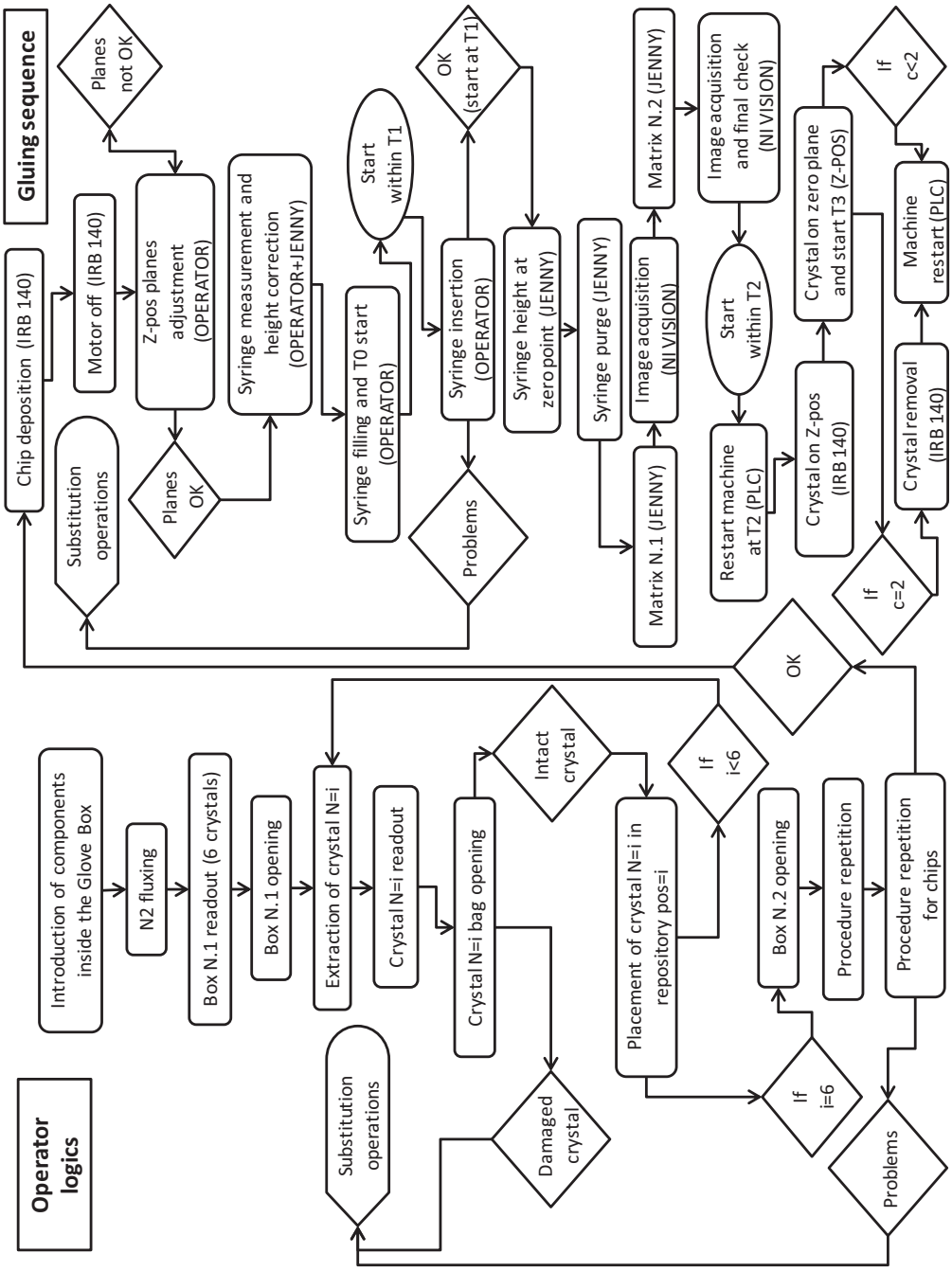

Figure 6.28: System flowchart for the gluing line, comprehensive of both the operator logics and the gluing sequence. In the diagram: i=1,...,6; c is the counter of crystals on the Z-positioners; T_3 = 30' - (T_1 + T_2 + displacement time).

Conclusion

The Ph.D. work presented here focused on optimizing major aspects of the Single Module of detection developed by the CUORE collaboration, in order to reach the requirements on both sensitivity and modularity needed by the imminent first step of the CUORE experiment, CUORE-0. At the same time, many of the results obtained provide a ready-to-go system for CUORE itself. The investigation regarded four elements which constitute the core of the detector.

The first issue discussed here was a strategy to reduce the contribution to the background counting rate in the 0ν-DBD(^{130}Te) region coming from surface contaminations in the copper structure that holds the crystal absorbers: this factor has been demonstrated to affect strongly the experiment's final sensitivity. Following the choice of the collaboration to pursue a strict program of material decontamination, a surface treatment protocol was selected for the Cu elements to be used in CUORE-0, and an upper limit on its foreseen realistic background was set at 0.12 c/(keV·kg·y). A satisfying protocol, in terms of radio-purity, dimensions and crystallographic orientation, has also been validated for the growth and surface treatment of TeO_2 crystal absorbers. Then, the contact geometry of the NTD-Ge thermistors used for signal read-out has been revised in order to obtain a dramatic improvement of reproducibility in the assembly of both CUORE-0 and CUORE: a campaign of low-temperature tests, completed with simulations on electric conductivity and thermal behaviour, allowed to choose, among the different thermistor designs investigated, the model that provides the best trade-off between performances and reliability. Finally, the realization of the thermistor-to-absorber coupling, which is limited by strong constraints, was studied thoroughly for an appreciable increase in its reproducibility among different detectors: the design of the semi-automated gluing line based on the guidelines defined here is now being ultimated at LNGS.

All the results presented in this work contribute in shaping the CUORE-0 detector, in both its components and assembly procedures: the sensitivity that the experiment will be able to reach, given the realistic background evidenced by tests, is reported as a function of time in Fig. 6.29. The results obtained pave also the way to the final definition of the CUORE array.

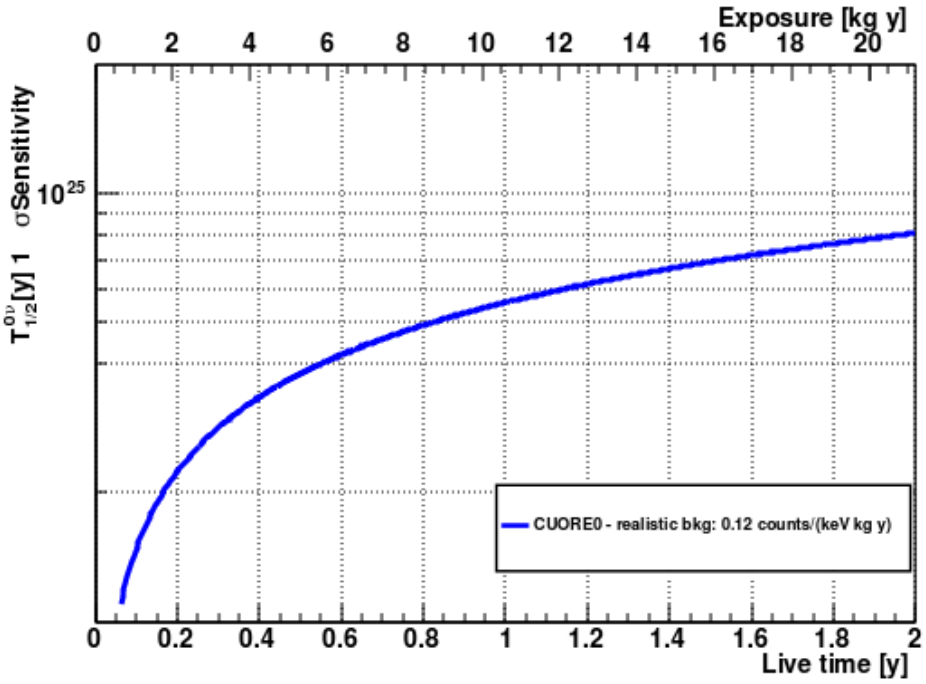

Figure 6.29: The sensitivity of CUORE-0 is reported here as a function of time, given the realistic estimation of 0.12 c/(keV·kg·y) for the background in the ROI.

Appendix A

Cryogenic systems

This appendix provides information on the cryogenic systems mentioned in this thesis and used to cool-down the detectors of the R&D activity.

Bolometers need to work at sub-K temperatures for the reasons explained in Sec. 1.3 and the needed work range, few mK, can be reached continuously only by means of *dilution refrigerators* (DRs). This technology was first proposed by H. London in 1951. Very low temperatures are obtained by a mechanism based on a change of phase. The simplest refrigerators exploit the liquid-to-gas change of phase: the removal, spontaneous or induced, of the vapour in equilibrium with the liquid state causes the latter to evaporate more; the process is endothermic, so heat is removed from the liquid, which gets cooled down. Dilution refrigerators exploit the change of phase of a ^{3}He-^{4}He mixture. The mixture is kept at room temperature in a tank; a system of vacuum pumps extracts it from there and sustains its circulation in the system. The condensation mechanism is based on the Joule-Thomson effect. Helium is compressed on a flow impedance and cooled down to 2.5 K, by means of subsequent expansion; or it is put in thermal contact with a pumped L-He bath at 1.5 K. At this point, the main refrigeration process is vapour pumping from the surface that separates the liquid phase from the gaseous phase formed in the refrigerator.

^{4}He can be treated as an ideal boson gas that does not obey the Pauli exclusion principle, hence it undergoes Bose-Einstein condensation at low temperatures. On the other hand, ^{3}He is a fermion with asymmetric total wavelength and follows the Pauli principle. In liquid refrigerators, ^{3}He behaves as a classic dense gas with no super-fluid phase. Below 1 K, at given temperatures and average molar concentrations of ^{3}He, ^{3}He-^{4}He mixtures appear as two separate phases: a lighter concentrated phase rich in ^{3}He and a heavier diluted phase rich in ^{4}He. The phase diagram of the mixture is reported in Fig. A.1. The lighter phase is distributed in the upper part of the mixture and a surface if separation between the two phases is formed. If ^{3}He is removed from the diluted phase, an evaporation of this isotope is established towards it from the concentrated phase causing a cool-down. Details on the process can be found in [132] and [129]. The basic structure of dilution refrigerators is composed by the still (where ^{3}He is removed by pumping from the diluted phase to be reinserted into the concentrated phase) and by the mixing chamber (where the osmotic pressure difference caused by still pumping drives a flow of ^{3}He to the still, and the lowest temperature of the system is obtained); the elements are connected to each other by heat exchangers. A full leak-tight pumping system at room temperature is used to remove ^{3}He from the still and compress it to a pressure of a few hundred mbars. The gas is then passed through filters and cold traps to remove impurities and finally returned to the cryogenic system, where it is pre-cooled in a liquid helium bath (that can nowadays be replaced by a cryo-generator named *Pulse*

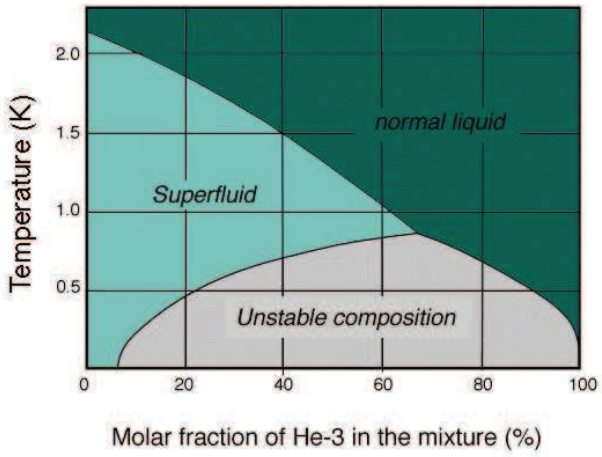

Figure A.1: Phase diagram of liquid ^{3}He-^{4}He mixtures at saturated vapour pressure.

Tube); then it is condensed on a dedicated independent pumped helium bath called *1K pot* or through the Joule-Thomson effect, by means of flow restriction. The detector is connected tightly to the mixing chamber, reaching the needed sub-K temperatures.

The Hall A cryostat

The Cuoricino cryostat was also used for the operation of the Three Towers Test described in Sec. 3.4.2. The system, which is site in the Hall A facility at LNGS, uses a LHe main bath to pre-cool the mixture and a 1 K pot for condensation, so that helium refills are necessary approximately every two days; it is also connected to a recovery system that allows for the evaporated helium to be collected in the reservoir of a He liquefier. The dilution refrigerator has a cooling power of 1000 μW at 100 mK; the upper part of the cryostat is connected to the pumping system, which sustains the circulation of the ^{3}He-^{4}He mixture and carries out other tasks: it keeps vacuum inside the system and pumps away the He evaporated from both the main bath, the ^{4}He bath at 4.2 K where the central part of the cryostat is immersed, and the 1K-pot. The cryostat is housed inside a Faraday cage to suppress electromagnetic interference. The available experimental volume at base temperature is about 16 dm^3. All the cryostat's materials were validated in terms of radio-purity by HP-Ge analysis, given the basic requirements of the following upper limits for contaminations: less than 100 mBq/Kg for materials used in quantities lower than 1 Kg and less than 10 mBq/Kg for those used in higher quantities. The Hall A low temperatures setup is shielded by two layers of lead with 10 cm minimum thickness each; the outer layer is made of commercial low radioactivity lead, while the internal one is made with special lead with a ^{210}Pb contamination of 16$\pm$4 Bq/kg. The external lead shields are surrounded by an air-tight box flushed with fresh nitrogen from a dedicated evaporator to avoid radon contamination of the gas close to the cryostat. In order to shield the detectors against the unavoidable radioactive contamination from some fundamental components of the dilution refrigerator, thick layers of Roman lead are placed inside the cryostat just around the detectors. A borated polyethylene neutron shield (10 cm) was also added in 2001. Typical operation temperatures with the Cuoricino detector are in the range of 10 mK. The cryostat in Hall A hosted both Cuoricino and the Three Towers Test; after a refurbishing regarding its mechanical stabilization and its read-out wiring, the setup will be also used to operate CUORE-0. A scheme of the setup is reported in Fig. A.2.

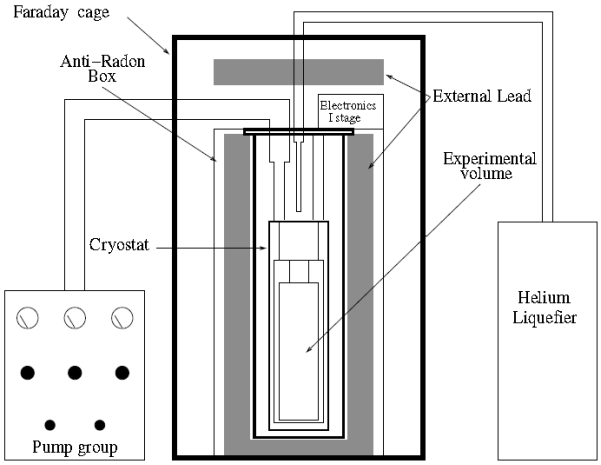

Figure A.2: Scheme of the Hall A setup that hosted Cuoricino and the Three Towers Test and will host CUORE-0.

The Hall C R&D facility

This cryostat was used to operate the detectors described in sections 4.3.1, 4.3.2, 5.4.3, 5.5.2, 5.5.3, 5.6.1 and 5.6.2. The experimental setup, located in the Hall C facility at LNGS, was built at the beginning of the Nineties by Oxford Instruments and is composed by a cryogenic apparatus similar to the Cuoricino one, but with a space for detectors less than one third than Hall A's: a few Cuoricino-like floors can fit in a single test (the typical R&D array is two or three floors high). The cooling power of the system, which is able to reach a minimum temperature of 5.5 mK, is 200 μW at 100 mK. The cryostat's shielding, constituted by $\sim$5 cm of Cu and $\sim$10 cm of Pb, is surrounded by an anti-radon box. Even if proper shielding is present to reduce the background from environmental γs and muons, the Hall C apparatus has a quite high ^{232}Th contamination in the radiation shields. As a consequence, the background in the 0ν-DBD region is rather high compared to Cuoricino. Nevertheless, the Hall C apparatus is well suited for the investigation of the continuous background in the 3-4 MeV region, above the ^{208}Tl line, which is the most interesting region to look at. The dilution unit is shown in Fig. A.3. The refigerator is coupled with a helium liquefier, which is useful to keep the liquid helium level inside the main bath at a constant level.

The L-He free refrigerator in Como

The setup was used to cool-down the detectors described in sections 4.4.1, 5.4.2 and 5.5.1. The dilution refrigerator used in the Cryogenics Laboratory in Como is substantially a small prototype of the cryostat that will be used for CUORE [86]. It is designed to work without the L-He bath: the condensation of the mixture is achieved by means of a cryo-cooler (a Pulse Tube) and a JT expansion. Details on the concept of PT cryo-cooling, which will not be given here, can be found for example in [133]. The cryostat was constructed by the French company Air Liquid and is equipped with two stages that can reach about 65 K and 4 K respectively, by means of a closed cycle regenerative process. The mixture is pushed out of the storage dump and then circulated by means of a turbo-molecular pump, a rotative pump and a compressor. A common LN_2 trap is present on the inlet line followed by an inert gas purifier. The mixture then gets into the dilution unit and is thermalized on the 65 K and 4 K flanges. These two flanges are

cooled directly by the two PT stages. To reduce vibration from the PT cold heads, the flanges are connected to the PT exchangers by means of copper braids (Fig. A.4). A Joule-Thomson expansion is used to condense the mixture given the lack of a 1 K pot. A secondary impedance is installed after the still to ensure an adequate pressure and avoid immediate evaporation. The mixture reaches the mixing chamber after passing by the continuous and step heat exchangers. The advantages of this technique are many, in terms of a large mass experiment like CUORE. Many problems are avoided by incorporating PT cryo-coolers in the system: instabilities due to the evaporation rate of LHe in the main bath, which are an issue for an experiment with planned running of 5 years (the advantage brought by PT-cooling was demonstrated especially by the run described in 4.4.1, where about three months of stable cryogenic conditions were kept unaltered in the Como laboratory); the reduction of live time caused by LHe refills and by the period necessary for detectors to return to a stable condition; fundings for LHe refills. Moreover, the noise that affects the system, now coming from PT vibrations, has been demonstrated to be comparable to the classic system at LNGS [134].

Unfortunately, due to sudden air entrance inside the inner vacuum chamber that damaged the dilution unit, the Como cryostat was damaged by a permanent failure that affected badly the measurements reported in 5.5.1. The problem can be traced back to the presence of a so-called *super-leak*, which is a crack that lets helium through when it is below the 2.18 K lambda point (the temperature at which liquid ^{4}He passes into the superfluid state); at the same time, the crack is impermeable to liquid helium or gaseous helium. Due to this feature, the super-leak (also known as lambda-leak) is extremely difficult to be detected and manifests only when the cool-down process is almost complete, or even a few hours after the system has reached its final base temperature. The position of the super-leak in the Como cryostat was finally determined to be in one of the step heat exchangers by tests based on the local heating of different areas of the dilution unit performed during the mixture's condensation. The various repairing attempts, from the sealing of the heat exchanger with a glycerine-soap compound to soldering, gave only temporary results. The cryostat was dismantled and is currently being repaired by its own manufacturer in Grenoble, France.

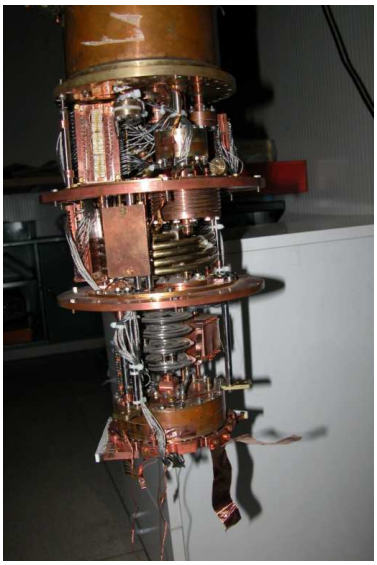

Figure A.3: View of the dilution unit of the Hall C cryostat.

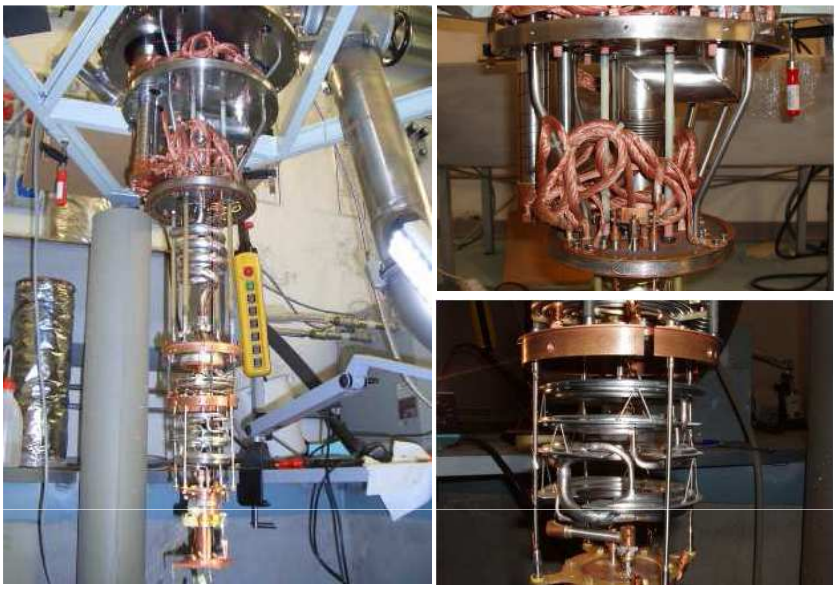

Figure A.4: Pictures of the Como cryostat. View of the dilution unit (left), thermalization of the 65 K and 4 K flanges by means of Cu braids (top right) and the step heat exchangers (bottom right).

Appendix B

Signal read-out

LNGS

The electrical connection of the bolometric signals from 10 mK to room temperature is divided in a first part, made by twisted pairs of low radioactivity constantan wires, and a second part that starts after the mixing chamber, made by twisted pairs of coaxial cables constituted by a core of super-conductive NbTi alloy surrounded by a CuNi low resistance alloy. The wires pass through several thermalization stages and reach the front end electronics boards at room temperature.

The analog part of the readout system performs three operations: thermistor biasing, signal amplification and signal filtering. All the programmable parameters for the front end electronics and for the biasing circuit can be selected remotely using a I2C bus, allowing a channel by channel detector optimization.

Thermistor biasing is accomplished by applying a programmable voltage across a series combination of the thermistor and two load resistors R_L. The value of R_L must be big compared to the sensor's resistance at the working temperature, in order to have constant current bias and high signals (R_L $\sim$27 GΩ is the value chosen for each resistance). In order to account for the spread in the static resistance of different detectors a programmable offset voltage is added to the thermistor signals before amplification: the signal out of the read-out chain is suitable for the range of the ADC boards (from 0 to 10 V).

The amplification stage consists of a first differential low noise differential preamplifier with fixed gain followed by a second programmable gain amplifier, with total gain of the readout chain ranging from 448 to 10000 V/V. The differential configuration has been adopted to minimize cross talk and microphonic noise coming from the wires inside the cryostat. For several readout channels, the preamplifier stage, as well as the load resistors, are housed inside the cryostat, at a temperature of $\sim$110 K: however, the noise reduction provided by cold electronics does not improve the detector's sensitivity for double beta decay search, since other factors dominate the resolution at high energy. The noise coming from the readout chain over the signal bandwidth is dominated by the Johnson noise of the load resistors and from the preamplifier stage.

After the amplification stage, the signal goes through an anti aliasing 6 poles Bessel low-pass filter with an attenuation of 120 dB/decade and programmable cutoff frequency (in the range 8-20 Hz). Signals are then acquired by commercial 16 bit digitizing boards operating in the range from 0 to 10 V. Given the low event rate and the small bandwidth of the signals, a small software trigger algorithm could be incorporated. Signals are

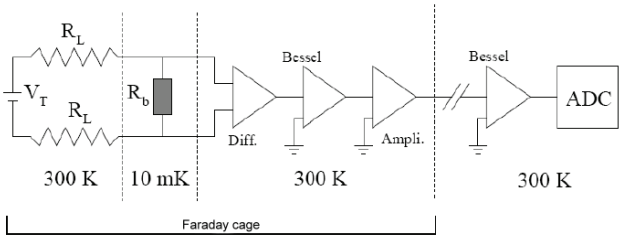

Figure B.1: Read-out setup at LNGS.

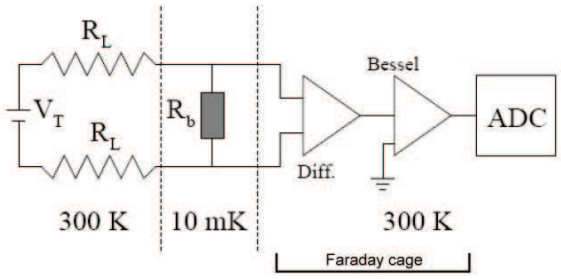

Figure B.2: Read-out setup in Como.

shaped by a digital filter to remove the DC component and are saved if their amplitude exceeds the threshold for a given amount of time. Trigger parameters can be set independently for different channels. When a trigger is found, the signal is recorded in a window of 4 s, with a sampling period of 8 ms (125 Hz). About one second of detector baseline preceding the trigger is recorded too. Selected events are then written to disk for offline processing. In the case of Hall C at LNGS, the DAQ is based on the standard VXI and allows to record the entire pulse shape by acquiring 1024 points for each pulse with a 2 ms step.

Como

Details of the chain until the DAQ will be omitted as the same principles of the other cases hold. As for thermistor biasing, the main difference is that work resistances in the Como setup are of order $\sim$100 kΩ, so that R_L $\sim$200 MΩ are chosen. After the Bessel filter, The signal is sent simultaneously to the Analog to Digital Converter (ADC) and to the trigger that commands it. The acquisition system is made up by a portable LeCroy 8013A crate, a LeCroy 8901A crate controller and ADC LeCroy 6810 modules. If the pulse amplitude is higher than the trigger threshold, the signal is digitalized and then transmitted to a computer (500 MHz Intel with 256 Mb of RAM), where a PCI card works as GPIB communication controller. Every ADC has four differential entries; the trigger, than can be on channel 1, channel 2, external or manual, has the same level for all the channels. The entries are inverting, non inverting, differential or ground. 12-bit digitalization and segmenting memory are used to allow many signals sampling before data is stored. The sample time is 100 ms and the number of samples of the pulse is 1024, with a sample frequency of 5 kHz. Complete information can be found in [135].

Appendix C

First-level data analysis

This appendix is meant to give a brief review on the procedures for first-level data analysis used for the detectors presented in this thesis. For details on data analysis in the Cuoricino experiment, [107] offers a thorough review of every step.

Data analysis is completely performed offline by means of dedicated softwares. Its main goal is the extraction of relevant physics informations from the large amount of raw data recorded by DAQ. The first level is raw detector pulse analysis, aiming at the definition of a proper number of parameters for each pulse and of energy spectra. The second level is a multi-dimensional analysis aiming at obtain the physics results sought for, together with the identification of the various background sources. This appendix is focused on the first level, which is divided in the following steps:

- an accurate evaluation of pulse amplitudes;
- the rejection of spurious pulses;
- the study of coincidences among different channels;
- the study of pulse shapes.

Optimum filtering

Pulses exceeding a given threshold amplitude, depending on the noise RMS, are fully sampled and recorded on a hard disk. In order to maximize the signal–to–noise ratio and to estimate at best its amplitude, each recorded pulse is Optimally Filtered (OF). This technique is frequently used with bolometers to evaluate the amplitude of a signal superimposed on stochastic noise. This algorithm has proved to provide the best estimate of the pulse amplitude under general conditions. Relative to a simple maximum–minimum algorithm, this technique allows the evaluation of the signal amplitude with much higher efficiency resulting in an improvement in energy resolution by as much as a factor of two. To use the OF technique, it is necessary to obtain the noise power spectrum and the response function (i.e. the shape of the signal in a zero noise condition). Given these two elements, the transfer function of the filter can be determined.

The noise power spectrum is periodically evaluated by randomly acquiring a few hundreds of noise pulses. The expected response function of the system (the reference pulse) is obtained by averaging over a large number of real pulses acquired with an external calibration source. When noise is present, the system, constituted by the detector and by the electronics, reacts to the deposition of an energy E in the absorber (seen as instantaneous) with a response

$$R(t) = E \cdot S(t) + N(t)\,,$$

where $S(t)$ is the shape of the signal without the noise $N(t)$. If $N(\omega)$ is the noise power spectrum in the frequency dominion and $H(\omega)$ is the transfer function of the optimum filter, then the signal-to-noise ratio ρ is, by definition, the ratio of the signal's maximum without noise to the root mean square of noise itself:

$$\rho = \frac{\left|E \cdot S(t_M) * H(t_M)\right|}{N_{\mathrm{rms}}} = \frac{\frac{1}{2\pi}E\left|\int_{-\infty}^{+\infty} S(\omega)H(\omega)e^{i\omega t_M}d\omega\right|}{\sqrt{\frac{1}{2\pi}\int_{-\infty}^{+\infty} N(\omega)\left|H(\omega)\right|^2 d\omega}}$$

$S(\omega)$ is the Fourier transform of $S(t)$; the signal reaches its maximum at t_M. It can be demonstrated that the function $H(\omega)$ that maximizes ρ is

$$H(\omega) = K\frac{S^*(\omega)}{N(\omega)}e^{-i\omega t_M}\,,$$

with K an arbitrary constant. The energy deposited in the absorber can be therefore be determined. It is proportional to the maximum of the anti-transform of the optimum filter's output signal:

$$E \propto \max_t \left\{\mathcal{F}^{-1}[S^*(\omega)H(\omega)]\right\}$$

In order to distinguish actual pulses from the randomly acquired ones induced by microphonic or electronic noise, a pulse shape analysis is performed. Each optimally filtered pulse is compared, after proper normalization and time shift, with the optimally filtered reference pulse. Their point-by-point squared differences are taken as a shape parameter. Since noise frequencies are suppressed by Optimum Filter, this parameter is very effective and noise pulses are always fully identified and rejected for energies higher than 50 keV.

N-ples

An important step of the data analysis consists in the production of the so called *n–ple*. The idea is to convert the main characteristics of the pulses in simple information that can be readily understood. Each recorded pulse is associated to a set of parameters that represents its main variables. In this way, the n–ple is produced for each pulse: it is a vector that contains, for example, the OF amplitude, the rise time, the decay time, and other parameters associated with the shape of the recorded signal. The next step consists on the selection of the pulses. To do this it is useful to analyze the n–dimensional space of parameters. This permits identification regularity and the selection of only the pulses with the desired characteristics.

Coincidence analysis

A powerful tool of data analysis is represented by the coincidence analysis. In fact coincidence spectra between different detectors are used to identify background sources. Part of the continuous radioactive background is due to degraded alpha particles that release energy in more than one single crystal. Events can be rejected by making a scatter plot of the energy of simultaneous pulses in two adjacent crystals; α-decays are identified by lines with alpha transition energy equal to the sum of the energy released in the two detectors. This discrimination allows background reduction. The topic has been discussed in Sec. 3.1.1.

Offline stabilization

The offline stabilization procedure used by the CUORE collaboration has already been described in Sec. 2.1.4 and will not be repeated here. Si heaters are connected to each detector to release periodically a fixed amount of energy that generates a detector response as similar as possible to the signal of interest: this is a solution to compensate for thermal instabilities in the cryogenic system. Heater pulses are now flagged in the raw data, which, in Cuoricino, was done only after a few hundred runs; moreover, the hardware flagging of heater pulses performed from that point on was not 100% efficient, leaving some of them identified as signal events. If heater pulses are not flagged in raw data, they must be recognized correctly in order to remove them from spectra and to use them for stabilization: this is done by an offline heater flagging algorithm [107]. On the other hand, the use of the new CUORE DAQ in the Three Towers Test (3.4.2) identifies all heater pulses. No heaters were used in any of the Como runs because they were not allowed by the characteristics of the cryogenic setup.

Calibration and linearization

To obtain an energy spectrum from the recorded pulses, the conversion of their signal amplitudes to energy is necessary. The simple, monolithic bolometric model presented in Chapter 1 assumes the linearity of the OF pulse ΔV with energy; however, several parameters depend on the crystal's temperature, making the corresponding equation non-linear. In the tests performed at LNGS, the relation between ΔV and E is obtained periodically by the use of radioactive calibration ^{238}U and ^{232}Th sources introduced into the lead shields, near the cryostat, to calibrate the spectrum. The ratio of ΔV to E is measured for several γ-lines, and data fits are obtained taking into consideration the fact that the bolometer's resistance and the crystal's heat capacity are temperature dependent. This provides the calibration functions, which are then used to convert the OF amplitudes into energy values.

Glossary

This is a list of some acronyms used in the thesis.

SM	Standard Model (Chap. 1)
PMNS	Pontecorvo Maki Nakagawa Sakata matrix
SNO	Subdury Neutrino Observatory
DBD	Double Beta Decay
NME	Nuclear Matrix Elements
QRPA	Quasi Random Phase Approximation
IBM	Interacting Boson Model
HM	Heidelberg-Moscow
GERDA	GERmanium Detector Array
NEMO	Neutrino Ettore Majorana Observatory
CUORE	Cryogenic Underground Observatory for Rare Events
LNGS	Laboratori Nazionali del Gran Sasso
m.w.e.	meters of water equivalent
ROI	Region Of Interest
BR	Branching Ratio
SM	Single Module (from Chap. 2 on)
NTD	Neutron Transmutation Doping
VRH	Variable Range Hopping
HEM	Hot Electron Model
RAD	Radioactive Array Detector
CAW	CUORE Assembly Working group
SSB	Surface Sensitive Bolometer
TTT	Three Towers Test
HPGe	High Purity Germanium
ICP-MS	Inductively Coupled Plasma Spectrometry
SBD	Surface Barrier Detector
SICCAS	Shanghai Institute of Ceramics Chinese Academy of Science
CTI	Crystal Technology Inc.
GWI	Great Western Inorganic
CCT	Chinese Crystals Test
DFM	Detector Factor of Merit

List of Figures

List of Tables

References

[1] B. Gorion, Die sagen der juden, in *Crowds and Power*, Elias Canetti, 1960. 3

[2] E. Fermi, Z. Physik **88**, 161 (1934). 3

[3] C. Lee, T.D. Yang, Phys. Rev. **104**, 254 (1956). 3

[4] C. Reines, F. Cowan, Phys. Rev. **113**, 273 (1959). 3

[5] K. Kodama *et al.*, Phys. Lett. B **504**, 218 (2001), hep-ex/0012035. 3

[6] D. Davis, R. Harmer and K. Hoffman, Phys. Rev. Lett. **20**, 1205 (1968). 3, 8

[7] V. Bernard, N. Kaiser, and U.-G. Meissner, International Journal of Modern Physics **4**, 193 (1995). 4

[8] F. Maltoni, J. M. Niczyporuk, and S. Willenbrock, Phys. Rev. Lett. **86**, 212 (2001). 5

[9] E. Majorana, Nuovo Cimento **14**, 171 (1937). 6

[10] R. N. Mohapatra and G. Senjanović, Phys. Rev. Lett. **44**, 912 (1980). 7

[11] Strumia and F. Vissani, Neutrino masses and mixings, 2010. 7, 15

[12] B. Pontecorvo, Sov. Phys. JETP **6**, 429 (1958). 8

[13] B. Pontecorvo, Sov. Phys. JETP **33**, 549 (1967). 8

[14] M. Maki, Z. Nakagawa and S. Sakata, Prog. Theor. Phys. **28**, 870 (1962). 8

[15] R. Slansky, S. Raby, T. Goldman, and G. Garvey, The oscillating neutrino, in *Celebrating neutrinos*, Los Alamos Science 25, 1997. 9

[16] R. D. McKeown and P. Vogel, Neutrino masses and oscillations: Triumphs and challenges, 2004. 10

[17] S. Abe *et al.*, Physics Review Letters **100**, 221803 (2008). 10

[18] A. de Gouvea, J. Jenkins, and B. Kayser, Neutrino mass hierarchy, vacuum oscillations, and vanishing u_{e3}, 2005. 9, 11

[19] A. Bellerive, International Journal of Modern Physics A **19**, 8 (2004). 8

[20] Q. R. Ahmad *et al.*, Phys. Rev. Lett. **87**, 071301 (2001). 8

[21] T. Schwetz, M. Trtola, and J. W. F. Valle, New Journal of Physics **10**, 113011 (2008). 9

[22] J. Bonn *et al.*, Nuclear Physics B - Proceedings Supplements **91**, 273 (2001). 11

[23] G. L. Fogli *et al.*, Phys. Rev. D **78**, 033010 (2008). 11

[24] M. Goeppert-Mayer, Phys. Rev. **48**, 512 (1935). 11

[25] J. Schechter and J. W. F. Valle, Physics Review **D25**, 2951 (1982). 14, 15

[26] V. Rodin, 2009. 14

[27] E. Caurier, G. Martinez-Pinedo, F. Nowacki, A. Poves, and A. P. Zucker, 2005. 14

[28] I. Ogawa *et al.*, Nuclear Physics A **730**, 215 (2004). 16

[29] H. V. Klapdor-Kleingrothaus *et al.*, European Physics Journal **A12**, 147 (2001). 16, 17

[30] H. V. Klapdor-Kleingrothaus, I. V. Krivosheina, A. Dietz, and O. Chkvorets, Physics Letters **B586**, 198 (2004). 16, 17, 18, 35

[31] R. Arnold *et al.*, Physics Review Letters **95**, 182302 (2005). 16, 17, 18

[32] R. Arnold *et al.*, Nuclear Physics A **658**, 299 (1999). 16

[33] F. A. Danevich *et al.*, Physics Reviews **C68**, 35501 (2003). 16

[34] C. Arnaboldi *et al.*, Phys. Rev. C **78**, 35502 (2008). 16, 17, 67

[35] R. Bernabei *et al.*, Physics Letters **B546**, 23 (2002). 16

[36] J. Argyriades, Measurement of the double beta decay half-life of 150-nd and search for neutrinoless decay modes with the NEMO-3 detector, 2008. 16

[37] R. Arnold *et al.*, Nuclear Instrument Methods **A536**, 79 (2005). 16

[38] A. Staudt, K. Muto, and H. V. Klapdor-Kleingrothaus, Europhysics Letters **13**, 31 (1990). 17

[39] H. V. Klapdor-Kleingrothaus, I. V. Krivosheina, A. Dietz, and O. Chkvorets, Mod. Phys. Lett. **A16**, 2409 (2001). 17

[40] GERDA, collaboration, Proposal to LNGS P38/04 (2004). 17, 37

[41] E. Fiorini and T. Niinikoski, Nucl. Instr. Meth. **A 224**, 83 (1984). 19

[42] D. McCammon *et al.*, J. Appl. Phys. **56**, 1257 (1984). 19

[43] N. Mott and J. Davies, Phil. Mag. B **42**, 845 (1980). 22

[44] B. Shklovskii and A. Efros, *Electronic Properties of Doped Semiconductors* (Springer, Berlin, 1984). 22

[45] D. McCammon, (2005), physics/0503086. 23

[46] B. Shklovskii and A. Efros, Sov. Phys. - JETP **33**, 468 (1971). 23

[47] J. Zhang *et al.*, Phys. Rev. B **57**, 4472 (1998). 23

[48] M. Pedretti, *The single module for Cuoricino and CUORE detectors: tests, construction and modelling*, PhD thesis, Insubria University, 2004. 25, 172, 181, 187

[49] J. C. Mather, Appl. Opt. **21**, 1125 (1982). 31

[50] V. A. Rodin, A. Faessler, F. Simkovic, and P. Vogel, Assessment of uncertainties in qrpa 0nu beta beta-decay nuclear matrix elements, 2006. 33, 35

[51] O. Civitarese and J. Suhonen, Nuclear Physics **A761** (2005). 33, 35

[52] E. Caurier, F. Nowacki, and A. Poves, European Physics Journal **A36** (2008). 33, 35

[53] T. Tomoda, Rept. Prog. Phys. **54** (1991). 33

[54] S. Stoica and H. V. Klapdor-Kleingrothaus, Physics Review **C63** (2001). 33

[55] A. Staudt, T. T. S. Kuo, and H. V. Klapdor-Kleingrothaus, Physics Review **C46** (1992). 33

[56] C. Barbero, F. Krmpotic, A. Mariano, and D. Tadic, Nuclear Physics **A650** (1999). 33

[57] A. Faessler and F. Simkovic, J. Phys. **G24** (1998). 33

[58] G. Pantis, F. Simkovic, J. D. Vergados, and A. Faessler, Phys. Rev. **C53** (1996). 33

[59] F. Simkovic, G. Pantis, J. D. Vergados, and A. Faessler, Phys. Rev. **C60** (1999). 33

[60] J. Engel, P. Vogel, X.-D. Ji, , and S. Pittel, Physics Letters **B225** (1989). 33

[61] M. Moe and P. Vogel, Ann. Rev. Nucl. Part. Sci. **44** (1994). 33

[62] J. Suhonen, O. Civitarese, and A. Faessler, Nuclear Physics **A543** (1992). 33

[63] M. Aunola and J. Suhonen, Nuclear Physics **A643** (1998). 33

[64] K. Muto, E. Bender, and H. V. Klapdor, Z. Phys. **A334** (1989). 33

[65] V. E. Guiseppe *et al.*, (2008), 0811.2446. 37

[66] R. Ardito *et al.*, (2005), hep-ex/0501010. 37

[67] D. Akimov *et al.*, Nucl. Phys. Proc. Suppl. **138**, 224 (2005). 37

[68] NEMO, collaboration, (2004). 37

[69] A. Alessandrello *et al.*, Physical Review Letters **82**, 513 (1999). 39

[70] A. Alessandrello *et al.*, Nuclear Instruments and Methods in Physics Research A **440**, 397 (2000). 39

[71] A. Alessandrello *et al.*, Nuclear Instruments and Methods in Physics Reasearch A **370**, 269 (1996). 39

[72] J. Barea and F. Iachello, Physical Review C **79**, 044301 (2009). 41, 42

[73] T. B. Coplen *et al.*, Pure and Applied Chemistry **74-10**, 1987 (2002). 40

[74] N. D. Scielzo *et al.*, Physical Review C **80**, 025501 (2009), arXiv:0902.2376v1 [nucl-ex]. 40

[75] E. E. Haller, Infrared Physics and Technology **35**, 127 (1994). 44, 117

[76] Alessandrello *et al.*, Nuclear Instruments and Methods in Physics Research Section B: Beam Interactions with Materials and Atoms **93**, 322 (1994). 44

[77] A. Alessandrello *et al.*, Journal of Physics D: Applied Physics **32**, 3099 (1999). 44

[78] E. Andreotti, *Application of doped semiconductor devices to the development of bolometric detectors to be used in experiments for the measurement of the neutrino mass*, PhD thesis, Insubria University, 2009. 48

[79] M. Mancuso, Caratterizzazione a temperature criogeniche di termistori drogati tramite trasmutazione neutronica per l'esperimento CUORE-0, Master's thesis, Insubria University, 2009. 49, 121, 125

[80] M. Barucci *et al.*, Journal of Low Temperature Physics **123**, 303 (2001). 49, 88

[81] A. Alessandrello *et al.*, Czechoslovak Journal of Physics **46-S5**, 2893 (1996). 49, 50, 108, 121, 187

[82] P. Gorla, *Optimization of the CUORE detector performance*, PhD thesis, Milano Bicocca University, 2005. 54, 61, 95

[83] S. Pirro, Proceedings of the 11th International Workshop on Low Temperature Detectors - LTD-11 **559-2**, 672 (2006). 54

[84] A. Giachero, *Characterization of cryogenic bolometers and data acquisition system for the CUORE experiment*, PhD thesis, Genova University, 2008. 54, 61, 70, 181

[85] A. Nucciotti *et al.*, AIP Conference Proceedings **1185**, 677 (2009). 55

[86] A. Nucciotti *et al.*, Journal of Low Temperature Physics **151, 3-4**, 662 (2008). 55, 219

[87] M. Pedretti, N. D. Scielzo, E. B. Norman, and C. Angell, APS Meeting Abstracts , L3+ (2009). 56

[88] M. Ambrosio *et al.*, Physical Review D **52,7**, 37933802 (1995). 56

[89] E. Andreotti *et al.*, Muon-induced backgrounds in the Cuoricino experiment, Accepted by Astroparticle Physics and in press, 2010, arXiv:0912.3779v2 [nucl-ex]. 56, 71

[90] ILIAS project, *Home page*, http://www-ilias.cea.fr/. 56

[91] S. Cebrian *et al.*, Astroparticle Physics **33**, 316 (2010). 56

[92] S. Elliott and P. Vogel, Annual Review of Nuclear and Particle Science **52**, 115 (2002). 57

[93] F. Bellini *et al.*, Astroparticle Physics **33**, 169 (2010). 57

[94] S. Capelli, *Background analysis of the experiments MiDBD, CUORICINO and CUORE*, PhD thesis, Milano Bicocca University, 2004. 65

[95] K. W. Bagnall, The chemistry of polonium, in *Advances in inorganic chemistry and radiochemistry*, Academic Press, 1962. 67

[96] L. Foggetta *et al.*, Applied Physics Letters **86**, 134186 (2005). 73

[97] L. Foggetta *et al.*, Composite macro-bolometers for the rejection of surface radioactive background in rare-event experiments, Submitted in January 2010. 74, 76, 77

[98] C. Salvioni, Discriminazione attiva del fondo in esperimenti bolometrici per la ricerca del doppio decadimento beta, Master's thesis, Insubria University, 2005. 74

[99] C. Nones, *Identification of surface events in massive bolometers for the search for rare events in the CUORE and EDELWEISS experiments*, PhD thesis, Milano Bicocca University, 2007. 74, 77

[100] P. Gorla *et al.*, Journal of Low Temperature Physics **151**, 854 (2008). 77

[101] L. Gironi, Scintillating bolometers for double beta decay search, 2009, Proceedings of 11th Pisa Meeting on Advanced Detectors. 77

[102] M. Grassi, Advanced technologies for radioactive background suppression in a bolometric search for neutrinoless double beta decay, Master's thesis, Insubria University, 2010. 77

[103] M. Biassoni, Studio comparativo di tecniche per la riduzione del fondo radioattivo alfa, in vista dell'esperimento CUORE, svolto per mezzo di un rivelatore bolometrico modulare di TeO_2, Master's thesis, Milano Bicocca University, 2009. 79, 85

[104] M. Wójcik and G. Zuzel, Topical Workshop on Low Radioactivity Techniques: LRT 2006 **897**, 53 (2007). 80

[105] S. D. Domizio, *Search for Double Beta Decay to excited states with Cuoricino and data acquisition system for CUORE*, PhD thesis, Genova University, 2009. 83

[106] M. Vignati, *Model of the response function of CUORE bolometers*, PhD thesis, Rome Sapienza University, 2009. 83

[107] A. Bryant, *A search for Neutrinoless Double Beta Decay of* ^{130}*Te*, PhD thesis, University of California, Berkeley, 2010. 85, 225, 227

[108] S. Capelli, Internal CUORE collaboration report, 2010. 85

[109] G. K. White, S. J. Collocott, and J. G. Collins, Journal of Physics: Condensed Matter **2**, 7715 (1990). 88, 89, 108

[110] N. Uchida, Physical Review B **4**, 3736 (1971). 88

[111] R. H. Carr, R. D. McCammon, and G. K. White, Proceedings of the Royal Society of London A **280**, 72 (1964). 89

[112] C. Arnaboldi *et al.*, Journal of Crystal Growth , arXiv:1005.3686v1 [cond-mat.mtrl-sci], Accepted in June 2010. 89, 90, 92, 105

[113] C. D. Brandle, Journal of Crystal Growth **264**, 593 (2004), Proceedings of the Symposium - Progress in Crystal Growth. 106

[114] P. Rudolph, M. Neubert, S. Arulkumaran, and M. Seifert, Crystal Research and Technology **32**, 35 (1997). 106

[115] NASA Electronic Parts and Packaging, *Assurance Issues Related to Electronic Wire Bonds*, http://nepp.nasa.gov/wirebond/. 118

[116] G. Harman, *Wire Bonding in Microelectronics - Third edition* (McGraw-Hill, 2009). 118

[117] West-Bond Inc., *Model 7700E, Ball-Wedge Wire Bonder, Manual X-Y-Z specifications*, http://www.westbond.com/7700espc.htm. 119

[118] M. Pecht, P. McCluskey, and J. Y. Evans, Failures in electronic assemblies and devices, in *Product Integrity and Reliability in Design*, Springer, 2001. 119

[119] E. Aubourg *et al.*, Journal of Low Temperature Physics **93**, 289 (1993). 121

[120] COMSOL AB, *COMSOL Multiphysics*, http://www.comsol.com/products/multiphysics/. 123

[121] E. E. Haller, K. M. Itoh, and J. W. Beeman, Submillimetre and Far-Infrared Space Instrumentation, Proceedings of the 30th ESLAB Symposium held in Noordwijk **ESA SP-388**, 115 (1996). 134

[122] E. Olivieri, M. Barucci, J. Beeman, L. Risegari, and G. Ventura, Journal of Low Temperature Physics **143, 3-4**, 153 (2006). 163

[123] R. Gilbert *et al.*, The Secret of Monkey Island, in *The Monkey Island series*, LucasArts Entertainment Company, 1990. 177

[124] J. W. Sinclair, Journal of Adhesion **38**, 219 (1992). 184

[125] J. J. Imaz, N. Markaide, and M. J. Jurado, European Polymer Journal **28(3)**, 299 (1992). 184

[126] F. Lapique and K. Redford, International Journal of Adhesion and Adhesives **22**, 337 (2002). 184, 185

[127] A. Salvini *et al.*, Journal of Physics: Conference Series **41**, 417 (2006). 185

[128] Huntsman Advanced Materials, *Araldite 2012 technical data sheet*, https://www.huntsmanservice.com/. 186

[129] F. Pobell, *Matter and Methods at Low Temperatures -Third edition* (Springer, 2007). 187, 217

[130] D. H. Kaelble, J. Moacanin, and A. Gupta, Physical, mechanical properties of cured resins, in *Epoxy Resins. Chemistry and Technology - Second edition*, Marcel Dekker Inc., 1988. 188

[131] S. G. Prolongo, G. del Rosario, and A. Urena, International Journal of Adhesion and Adhesives **26**, 125 (2006). 188

[132] G. K. White and P. J. Meeson, *Experimental Techniques in LowTemperature Physics -Fourth edition* (Oxford University Press, 2002). 217

[133] R. Radebaugh, Pulse tube cryocoolers, in *Low temperature and cryogenic refrigeration*, NATO Science Series, 2003. 219

[134] S. Sangiorgio, *Advanced detector techniques for the CUORE experiment*, PhD thesis, Insubria University, 2006. 220

[135] L. G. Foggetta, Sviluppo di un sistema di acquisizione per rivelatori criogenici innovativi, Master's thesis, Insubria University, 2004. 224

Acknowledgements

And so it's over. Only now that I come to the acknowledgements, I realize that a part of my life has just closed. I really need to thank anyone I met and worked with during these years. There are many, different reasons for acknowledgement; but the one these people share is that, somehow, I managed to learn from all of them.

I thank my Ph.D. advisor, Prof. Andrea Giuliani, because I learnt from him the facets and the challenges of scientific research. My acknowledgment also goes to the *seniors* from the CUORE collaboration in Milan and LNGS: the moments I spent working at the Laboratory have truly been the most intense ones in my experience. And a big "Thank you" to all the talented Ph.D. students–fresh Postdocs in the CUORE collaboration I had the pleasure to spend time with. I cannot mention you all but I believe you know very well who you are.

Among those who dwell in the *interregnum* previous to research senior-hood, often long and wearing, my very special thanks go to Marisa Pedretti and Paolo Gorla. The first one never ceased to support me or denied me her precious help: I am grateful to her generosity and fine competence. As for the other one, I thank him for failing to disguise his love for this work under his outstanding sarcasm and for conveying his enthusiasm to me in my work days at Gran Sasso (and also, yes, for putting the wax on, saving the cheerleader, and so on).

Thank you to the girls -and one boy- from the CryoLab in Como: Claudia Rusconi and Erica Andreotti (you have been so precious during the last years); Monica Pellicciari (with whom I started this experience); and Manuela Grassi, Marica Rebai, Margherita Tenconi, Luca Foggetta. Again, there are many reasons, but above all I enjoyed sharing the glorious madness of our old laboratory with your unique personalities.

The last lines are for people who have been particularly close to me during the Ph.D. years (or a part of them). For my parents, who have endowed me with the freedom of being proud for taking the responsibilities of my own deeds. For my closest friends Alessandra and Alberto, who have been constantly catching me just in time, in these years, when I was not minding the steps. And for Marco, who gave me continuous, reckless support, and also because of other valid reasons: the kind of stuff ranging from Templar churches to forks, and books on sailors. The help these people gave me is priceless. But I'm going to tell them in Italian, which I'm so much better at.